

ABSTRACT

Title of Dissertation: PLASMA OXIDIZED AlO_x TUNNEL
BARRIERS AND Nb/Al BILAYERS
EXAMINED BY ELECTRICAL TRANSPORT

Zachary Barcikowski
Doctor of Philosophy, 2022

Dissertation directed by: Prof. John Cumings
Department of Material Science
and Engineering
Dr. Joshua M. Pomeroy
National Institute of Standards and Technology

Results are reported for two related projects: the examination of material stability of plasma oxidized, free energy confined aluminum oxide and the evolution of the electronic structure in Nb/Al bilayers as a function of Al thickness. Al/ AlO_x and Nb are critical materials for solid-state quantum computing, mostly driven by the relatively large superconducting gap of Nb (1.5 meV) and ~ 2 nm diffusion-limited oxide formed on Al with room temperature thermal oxidation. Plasma oxidation and free energy confinement of AlO_x with Co electrodes is used to produce homogeneous tunnel barriers with an O/Al ratio approaching Al_2O_3 . The weeks long time stability of resulting metal-insulator-metal tunnel junctions is found to greatly improve, as resistance measured over ≈ 8 months increases by 34.0 ± 5.4 % in the confined devices (Co/ AlO_x /Co) compared to an increase of 95.4 ± 7.8 % in unconfined devices (Co/Al/ AlO_x /Co). In the second experiment, normal metal-

insulator-superconductor (NIS) tunnel junctions are used to study the interplay of superconducting properties in Nb/Al bilayers as a function of Al thickness. The performance of superconducting quantum information devices is sensitive to the detailed nature of the superconducting state in the materials, which is drastically altered through proximity in the case of dissimilar materials. I extract the effective Nb/Al quasiparticle DOS from the conductance spectra of NIS tunnel junctions with Nb/Al superconducting electrodes. The conductance spectra evolve from a primarily single-gapped structure for thin Al ($\lesssim 20$ nm) to a dual gapped structure at thicker Al. I present a modified Blonder-Tinkham-Klapwijk (BTK) based model interpreting the conductance spectra as a steady-state convolution of the Al-like DOS and the Nb-like DOS in the bilayer. These results inform future device design for quantum information by providing additional grounding to current proximity effect theory.

PLASMA OXIDIZED AlO_x TUNNEL BARRIERS
AND NB/AL BILAYERS EXAMINED BY ELECTRICAL
TRANSPORT

by

Zachary Barcikowski

Dissertation submitted to the Faculty of the Graduate School of the
University of Maryland, College Park in partial fulfillment
of the requirements for the degree of
Doctor of Philosophy
2022

Advisory Committee:
Prof. John Cumings, Chair/Advisor
Dr. Joshua M. Pomeroy, Co-Advisor
Prof. Ichiro Takeuchi
Prof. Lourdes Salamanca-Riba
Prof. Daniel Lathrop

© Copyright by
Zachary Barcikowski
2022

Foreword

Chapter 3 is partially reproduced from Z. S. Barcikowski, J. M. Pomeroy. Reduced resistance drift in tunnel junctions using confined tunnel barriers. *J. Appl. Phys.* 122, 185107 (2017); <https://doi.org/10.1063/1.4996497>, with the permission of AIP publishing. (I am the first author of this paper).

Acknowledgments

I would first like to thank my research advisor at NIST, Dr. Joshua Pomeroy. The training I received under Josh has been essential in my development as a young scientist. Josh guided me with great patience, providing support and words of wisdom that I will continue to carry moving forward. I would also like to thank my UMD advisor Dr. John Cumings. John was always available with insightful advice and our discussions always had a way bringing me back to center, helping me to see the way forward more clearly.

Thank you to Dr. Michael Stewart, Jr. Stew's support and friendship through the years has meant the world to me. I thank him for always having his door open to me, where our discussions helped me through both professional and personal challenges. Thanks are also due to Dr. Neil Zimmerman, who has always been one of my biggest supporters and provided exceptional encouragement throughout my graduate career. In addition, I would like to thank Dr. Garnett Bryant for funding my position at NIST.

I've had the pleasure of being surrounded by exceptional friends and researchers at NIST over the years including Dr. Kevin Dwyer, Dr. Ryan Stein, Dr. Yanxue (Shirley) Hong, Dr. Ke (Kirk) Tang, Dr. Aruna Ramanayaka, Dr. Hyun Soo Kim, and Dr. Sujitra Pookpanratana. Thank you all for our helpful

interactions and discussions. I look forward to plenty more in the future. To all of my friends outside of school, thank you for all the good times and keeping me sane through this process.

I cannot thank my parents Carl and Sherry enough. Thank you for always being in my corner and believing in me. This thesis and degree would not have been possible without the endless love and encouragement that you've provided from day one. I look up to the example that you have both set as parents and am beyond grateful for everything you've done for me.

Finally, I would like to thank my wife and love of my life, Ashley. This thesis is dedicated to you, my rock and inspiration. I cannot wait for what lies ahead in our lives together. Peas and carrots.

Table of Contents

Foreword	ii
Table of Contents	v
Permission to Reuse Content	viii
List of Tables	ix
List of Figures	x
Chapter 1: Introduction	1
1.1 Overview	1
1.2 Quantum Computing	2
1.3 Materials for Quantum Information	4
1.3.1 Aluminum Oxide	6
1.3.2 Al and Nb	10
1.4 Introduction to Superconductivity	12
1.4.1 Superconducting Proximity Effect	17
1.5 Objectives	18
1.6 Outline	21
Chapter 2: Experimental Methods	24
2.1 Context	24
2.2 Wafer Fabrication System	25
2.3 Tunnel Junction Fabrication Process	36
2.3.1 Metals Deposition	36
2.3.2 Shadow Masks	40
2.3.3 Plasma Oxidation	45
2.4 Device Characterization	50
2.4.1 Room Temperature Device Characterization	51
2.4.2 Cryogenic Device Characterization	60
2.5 Chapter Summary	67
Chapter 3: Plasma Oxidation for AlO _x Tunnel Barriers	69
3.1 Context	69
3.1.1 Background	70
3.2 Plasma Oxidation of thin Al layers on Co	73

3.2.1	Oxidation of Al	73
3.2.2	Plasma Oxidation Recipe	79
3.3	Reduced Resistance Drift of Co Confined AlO _x Tunnel Barrier	92
3.3.1	Experiment	92
3.3.2	Results	97
3.3.3	Discussion	104
3.4	Chapter Summary	107
Chapter 4: Photoelectron Spectroscopy for Ultrathin AlO _x Layers		110
4.1	Context	110
4.2	Background - Photoelectron Spectroscopy	112
4.3	Experimental Apparatus	115
4.4	Monitoring Oxidation with XPS	118
4.5	Film Thickness Determination with ARXPS	120
4.6	Chapter Summary	133
Chapter 5: Tunneling Spectroscopy of Nb-Al Based NIS Junctions		137
5.1	Context	137
5.2	Experiment	139
5.2.1	Fabrication	139
5.2.2	Device Characterization	142
5.2.3	NIS Tunneling	155
5.2.4	Nb/Al bilayer - quasiparticle density of states	160
5.2.5	NIS conductance	165
5.2.6	Characteristic features	165
5.3	Results	168
5.3.1	Conductance feature trends	170
5.3.2	Temperature dependence	176
5.4	Discussion	178
5.4.1	Weighted sum model	178
5.4.2	BTK fitting of conductance spectra	185
5.5	Chapter summary	190
Chapter 6: Conclusions and Future Studies		192
6.1	Conclusions	192
6.1.1	Plasma Oxidation for AlO _x Tunnel Barriers	192
6.1.2	Photoelectron Spectroscopy for Ultrathin AlO _x Layers	195
6.1.3	Tunneling Spectroscopy of Nb-Al Based NIS Junctions	197
6.2	Future Studies	200
6.2.1	Quantitative XPS Analysis of AlO _x : Correlation with WKB transport modeling	200
6.2.2	Monolithic Nb/Al-based resonators	201
Appendix A Monolithic Superconducting Resonators For Gate-Based Quantum Dot Readout		203

Appendix B:Cross sectional SEM of Nb/Al based NIS junctions	214
Bibliography	219

Permission to Reuse Content

Requirements to be followed when using any portion (e.g., figure, graph, table, or textual material) of an IEEE copyright paper in a thesis:

1. In the case of textual material (e.g., using short quotes or referring to the work within these papers) users must give full credit to the original source (author, paper, publication) followed by the IEEE copyright line ©2011 IEEE
2. In the case of illustrations or tabular material, we require that the copyright line ©[Year of original publication] IEEE appear prominently with each reprinted figure and/or table
3. If a substantial portion of the original paper is to be used, and if you are not the senior author, also obtain the senior author's approval.

List of Tables

2.1	QCM input parameters	39
3.1	As-fabricated R·A products and *10 day tunnel barrier characteristics	92
5.1	3.9 K BTK model fits with Dynes broadening, as seen in Fig. 5.25. .	186
5.2	15 mK BTK model fits with Dynes broadening, corresponding to the data in Fig. 5.26.	188

List of Figures

1.1	Examples of semiconductor and superconductor qubit implementations	5
1.2	Historical progression of superconducting qubit coherence times	7
1.3	Microscopic TLS in amorphous AlO_x	8
1.4	BCS single-particle density of states and temperature dependence of the superconducting energy gap	16
2.1	CAD rendering of the tunnel junction fabrication system	26
2.2	Stainless steel wafer cassettes	28
2.3	Wafer cassettes on a transfer rod and in the MMAPS magazine	30
2.4	RGA spectrum of deposition system at base pressure	32
2.5	5-axis sample manipulator on the deposition chamber	34
2.6	Generation I shadow mask and die designs	43
2.7	Generation II shadow mask and micrograph of an “A” die	46
2.8	Optical spectrum of a DC oxygen plasma	48
2.9	XPS survey scan of a Si wafer surface before and after oxygen plasma cleaning	49
2.10	Four point I-V measurement configurations on an “A” die dog bone wire and tunnel junction.	52

2.11	dI/dV(V) demonstrating “negative resistance” correction	54
2.12	Electron energy diagram in a metal-insulator-metal tunnel junction .	57
2.13	Chow-WKB fits of dI/dV(V) spectra	61
2.14	24 pin DIP with “A” dies	63
2.15	Tunnel junction devices mounted in the cryocooler and DR	64
2.16	Tunnel junction conductance as a function of temperature	66
3.1	Oxygen content thickness with plasma oxidation time	78
3.2	Oxygen radical intensity with power and pressure for an oxygen plasma	82
3.3	Oxygen Paschen curve for a 1.13 cm electrode spacing	84
3.4	Oxygen plasma with an electrode spacing of 3.87 cm	86
3.5	Changes in the oxygen plasma from electrode spacing	87
3.6	Photovoltage with applied plasma power	88
3.7	B type device and RA product with oxidation time	91
3.8	RA product and barrier width drift for several oxidation times	93
3.9	Drift in WKB barrier heights for several oxidation times	94
3.10	Tunnel junction stack for the confined and unconfined devices	96
3.11	Resistance with temperature for a confined and unconfined device . .	98
3.12	RA product drift for the confined and unconfined device	100
3.13	dI/dV(V) for a confined an unconfined device	102
3.14	Drift in tunnel barrier characteristics for a confined and unconfined device	105
4.1	XPS spectra for Au and Al/AlOx	113

4.2	CAD rendering of the SPECs photoelectron spectroscopy system . . .	116
4.3	XPS measurement diagram	118
4.4	XPS spectra of AlOx for different oxidation times	121
4.5	XPS spectrum of Al/AlOx on Nb	122
4.6	ARXPS diagram and Al/AlOx XPS waterfall plot	126
4.7	Hill equation plot and film stack for Al/AlOx devices	127
4.8	Comparison of WKB and ARXPS determined thicknesses	129
4.9	AlOx/Al/Nb waterfall and Hill equation plots	131
4.10	AlOx/Co waterfall and Hill equation plots	132
5.1	NIS film stack and crossed wire tunnel junction	141
5.2	Room temperature conductance per square of the Nb/Al bilayers . .	143
5.3	Room temperature RA products and representative WKB fit	145
5.4	Room temperature WKB fit parameters for Nb/Al tunnel junctions .	147
5.5	RMS roughness of Nb/Al bilayers and specific conductance	148
5.6	Nb/Al residual resistivity ratio with Al thickness	149
5.7	NIS wide bias $dI/dV(V)$ as a function of temperature	151
5.8	Nb/Al bilayer T_c with Al thickness	153
5.9	Nb/Al stretched I_c transition and R_vT	154
5.10	Evolution in calculated $dI/dV(V)$ with Dynes broadening and BTK Z	158
5.11	Thickness dependence of the order parameter and energy gap	163
5.12	Nb/Al quasiparticle density of states calculated with the Usadel equa- tions	164

5.13	NIS $I(V)$ and $dI/dV(V)$ at 15 mK	166
5.14	Characteristic features observed in Nb/Al conductance spectra	167
5.15	Effective electron temperature from coherence peak height	169
5.16	$dI/dV(V)$ evolution with Al thickness at 15 mK	170
5.17	$dI/dV(V)$ evolution with Al thickness at 15 mK	172
5.18	Thick Al bilayer $dI/dV(V)$ with sub-gap shoulder feature	174
5.19	Temperature dependence of the sub-gap shoulder feature	175
5.20	Zero-bias conductance as a function of Al thickness and peak voltage	177
5.21	Zero-bias conductance as a function of temperature	179
5.22	Dual-gapped transport diagram	180
5.23	Normalized $dI/dV(V)$ peak height as a function of thickness	182
5.24	Calculated weighted-sum NIS conductance spectra	183
5.25	3.9 K NIS conductance spectra with BTK fits	186
5.26	15 mK NIS conductance spectra with BTK fits	189
6.1	Charge offset drift for Al/ AlO_x /Al SETs	196
A.1	LC resonator design	206
A.2	Resonator fabrication process	207
A.3	Microscope images of parallel LC resonator	207
A.4	Custom resonator measurement PCB and measurement diagram in the DR	208
A.5	Resonator transmission measurements at 15 mK	209
A.6	Resonator quality factor	210

A.7	NbTiN resonator and transmission measurements	211
A.8	Homodyne detection circuit	212
B.1	Cross sectional SEM image of an Nb/Al-based NIS tunnel junction .	216
B.2	Cross sectional SEM comparison	217
B.3	Al thickness correction	218

Chapter 1: Introduction

1.1 Overview

Solid-state quantum computing is gradually approaching experimental reality, evidenced by milestones such as Google’s claim of demonstrating “quantum supremacy”, where a quantum computer solves a particular problem exponentially faster than possible with a classical computer [1]. Yet many challenges remain in realizing fault-tolerant large-scale systems, as reduced device error rates must be demonstrated in scalable platforms [2]. Quantum computing hardware, including ancillary hardware such as control circuitry, is being developed in a range of platforms, each with their own merits. One common thread is the benefit that can be gained in materials optimization. In other words, moving beyond down-selection of materials to instead working to improve and further understanding material properties will open new experimental pathways for quantum computing systems. I will begin with a brief introduction to quantum computing, followed by a discussion on several materials critical for quantum information (Al, AlO_x, Nb), including efforts to manipulate material properties through processing and proximity effects. An introduction to superconductivity is also given to provide context for the interplay between Nb and Al thin films.

1.2 Quantum Computing

The advantage of quantum computing over classical computing stems from a fundamental difference in how information is encoded and processed. Classical bits are binary and therefore can assume one of two states, typically realized by transistors in an on (“1”) or off (“0”) state. Naturally, the processing power of classical systems has progressed over time by increasing the number of transistors found on a given integrated circuit, enabled by a continual decrease in feature size. This results in a linear relationship between the number of bits N and the number of states that can be simultaneously represented. However, the size of a transistor can only be made so small before reaching practical limitations based on leakage/thermal dissipation or fundamental limitations based on quantum effects [3, 4]. In theory, quantum computing outperforms classical computing by leveraging quantum superposition and entanglement. As opposed to a binary bit state, a qubit state (i.e., quantum bit state) can assume a coherent superposition of two basis states given by $|\Psi\rangle = \alpha |0\rangle + \beta |1\rangle$, where α and β are probability amplitudes with $|\alpha|^2 + |\beta|^2 = 1$. In other words, the qubit can assume the analogous classic states “0” and “1” states simultaneously. Multiple qubits can be correlated, or entangled, to form a state which is a linear combination of the constituent qubit states. Therefore, the computing power of a classical system scales with the number of bits N and the computing power of a quantum computer scales as 2^N .

The capabilities afforded by quantum computing comes at the cost of fragility. Unintended interactions of a qubit with its environment can cause decoherence, or a

loss of information from the original coherent qubit state. A key metric for describing qubits is the time over which this information is maintained, called the coherence time (T_2). This time is governed by effects such as relaxation from an excited state to a ground state or, since the qubit state has both phase and amplitude information, a loss of phase coherence (i.e., dephasing). A qubit's coherence time is typically compared to the gate time for a given architecture. The gate time describes how long it takes to make a single manipulation of a qubit state. In essence, efficiently performing a quantum algorithm requires a large number of gate operations, or manipulations, prior to a loss of coherence. Therefore, an ideal qubit architecture would have a long coherence time compared to the gate time. Limitations to both are highly dependent on the material platform or operation scheme being implemented for a given architecture.

Physical realization of qubits have been demonstrated for a number of material systems, including superconducting tunnel junctions [5], defect centers in diamond [6], trapped ions [7], semiconductor devices [8], etc. While each of these material platforms excel for different reasons, merging elements from several platforms will likely be required in advancing towards large-scale quantum computing. For example, merging superconducting and semiconducting systems is of great interest to the community to leverage benefits of each platform. Metal-oxide-semiconductor (MOS) qubits, such as those in Si, typically encode information in the occupation or spin of electrons in quantum dots. An example, taken from Ref.[8], is shown in Fig.1.1(a) of a spin qubit in a Si quantum dot architecture, which is electrostatically defined using Al/ AlO_x gates. Long coherence times of several hundred

microseconds have been realized for single electron spins in Si [9], but the typical gate complexity and the short range connectivity between qubits makes scaling to larger systems difficult. Superconducting qubits, such as the transmon qubits, are more straightforward to couple together and have relatively fast gate times. The Transmon qubit in Fig.1.1(b), taken from Ref.[5] is made up of superconducting tunnel junctions, or Josephson junctions, shunted by an interdigitated capacitor. Coupling between qubits is typically mediated by superconducting resonators, providing a relatively simple method to connect qubits with a comparatively large coupling strength. However, the coherence time for superconducting qubits such as the Transmon is small ($\sim 100 \mu\text{s}$) compared to semiconductor spin qubits (up to seconds or minutes) [5, 10, 11, 12]. Combining elements of these systems to take advantage of both has already been demonstrated, for example by embedding semiconductor spin qubits in superconducting cavities to increase coherence times or coupling superconducting and semiconductor qubits with superconducting resonators to merge long coherence times with long-range coupling. [13, 14]. Merging these material platforms continues to progress as mutually compatible materials and device designs are studied [15].

1.3 Materials for Quantum Information

Much of the progress in advancing quantum computing has focused on device design or operation schemes, intended to minimize the influence of material imperfections [2]. Take the plot in Fig.1.2 for example, where improvements to

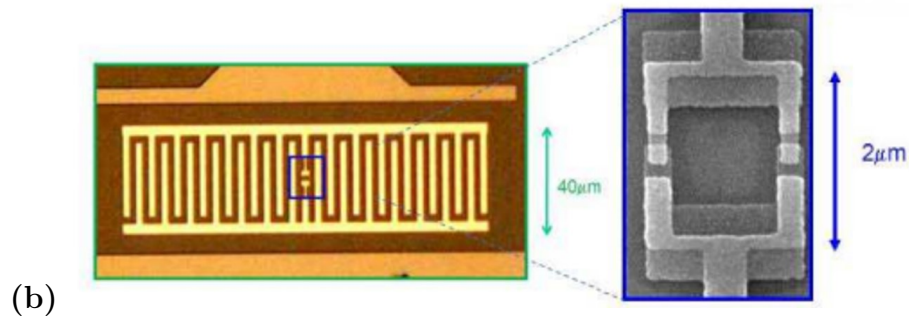
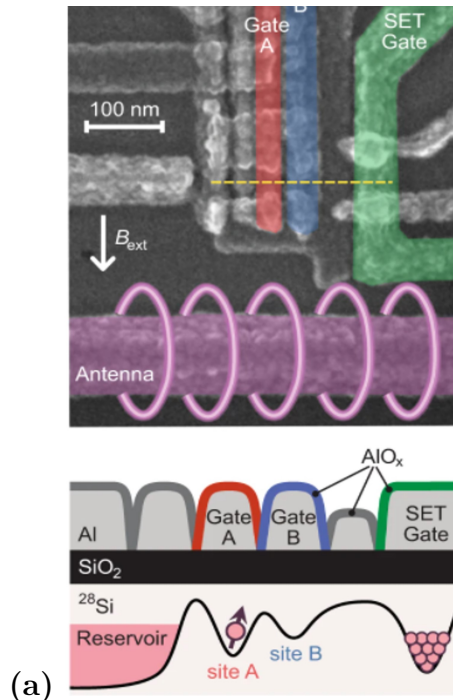


Figure 1.1: (a) Diagram and scanning electron microscope (SEM) image of a linear array of Si metal-oxide-semiconductor (MOS) quantum taken from Ref.[8]. The dots are electrostatically defined using Al gates separated by AlO_x gate oxides. (b) Taken from Ref.[5] (©2019 IEEE), the optical microscope image is of an Al/ AlO_x transmon qubit. The accompanying SEM image shows overlapped regions of Al which define the tunnel junctions. Ref [8] is an Open Access article under a Creative Commons Attribution License.

superconducting qubit coherence time is mostly attributed to changes in qubit operation or architecture [16]. Referred to as "Moore's Law" for qubit coherence times by the authors, Vion *et al* improved the coherence time from nanoseconds to hundreds of nanoseconds in superconducting charge qubits by operating at charge noise-insensitive bias points, or "sweet spots" [17]. The "transmon" style qubit developed by Schoelkopf *et al* further reduced sensitivity to noise, specifically charge noise, and increased coherence times by adding a shunting capacitor to the traditional charge qubit architecture [18, 19]. However more recently, material improvements to mitigate sources of noise, loss, and decoherence have driven much of the progress and are recognized as a critical frontier moving forward [2, 16]. Despite empirical evidence that shows material imperfections hinder, for example, coherence times in superconducting qubits, the direct connection between specific material characteristics and qubit behavior remains a very active area of research for all qubit implementations. Further connective tissue can be gained by research on how material properties are affected by processing or interactions with other material systems.

1.3.1 Aluminum Oxide

Of the many materials employed in quantum relevant devices, aluminum oxide layers have been used extensively for gate oxides and tunnel barriers as seen in Fig 1.1. The popularity of AlO_x layers has largely been driven by ease of fabrication, where the diffusion-limited oxidation of an Al base layer at room temperature reliably forms a thin ($\sim 1-2$ nm) and relatively uniform amorphous oxide layer [16]. In

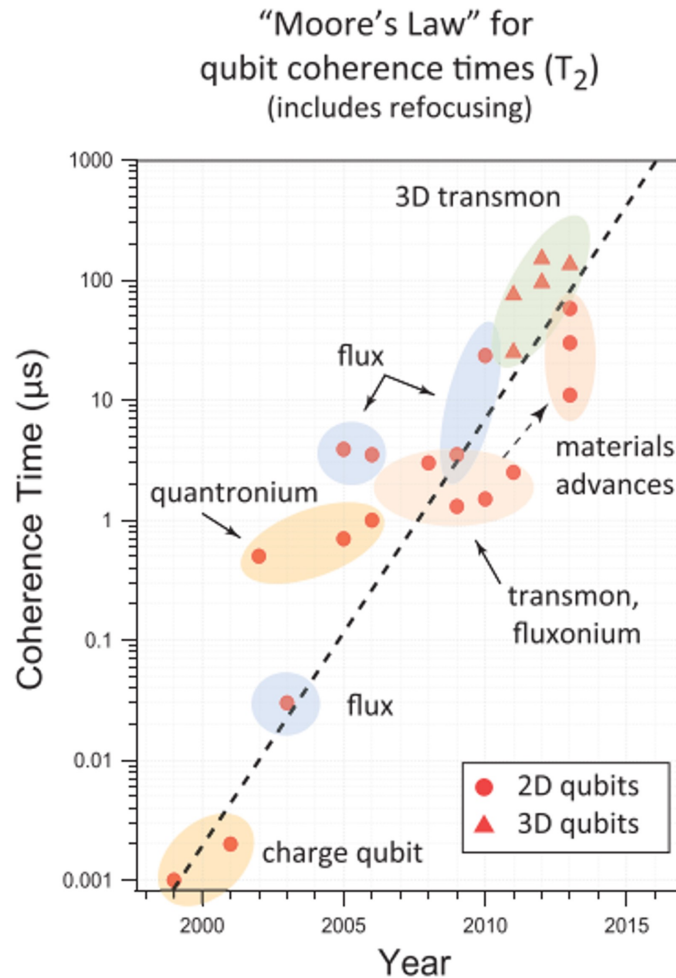


Figure 1.2: The coherence time for superconducting qubits has increased nearly exponentially for the last several decades. While mostly attributed to changes in qubit type, advancements from material selection and processing indicates that material science will continue to play a prominent role moving forward. This figure is reused from Ref.[16] with permission from Springer.

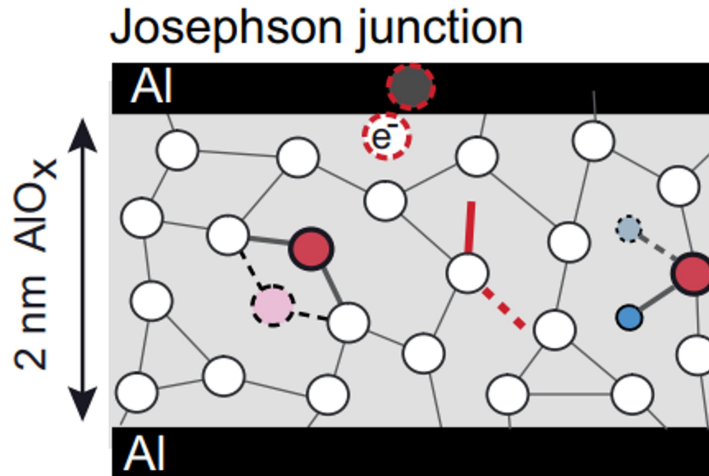


Figure 1.3: Examples of microscopic TLS in amorphous AlO_x layers, including atoms tunneling between configurations, trapped electrons, the orientation of dangling bonds, and the orientation of hydroxyl groups. This figure was reused from Ref.[21], an Open Access article under a Creative Commons Attribution License.

addition, AlO_x layers are well described as WKB-like (Wentzel-Kramers-Brillouin) barriers owing to a uniform attenuation of states. Although preferable over most native, thermal oxides, amorphous AlO_x layers typically suffer from a significant density of electrically active defects [20]. Many of these defects have been attributed to the initial non-equilibrium structure of the oxide, where metastable atomic configurations can form microscopic two-level systems (TLS) [21, 22]. Examples of several defects which manifest as TLS, such as atoms tunneling between configurations or changing orientations of dangling bonds on under-coordinated atoms, are shown in Fig.A.8 from Ref.[21].

Interactions between TLS in Josephson junction tunnel barriers and superconducting qubits is recognized to be one of the leading causes of decoherence [2, 20].

By absorbing a photon from the qubit or associated resonator, a TLS can be excited and subsequently emit a phonon. This TLS dielectric loss effectively siphons energy from the qubit, leading to relaxation to the ground state [23]. In addition, dephasing can occur as low-frequency charge fluctuations from TLS cause fluctuations in the Josephson junction tunnel barrier properties. The superconducting qubit community has largely attempted to avoid these interactions by designing qubits with smaller tunnel junction sizes, which results in a fewer net number of defects [24]. However when scaling to thousands or millions of Josephson junctions, reducing TLS density is still necessary to reduce the chance of individual qubits behaving poorly as a result of strong couplings to TLS [16, 20].

The electrically active defects in AlO_x also have deleterious effects in many applications outside of quantum computing, such as magnetic random access memory (MRAM). Relaxation of TLS defects in AlO_x tunnel barriers, a consequence of chemical profile or structural relaxation, can cause drift in electrical properties over time. For devices such as magnetic tunnel junctions (MTJs) used in magnetic random access memory (MRAM), drifting electrical properties can manifest as a change in tunneling magnetoresistance (TMR) [25]. TMR is tunneling resistance which is dependent on the alignment of magnetic electrodes separated by a thin insulating layer. Drift in TMR hinders the long term reliability of MRAM, providing just another example of the broad impact of reducing electrically active defect density in AlO_x .

Optimizing AlO_x fabrication to mitigate defect density remains a critical venture towards performing device performance. AlO_x layers with O-content approach-

ing stoichiometric Al_2O_3 have been shown to have fewer TLS defects compared to O-deficient layers [26]. Low-coordinated Al atoms as a result of O-deficiency have been proposed as a source of several types of TLS defects. Oxygen vacancies can act as charge traps, where the varying charge state of the vacancy causes fluctuations in the electrostatic environment [27]. Decreased film density and low-coordinated Al atoms also give way to a higher density of metastable atomic configurations, where Al and O atoms can tunnel between atomic positions [28, 29]. Applying these lessons to nm-scale tunnel barriers, however, remains a challenge. For example, reduction in TLS density has been demonstrated with single crystal tunnel barriers [30]. However, such epitaxial growth is considerably more daunting compared to typical amorphous tunnel barrier formation. Processes such as multiple oxidation steps and free energy tunnel barrier confinement have been used with thermal oxidation to improve AlO_x stoichiometry towards Al_2O_3 , however extended oxidation times are detrimental to industrial applications.

1.3.2 Al and Nb

Aluminum is to superconducting quantum computing as silicon is to modern integrated circuitry. Most superconducting qubit architectures, including transmon qubits favored by industrial leaders of the field such as IBM and Google, use Al/ AlO_x /Al Josephson junctions as the critical element [31, 32]. As discussed above, Al enables the formation of suitable tunnel barriers. In addition, Al is highly conductive in the normal state and the relatively high dielectric constant of AlO_x makes

it suitable for gate isolation. It has a superconducting transition temperature (T_c) of 1.2 K and a superconducting energy gap, explained in the next section, of $\approx 180 \mu\text{eV}$.

Nb, on the other hand, has the highest T_c of the elemental superconductors at 9.2 K and an energy gap of $\approx 1.5 \text{ meV}$. Al-based Josephson junctions are often coupled to Nb resonators or, for qubit architectures such as the transmon, shunted by a Nb-based capacitor. Control circuitry for Al superconducting qubits is often comprised of Nb digital electronics called rapid single flux quantum (RSFQ), where information is stored in the form of magnetic flux quanta [33]. The relatively high T_c of Nb allows the control circuitry to be at liquid He temperature (4 K), which is much less demanding than the temperatures required for the superconducting qubit (typically below 100 mK) [34].

Nb and Al are often combined to take advantage of desirable properties in each material. The high Nb T_c of 9.2 K increases the operational temperature range for a given superconducting device, such as control electronics discussed above, but forms numerous metastable oxide phases with a range of electrical characteristics (metallic, semiconducting, etc.) [35]. These oxides have also been shown to host a higher density of TLS compared to AlO_x [36]. The ease of AlO_x tunnel barrier fabrication drives the use of Al, but Al suffers from a relatively low T_c of 1.2 K (and proportionally small superconducting gap). Contact between the materials influences the superconducting state of each material via the superconducting proximity effect. However, gaps remain in the published experimental work concerning the interplay of these superconducting systems, particularly in regards to the evolution of the quasiparticle density of states with film thickness. Of particular import is the

energy distribution of quasiparticles, as well as their generation and diffusion. In superconducting qubits, tunneling of athermal quasiparticles (i.e., $E > \Delta$) in Josephson junctions leads to state relaxation. This will be the focus of Chapter 5, where the evolution of the Nb/Al superconducting state is probed as a function of film thickness. However, an introduction to superconductivity is necessary to provide further context.

1.4 Introduction to Superconductivity

The phenomenon of superconductivity was discovered in 1911 by Kamerlingh Onnes when investigating the low temperature transport of metals cooled with liquefied He. He found that the resistivity of several metals vanished at low temperature and that these materials could tolerate a persistent current without dissipation. A microscopic theory for the behavior was introduced by Bardeen, Cooper, and Schrieffer (BCS) in 1957, which postulated that this dissipationless current is carried by Cooper pairs [37]. For some metals below a critical temperature (T_c), electrons near the Fermi energy (E_F) experience a net attractive potential and condense into Cooper pairs, or pairs of electrons with opposite spin and momenta. The attraction between the electrons is a result of interactions with the crystal lattice. Motion of the positive ion cores towards an electron results in a polarized medium, which in turn attracts a second electron. Superconductivity occurs in materials which exhibit sufficient electron-phonon coupling to overcome the repulsive Coulomb interaction between the electrons.

The Cooper pairs occupy a single, macroscopic coherent ground state at the Fermi level. The energy separating this ground state from the nearest excited state is Δ_g , or the superconducting energy gap. Within the mean-field Ginzburg-Landau theory, the superconducting state is described by a thermodynamic order parameter $\Delta = |\Delta|e^{-i\phi}$ with amplitude $|\Delta|$ and phase ϕ . The order parameter is proportional to the density of cooper pairs n_s . In a uniform system, the BCS energy gap Δ_g is the real part of Δ . This formalism, which can be derived from BCS theory, will be useful in discussing spatially inhomogeneous superconducting systems.

Several characteristic length scales are used to describe the spatial variation of superconducting properties. In general, the coherence length (ξ) describes the characteristic distance over which the order parameter recovers to a bulk value from a perturbation. Within BCS, this can be thought of as the distance over which phase coherence is maintained between paired electrons, i.e., roughly the “size” of a Cooper pair. The coherence length is related to the order parameter by $\xi = \hbar v_F / \pi \Delta$, where v_F is the Fermi velocity in m/s. The electronic mean free path in m is given by $l = 3D / v_F$, where D is the electron diffusion constant with units m^2/s . The diffusion constant is given by $D = 1 / \rho_0 N(0) e^2$, where ρ_0 is the residual resistivity in ohms, $N(0)$ is the two spin density of states at the Fermi energy in $\text{J}^{-1}\text{m}^{-3}$, and e is the elementary charge in coulombs [38, 39]. By comparing ξ to the electronic mean free path (l), superconductors are typically categorized into the clean limit ($\xi < l$) or the dirty/diffusive limit ($\xi > l$). In essence, this classification modifies the spatial dependence of the superconducting properties. Most thin film superconductors tend to be in the diffusive limit, due to a relatively short mean free

path or diffusive scattering from boundaries [39]. In this limit, the effective coherence length ξ^* is given by $\xi^* = \sqrt{\hbar D / 2\pi k_B T_c}$, where k_B is the Boltzmann constant in J/K. Finally, these length scales are compared to film thickness (d). For example, estimations of these length scales for the ≈ 45 nm Nb films discussed in Chapter 5 correspond to the conditions $d_{\text{Nb}} (\approx 45 \text{ nm}) > \xi_{\text{Nb}}^* (\approx 15 \text{ nm}) > l_{\text{Nb}} (\approx 5 \text{ nm})$. In other words, perturbations to the Nb superconducting state, such as contact with another material as discussed in the next section, would result in a spatially varying order parameter within the Nb film as the thickness is larger than ξ^* .

The BCS theory predicts the relationship between the 0 K Cooper pair binding energy ($2\Delta_g$) and the temperature below which this binding becomes favorable (T_c), as both are related to the density of states (N) and the interaction potential between electrons (V) as given below [40].

$$2\Delta_g = 3.52k_B T_c = 4\hbar\omega_D \exp(-1/NV) \quad (1.1)$$

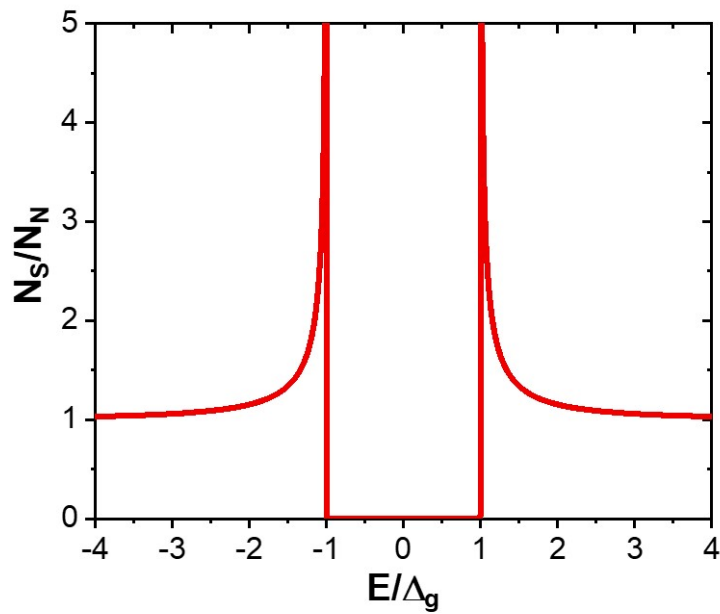
The phonon cutoff frequency is given by the Debye frequency, ω_D . Experiments have shown the BCS predicted factor of 3.52 to vary between 3-4.5 depending on the electron-phonon coupling, with most materials around the BCS predicted value of 3.5. T_c is also correlated with H_c , a critical magnetic field. In addition to resistivity dropping to zero through the superconducting transition, applied magnetic fields are dispelled from the interior of the material up to H_c . It follows from Ampere's law that a critical current (I_c) exists, corresponding to when the magnetic field generated by the current exceeds H_c at the material surface. In Chapter 5, T_c is determined

in two ways in an effort to characterize the evolution of the superconducting state with wire thickness: (1) measuring the wire resistance as a function of temperature with a constant current bias $I \ll I_c$ and (2) measuring I_c at subsequent steps in temperature until no super-current, or dissipationless current, is observed.

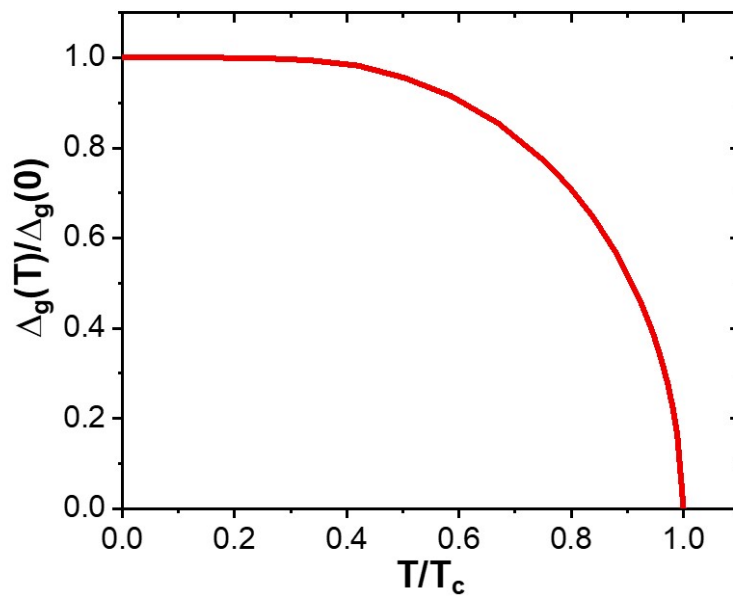
Single particle excitations in a superconductor, called quasiparticles, are characterized as a superposition of negatively charged electrons and positively charged holes. Breaking a Cooper pair requires a minimum energy $E = 2\Delta_g$, as the unoccupied quasiparticle states are Δ_g above the Fermi energy and this process creates two quasiparticles. This binding energy is typically of order 10^{-3} - 10^{-4} eV, much less than the analogous band gap in semiconductors. As seen in Fig.1.4(a), the BCS single-particle density of states (N_S) has no states within $\pm\Delta_g$ of E_F and singularities at the gap edge. This does not represent Cooper pair density, as Cooper pairs are Bosons and all reside at E_F . N_S/N_N is given by

$$\frac{N_S}{N_N} = \left| \text{Re} \left[\frac{E}{\sqrt{E^2 - \Delta_g^2}} \right] \right| \quad (1.2)$$

where N_N is the normal state electron density of states. The energy gap Δ_g scales with T/T_c as discussed in Ref. [40], and remains relatively constant for $T/T_c \lesssim 0.45$. The temperature dependence of the Δ_g is seen in Fig.1.4(b). This temperature dependence is separate from Fermi distribution broadening of the quasiparticle density of states at finite temperatures, which is included when calculating tunnel junction current in Chapter 5.



(a)



(b)

Figure 1.4: (a) The BCS quasiparticle density of states normalized by the normal state electron density of states. E represents the energy relative to E_F . (b) Temperature dependence of the BCS energy gap scaled to T_c .

1.4.1 Superconducting Proximity Effect

When a superconductor S is in electrical contact with a normal metal N, the electronic structure of both are altered near the interface. This influence, referred to as the “proximity effect”, results in an induced superconducting gap in N as the electron pairs leaking from S maintain their phase coherence for a time. Likewise, the order parameter is depressed in S as uncorrelated carriers leak into N. This effect extends a superconductor S in electrical contact with another superconductor S', with $T_{c, S} > T_{c, S'}$. In this case, the order parameter $\Delta(x)$, where x is the coordinate normal to the S-S' interface, is modified at the interface and evolves towards the bulk (or stand-alone thin film) values away from the interface. The distance over which this influence is apparent from one material to the other scales according to the coherence length in each material. The magnitude of the influence scales, in part, with the normal state DOS N and interaction potential V of each material. An example of this can be seen in the bilayer T_c dependence on thickness of the constituent materials. If, for instance, the thickness of an S' layer is increasing from zero on an S thin film, T_c will smoothly evolve from $T_{c, S}$ to $T_{c, S'}$ [38, 41]. However, the rate at which T_c changes with thickness is largely governed by the density of states N and the interaction potential V of each material [41]. In the context of Eq. 1.1, the film thickness is governing the weight of “NV” from each material.

As I will discuss in Chapter 5, the literature includes a variety of studies that have calculated the electronic structure of superconducting bilayers (spatially dependent order parameter, density of states, etc). While some have investigated the

transport characteristics of Nb/Al bilayers, the vast majority are within the context of superconductor-insulator-superconductor (SS'-I-S''S) tunnel junctions, where the transport is complicated by sum-gap and gap-difference features from the separate superconducting electrodes ($\Delta_{g, SS'} \pm \Delta_{g, S''S}$). In addition, many studies are at temperatures near $T_{c, Al}$, effectively sampling SN layers instead of SS' layers. Therefore, there is still much to be learned by examining the evolution of this system via transport in the SS' regime. Of particular interest is the energy distribution of quasiparticles, as well as their generation and diffusion. In superconducting qubits, tunneling of athermal quasiparticles (i.e., $E > \Delta$) in Josephson junctions can induce qubit transitions [42]. One of the methods pursued in the literature is engineering the superconducting gap structure with bilayers to effectively trap quasiparticles, where transport data reflecting the quasiparticle distribution in SS' layers can provide valuable insight.

1.5 Objectives

The overarching objective of this thesis is to improve and further understand the properties of materials critical to solid state quantum information, specifically regarding superconducting tunnel junction materials AlO_x , Al, and Nb. Tunnel junction devices are fabricated with these materials, which represent precursors to hybrid quantum systems. In particular, several primary objectives for studying these materials and a brief restatement of motivations are given below:

- **Evaluate the use of plasma oxidation and enthalpy confinement of oxygen in fabricating ultrathin AlO_x layers with fewer electrically active defects.**

Amorphous AlO_x layers typically have a significant density of electrically active defects, often attributed to the initial non-equilibrium structure and exacerbated by O-deficiency. Therefore, fabricating AlO_x layers with an initially uniform oxygen profile and Al/O ratio approaching stoichiometric Al_2O_3 is likely to result in layers with fewer TLS. Fritz *et al* showed this in principle, by measuring the dielectric loss of millimeter scale capacitors [26]. Capacitors with an AlO_x dielectric were fabricated, where O-content was increased during oxidation by the use of UV light. Fewer TLS were inferred in the samples with higher O-content from dielectric loss measurements. In addition, several studies have shown that annealing AlO_x tunnel barriers hastened relaxation of the non-equilibrium oxide structure and annihilated vacancy-type defects as the oxygen profile became more uniform [43, 44]. However, tunnel junction annealing will likely result in an unpredictably large change in the as-fabricated tunneling resistance, as well as undesirable diffusion elsewhere in the junction.

Plasma oxidation of Al has been shown to result in layers with higher O-content in a shorter amount of time compared to room temperature thermal oxidation [45, 46]. Plasma oxidation, discussed in Chapter 3, exhibits an aggressive oxidation front as a result of a high density of reactive oxygen radicals, compared to O_2 supplied by thermal oxidation [47]. Taking a cue from from AlO_x oxidation kinetics observed

in magnetic tunnel junctions, enthalpy confinement of the oxygen profile is used to achieve a uniform oxide. When plasma oxidizing ultrathin Al layers on Co, Kuipers and Gillies observed that, even after the oxidation front reaches the Al/Co interface, the O-content of the Al increases for a time prior to Co oxidation [45, 46]. This was attributed to formation of Al-oxide being more energetically favorable than the formation of Co-oxide. Leveraging plasma oxidation in combination with enthalpy confinement potentially provides an athermal (i.e., non-annealing) route to fabricating uniform AlO_x barriers with relatively high O-content compared to thermal oxidation, likely reducing the density of electrically active defects.

- **Correlate *in situ* characterization of AlO_x tunnel barriers, in the form of X-ray photoelectron spectroscopy, with fabrication parameters and *ex situ* transport measurements.**

As fabrication and processing techniques are explored in improving material properties, *in situ* materials characterization can expedite process development. Photoelectron spectroscopy has proven useful in optimizing Al oxidation via chemical state identification and film thickness determination [45, 48]. Correlating such characterization techniques with the transport characteristics of finished devices provides a valuable feedback loop in tying materials processing to the improvement of material properties.

- **Study the interaction between the Nb and Al superconducting systems in Nb/Al bilayers, as the bilayer system transitions from a primarily uniform Nb-like system with thin Al to a nonuniform system with thick Al.**

AlO_x layers are critical for superconducting tunnel junction devices where Nb and Al are often used in tandem. The interplay of these superconducting materials can be leveraged to take advantage of desirable properties from each. In the Nb/Al system, this is often done with thick Nb and thin Al for AlO_x formation and the high Nb T_c . However, observing the evolution of this system from primarily Nb-like with thin Al to primarily Al-like with thick Al provides a more complete picture of the interplay between the systems, thereby informing future device integration towards hybrid quantum systems. Typical Nb/Al systems are studied in SIS junctions, where the transport convolves the superconducting state of both electrodes. Even in this configuration, few studies have been published which study the Nb/Al electronic structure with film thickness. By providing further investigating the Nb/Al electronic structure with film thickness, light can be shed on quasiparticle diffusion and generation in the system.

1.6 Outline

- **Chapter 2:** Experimental methods to fabricate and characterize metal-insulator-metal tunnel junctions are discussed. The ultrahigh vacuum fabrication system is described, which provides clean and high-throughput device processing. In

addition, room temperature and cryogenic device characterization is discussed using electrical transport measurements.

- **Chapter 3:** Reduced defect density in AlO_x tunnel junctions is inferred from enhanced time stability, providing a non-annealing and fast method to produce high quality tunnel junctions. Recipe optimization of aluminum plasma oxidation confined by cobalt electrodes is described. Plasma oxidation parameters (time, power, pressure) are tuned to achieve uniform AlO_x layers on Co with an O/Al ratio approaching stoichiometric Al_2O_3 . Oxide enthalpy confinement (Co confinement) results in significantly reduced tunnel junction resistance drift (34% with confinement over 8 months, 95% without Co confinement). Given the connection established to resistance drift, we attribute this to a smaller density of electrically active defects.
- **Chapter 4:** Preliminary correlation between *in situ* X-ray photoelectron spectroscopy (XPS) measurements and *ex situ* transport measurements are presented, which helps pave the way for future optimization of layer stoichiometry device performance. AlO_x tunnel barriers with several different underlying electrode materials (Al, Co, Nb) are inspected with X-ray photoelectron spectroscopy (XPS). Elemental and chemical state identification verify that the plasma oxidation recipe, optimized for Al/Co layers in Chapter 3, oxidizes Al metallic Al with negligible Co oxidation. Angle-resolved XPS is used to determine AlO_x layer thickness and preliminary data is discussed for correlating this thickness with *ex situ* transport determined thickness. Correlation varies

depending on the material stack (e.g., AlO_x/Co vs. AlO_x/Al), signifying the need for further investigation.

- **Chapter 5:** The interplay between the Nb and Al superconducting systems is studied as a function of Al thickness in Nb/Al bilayers, where the density of states evolves from a uniform Nb-like system at thin Al to a convolution of the Nb and Al states at thick Al. The evolution of the Nb/Al bilayer superconducting state with Al thickness is probed using normal metal-insulator-superconducting (NIS) tunnel junctions. The bilayer T_c remains above 6 K for Al thickness exceeding 300 nm on 45 nm Nb. The low temperature tunneling conductance spectra transition from primarily single-gapped spectra at thin Al ($\lesssim 15$ nm) to spectra exhibiting dual gap-like features. A modified Blonder-Tinkham-Klapwijk based model is proposed, which interprets the transport as a convolution of Al-like and Nb-like states. Calculated conductance spectra qualitatively match the evolution of the conductance spectra with Al thickness, with the Nb-like states dominating the conductance over all Al thicknesses.
- **Chapter 6:** A summary is given of the work presented, including potential impacts and future experiments enabled by these results.

Chapter 2: Experimental Methods

2.1 Context

Metal – insulator – metal (MIM) tunnel junctions are employed as critical components in quantum information, metrological standards, and tunneling spectroscopy [49, 50, 51, 52]. In this context, a tunnel junction refers to two metal contacts separated by a thin insulating layer such that electrical transport is dominated by quantum mechanical tunneling [53]. The current-voltage (I-V) characteristics of the device is determined by the density of states in each metal electrode and the shape of the potential energy barrier between the two formed by the insulating tunnel barrier. As the tunneling probability is exponentially dependent on the height and width of the potential energy barrier, minute changes in these properties from contaminants or process deviations can significantly change the tunnel junction transport characteristics [44, 52]. This sensitivity necessitates the utmost care during fabrication in maintaining sample cleanliness and precise process parameters.

Experiments described in this thesis utilize both normal metal-insulator-normal metal tunnel junctions, described as NIN tunnel junctions moving forward, and normal metal-insulator-superconductor (NIS) tunnel junctions. All tunnel junctions discussed here are fabricated on 75 mm thermally oxidized Si wafers. Metals

are deposited with electron beam deposition through etched Ni shadow masks held ≈ 1.5 mm above the wafer surface. The tunnel barriers used for all devices are AlO_x fabricated by plasma oxidation of metallic aluminum thin films. Device characterization is performed with *in situ* X-ray photoelectron spectroscopy (XPS) and *ex situ* electrical measurements. Detailed tunnel junction layer stacks will be discussed in later chapters. All of the measurements and device fabrication discussed in this thesis takes place at the National Institute of Standards and Technology (NIST) in Gaithersburg, MD.

The following chapter describes the equipment and methods utilized to fabricate and characterize mesoscopic tunnel junctions. I will discuss the design of our custom ultrahigh vacuum (UHV) deposition system in section 2.2, which enables entirely *in situ* fabrication. The procedure for fabricating tunnel junctions with this system follows in section 2.3. Section 2.4 closes out the chapter with a discussion on the room temperature and cryogenic methods used for device characterization.

2.2 Wafer Fabrication System

The fabrication system was designed to ensure device cleanliness throughout processing, while maintaining expedited process development and prototyping. Scaled up from a separate system in our group [54], this system integrates sputtering and electron beam (e-beam) evaporation for metals deposition, plasma cleaning and oxidation, and photoelectron spectroscopy as seen in Fig. 2.1. Wafer storage elevators and vacuum transfer rods enable top to bottom wafer processing in an

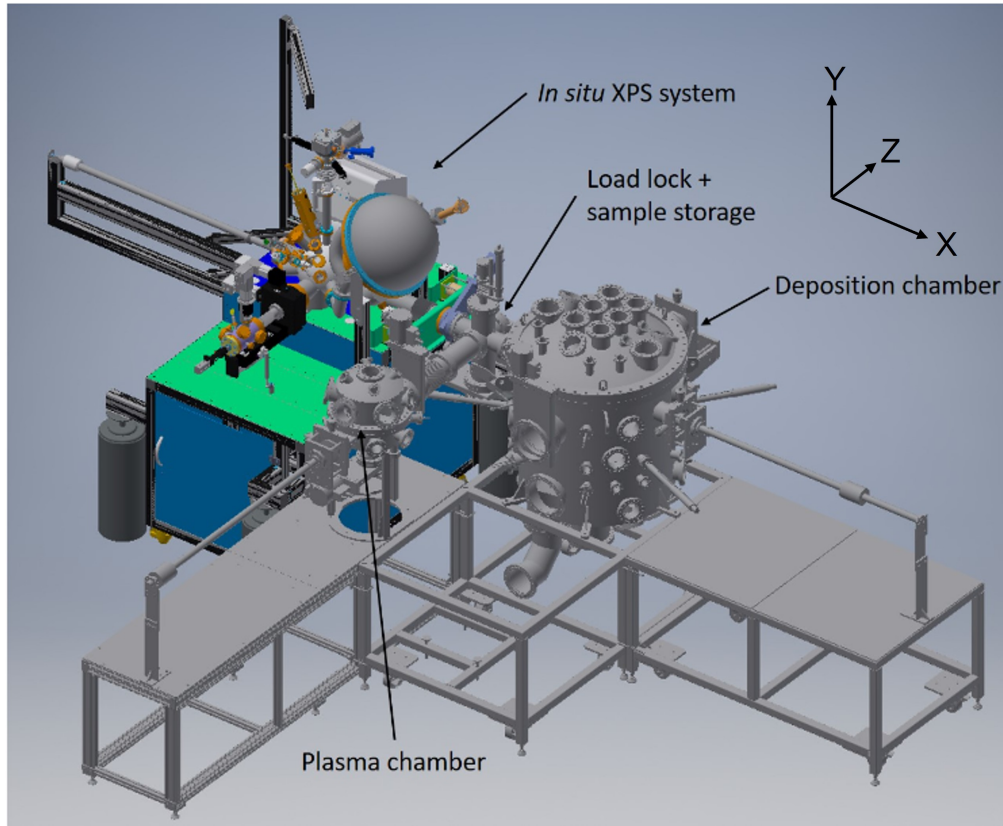


Figure 2.1: CAD rendering of the custom UHV wafer fabrication system. The four main chambers are identified as deposition chamber, load lock chamber, oxidation chamber, and XPS system. The Cartesian axes used for the system are shown in the upper right-hand corner.

ultrahigh vacuum environment not exceeding pressures of 10^{-8} Torr, except during *in situ* plasma oxidation in high purity oxygen.

The UHV deposition system is designed for 75 mm wafers, which are moved throughout the system via magnetic transfer rods. The wafers are individually placed in stainless steel wafer cassettes made up of a top and bottom portion. As seen in Fig. 2.2(a), the wafer is placed face down inside the cassette top according to the wafer flat and machined cassette flat. The cassette bottom has pins on the

interior to hold the wafer flush against the cassette top when the halves are bolted together. In Fig. 2.2(b), raceways can be seen on the cassette sides and are intended to mate with transfer forks of magnetic transfer rods. Once inside the cassette, the wafer has a maximum lateral excursion of $\approx 390 \mu\text{m}$ and a maximum rotational excursion of $\approx 3^\circ$ relative to the cassette. The cassette pins help to mitigate such excursions, but jostling of the wafer during magnetic transfer rod movement can cause the wafer to shift slightly. Wafer movement becomes relevant when attempting to align subsequent depositions through shadow masks and will be discussed later.

Once assembled, the wafer cassettes are loaded onto a twelve slot wafer elevator inside the load lock chamber. The load lock chamber, intended for sample exchange to and from vacuum, is centrally located in the system and connects to the deposition chamber, oxidation chamber, and XPS chamber with pneumatic gate valves separating each. The relatively small chamber volume enables fast vent and pump down times. In order to access each of the elevator slots with transfer rods, the elevator can be raised and lower via a vacuum compatible Z-stage translator with stepper motor control. In addition, the elevator can be hand rotated 360° to face any of the three attached chambers or the viewport used for sample loading and unloading. After sample loading, the load lock is pumped to below 50 mTorr with an Anest Iwata ISP-250 scroll pump followed by an Edwards STP-451 turbomolecular pump down to the chamber base pressure of approximately 5×10^{-9} Torr.

Once in vacuum, the cassettes are shuttled around the system via magnetic transfer rods. A magnetically coupled slide glides over the outside of the transfer rod tube and translates the rod. Forks on the end of the transfer rod slide into the

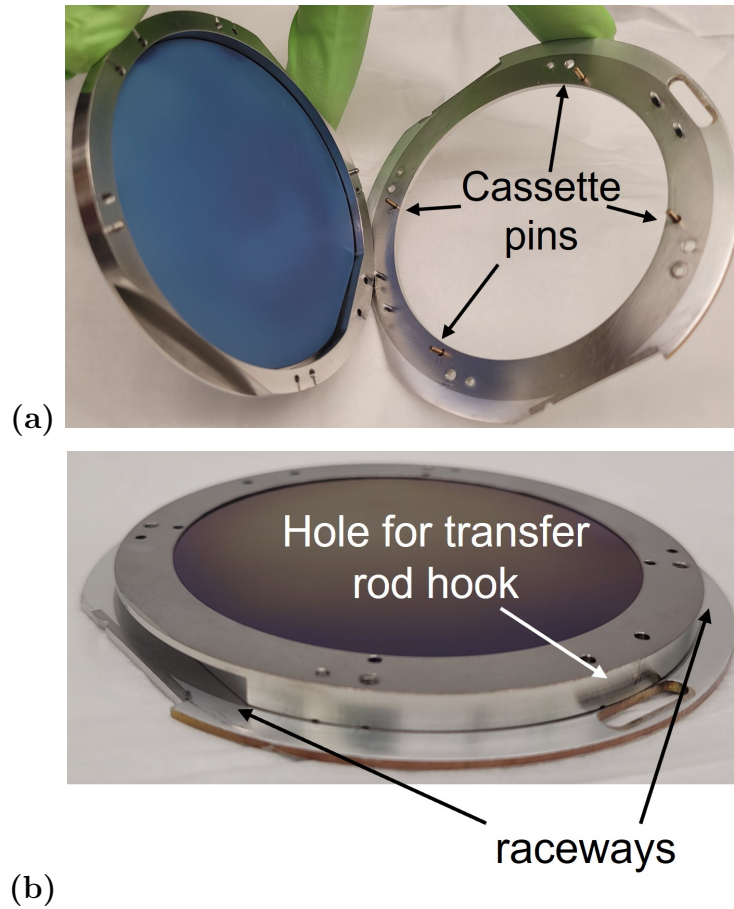


Figure 2.2: Stainless steel wafer cassette. (a) The Si wafer is placed face down in the left (top) cassette half. Pins on the right (bottom) cassette half keep the wafer flush against the top of the cassette and mitigate wafer shifts. (b) The assembled cassette has lateral raceways to mate with transfer rod forks and a slot at the front for the transfer rod latching mechanism.

cassette rails on either side as shown with a shadow mask cassette in Fig. 2.3(a). The slide can be rotated to engage the wafer cassette with a small hook. Once engaged, the wafer can be pulled out of an elevator or magazine slot and transferred to another. The tension loaded pins on the elevator slots catch the cassette and the forks can be withdrawn after the hook is disengaged.

Metals deposition occurs via three UHV compatible AJA International sputter guns and a Thermionics five pocket electron beam (e-beam) deposition gun in the deposition chamber. The chamber is a 32 in. diameter x 32 in. tall cylinder with a rounded base and lid, supporting 94 vacuum ports in total. The chamber base pressure is $2\text{-}5 \times 10^{-10}$ Torr maintained by a Pfeiffer TMU 1000M turbomolecular pump and a Gamma Vacuum ion pump. In addition, the ion pump is equipped with a titanium sublimation pump (TSP). The turbo pump is backed by an Edwards XDS35i scroll pump. A residual gas analyzer (RGA) is mounted on the chamber lid and monitors the partial pressures of species in the chamber. The RGA scan in Fig. 2.4 was recorded for a chamber pressure of 4×10^{-10} Torr as measured with the chamber ion gauge. The scan, which shows the partial pressure of species in the chamber as a function of mass, shows commonly seen residual gases in vacuum. Specifically, H_2O is expected as the chamber has not been baked and is difficult to remove otherwise. Also mounted on the chamber lid are the sputter guns, with sputter gas feedthrough lines on their respective flanges. Each sputter gun can have the angle of the sputter target adjusted to face a wafer located centrally in the deposition chamber and each is equipped with a pneumatic shutter. The e-beam deposition system is located at the bottom of the chamber near the chamber wall.

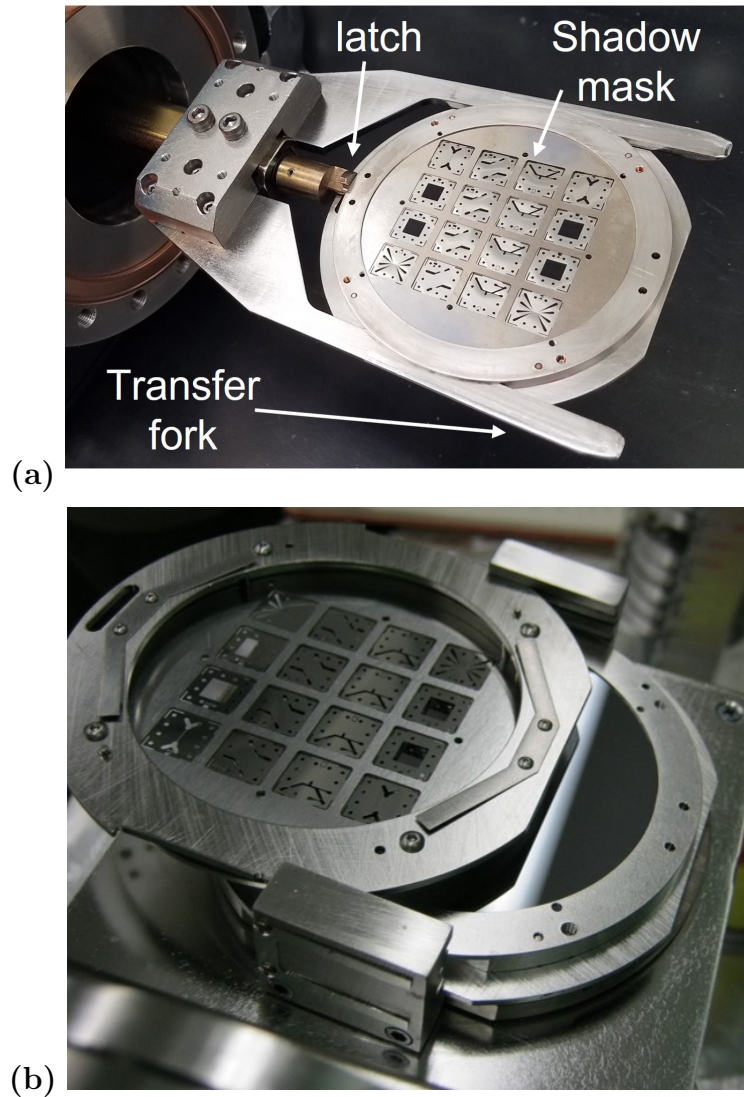


Figure 2.3: Wafer and shadow mask cassettes are moved around the system via magnetic transfer rods. (a) Taken outside of vacuum during maintenance, a shadow mask cassette is engaged with the transfer rod forks. (b) The shadow mask cassette, not fully seated here, is inserted upside down relative to the wafer cassette to keep the wafer and mask in close proximity.

An external stepper motor is used to switch between five source pockets.

A toroidal cryogenic shroud sits in the middle of the chamber and is covered with a circular copper plate. The shroud acts as a sorption pump to significantly decrease the chamber pressure when filled with liquid nitrogen. The low ($\approx -165^\circ$ C) surface temperature of the shroud greatly increases the probability that impinging gas molecules will adsorb or condense, thus removing them from vacuum. Leading up to a deposition, the chamber pressure can be reduced to $\approx 10^{-11}$ Torr when cooled. The copper plate on the shroud serves to both increase the area of the cryogenic shroud, thereby increasing pump capacity, and to break line of sight between sputter deposition and e-beam deposition source. In addition, the shroud provides protection against the pressure increase as a result of the hot source, as the pressure above and below the shroud is likely not in equilibrium during deposition. Holes in the copper plate provide line of sight from the e-beam source to the wafer. Additional openings provide line of sight between the source and quartz crystal microbalances located just above the copper plate. Pneumatic shutters just above the plate are used to selectively make or break line of sight to the wafer and QCMs from the e-beam source. Viewports are mounted around the chamber, enabling process inspection and wafer manipulation with the sample manipulator and transfer rod.

Wafers are held in the deposition chamber on a 5-axis sample manipulator mounted on the side of the chamber. In addition, a twelve slot elevator is mounted on the chamber lid just above the load lock-deposition chamber port. The elevator can be moved down in line with the transfer rod to store additional wafers. A magnetic transfer rod is used to move wafers from the load lock elevator to a two

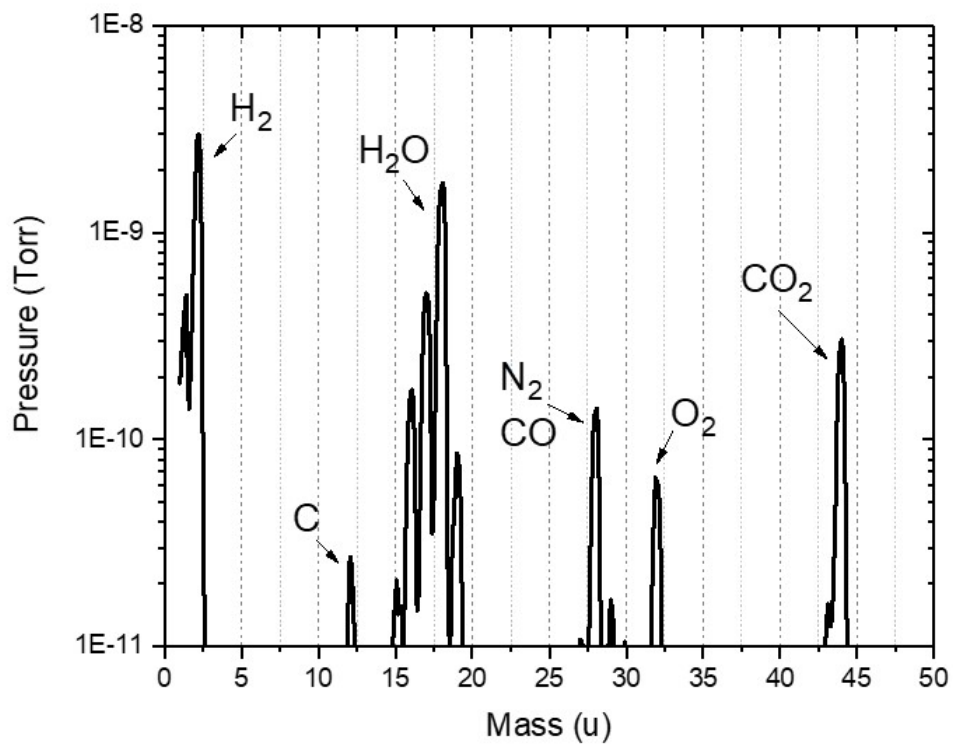


Figure 2.4: RGA mass spectra from the deposition chamber at a pressure of 4×10^{-10} Torr. Residual species commonly seen in vacuum are identified in the scan: H₂, C, H₂O, CO, N₂, O₂, and CO₂.

slot magazine on the manipulator. The bottom slot is intended for wafer cassettes and the top slot is intended for shadow mask cassettes, shown in Fig. 2.3(b). The two are oriented in such a way to keep the mask and wafer in close proximity, thus reducing pattern spread from the stencil to the wafer during deposition. The cassette magazine is attached to a vacuum port by a 24 in. hollow support as seen in Fig. 2.5(a). Rods inside the support translate rotation from external stepper motors to azimuthal or polar rotation of the manipulator magazine. The manipulator is mounted on a translation sled with vacuum bellows as seen in Fig. 2.5(b). A worm gear assembly enables stepper motor controlled movement of the manipulator in the Z direction. Limited movement of the manipulator in the X and Y directions is achieved with a port aligner. A thermocouple temperature gauge and a ceramic heater, seen in Fig. 2.5(a), are located in the manipulator just below the wafer allowing for annealing or heating during depositions. In addition to a thermocouple thermometer, a pyrometer can be used to measure the wafer temperature through viewports on the chamber lid.

Oxygen plasma cleaning and plasma oxidation occurs in the plasma chamber, seen connected to the load lock in Fig. 2.1. This chamber is attached to the load lock and houses a three-slot cassette elevator. The elevator is controlled by a stepper motor and external Z-stage translators. Base pressure is approximately 10^{-9} Torr, maintained by an Edwards STP-301 turbo molecular pump backed by an Edwards nXDS10i scroll pump. A magnetic transfer rod moves wafer cassettes from the load lock to the oxidation chamber elevator. With the cassette on the top slot, the elevator raises the cassette to be flush and concentric with a circular cathode

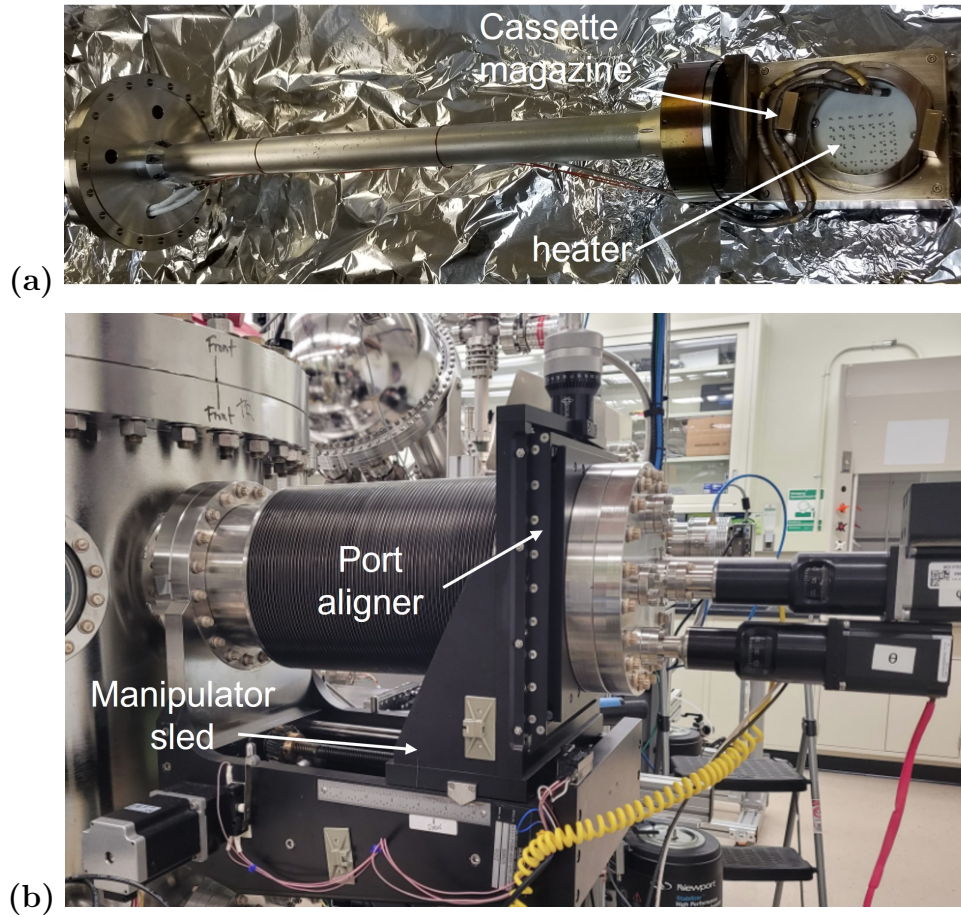


Figure 2.5: 5-axis sample manipulator on the deposition chamber. (a) The hollow support tube houses rods to translate stepper motor rotation to manipulator rotation. Current leads run along the support to the ceramic heater. (b) The sled assembly supports the manipulator and enables lateral movement.

at ground potential. A circular anode hangs above the cathode, supported by four cylindrical insulators with tapped holes on either end. These insulators electrically isolate the anode from the chamber and set the anode-cathode spacing at 3.87 cm for the devices discussed in this thesis. Both electrodes have a diameter of 6 in. A metal wire with fish scale insulators connects the anode to a high voltage feed through. Once oxygen is introduced to the chamber, RF or DC bias can be applied to the anode to spark a glow discharge. An optical spectrometer sits outside of a viewport and is used to monitor the optical spectrum of the plasma, which indicates the species present. Oxide growth and oxidation recipes will be discussed in Chapter 3.

Several changes have been made to the oxidation chamber over time, mostly to mitigate plasma contamination or bolster oxidation reproducibility. The insulators that support the anode were originally alumina but were eventually changed to a coated ceramic, as outgassing from the relatively porous alumina caused elongated pump down times and contamination of the plasma. The Kapton coated wire originally connecting the high power feedthrough to the anode was replaced with a bare metal wire with fish scale insulators, also to avoid unintended species in the plasma. The transfer rod mounted on the oxidation chamber traverses underneath the sample elevator, necessitating off-axis driving of the elevator via the external z-stage. A stainless steel rod is coupled to the elevator on one end and welded on the other end to a 2.75 in. flange. This flange, attached to the chamber by a vacuum bellows, moves up and down inside the external Z-stage translator. However, it was difficult to seat the wafer cassette level with the cathode when only being driven and adequately supported on one side. This exacerbated variations in device characteristics

across a given wafer, as the oxidation rate is very sensitive to the height of a device within the plasma. By installing an second Z-stage assembly on the opposite side of the elevator, the seating of the wafer cassette within the cathode was improved.

The final system connected to the load lock, also shown in Fig. 2.1, is a SPECS photoelectron spectroscopy system. The system is capable of X-ray photoelectron spectroscopy (XPS), ultraviolet photoelectron spectroscopy (UPS), and Auger electron spectroscopy (AES). As with the other chambers, a magnetic transfer rod is used to retrieve a wafer cassette from the load lock and move it to the sample manipulator in the center of the analysis chamber. A more in-depth discussion of the XPS system and related measurements can be found in Chapter 4.

2.3 Tunnel Junction Fabrication Process

Fabricating our crossed wire tunnel junctions occurs in four steps: plasma cleaning of the Si/SiO_x wafer, deposition of the bottom metal layers through one shadow mask (M1), *in situ* tunnel barrier formation via plasma oxidation, and deposition of the top metal layers through a second shadow mask (M2). This section describes process details for each of these steps in our UHV system.

2.3.1 Metals Deposition

Metal thin film deposition takes place in the UHV deposition chamber. Prior to deposition, the cryogen shroud is filled with liquid nitrogen and cools the shroud and central copper plate to approximately -170° C. The cooled shroud acts as a

sorption pump and reduces the chamber pressure the 10^{-11} Torr range. Depositing our films in UHV helps to mitigate the number of impurities included in the films from residual gases in the chamber. Assuming unity sticking coefficient, around one monolayer of impurities can form on the Si wafer surface per second at a pressure of 10^{-6} Torr [55]. The low pressure of residual gases during a deposition and between depositions ensures minimal impurities in the film and at film interfaces. Impurities from residual gases, such as oxygen or hydrogen, can significantly affect structural, mechanical, and electrical properties of a deposited film [56]. In particular, the superconducting properties (transition temperature T_c , coherence length ξ , etc.) of Nb films, discussed in Chapter 5, can be severely degraded by oxygen incorporation. The chamber pressure can also further decrease during the deposition of materials such as Co or Nb, which effectively getter residual gases.

While the deposition chamber is equipped with sputter guns, only e-beam evaporation is employed for the devices discussed in this thesis. A Thermionics RLC electron beam source with 5 pockets is installed on the chamber below the sample manipulator. The pockets are filled with shot or pellets of Al, Co, Nb, Au, and Cu. The pockets are linearly translated via an external stepper motor, exposing the source pocket of choice to the electron beam. The electron beam hearth is cooled with chilled water, typically at 15° C. Crucible liners can be used in each pocket to decrease heat transfer between the source and the hearth.

By bombarding the e-beam source material with a focused electron beam, the source material is heated to increase the materials vapor pressure. As the vapor pressure exceeds the background chamber pressure, the evaporant condenses on the

exposed wafer surface approximately 46 cm above. The e-beam process is as follows. A filament assembly is held at -10 kV relative to the crucible. Current is passed through the filament to achieve thermionic emission. The electrons are accelerated away from the filament into a permanent magnetic field, which directs the beam into the crucible. In addition, current passing through sweep coils on either side of the beam path generate a magnetic field to focus and sweep the beam on the crucible [57]. The user primarily controls the emission current to determine evaporation rate and the sweep current to determine the beam spot size or sweep pattern. The evaporation rate depends on the power deposited, radiative and conductive heat loss from the source, and the latent heat of vaporization. Once the desired source material is selected, the emission current is slowly raised to approximately 25 mA to warm the source. After a few minutes, the emission current is increased to reach the desired evaporation rate.

The emission current necessary to reach a desired deposition rate is determined empirically with a quartz crystal microbalance (QCM). Evaporated material condenses on the surface of a quartz crystal whose resonant frequency is monitored with an Inficon SQC-310 Deposition Controller [58]. The resonance frequency changes with mass from the condensate. The change in resonant frequency with time is converted into a deposition rate using the acoustic impedance of the quartz and evaporant, the density of the evaporant, and the tooling factor as input parameters. The tooling factor is a geometric correction that accounts for the different position of the QCM sensor relative to the wafer of interest. The tooling factor (TF), defined in Eq. 2.1, is determined by comparing the thickness of a deposited film as measured

Source	Z ratio	ρ (g/cm ³)
Nb	0.492	8.578
Al	1.080	2.7
Co	0.343	8.9
Cu	0.437	8.930
Au	0.381	19.30

Table 2.1: QCM input parameters

by the QCM (t_x) and the actual thickness measured with profilometry (t_m).

$$TF_f = TF_i \frac{t_m}{t_x} \quad (2.1)$$

TF_f is the calibrated tooling factor and TF_i is the initial tooling factor used prior to calibration. Four separate QCMs are located around the perimeter of the deposition chamber just above the cryogenic shroud, each with their own crystal tooling factor ranging from 80% to 135%. Material input parameters are listed in Table 2.1 [58]. Tooling factors for each individual film are all set to 100%. As material builds up on a QCM over time, the accuracy decreases. Having multiple QCMs provides longer intervals between chamber servicing.

In addition to QCM monitoring, the deposition controller also controls pneumatic shutters installed just over the copper shroud plate. Two shutters are used to control line of site between the e-beam source and the wafer on the sample manipulator. A film recipe is entered into the deposition controller, which includes the QCM input parameters for a given source material and the desired film thickness. Once the selected QCM is registering the desired deposition rate, the recipe can be started and the shutters are automatically retracted. The shutters move back to

break wafer-source line of sight once the desired film thickness reading is reached. The emission current is then decreased to 0 mA.

2.3.2 Shadow Masks

The deposited metal wires that constitute our crossed wire tunnel junctions are defined using shadow masks. The shadow masks are 0.001 in. thick etched Ni stencils fabricated via electroforming. Using shadow masks to define devices, as opposed to photolithography, is primarily motivated by expedited processing and cleanliness. Photoresist residue is an oft cited source of contamination in mesoscopic devices that can be disregarded here [59]. The masks have sixteen 0.4 in. x 0.4 in. dies with individual stencil designs laid out in a 4 x 4 pattern, as shown by Fig. 2.6(a) for a Gen I mask. Separate mask cassettes are used for the bottom (M1) and top (M2) tunnel junction layers. While both stencils are identical, one is flipped over relative to the other along the dashed line in Fig. 2.6(a). In other words, the two masks are mirror images of each other. The tunnel barrier is formed via oxidation of the first layer prior to deposition of the second layer and will be discussed later. In the upright orientation according to the letter labels in Fig. 2.6(a), the die designs are laid out such that the left 2 x 4 dies and the right 2 x 4 dies superimposed on each other form the completed die designs. Twelve open circles around the perimeter of each die provide contact pads for electrical measurements.

The Ni stencil is sandwiched between two stainless steel supports shaped as 75 mm wafers to provide rigidity. This assembly is placed in a stainless steel cassette

in the same manner as our wafers and stored in the load lock chamber elevator. M1 and M2 cassettes are typically stored in the load lock chamber. The only difference between the two is that the mask assemblies are flipped over relative to each other prior to cassette assembly such that they are mirror images when viewed straight on. Once a wafer cassette is placed on the sample manipulator of the deposition chamber, the manipulator magazine is rotated 180° along the polar angle such that the wafer surface is facing the bottom of the chamber. The mask cassette can then be loaded onto the sample manipulator in the same manner as the wafer cassette. This arrangement, shown for a partially seated mask cassette in Fig. 2.3(b), puts the shadow mask and wafer surface in close proximity to each other to minimize spreading of the stencil pattern during deposition.

2.3.2.1 Generation 1 Masks

Individual die designs for the first generation masks, fabricated by Tecan, are shown on Fig. 2.6(b). The dashed line in Fig. 2.6(b) indicates the separation between the two designs halves. After the top layer has been deposited through M1 and bottom layer through M2, the wafer will have four unique die designs. The square or “D” design devices, seen in the middle of the first and last row of the mask, can be used in a clean room setting to create structures such as nanopillars. In addition, the “D” devices provide a relatively large area useful for photoelectron spectroscopy. The other three die designs can be seen in Fig. 2.6(b) with the designs labeled “A”, “B”, and “C.” The “A” die design is composed of a 0.002 in. wide “dog

bone” shaped wire and four 0.001 in. wide cross wires spaced 0.002 in. apart. This design results in tunnel junction areas of $\approx 55 \mu\text{m} \times 75 \mu\text{m}$. The dog bone wire has two contacts on either end allowing for four terminal resistance measurements of the layer. In addition to simply offering four crossed wire tunnel junctions to measure for better statistical analysis, the arrangement of the “A” devices can theoretically be employed for spin injection experiments [60]. However, it was typical that one or two of the vertical cross wire apertures would not fully open during mask etching since closely spaced apertures of 0.001” on a 0.001” thick stencil are difficult to achieve. The “B” design results in two crossed wire junctions, each composed of perpendicular wires of 0.002 in. width. This design allows for significant misalignment between top and bottom layer depositions while maintaining the cross wire geometry with the desired junction area. The “C” design results in one junction per die with the two sides overlapped in the middle of the die. As the junction area is defined by the lateral overlap in this case, as opposed to wire widths for crossed wire devices, the junction area can be controlled via angled deposition. However, this design is quite sensitive to misalignment between top and bottom layer masks.

The alignment of the top and bottom tunnel junction layers was originally the dominant factor in determining device yield. Shifts between the top and bottom layer can cause the patterns to overlap in unintended places giving rise to poorly defined junction areas. Misalignment of the contact pads between the layers makes room temperature characterization difficult in our custom measurement jig, discussed later in this chapter. Misalignment typically occurred due to poor or inconsistent seating of the wafer and mask cassettes in the sample manipulator, as well

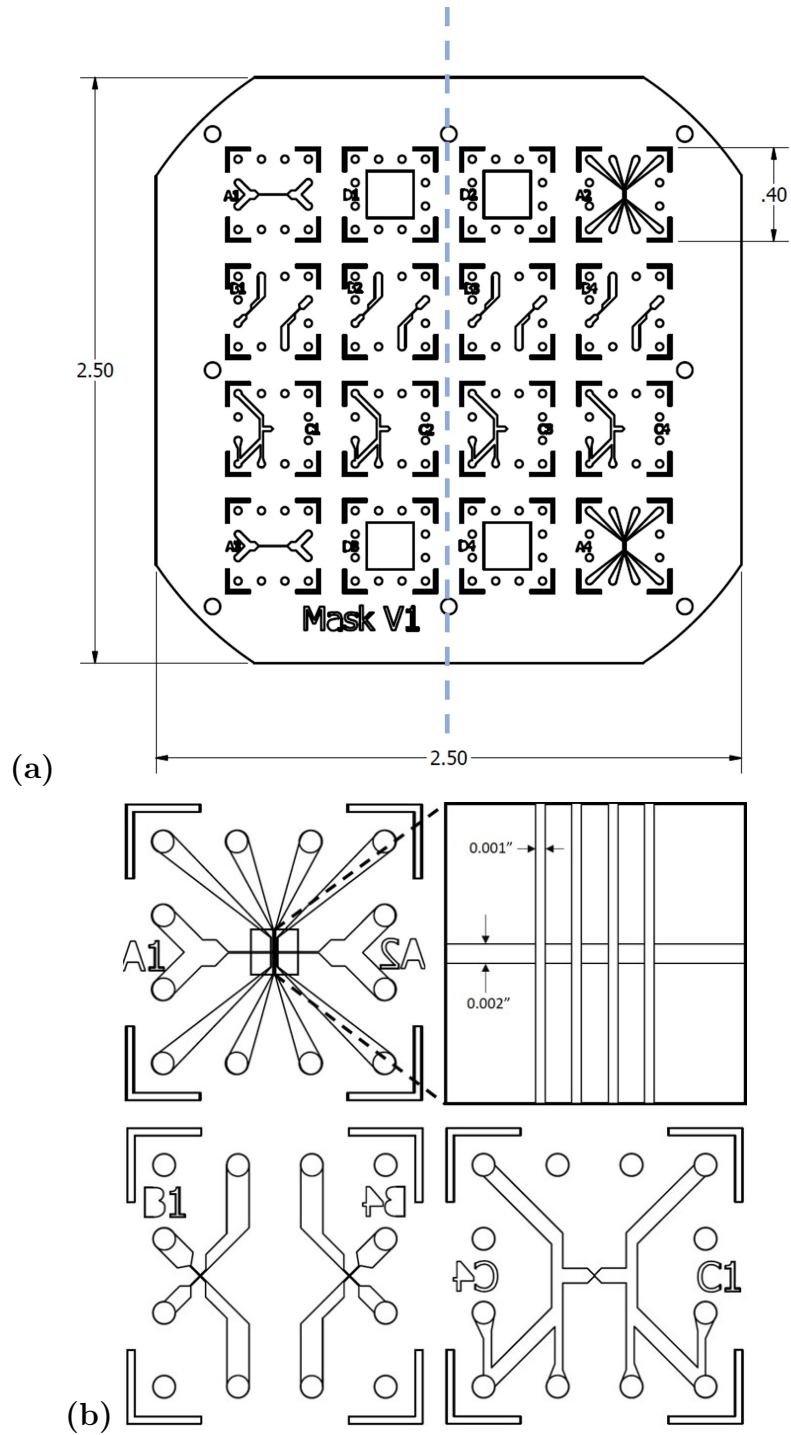


Figure 2.6: Generation I stencil and completed die designs. (a) The dashed line indicates the left and right side designs to be superimposed on each other once both tunnel junction layers are deposited. (b) The individual die designs for the Gen I masks, including the stencil aperture dimensions for the “A” design.

as shifting of the mask or wafer in their respective cassettes. When the magnetic transfer rod forks disengage from the cassettes and slide away, the cassette can shift in the manipulator magazine slot. To remedy this, the tip of the magnetic transfer rod forks were used to push each cassette fully into their respective slots without the fork entering the cassette side rails. Inspection by camera confirmed this method typically avoided shifts from M1 and M2 relative to the wafer cassette greater than $\approx 50 \mu\text{m}$. Misalignment from the wafer shifting inside it's cassette occurred during cassette transfers. This was remedied by ensuring smooth magnetic transfer rod movement and cassette - elevator interactions.

Misalignment due to masks shifting in their respective wafers was the most prevalent source and necessitated several changes. First, the Ni stencil and stainless steel mask support assembly was tack welded together as the stencil would often slide inside the supports. Second, four 1/16 in. diameter dowel pins were welded around the interior of the top mask cassette half. These pins went through holes in the mask assembly and served to stabilize the position of the assembly relative to the cassette. With the improved mask assembly - cassette design and proper seating of cassettes with the transfer rod forks, misalignment between the top and bottom tunnel junction layers was reduced to $\approx 50 \mu\text{m}$. Given the leniency allowed from the die designs, this practically removed layer misalignment from device yield considerations.

2.3.2.2 Generation II Masks

Several issues, including a dwindling supply and incomplete aperture openings, lead to a second generation of masks fabricated by Bluering Stencils. The overall shape of the mask, 2.5 in. x 2.5 in. with sixteen dies, was retained as seen in Fig. 2.7(a). The “C” type devices were removed in favor of more “A” type devices, allowing for a greater number of tunnel junctions per wafer. The spacing of the vertical cross wires in the “A” devices was increased to improve pattern etch yield during mask manufacturing. The resulting tunnel junctions, seen in Fig. 2.7(b), typically had an area of $\approx 55 \times 55 \mu\text{m}^2$. Finally, test bars of different widths were included in the “D” dies. This allowed for four terminal resistance measurements of the top and bottom metal layers with a clearly defined area, enabling calculation of the specific resistance, or resistance per square, of each layer.

2.3.3 Plasma Oxidation

Prior to metals deposition, wafers undergo oxygen plasma cleaning in the oxidation chamber. Organic contaminants on the wafer surface can be deleterious to film growth and device performance [61, 62]. The species present in the plasma primarily consist of oxygen ions (O^+ , O_2^+) and excited radicals (O^*), confirmed by the optical spectrum of the plasma shown in Fig. 2.8. These species react with the organic molecules found on the wafer surface, forming molecules with relatively high vapor pressures such as hydrocarbons and are pumped away. The oxidation chamber elevator has three slots with the top slot being used for plasma exposure. With the

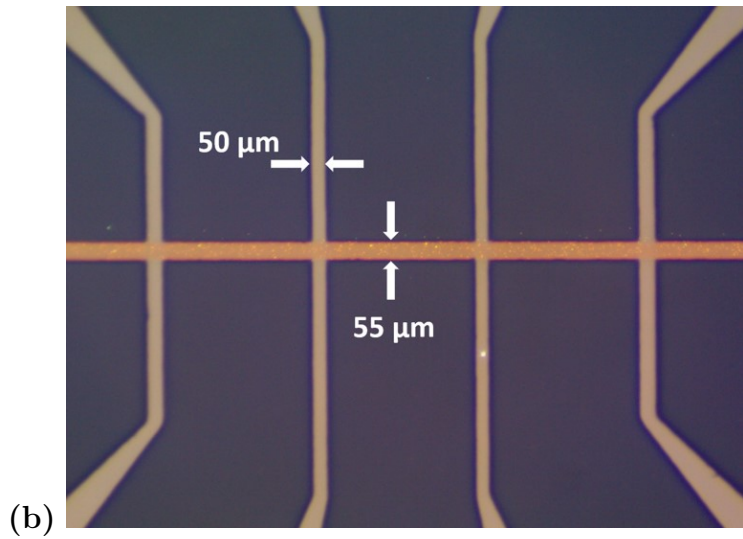
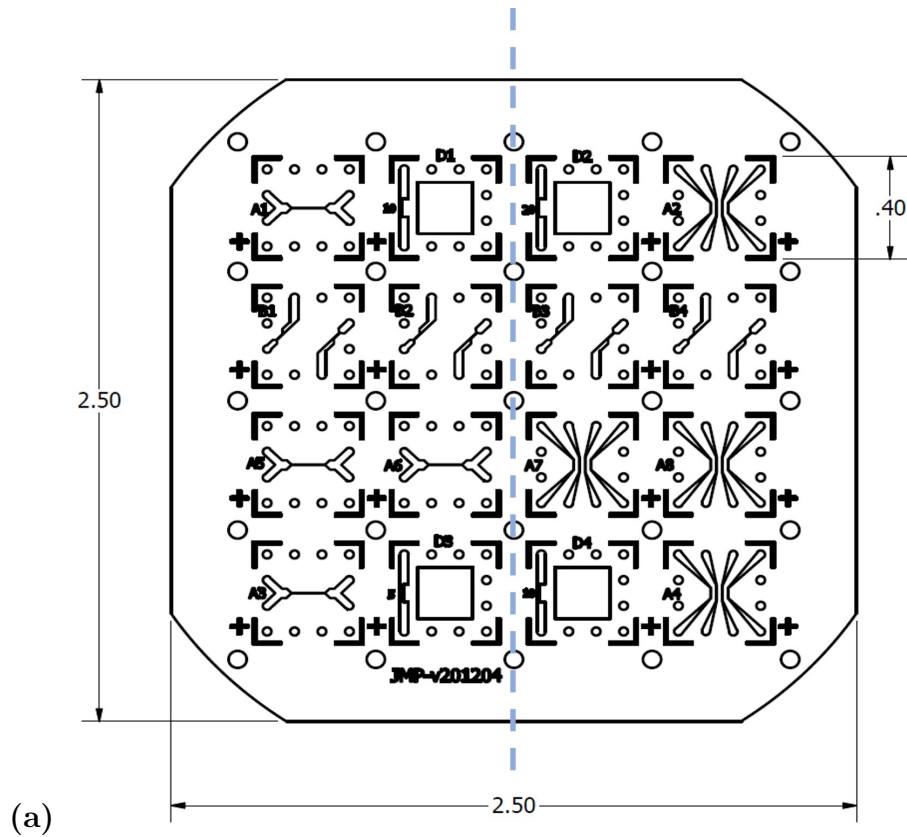


Figure 2.7: Gen II stencil design and device micrograph. (a) The 2.5 in. x 2.5 in. Gen II stencils include more “A” type dies and test wires to the sides of the “D” dies. (b) Completed “A” device with the layer stack Nb/Al/AlO_x/Au/Cu/Au and good pattern alignment. In this image, the vertical wires are the bottom layer Nb/Al/AlO_x and the horizontal wire is the top layer Au/Cu/Au.

elevator raised up, a magnetic transfer rod moves underneath of it to retrieve a wafer from the load lock. Once the transfer rod is fully retracted back into the oxidation chamber, the elevator is lowered and the wafer is loaded onto the top elevator slot. With the wafer raised to the anode, a gate valve isolates the chamber from the turbo pump and the valve connecting the tri-scroll backing pump to the turbo pump is closed. Research grade 99.99% oxygen is leaked into the chamber. The roughing valve, connecting the backing pump directly to the chamber, is opened to continuously pump species away maintaining a dynamic pressure of ≈ 160 mTorr. A Kepco DC power supply, operating in constant current mode, applies a high negative voltage to the cathode and ignites the plasma. A recipe programmed into the power supply controls the time and DC current [63]. The recipe used for wafer cleaning is 40 s at 100 mA and ≈ -570 - -600 V (57 - 60 W). The parameters in this recipe were scaled from a different system to achieve similar results [54]. XPS was used to check for contaminants on the wafer surface and to verify the efficacy of the plasma cleaning recipe. Fig. 2.9 displays XPS survey scans on a Si/SiO_x wafer before and after plasma cleaning. The only contaminant identified is C, which is no longer discernible after plasma cleaning in the inset of Fig. 2.9. Furthermore, no contaminants that could potentially result from sputtering (Fe, Cr, etc.) in the oxidation chamber are detected. Once the recipe finishes after 40 s, the high voltage is turned off and the plasma ceases. The roughing pump reduces the chamber pressure to below 50 mTorr, roughly 60 s after the O₂ leak valve is closed. The roughing valve is closed and the turbo backing valve is opened, followed by the turbo pump gate valve opening to evacuate the chamber down to its typical base

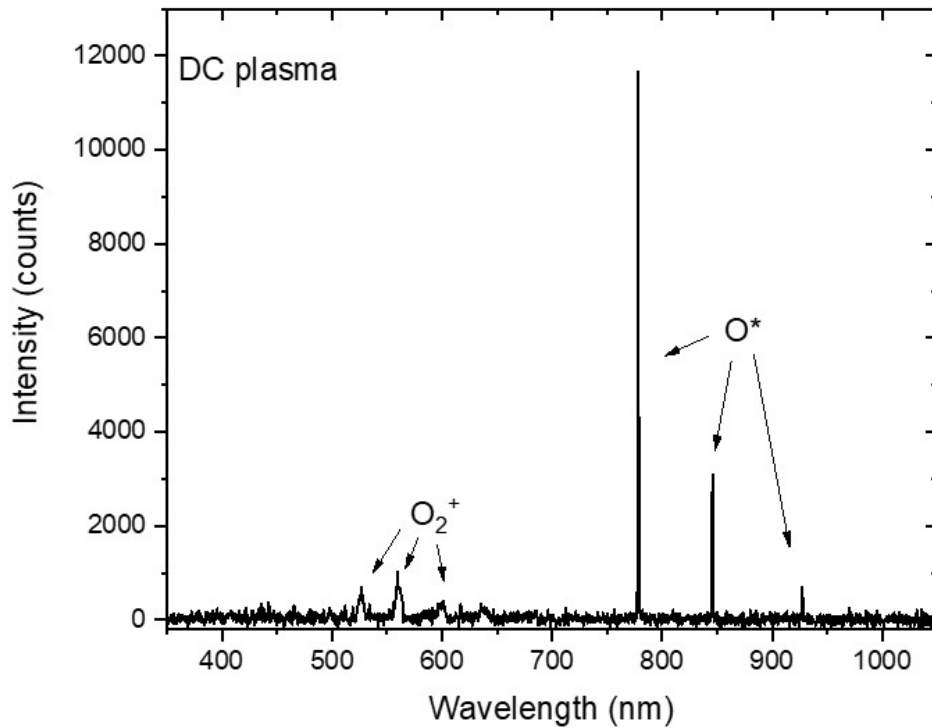


Figure 2.8: Optical spectrum of DC oxygen plasma operating at 58.8 W (-588 V, 100 mA). The chamber pressure is 160 mTorr. The only identifiable species in the plasma are oxygen ions and oxygen radicals.

pressure in the 10^{-9} Torr range.

Plasma oxidation is performed in a similar manner to plasma cleaning. After the bottom tunnel junction layer deposition ending in Al, the wafer is transferred to the oxidation chamber. Instead of using a continuous flow of O₂ from the leak valve, the chamber is filled to a static pressure of ≈ 160 mTorr and the leak valve is closed. The typical oxidation recipe used to form our AlO_x tunnel barriers is 100 mA (57 - 60 W) for 7 s. Details on determining this recipe will be discussed

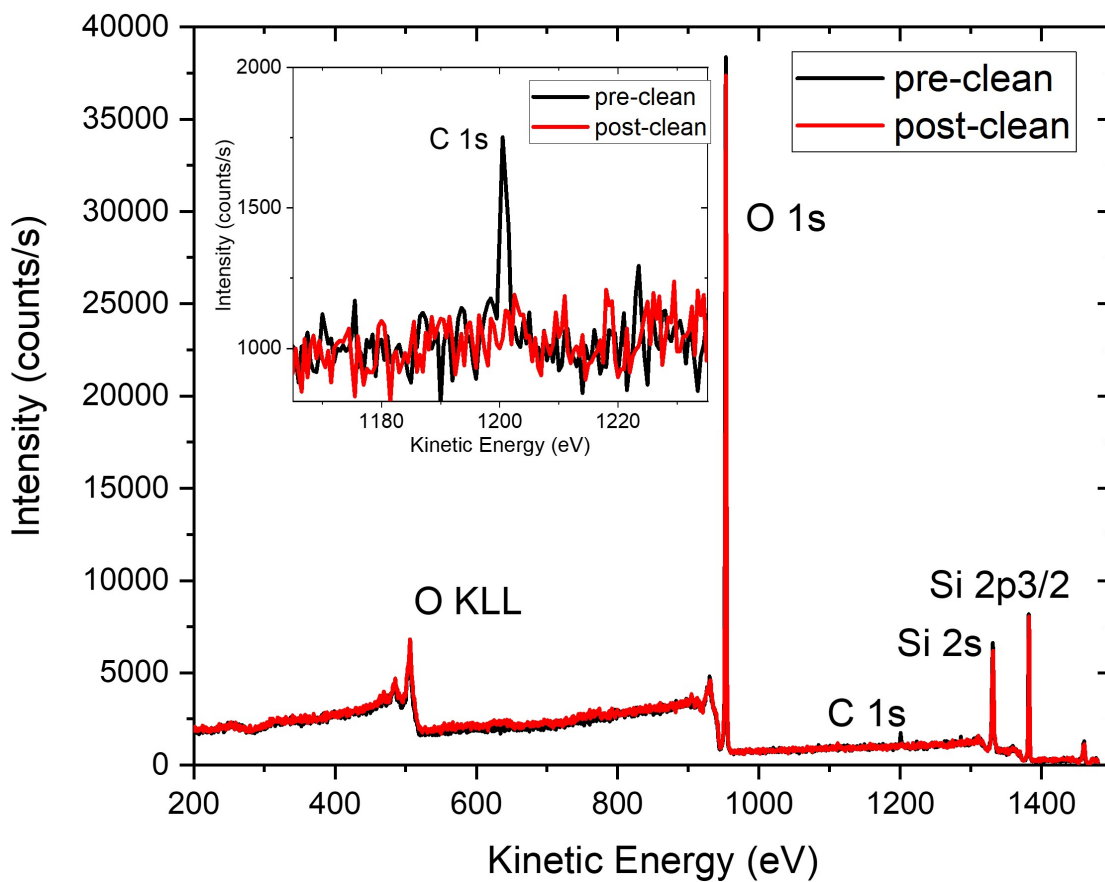


Figure 2.9: XPS survey scan of a 75 mm Si wafer with 100 nm of SiO_x before and after plasma cleaning. The measurement is performed using a high power (100 W) setting and the spot size is $\approx 100 \mu\text{m}$ in diameter. The only identifiable peaks are of O, Si, and C. (inset) The C 1s peak is no longer discernible within the measurement sensitivity after plasma cleaning.

in Chapter 3. The direction of the electric field ensures that the positive ions are accelerated away from the wafer surface, reducing the possibility of sputtering the wafer surface via the positively charged ions. Once the oxidation is complete, the chamber is quickly evacuated back to base pressure. The wafer sits for at least twelve hours under vacuum before returning to the deposition chamber for the top metal layers. Empirical observations from within our group have shown that deposition of the top metal layers directly after oxidation results in tunnel junctions with higher rates of tunnel junction resistance drift in time. It is possible that the benefit of reduced resistance drift, when allowing the wafer to sit prior to top layer deposition, arises from relaxation of atoms in the barrier to lower free-energy configurations prior to perturbation of the top metal layer deposition. Tunnel junction drift, which is correlated with electrically active defects, is further discussed in Chapter 3.

2.4 Device Characterization

After the top tunnel junction layers have been deposited, the wafer is transferred to the load lock and removed from vacuum. Both room temperature and cryogenic measurements are used to characterize the tunnel junctions. In this section, I will describe the measurement systems used and provide details on performing specific measurements.

2.4.1 Room Temperature Device Characterization

The room temperature I-V characteristics of the tunnel junctions and their leads are measured using a custom jig, where mechanical and electrical contact is enabled by spring-loaded pins. The wafer is held in a shallow recess on a clean metal plate and a printed circuit board (PCB) with spring loaded pins is placed over top of it. The layout of the pins matches the layout of the contact pads on the wafer, thus making electrical contact to each individual wire and allowing for fast wafer characterization. I-V measurements were performed in a four point configuration to remove the lead resistances from consideration. For example, the four point configuration to measure conductance of an “A” die dog bone wire is shown in Fig. 2.10(a). A Hewlett-Packard 3468B multimeter sources a constant current (I_s) from I^+ to I^- . A Keithley 2000 multimeter is placed in series and independently measures the source current. The voltage drop (ΔV) over the wire is measured as $\Delta V = V^+ - V^-$ and read from the front display of the multimeter.

Due to the symmetry of the mask pattern, there are four “A” dies with horizontal dog bone wires on completed wafer: two on the left side from the bottom layer (M1) and two on the right side from the top layer (M2). Given that the resistance along the wire is inversely proportional to the width, the vast majority of the voltage drop can be assumed to occur over the narrow section of the wire indicated in Fig. 2.10(a). Once the length (l) and width (w) of the wire have been measured, the layer’s square resistance is calculated as $R_{sq} = R(w/l)$. Thin films with the same thickness and resistivity will have the same R_{sq} regardless of area,

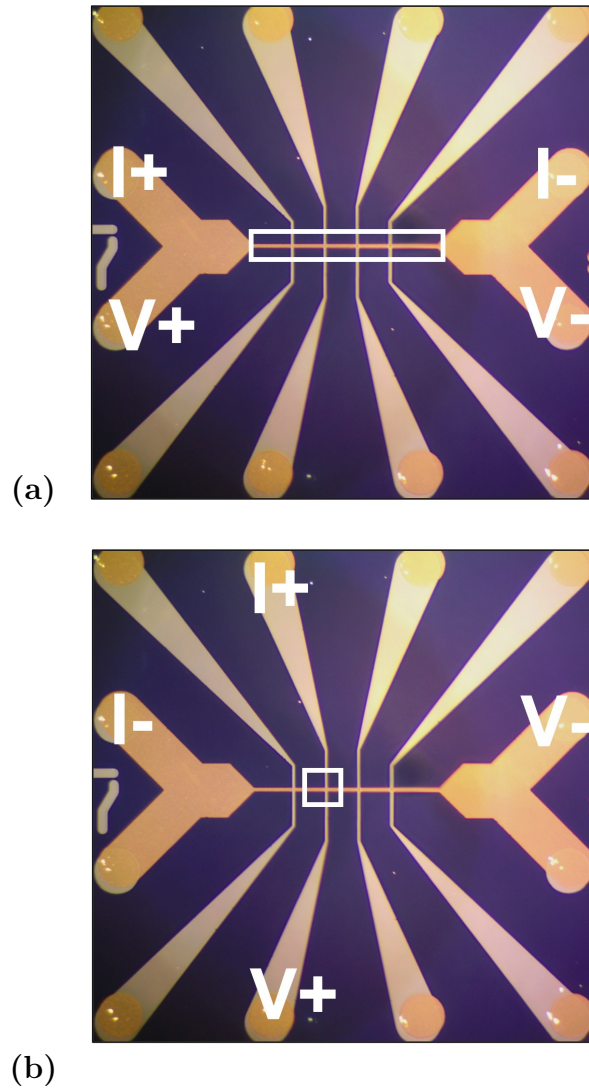


Figure 2.10: Four point I-V measurement configurations on an “A” die. The horizontal “dog bone” wire is top layer of Au/cu/Au and the vertical cross wires are the bottom layers of Nb/Al/AlO_x. (a) The square resistance for the top and bottom tunnel junction layers is typically determined by measured the dog bone resistances on “A” dies. As the resistance along the wire is inversely proportional to the width, the measured ΔV can be assumed to occur over the long narrow section indicated by the white rectangle. The length and width of the wire is determined via optical microscopy. (b) R_{4pt} for each tunnel junction is measured in a four point configuration. The “A” dies offer four evenly spaced tunnel junctions with a common wire.

providing a useful metric when comparing devices. In addition, R_{sq} is needed for the “negative resistance” correction described later in this chapter.

The four point measurement configuration for a tunnel junction is shown in Fig. 2.10(b). The current biased I-V characteristics are measured over $\Delta V \approx \pm 100$ mV with a Keithley 2612 source meter. This bias range is used to avoid Fowler-Nordheim (FN) tunneling. FN tunneling describes tunneling through a triangle barrier as a consequence of the bias eV approaching the barrier height ϕ . Therefore, the trapezoidal barrier approximation is no longer valid. The data is then smoothed and numerically differentiated to obtain the differential conductance (dI/dV).

2.4.1.1 Negative Resistance Artifact

While effective eliminating lead and contact resistance from the measurement, four point measurements of crossed wire tunnel junctions returns a value for device resistance $R_{4\text{pt}}$ less than that of the actual device resistance R_{dev} [54, 64]. In such a configuration, the voltage drop from the tunneling current through the junction is convolved with the voltage drop from current flowing laterally in the cross wire regions just above and below the junction. A systematic correction can be applied to $R_{4\text{pt}}$ to obtain the actual R_{dev} using the equations shown below.

$$\Delta R_{\infty} = \frac{1}{6} \left(R_{\text{sq,t}} \frac{w_{\text{b}}}{w_{\text{t}}} + R_{\text{sq,b}} \frac{w_{\text{t}}}{w_{\text{b}}} \right) \quad (2.2)$$

$$R_{4\text{pt}} = \frac{\sqrt{6(\Delta R_{\infty} + \Delta R_0)R_{\text{dev}}}}{\sinh(\sqrt{6(\Delta R_{\infty} + \Delta R_0)/R_{\text{dev}}})} + \Delta R_0 \quad (2.3)$$

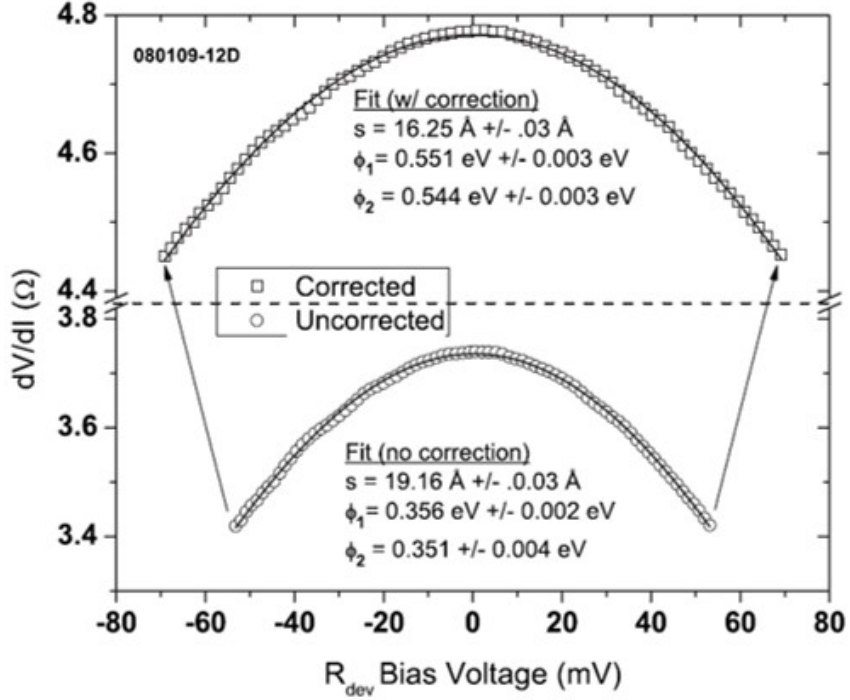


Figure 2.11: $dV/dI(V)$ for a low resistance tunnel junction is shown before and after correction for the negative resistance effect. By correcting the differential resistance, the extracted tunnel barrier parameters are also corrected. Adapted from Ref [64] with permission from AIP publishing.

ΔR_0 is the measured R_{4pt} for a proxy device fabricated without an a tunnel barrier. $R_{sq,t}$ ($R_{sq,b}$) is the square resistance of the top (bottom) layer and w_t (w_b) is the wire width of the top (bottom) layer. ΔR_∞ is the upper bound on the error, representing the case where $R_{dev} \rightarrow \infty$. By solving for the root R_{dev} in Eq. 2.3 for each $R_{4pt}(V)$, the corrected differential resistance as a function of bias can be obtained as seen from Fig. 2.11 taken from Ref. [64].

The relative error due to the negative resistance artifact is nonlinear with R_{dev} , decreasing with increasing device resistance. Naturally, the effect is also mitigated as lead resistance decreases. The tunnel junctions discussed in Chapter 3, which

have resistance-area ($R_{\text{dev}}A$) products of $\approx 3\text{-}7 \times 10^4 \Omega \cdot \mu\text{m}^2$, suffer a relative error of $<3\%$. The tunnel junctions discussed in Chapter 5, which have higher $R_{\text{dev}}A$ products of $\approx 0.5\text{-}1.5 \times 10^6 \Omega \cdot \mu\text{m}^2$, suffer a relative error of $<0.5\%$.

2.4.1.2 Tunnel Junction Resistance Modelling

Three criteria, described by Rowell [53], are often used to verify that quantum tunneling of electrons is the dominant transport mechanism in a tunnel junction: 1) an exponential dependence of conductance with insulator thickness, 2) a parabolic dependence of conductance with voltage, and 3) an insulating-like temperature dependence of conductance. These criteria are typically applied to rule out significant contribution to the conductance from pinholes, or metallic shorts through the barrier from one electrode to the other. Criteria #1 and #2 can be viewed as necessary but not sufficient, as they can be demonstrated in tunnel junctions with metallic shorts (pinholes) [65, 66]. As a practical matter, criterion #1 is not addressed here as it cannot be used to evaluate a single device with a chemically defined barrier thickness. Criterion #2, a parabolic conductance with voltage, is typically demonstrated by adequately fitting the conductance of a tunnel junction with an appropriate theoretical expression, such as the Simmons [67] or Brinkman-Dynes-Rowell (BDR) [68] model, and extracting physically meaningful tunnel barrier parameters [65]. The following section discusses such a model by Chow, which is used in this thesis [69].

As an introduction to the model described by Chow, we consider two parallel electrodes separated by a thin insulating layer. The insulating dielectric forms a

potential barrier between the two electrodes due to the energy gap between its valence and conduction bands. For a sufficiently thin insulating layer, electrons can quantum tunnel between the two electrodes. The energy diagram for such a system without an applied bias is shown in Fig. 2.12(a), taken from Ref. [69]. Once the materials are brought into electrical contact, electrons tunnel between the electrodes and align the Fermi levels once equilibrated. Under an applied bias V between the electrodes, an integral expression for the tunneling current density J is given by Eq. 2.4 below. [67, 69]:

$$J = \frac{4\pi me}{h^3} \int_0^{E_m} \rho(E_x, V) D(E_x) dE_x \quad (2.4)$$

Here, e is the electron charge, h is Planck's constant, m is the electron mass, E_m is the maximum energy of electrons in the electrode, E_x is the energy of an electron with momentum perpendicular to the barrier (direction of tunneling), $\rho(E, V)$ is the supply function, and $D(E, V)$ is the tunneling probability. The supply function is calculated using the density of states of each electrode $\rho_{1,2}(E, V)$ and their respective distributions governed by the Fermi-Dirac distribution function $f(E, V)$ [68]:

$$\rho(E, V) = \rho_1(E) \rho_2(E - eV) [f(E) - f(E - eV)] \quad (2.5)$$

For normal metal electrodes at low bias ($V \rightarrow 0$), the density of states for each metal can be considered energy independent and removed from the integral.

The tunneling probability is expressed using the Wentzel-Kramers-Brillouin

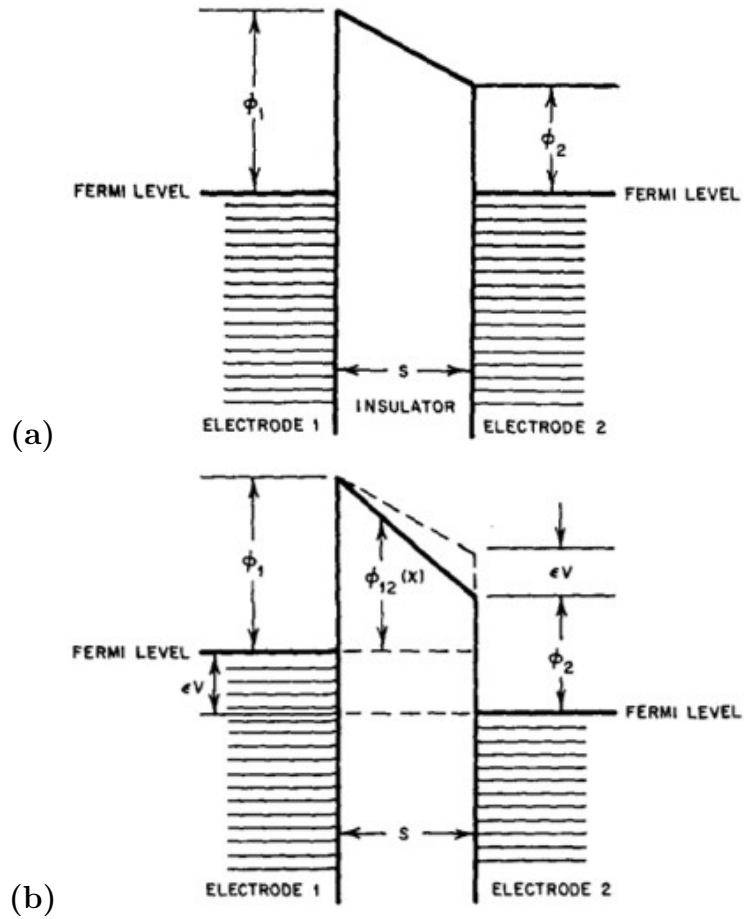


Figure 2.12: Electron energy diagram in a metal-insulator-metal tunnel junction. (a) The Fermi levels are aligned when the junction is not biased and the electrodes have equilibrated. The larger work function of electrode 2 leads to $\phi_1 > \phi_2$. (b) With a positive bias on electrode 2, the Fermi level of electrode 2 is pushed down relative to electrode 1. In Chow's convention, this is considered the reverse bias direction. Adapted from Ref [69] with permission from AIP publishing.

(WKB) approximation [67, 68, 69]:

$$D(E_x) = \exp \left\{ -\frac{4\pi(2m)^{1/2}}{h} \left(\int_{x_1}^{x_2} [\phi(x) + E_F - E_x]^{1/2} dx \right) \right\} \quad (2.6)$$

The barrier potential $\phi(x)$ is measured with respect to E_F , the Fermi level of the negatively biased electrode in this convention. The integral limits x_1 and x_2 are the classical turning points within the WKB formalism, where $\Delta x = x_2 - x_1$ represents the tunnel barrier width. Within this formalism, the expression for tunneling probability begins to fail if Δx approaches the tunneling electron's wavelength or if the electron's energy is near the maximum of the potential barrier $\phi(x)$. In other words, the WKB tunneling probability is best suited for wide and tall barriers.

As Eq. 2.6 has no closed form solution with an arbitrary potential barrier shape, the barrier potential $\phi(x)$ is often replaced with a rectangular or trapezoidal barrier. The exact shape of $\phi(x)$ is extremely difficult to express, as it depends on the electrode work functions, electron affinity of the insulator, image forces, dielectric constant of the insulator, and applied bias [69]. The Simmons model found success by approximating an arbitrary potential barrier shape $\phi(x, V)$, with the barrier width along the x direction, with an average barrier height $\phi(V)$ [67]. By providing the following function for an arbitrary tunnel barrier potential in Eq. 2.7, the Chow model builds upon the Simmons model by accurately capturing asymmetry in the I-V characteristics at low voltage [69]:

$$\phi_t = \left\{ \frac{1}{\Delta x} \int_{x_1}^{x_2} [\phi(x)] dx \right\}^2 = \frac{4 \left[\phi_1^{\frac{3}{2}} - (\phi_2 - eV)^{\frac{3}{2}} \right]^2}{9(\phi_1 - \phi_2 + eV)^2}. \quad (2.7)$$

With $\phi_1 \neq \phi_2$, the shape of the barrier depends upon the polarity of applied bias. The convention used for Eq. 2.7 is that the electrode with the smaller work function (read as barrier height here) is being biased, as shown in Fig. 2.12(b). When biasing the electrode with the larger work function, simply swap ϕ_1 and ϕ_2 on the right side of Eq. 2.7. For low bias voltages ($-\phi_1/e \leq V \leq \phi_2/e$), the tunnel current density can be expressed by substituting Eq. 2.7 and Eq. 2.6 into Eq. 2.4:

$$J = \frac{3e(2m)^{\frac{1}{2}}}{Bh^2s^2} \left\{ \phi_t \exp[-Bs\phi_t^{\frac{1}{2}}] - (\phi_t + eV) \exp[-Bs(\phi_t + eV)^{\frac{1}{2}}] \right\} \quad (2.8)$$

where $s = \Delta x$ and

$$B = 4\pi(2m)^{\frac{1}{2}}/h = 1.025 \text{ eV}^{-\frac{1}{2}} \text{ \AA}^{-1}. \quad (2.9)$$

The tunnel current in Eq. 2.8 is evaluated using the 0 K Fermi-Dirac distribution, thus ignoring thermal contributions to the current. Again, low bias is used to avoid Fowler-Nordheim (FN) tunneling characterized by a triangular barrier. The differential conductance is then given by the partial derivative of Eq. 2.8 with respect to V :

$$\frac{\delta I(V)}{\delta V} = G(V) = A(\delta_V J) \quad (2.10)$$

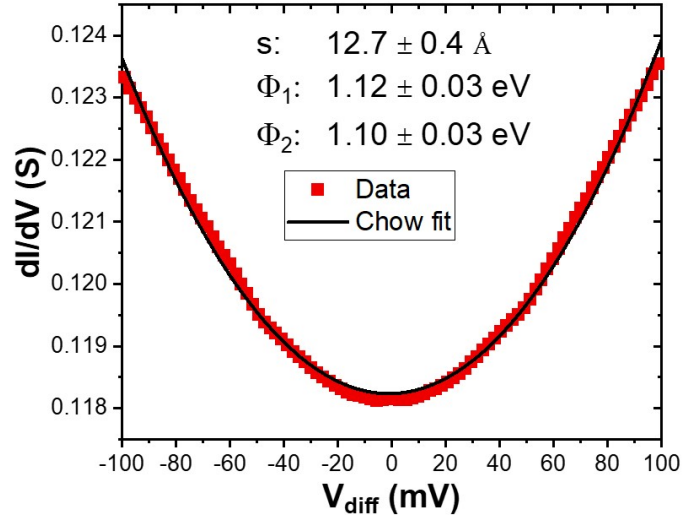
where A is the device area in this context.

Given the device area, Eq. 2.10 can be used to fit the differential conductance, obtained by taking the numerical derivative of the DC voltage with respect to the current, with free parameters s , ϕ_1 , and ϕ_2 . Fig. 2.13 displays the differential conductance fits for two devices at room temperature and the extracted fit parameters.

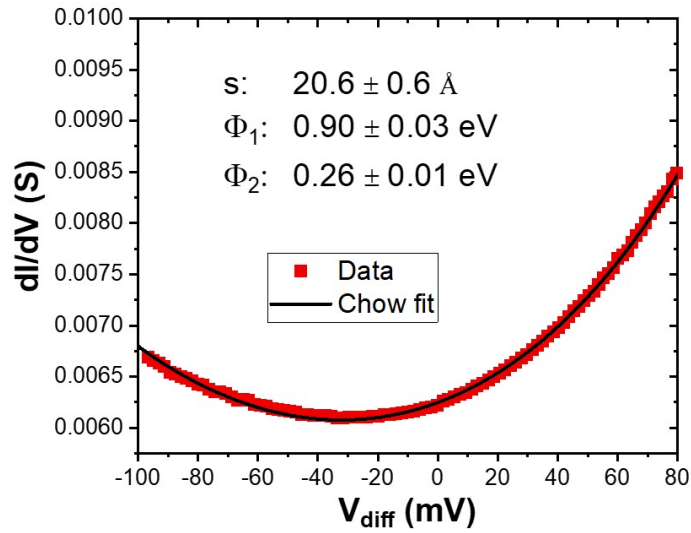
Below the FN limit, the differential conductance has a approximately V^2 dependence [68]. For the case of $\phi_1 = \phi_2$, the conductance minimum is centered at 0 V. This is nearly the case in Fig. 2.13(a), where $\phi_1 \approx \phi_2$ for this Co/AlO_x/Co tunnel junction. However, the minimum in Fig. 2.13(b) is shifted in bias away from 0 V due to large barrier asymmetry in this Nb/Al-AlO_x/Au tunnel junction. Any real tunnel junction will have some degree of asymmetry, which is typically attributed to different work functions in the electrodes or a nonuniform chemical composition in the barrier. For the Co/AlO_x/Co measurement in Fig. 2.13(a), the oxidation is thought to be relatively uniform and closer to stoichiometric Al₂O₃ as discussed in Chapter 3 [70]. Combined with similar electrodes, the nearly symmetric barrier is expected. For the Nb/Al-AlO_x/Au measurement in Fig. 2.13(b), the aggressive plasma oxidation front acting on a relatively thick Al layer likely leads to a nonuniform, sub-stoichiometric oxide profile [46, 70]. Combined with dissimilar electrodes, it is not surprising that significant barrier asymmetry is observed. The device in Fig. 2.13(b) also has a larger barrier width compared to Fig. 2.13(a), which makes the conductance change more gradually with bias.

2.4.2 Cryogenic Device Characterization

Measuring the conductance of tunnel junctions and their metallic leads as a function of temperature can provide valuable insight concerning material quality and character. This may include information on the dominant conduction mechanisms through the tunnel barrier or the prevalence of impurities or defects in the device.



(a)



(b)

Figure 2.13: dI/dV as a function of bias voltage V and Chow model fits for (a) $\text{Co}/\text{AlO}_x/\text{Co}$ and (b) $\text{Nb}/\text{Al}-\text{AlO}_x/\text{Au}$ tunnel junctions.

Furthermore, cryogenic temperatures open the door to interesting physics such as superconductivity discussed in Chapters 1 and 5. The following section describes the cryogenic systems utilized in this thesis and provides details on cryogenic electrical measurements.

Individual sample dies are cleaved from finished tunnel junction wafers and silver pasted into a 24 pin dual in-line package (DIP), as seen in Fig. 2.14. Wire bonds are made between the die and DIP contact pads. Cryogenic measurements discussed in this thesis take place in two commercial systems, an Advanced Research Systems (ARS) closed cycle cryocooler and a Bluefors Cryogenics BF-LD400 dilution refrigerator (DR). The base temperature of the cryocooler is approximately 3.9 K. The DR is capable of reaching ~ 10 mK. Discussion on the effective electron temperature in the DR can be found in Chapter 5. The measurements in this thesis do not utilize any passive filters on the signal lines. Shown in Fig. 2.15, the sample DIP is mounted onto the base temperature sample stage for both systems. A custom multiplexing (MUX) board, shown in Fig. 2.15(b), is attached to the DR sample stage, allowing for high measurement throughput. Room temperature checks are performed prior to cooling down, consisting of I-V measurements on the tunnel junction and lead wires. Cryogenic four terminal I-V characteristics are measured in the same manner as the room temperature measurements, the configuration of which is shown in Fig. 2.10(b). The source current I_s is set by applying a bias voltage to I+ and measured at I- with a current preamplifier at ground potential. The differential voltage V_{diff} is measured as $V_+ - V_-$.

The residual resistivity ratio (RRR) of the metallic tunnel junction leads can

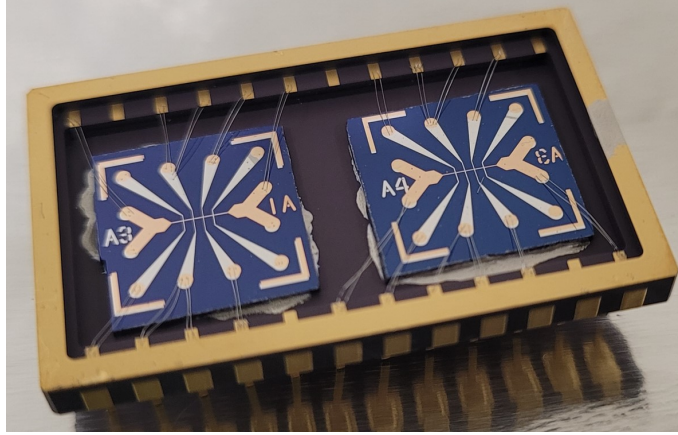


Figure 2.14: 24 pin DIP with two “A” design tunnel junction dies. The chips are silver pasted to the DIP. Wire bonds connect the DIP and die contact pads.

be determined by comparing the resistivity at room temperature and cryogenic temperatures. RRR is commonly used as a gross indicator of material quality. For non-superconducting materials, this is defined as $RRR = R_{300\text{ K}}/R_{0\text{ K}}$. As 0 K is not practical, the resistivity at the coldest measurement temperature (typically 2-4 K) is referenced. For superconducting materials, resistivity is exactly 0 below the superconducting transition temperature (T_c) so $R_{0\text{ K}}$ is replaced by the resistivity at a temperature just above T_c . According to Matthiesen’s Rule, the resistivity of metals can be treated as the sum of two parts: 1) ρ_{ph} , a temperature dependent resistivity resulting from phonon scattering of a carrier in the lattice, and 2) ρ_r , a temperature independent resistivity resulting from scattering of a carrier off material impurities, lattice defects, and grain boundaries [71]. As temperature is decreased, phonon scattering probability and ρ_r decreases. As $T \rightarrow 0\text{ K}$, only the residual resistivity (ρ_r) remains, thus providing a metric for the prevalence of impurities and defects in the material. For reference, the RRR of Cu wire for telecommunications



(a)



(b)

Figure 2.15: Sample DIPs mounted on the nominally base temperature sample stages for the (a) cryocooler and (b) the DR. Multiple samples can be addressed on the DR multiplexing board, shown in (b), allowing for increased measurement throughput.

is ~ 40 -50. RRR for superconducting films will be discussed in Chapter 5, where our Nb wires with thin Al overlayers have $\text{RRR} \approx 1.8$ in good agreement with other polycrystalline Nb films [39, 72].

Rowell's third, and most rigorous [65, 66], criterion of junction conductance dominated by tunneling is demonstrated by measuring conductance $G(V \rightarrow 0)$ as a function of temperature. Again, this is most useful in ruling out a significant contribution from pinhole conduction. This criterion is typically stated as a tunnel junction displaying conductance with an insulating-like temperature dependence, i.e. the conductance decreases with decreasing temperature. For an ideal MIM system with single-step elastic tunneling as the dominant conduction mechanism, the relative change in conductance is governed by Fermi-Dirac statistics. [73, 74]. In this case, the conductance is predicted to decrease by several percent between room temperature and 10 K, given that the tunnel barrier heights seen here are much larger than kT . Consider the example in Fig. 2.16, where the conductance of a Nb/Al/ AlO_x /Au tunnel junction, discussed in Chapter 5, decreases by 80% between room temperature and 4 K. This trend, which is typical for the tunnel junctions discussed in this thesis, fulfills Rowell's third criterion, dispelling the notion of significant pinhole conduction through the barrier. The stronger temperature dependence of the conductance compared to the ideal Fermi-Dirac limited case, often seen in literature for devices with amorphous tunnel barriers, suggests additional thermally activated conduction mechanisms such as inelastic tunneling via localized defect states in the barrier [65, 75, 76].

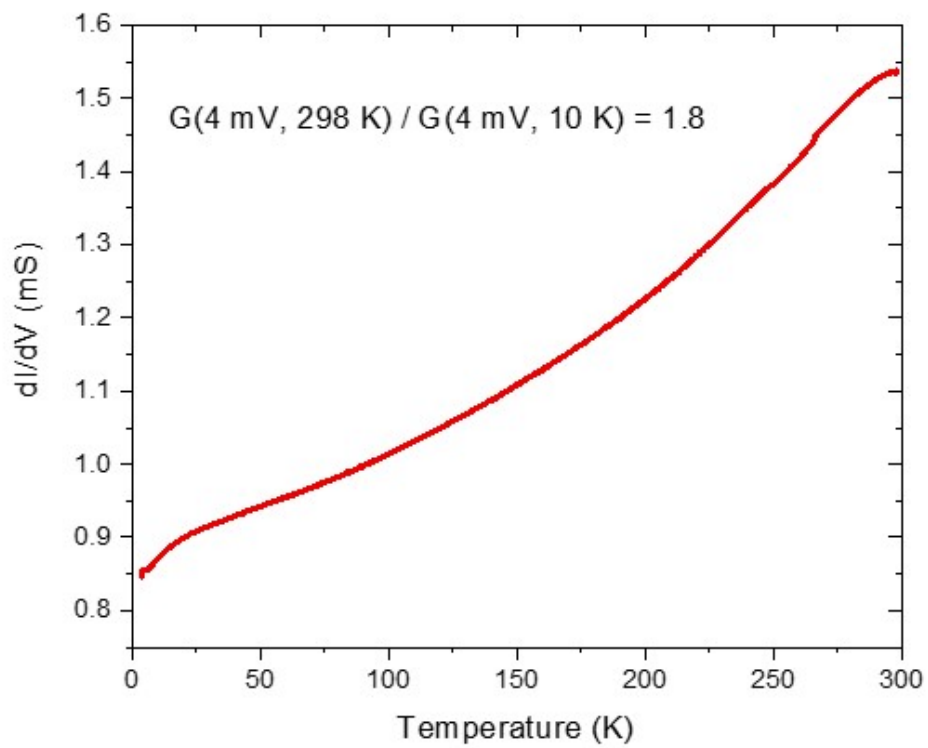


Figure 2.16: A conductance decrease of 80% for a Nb/Al/AlO_x/Au tunnel junction is seen between 300 K and 4 K.

2.4.2.1 Normal metal - Insulator - Superconductor Tunnel Junctions

The devices discussed in Chapter 5 incorporate a Nb/Al bilayer electrode, which undergoes a superconducting phase transition below a critical temperature T_c . I-V measurements are performed on the superconducting bilayer and the NIS tunnel junction in the same four point manner as described for room temperature characterization. As discussed in Chapter 1, determining T_c of the bilayer sets a relative scale for superconducting properties such as the superconducting energy gap and the coherence length. As I will discuss in Chapter 5, T_c is determined using the temperature dependence of the Nb/Al wire resistance and the temperature dependence of the superconducting critical current I_c .

The differential conductance of the NIS tunnel junctions is measured in the vicinity of the superconducting gap energy, typically ± 10 mV. The NIS conductance spectrum represents an analogue to the thermally smeared quasiparticle density of states in the superconducting region near the insulator. Information pertaining to the superconducting state and the tunnel barrier can be inferred from this conductance spectrum, such as the superconducting energy gap or BTK tunnel barrier strength [77]. Further discussion on Nb/Al bilayer-based NIS tunnel junctions can be found in Chapter 5.

2.5 Chapter Summary

The UHV system described here enables complete tunnel junction fabrication entirely in UHV conditions. This mitigates the inclusion of material impurities or

contamination from residual gases and limits uncontrolled oxide formation. The multitude of fabrication capabilities provided by the system enable us to explore a large phase space of sample processing. In the following chapters, these capabilities are leveraged, alongside *in situ* and *ex situ* material characterization methods, to improve or gain insight on properties of several technologically critical material systems.

Chapter 3: Plasma Oxidation for AlO_x Tunnel Barriers

3.1 Context

The focus of this chapter is the optimization of the plasma oxidation recipe for ultra-thin Al layers confined by Co electrodes and the reduced aging observed when compared to AlO_x tunnel barriers without Co confinement. The term “Co confinement” here refers to an ultrathin AlO_x tunnel barrier (≈ 1 nm) with Co electrodes on either side intended to “confine” oxygen within the designed tunnel barrier. Crossed wire tunnel junctions with Co confined tunnel barriers have a bottom layer of [40 nm Co / 1 nm Co / (**1.1 nm Al** + Oxidation)] and a top layer of [5 nm Co / 40 nm Cu / 5 nm Au]. Plasma oxidation parameters (i.e., power, time, pressure) are tuned to achieve a fully oxidized Al layer with an oxygen density near to that of stoichiometric Al₂O₃. The resistance drift in time, or aging, of these “confined” tunnel junctions is compared to “unconfined” tunnel junctions with a bottom layer of [40 nm Co / 1 nm Co / (**10 nm Al** + Oxidation)] with an identical oxidation recipe and top layer. Resistance of a representative confined tunnel junction device increases by $34.0 \pm 5.4\%$ over ≈ 8 months, while the resistance of the unconfined tunnel junction device increases by $95.4 \pm 7.8\%$ over the same span. The mitigated aging in the confined tunnel junctions, compared to the unconfined

tunnel junctions, is attributed to an AlO_x tunnel barrier with an initially sharper and homogeneous oxygen profile with an O/Al ratio nearer to that of stoichiometric Al_2O_3 .

Section 3.2 will contain an introduction to plasma oxidation of Al and the development of the plasma oxidation recipe used for this thesis. This will include the effects of Co confinement layers on the oxidation process. Comparison of tunnel junction resistance drift with and without Co confinement is discussed in section 3.3. The results of section 3.3 are described in Ref. [70]. The chapter is then summarized in section 3.5.

The confined and unconfined barrier stability results of this chapter are published in Ref. [70].

3.1.1 Background

Ultrathin, amorphous aluminum oxide (AlO_x) layers are a popular choice as a tunnel barrier in metal-insulator-metal tunnel junctions implemented for Josephson junction devices, magnetic storage, and in spintronics applications [45, 78, 79]. This popularity is driven largely by the ease of fabricating ultrathin (≈ 2 nm) layers with self-limiting thermal oxidation at room temperature, as well as the essentially uniform attenuation of different spin and symmetry states described well within the WKB formalism [47, 80]. However, an undesirable property of AlO_x layers is “aging” as manifest in drifting electrical properties over time [22, 43, 44, 81]. Specifically, the tunneling resistance of AlO_x tunnel junctions has often been observed to

slowly increase with time. Such instability is an obvious drawback for commercial device applications where a drift in the normal state tunneling resistance can cause, for example, the critical current (I_c) of a Josephson junction or the tunneling magnetoresistance (TMR) of a magnetic tunnel junction to drift [81, 82].

Time dependent chemical and structural relaxation of the barrier profile changes the potential energy landscape in the tunnel junction, resulting in drifting (aging) of the tunnel junction resistance. One of the most commonly cited mechanisms is the “glassy” relaxation of the oxide and metal/oxide interface. Oxidation of a disordered base electrode, as is often the procedure for AlO_x tunnel barrier formation, results in a polycrystalline or amorphous oxide in which many atoms are not in a global equilibrium state or are under-coordinated (i.e., have dangling bonds) [22, 44, 83]. Electrically active defects resulting from such a structure include dangling bonds acting as charge traps or ions tunneling between local potential minima. Changes in charge distribution as a result of these defects manifests as changes in tunnel barrier height or width. The room temperature stabilization of atomic configurations and neutralization of such charge traps can take place over long time scales on the order of months [22, 44].

In addition, junction aging may manifest via structural ordering of the oxygen sub-lattice [43]. Pavolotsky *et al* suggest that, for example, vacancy flow can provide the non-thermal enhancement of oxygen diffusion required for such structural ordering. The resultant curing of structural defects or annihilation of vacancies manifests as aging as defect states and indirect tunneling paths are removed. Foreign species in or near the tunnel barrier can also lead to resistance drift. For

example, photoresist residue or water molecules present during oxidation can result in hydrogen and hydroxyl groups (-OH) in the barrier. Hydroxyl groups can form aluminum hydroxides ($\text{Al}_2\text{O}_3\text{H}_2\text{O}$, $\text{Al}_2\text{O}_3\cdot 3\text{H}_2\text{O}$), in turn lowering the potential barrier height [84, 85]. Resistance drift can occur as a result of hydroxide dissociation, but typically requires temperatures in excess of 145°C [85]. Likewise, diffusion of species due to concentration gradients can cause the tunnel barrier to change over time but, in the absence of non-thermal diffusion enhancement, typically occurs at higher temperatures.

The electrically active defects in amorphous AlO_x that give rise to aging are also thought to be prominent sources of decoherence for qubit, or quantum bit, states [22, 83, 86]. Atomic defects such as metastable atomic configurations, often found in substoichiometric or low density regions of an oxide [87], are believed to be the origin of many two-level fluctuators (TLS). The dipole moment of such defects can couple to nearby qubits and act as a major source of dissipation, thus reducing coherence times [30, 83, 86]. Therefore, mitigation of tunnel junction aging is likely to coincide with a mitigation of decoherence sources.

The stability, or aging, of the tunnel junction is expected to be strongly dependent on the initial oxide formation. An oxide which is denser and has a higher O/Al ratio is expected to contain fewer voids and O vacancies, thus constraining structural and chemical profile changes over time due to higher atomic coordination [83, 87, 88]. However, many process techniques used to achieve this can be technically challenging or have unintended consequences on the junction. Vacuum annealing has been shown to be effective in mitigating tunnel junction resistance

drift [44, 84]. Annealing hastens the glassy relaxation of the tunnel barrier by allowing atoms to (re)arrange into lower free energy configurations [43, 81]. However, this may result in an unpredictably large absolute change from the unannealed resistance and may also produce undesirable diffusion in the tunnel junction. In addition, single-crystal tunnel barriers show a decreased density of TLS defects, which are typically associated with aging. While these barriers may improve stability, the epitaxial growth is quite challenging. Moving forward, I will discuss how plasma oxidation and cobalt confinement are used to create AlO_x barriers with improved stoichiometry over thermal oxides and improve barrier stability.

3.2 Plasma Oxidation of thin Al layers on Co

3.2.1 Oxidation of Al

The growth of oxide layers on metals is a complex process in which the reactants are separated from each other after an initial monolayer formation. When exposed to an aluminum surface, oxygen impinges with some sticking probability (S) and is chemisorbed to begin the initial growth. This initial layer growth is rate limited by the supply of oxygen. For devices in this thesis, the first monolayer is likely formed in milliseconds for an oxygen pressure of 160 mTorr and S of 10^{-2} - 10^{-3} for O_2 [89]. From this point on, the reactants must diffuse through the oxide to reach each other. Due in part to a significant size difference, diffusion of aluminum ions dominates over diffusion of oxygen ions. Below roughly 4 nm, oxide growth is rate limited by aluminum ion diffusion and is well described by the Mott-Cabrera loga-

rhythmic growth law [45, 89, 90, 91]. The Mott-Cabrera model describes metal oxide formation that is limited by field-facilitated hopping of metal ions at the metal-oxide interface and through the existing oxide. Aluminum ions have been confirmed as the primary moving species using an isotope technique, in which oxidation was initiated with O^{16} before continuing with O^{18} [45]. Kuiper *et al* employed Rutherford backscattering (RBS) and secondary ion mass spectroscopy (SIMS) to show that the initial AlO^{16}_x layers were buried underneath the subsequent AlO^{18}_x layers, indicating that Al was diffusing through the initial layer to reach the surface. A build up of net charge from this ion diffusion current is avoided by electrons tunnelling from the metal substrate to the acceptor levels of oxygen adsorbed on the surface. This electron transfer establishes an equilibrium potential across the oxide, typically called the Mott potential (V_M). The resulting electric field assists aluminum ions as they diffuse through interstitial sites by a hopping process, lowering the energy barrier needed to diffuse.

3.2.1.1 Plasma Oxidation

Plasma oxidation of Al has been shown to produce oxides with a higher O/Al ratio in a significantly shorter time than typical (i.e., room temperature) thermal oxidation [45, 47, 92]. The key difference between the two processes, in this context, is the exposure of the Al to different oxygen species present in the plasma. For thermal oxidation, the Al surface is exposed mostly to O_2 which dissociates upon chemisorption. It is likely that the dissociation necessary is responsible for a rela-

tively low sticking probability (10^{-2} - 10^{-3}) [89]. For plasma oxidation, the Al surface is exposed to more reactive species such as ions (O^+ , O_2^+) or reactive neutrals (O^* , O_3). The plasma is overall neutral as electrons are present from ionization events, as well as a relatively small population of negative ions.

Oxygen radicals (O^*) have been identified in the literature to likely be the main species in the plasma oxidation process. Kuiper *et al* used optical spectra of an oxygen plasma to identify O_2^+ and O^* as the most populous species [45]. The oxidation rate was not observed to be bias dependent which suggested O^* was the primary driver of the oxidation process. However, the oxidation rate decreased with increasing pressure between 5 - 45 Pa even though the O^* density had a maximum near 25 Pa. They concluded that while O^* is likely the main actor, enhanced thermalization due to a shorter mean free path (MFP) was responsible for the decreased oxidation rate with pressure. In contrast, Knechten found an increase of oxidation rate with pressure between 5 - 15 Pa with O^* density increasing in kind [47]. However, the oxidation rate increased linearly with power up to 15 W while the O^* density was found to be relatively flat after 4 W. They, like Kuiper, supposed that O^* was a primary driver of the oxidation process, but a parallel process of ions delivering “thermal spikes” to the surface acted as a secondary driver.

For several reasons, the net effect of the plasma species is to enhance Al diffusion through the oxide. First, O^* has a much higher sticking probability than O_2 , so surface coverage is enhanced over thermal oxidation. Second, O^* atoms have a much higher electron affinity of 1.5 eV (deeper acceptor levels) compared to the 0.45 eV electron affinity of O_2 molecules [93]. Both the increased surface coverage and

higher electron affinity of O^* combine to increase the surface charge density, thus increasing V_M and the electric field across the oxide. The activation energy of Al hopping is decreased due to the larger electric field and, in Knechten's model, thermal energy provided by impinging ions. While there are common threads such as the effect of O^* , Knechten notes that differences in the overall oxidation mechanism, as well as oxidation rate dependencies on process parameters (pressure, power, etc.), may arise between plasma system configurations (e.g., line of site configurations of plasma electrodes relative to the oxidation surface of interest).

3.2.1.2 Effects of Co confinement

The devices discussed in this chapter utilize an ultrathin (≈ 1.5 nm) AlO_x tunnel barrier confined by Co electrodes on the top and bottom side. Plasma oxidation of thin Al layers on Co has been studied in great detail, as Co/ AlO_x /Co is a popular magnetic tunnel junction (MTJ) stack used in the tunneling magnetoresistance (TMR) community [45, 46, 47]. TMR is the different in tunneling junction resistance depending on the relative alignment of magnetic electrodes and is utilized in memory storage. A thin Al layer, typically 0.8-1.5 nm thick, is deposited on a Co underlayer and consumed by the oxidation process. After pioneering work by Moodera, Kuiper *et al* showed that the TMR of Co/ AlO_x /Co MTJs was maximized under two conditions: 1) the tunnel barrier is homogeneously oxidized to the stoichiometric O/Al ratio of 1.5 and 2) no Co oxide is formed [45, 94]. The homogeneous tunnel barrier ensures minimal pinhole conductance which couples

the magnetic electrodes, while CoO and Co₃O₄ are known to scatter spins and mix the spin-up and spin-down channels [95]. RBS and transmission electron microscopy (TEM) were used to observe the O content in the oxide layer and the layer thickness as a function of oxidation time, as seen in Fig. 3.1(a-b). The O content increased logarithmically with time, but the oxide thickness was constant between 10 s and 100 s. They concluded that the oxidation was found to occur in several steps, with a substoichiometric Al-rich oxidation front progressing to the Al/Co interface followed by a build up of O content in the oxide [45, 46]. After 100 s, sufficient O had built up at the Al/Co interface for the Co to begin oxidizing.

Following Kuiper's observations, the Co underlayer can be thought of as an oxidation stop for the thin Al layer above. This behavior can likely be attributed to the significantly larger (more negative) Gibbs free energy of formation of Al₂O₃ ($\Delta G_f^0 = -1581$ kJ/mol) compared to the Co oxides, CoO ($\Delta G_f^0 = -215$ kJ/mol) and Co₃O₄ ($\Delta G_f^0 = -770$ kJ/mol) [78, 96]. By utilizing a Co overlayer as well, the Al can be considered a potential well for O. Thus with the Co confinement, the tunnel barrier can be formed with an initially sharper O profile with an O/Al ratio near stoichiometric Al₂O₃ and retain a homogeneous oxidation profile over time. In general, metals whose oxides have relatively small (less negative) ΔG_f compared to Al, such as Ti or V, are expected to provide a qualitatively similar benefit [1]. Comparison of devices with confined barriers and unconfined barriers are discussed later in the chapter.

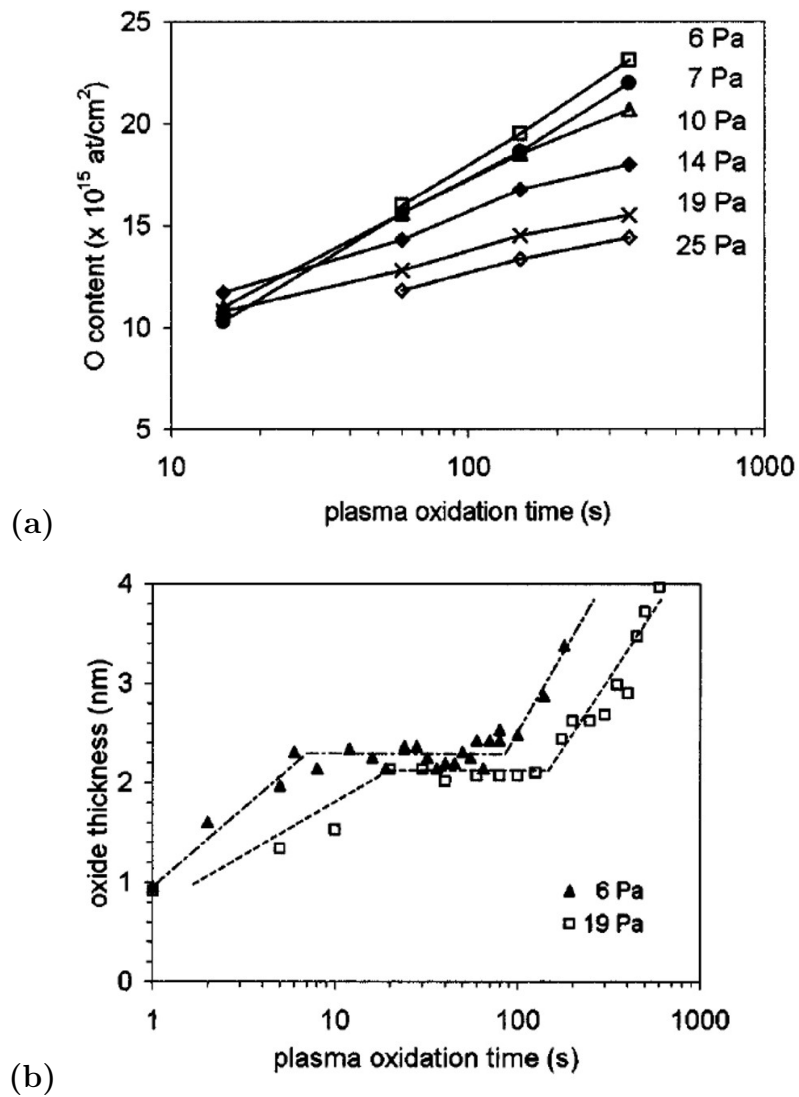


Figure 3.1: O content and thickness of an Al oxide layer with plasma oxidation time. (a) The O content for each oxidation pressures increases logarithmically with time. (b) The oxide thickness is determined from TEM line cuts. After a fast initial growth step up to 10 s, the thickness remains constant up to 100 s. These figures are reused from Ref. [45] with permission from AIP publishing.

3.2.2 Plasma Oxidation Recipe

The plasma oxidation parameters used throughout this thesis are as follows: 160 mTorr O₂, 55-60 W (100 mA, 550-600 V), 7 s, electrode spacing of 3.87 cm. How these parameters were set will be explained in the following section. This recipe is intended to optimally oxidize a ≈ 1 nm thin film of Al on a Co underlayer. Specifically, the aim is to minimize the density of electrically active defects in the tunnel barrier by oxidizing the entire metallic Al layer with an O content approaching that of Al₂O₃, while avoiding oxidation of the underlying Co layer. As previously discussed, the plasma oxidation process (rate, final thickness, etc.) is dependent on power, pressure, and time. Differences in oxidation rate dependencies on these parameters observed between Kuipers *et al* and Knechten also highlight the role that the configuration of the oxidation chamber (e.g., electrode spacing, wafer placement, etc.) can play when determining an oxidation recipe [45, 47]. For example, Knechten observed an increasing oxidation rate with oxygen pressure from 5.8 Pa through 15 Pa while Kuipers observed a decreasing oxidation rate with oxygen pressure from 6 Pa through 25 Pa. In both studies, the increase in oxidation rate was correlated with an increase in oxygen radical density.

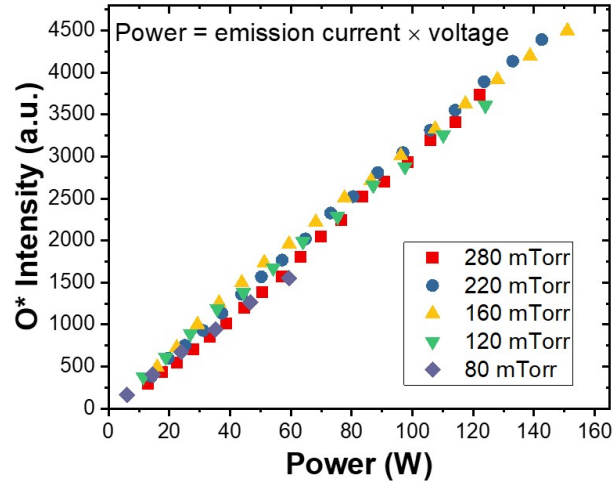
The time, oxygen pressure, and power of the plasma oxidation recipe in this thesis used work by prior members of our group as an initial recipe reference point and was further optimized to increase O* density. The oxidation chamber used in this thesis (wafer system) is a scaled up version of the referenced work (chip system) [54]. Furthermore, the tunnel junction material stack and fabrication proce-

dures used in Lake’s work, which resulted in tunnel junctions displaying remarkable time stability over multiple years, are nearly identical to that of devices discussed in this chapter [54]. The primary tools used to monitor the plasma are an optical spectrometer and photodiode, both mounted on viewports of the oxidation chamber. An optical fiber runs from the chamber window to a B&W Tek Quest X CCD spectrometer, which can measure the plasma optical spectrum between 200 nm and 1050 nm. Likewise, a photodiode mounted on the chamber window measures incident light over 300-1100 nm wavelengths with maximum responsivity at 950 nm. A photovoltage (V_{ph}) proportional to incident light in this range is read out using a Tektronix oscilloscope (TDS2000). The primary use of these probes when tuning our oxidation recipe is to correlate plasma processing conditions with the density of oxygen radicals in the plasma. The optical spectrometer allows one to isolate the intensity of the oxygen radical emission lines (777 nm, 844 nm) and compare over different parameters. As for the photodiode, the wavelength of these lines are near to the maximum spectral response of the photodiode such that the resulting V_{ph} can also be used as a proxy for oxygen radical density.

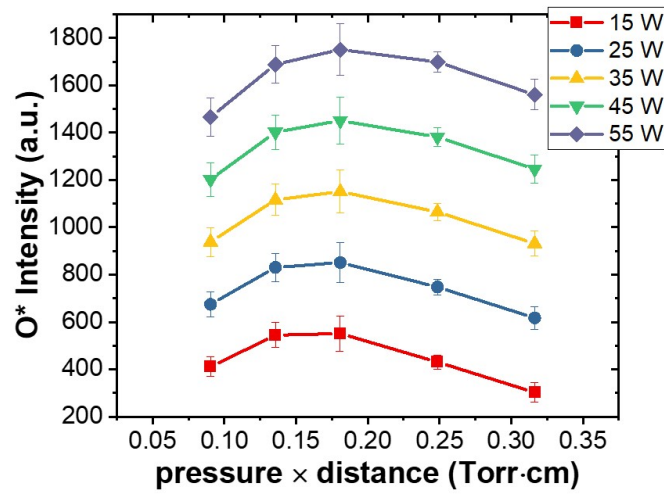
Initially, the electrode spacing in the wafer system plasma chamber was set at 1.13 cm to be near to that of the chip system at ≈ 1 cm. The first parameter explored was oxygen pressure. After filling the oxidation chamber with oxygen up to a desired pressure, optical spectra were recorded at 10 mA emission current steps for pressures of 80 mTorr, 120 mTorr, 160 mTorr, 220 mTorr, and 280 mTorr. The most prominent emission lines corresponding to oxygen radicals, 777 nm and 844 nm as seen in Fig. 2.8, were fit with a Voigt profile. The primary sources of line shape

broadening are well described by either Gaussian (spectrometer resolution, Doppler broadening) or Lorentzian (lifetime broadening, pressure broadening) line shapes [97]. Therefore a Voigt profile, a convolution of Gaussian and Lorentzian profiles, is often used to describe spectral emission lines. The peak areas of the 777 nm and 844 nm lines are added together and this intensity, with one standard deviation uncertainty, is correlated with the plasma power (emission current \times electrode bias) and pressure as seen in Fig. 3.2(a) and Fig. 3.2(b), respectively. For each pressure, the O* intensity is seen to be linear in power over the measured range. A linear fit to the intensity-power plot at each pressure is then used to extrapolate the O* intensity to arbitrary powers. This method is used to compare O* intensity at different pressure set points for a constant power as seen in Fig. 3.2(b). The error bars shown represent one standard deviation. 160 mTorr was initially chosen for the plasma oxidation recipe as O* intensity is peaked at this pressure.

An oxygen Paschen curve was also considered when determining the appropriate pressure during oxidation. Paschen's law relates the voltage necessary to start a glow discharge plasma, or breakdown voltage (V_B), with the product of pressure and the gap length between the electrodes (p·d). Minimizing V_B , thus reducing the accelerating voltage felt by ions in the plasma, decreases the probability of impurities being incorporated into the tunnel barrier as a result of electrode sputtering. Impurities in the barrier may increase leakage current through hopping conductance or serve as scattering sites. For a low p·d, fewer collisions due to longer mean free paths necessitates a higher V_B to ensure ionization. For a high p·d, more collisions due to a shorter mean free path leads to more energy loss. Thus, a higher V_B is



(a)



(b)

Figure 3.2: O^* intensity, calculated as the sum of the 777 nm and 844 nm peak areas, as a function of power and pressure for an electrode spacing of 1.13 cm (a) Measured values of O^* intensity vs. power is linear for each pressure. Power is calculated as the constant emission current set in the power supply multiplied by the required voltage applied between the plasma electrodes. (b) Calculated values of O^* intensity at several power values for each pressure set point.

needed to ensure that particles gain sufficient energy between collisions to cause ionization. Residing at a p-d minimum in between these regimes reduces the probability of impurities being sputtered from electrodes, as the reduced accelerating voltage reduces the energy of impinging ions. An oxygen Paschen curve measured at an electrode distance of 1.13 cm is shown in Fig. 3.3. The dashed line denotes 160 mTorr, the pressure which maximized O* intensity.

Ultimately, 160 mTorr was maintained for the oxidation pressure as, aside from maximizing O* intensity, this pressure was a compromise between the lower pressure used in the reference chip system (120 mTorr) and a higher pressure towards the Paschen minimum. In addition, the sputter yield at the 160 mTorr set point is relatively small for oxygen ions impinging on the stainless steel electrodes. One can estimate a maximum ion energy upon impingement normal to the electrode by multiplying the electric field by the mean free path and the elementary charge “e”. Using a mean free path of approximately 0.13 cm [98], an electrode spacing of 1.13 cm, and an electrode bias difference of 500 V, the impingement energy is estimated to be approximately 60 eV. The sputter yield for oxygen ions impinging on a 304 stainless steel electrode, using weighted averages for atomic masses and cohesive energy of the components in 304 stainless steel, is approximately 0.13 atoms/ion [99].

Prior to settling on a power and oxidation time for the plasma oxidation recipe, the electrode spacing was increased from 1.13 cm to 3.87 cm. At 1.13 cm and 160 mTorr, the cathode sheath extends very near to the wafer surface. While our group has not seen empirical evidence to suggest deleterious effects from this condi-

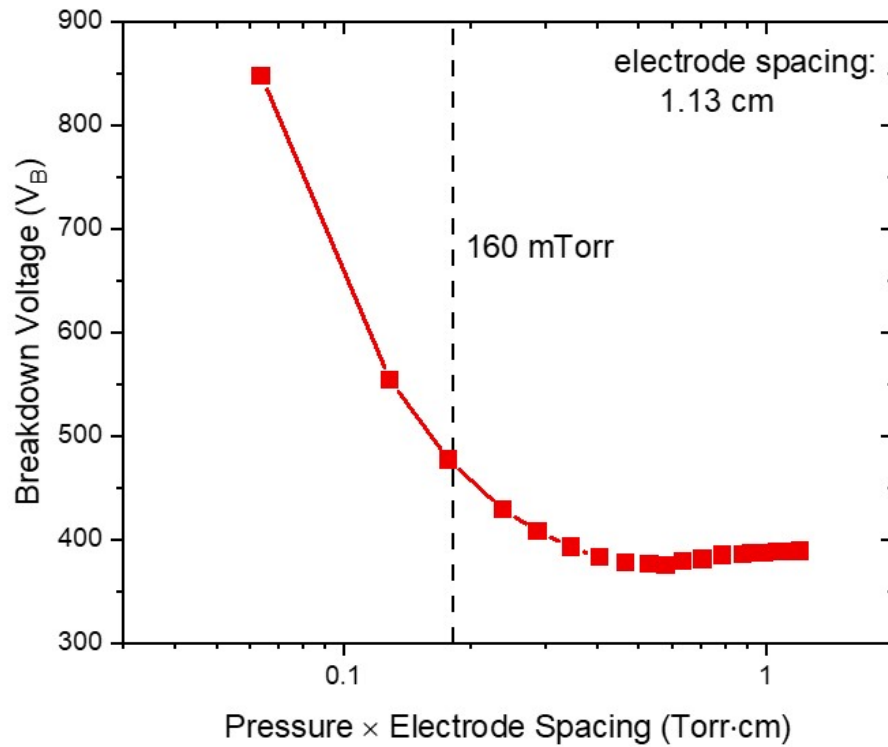


Figure 3.3: Oxygen Paschen curve for an electrode spacing of 1.13 cm. The breakdown voltage, V_B , was determined by increasing the plasma power supply voltage until a plasma ignites at a constant pressure set point and an emission current set point of 25 mA.

tion, standard practice was to ensure some distance between this sheath of high ion density and the wafer surface. This was achieved by increasing the electrode spacing to 3.87 cm, resulting in the configuration seen in Fig. 3.4. Fig. 3.5(a) shows the shift of the Paschen curve to higher $p \cdot d$ with 160 mTorr still reasonably near the V_B minimum. V_{ph} as a function of pressure, at a constant power of ≈ 13.5 W (set by a constant current) and electrode spacing of 3.87 cm, is shown in Fig. 3.5(b) alongside the 13.5 W O^* intensity extrapolated in the same manner as in Fig. 3.2(b). The photodiode measurements at 3.87 cm spacing were performed by Caroline Zhang, a student in the Summer Undergraduate Research Fellowship (SURF) program. A systematic investigation of O^* intensity as a function of pressure, such as one using the optical spectrometer and discussed in Fig. 3.2, was not repeated at this new electrode spacing. The peak V_{ph} is shifted to a slightly lower pressure relative to the extrapolated O^* intensity, but 160 mTorr was again maintained for the plasma oxidation recipe as V_B greatly increases with lower pressure.

Setting the oxidation power again began with mapping the reference chip system parameters to the wafer system used in this thesis. Fig. 3.6 shows V_{ph} as a function of power for both systems. This data was collected by SURF student Caroline Zhang. The oxidation recipe of the reference system used 21 W resulting in a V_{ph} of 2.56 V. Mapping this V_{ph} to the wafer system, as shown by the dashed lines in Fig. 3.6, resulted in an applied oxidation power of 51 W. When scaled to 160 mTorr in the wafer system, the oxidation power was increased to approximately 55 W to maintain a V_{ph} of 2.56 V.

Oxidation time was determined by comparing tunnel junction electrical char-

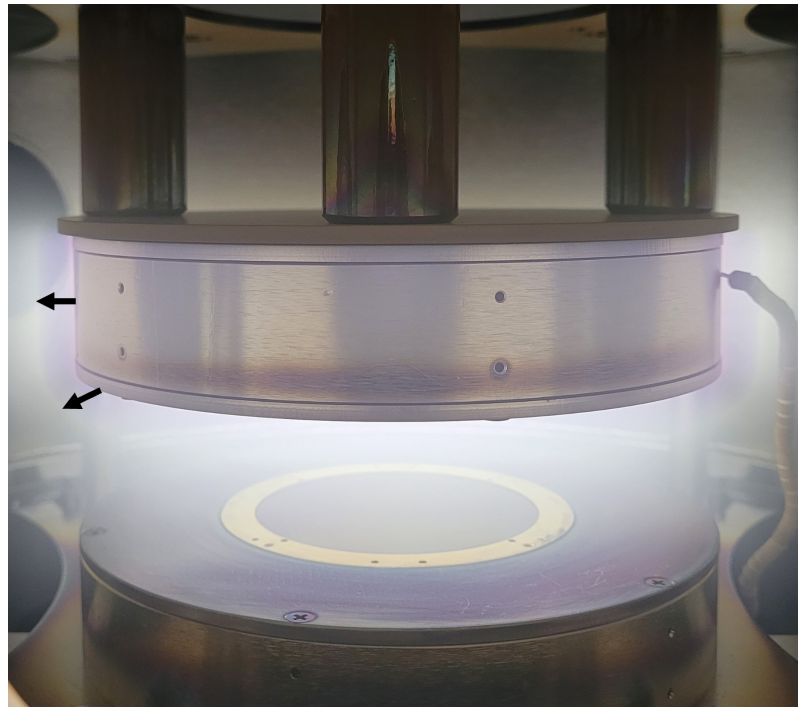
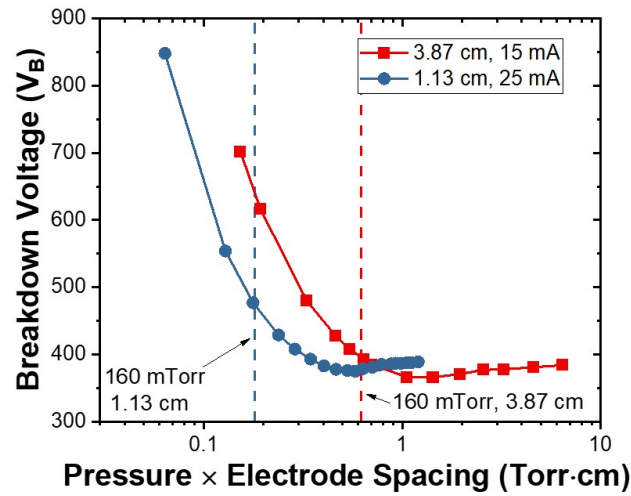
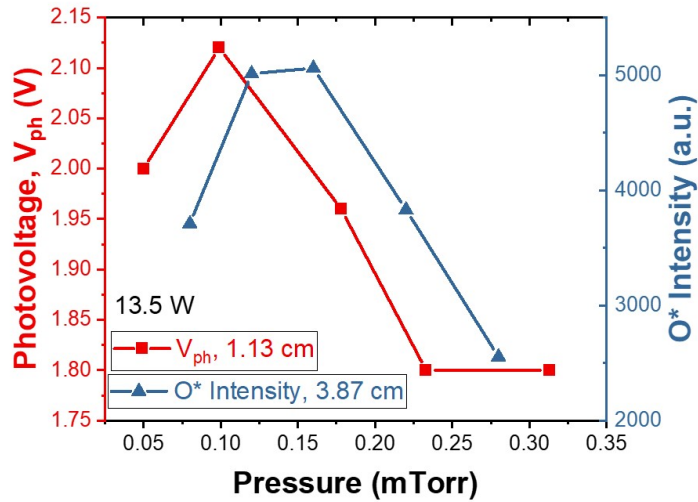


Figure 3.4: 160 mTorr oxygen plasma with an electrode spacing of 3.87 cm. The black arrows illustrate the approximate size of the sheath surrounding the negatively biased cathode.



(a)



(b)

Figure 3.5: Paschen curve and O^* intensity at an electrode spacing of 1.13 cm and 3.87 cm (a) The increased electrode spacing shifts the Paschen curve to higher $p \cdot d$. The dashed lines represent $p \cdot d$ for 160 mTorr of oxygen at the original 1.13 cm spacing and the final 3.87 cm spacing. (b) The red squares represent the measured V_{ph} as a function of pressure for the 3.87 cm spacing. The peak O^* intensity inferred from V_{ph} is shifted to slightly lower pressure relative to the peak O^* intensity extrapolated from optical spectrometer data, represented by blue triangles.

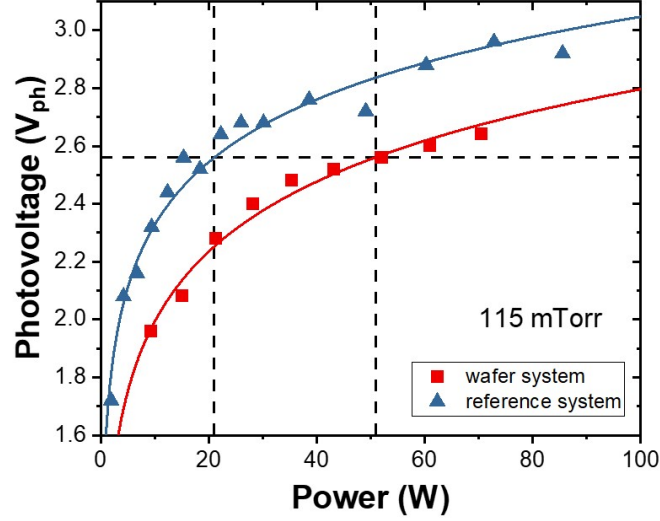


Figure 3.6: V_{ph} as a function of power at 115 mTorr O_2 for the wafer system and referenced chip system. The dashed lines indicate the V_{ph} -power mapping from the reference system to the wafer system.

acteristics of several different oxidation times. The goal was to identify an oxidation time that (a) minimized device aging (proxy for the density of electrically active defects) and (b) resulted in tunnel barrier characteristics close in line with a fully oxidized Al layer without oxidation of the Co underlayer. Four crossed wire tunnel junction wafers were processed with plasma oxidation times of 3 s, 5 s, 7 s, and 9 s. O_2 pressure was set to 160 mTorr and the power used was 55-56 W (100 mA, 550-560 V). The bottom wires were 40 nm Co through mask 1 followed by 1 nm Co and 1.1 nm Al, both with no mask. The 1 nm Co layer over the entire wafer acts as a wetting layer, improving adhesion and structural uniformity of Al on the sidewalls and transition region to the SiO_x surface. After *in situ* oxidation, each wafer sat in vacuum overnight prior to deposition of the top layer. The top wires were 5 nm Co

/ 40 nm Cu / 5 nm Au through mask 2. The 40 nm Cu layer in the top layer is intended to decrease the top wire resistance, thus mitigating current spreading and the negative resistance artifact [64]. The 5 nm Au capping layer maintains an inert surface and allows for relatively easy wire bonding. The following comparisons are done with a representative “B” type device from each wafer and in the same relative position on the wafer, shown in Fig. 3.7(a). Each device has an area of $\approx 55 \mu\text{m} \times 65 \mu\text{m}$. The R·A product, corrected for the negative resistance artifact, as a function of oxidation time is shown in Fig. 3.7(b). Fitting the data to an exponential growth function provides a time constant of $\tau = 2.9 \pm 0.4 \text{ s}$ and a scaling factor of $A_1 = 2.1 \pm 0.9 \text{ k}\Omega \cdot \mu\text{m}^2$, where the uncertainty is the standard error of the fit or one standard deviation.

The uncertainty in the R·A products shown is dominated by the uncertainty in determining the tunnel junction area, followed by the uncertainty in the negative resistance correction. The profile of each of the two device leads as captured by an optical microscope image is fit with dual error functions to determine device area, as discussed in Appendix D of Ref.[54]. Wire width is determined by the difference in the center points of the error functions plus twice the error function full width at half maximum (FWHM). Empirical work performed by previous group members determined that this determination of width captured the width of wire carrying current within a few percent. As the FWHM term represents the Gaussian σ , with the error function being the integral of a Gaussian, the uncertainty of each wire width is taken to be the FWHM. The relative uncertainty in the resistance value is taken as the relative uncertainty in the negative resistance correction compared to

a simulated “true” value, as shown in Fig. 8 of Ref.[64]. A conservative estimate of this uncertainty, between 2-8 % for the devices discussed in Fig. 3.7(b), dominates over the $\lesssim 0.1$ % variation in repeated measurements of the same device.

The as-fabricated R·A products shown in Fig. 3.7(b) are displayed in Table 3.1. Also shown are the effective tunnel barrier width and potential energy heights of each device ≈ 10 days after fabrication, extracted using the Chow model as discussed in Chapter 2. The relative uncertainty in these fit parameters is ≈ 3 %. This estimate is a result of a sensitivity analysis using the standard error in the input parameters, where the input parameters (area, I, V, etc.) were varied by 10 %. Only the junction area uncertainty results in changes to the fit values comparable to the standard error of the fit parameters (< 0.5 %). While the R·A products at 1 mA were recorded immediately after fabrication and removal from vacuum, ± 100 mV I-V data needed to extract tunnel barrier characteristics were not measured until ≈ 10 days after fabrication. Tunnel barrier characteristics for the 3 s oxidation time device are not listed, as measurement current limits and the low device resistance of $< 1 \Omega$ made it difficult to measure ± 100 mV R(V) data typically used to extract such parameters.

Barrier heights of 1.1 eV and barrier widths of 1.3 nm (7 s, 9 s), as well as negligible difference in barrier width between the two devices, is consistent with the Al layer being well oxidized with an oxygen concentration near to that of Al_2O_3 [46, 47, 100]. Fig. 3.8(a) shows the R·A product and Fig. 3.8(b) shows the extracted tunnel barrier width as a function of time. Fig. 3.9(a-b) show the corresponding barrier heights. Following an initial sharp increase in resistance and plateau, the R·A product of each device increases nearly logarithmically over ≈ 5500 h. With

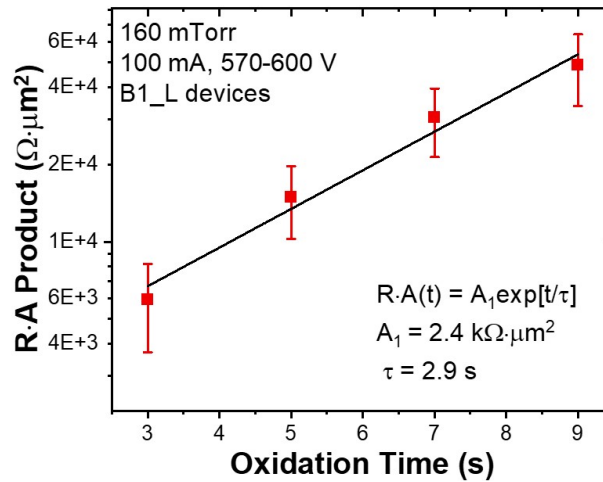
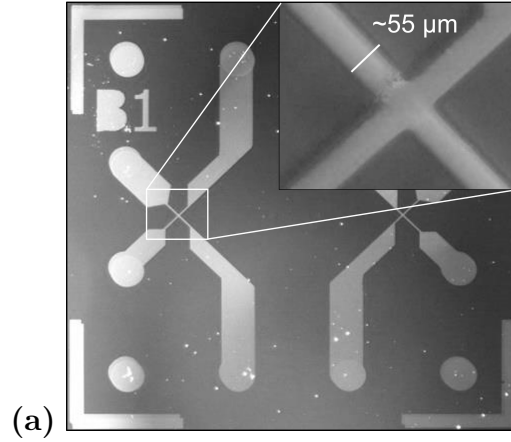


Figure 3.7: (a) The box is around the left device on the B1 die, or B1-L, used as the representative device from each wafer to compare across oxidation times. (b) The R·A product as a function of oxidation time is fit with an exponential growth function with a time constant of $\tau = 2.9 \pm 0.4 \text{ s}$ and a scaling factor of $A_1 = 2.4 \pm 0.5 \text{ k}\Omega \cdot \mu\text{m}^2$. Part (a) is reprinted from [70], with the permission of AIP Publishing.

Oxidation time (s)	R·A ($k\Omega \cdot \mu\text{m}^2$)	* Φ_{top} (eV)	* Φ_{bottom} (eV)	* Δx (nm)
3	5.9 ± 2.2	N/A	N/A	N/A
5	15.0 ± 4.7	1.12 ± 0.03	1.30 ± 0.04	1.18 ± 0.04
7	30.0 ± 9.1	1.10 ± 0.03	1.13 ± 0.03	1.28 ± 0.04
9	49 ± 15	1.15 ± 0.03	1.22 ± 0.04	1.29 ± 0.04

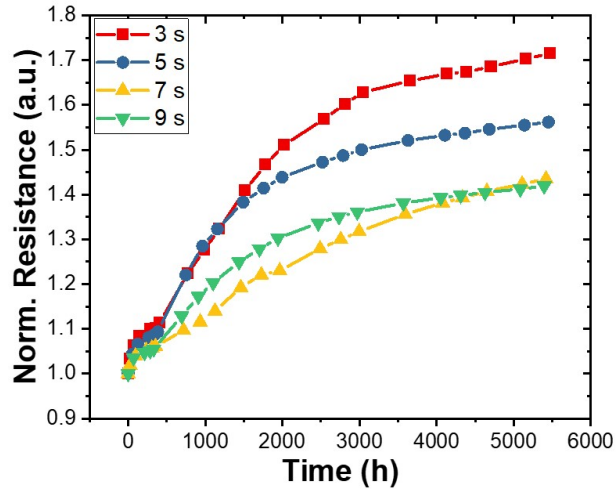
Table 3.1: As-fabricated R·A products and *10 day tunnel barrier characteristics

the exception of Φ_{bottom} in the 5 s device, Φ_{bottom} and Δx are relatively flat ($< 5\%$ drift) over the observed period. Similar long-term drift is observed for each device in Φ_{top} of $\approx 15\%$. It is possible that the potential gradient introduced by the deposited top layer results in prolonged relaxation of the disordered interface [22, 87, 88]. The oxidation recipe moving forward uses a 7 s oxidation time, as this set point resulted in the least amount of drift over the first several thousand hours and is discussed more thoroughly in the following section.

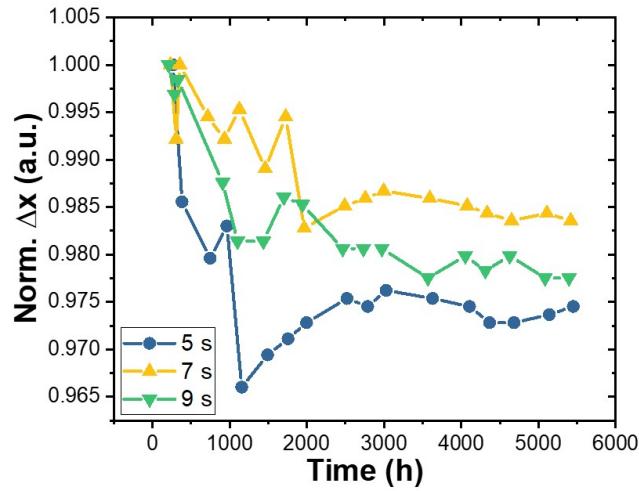
3.3 Reduced Resistance Drift of Co Confined AlO_x Tunnel Barrier

3.3.1 Experiment

As an extension of the recipe optimization for plasma oxidation, the time stability of devices with an AlO_x barrier sandwiched between Co layers (confined) is compared to devices without Co confinement (unconfined). The results of this section are published in Ref.[70]. Both the confined and unconfined devices reported in the following section utilize plasma oxidation, which produces oxides with relatively high oxygen concentration (i.e., relatively higher specific resistances) in shorter fabrication times when compared to thermal oxidation as previously discussed [45, 47, 101, 102, 103], but additional benefit is seen from the confinement.

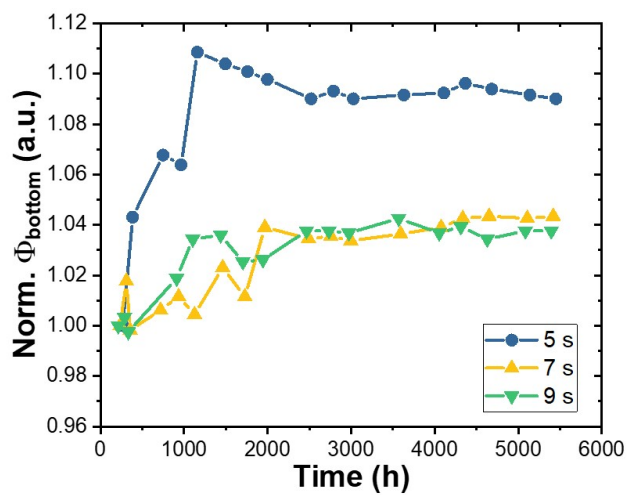


(a)

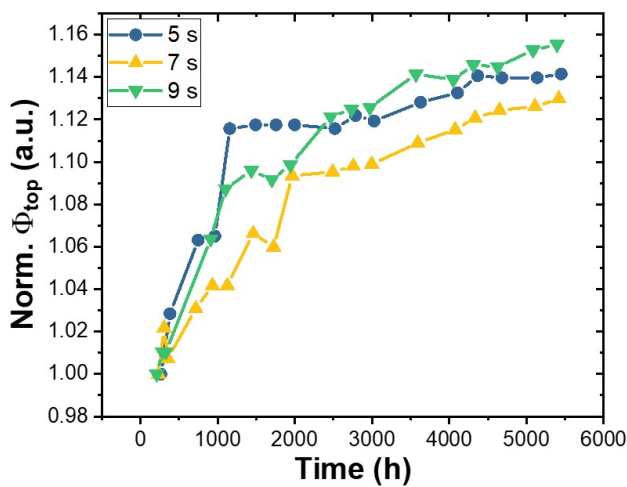


(b)

Figure 3.8: (a) Drift of tunnel junction characteristics for different oxidation times normalized to initial values shown in table 1. The Normalization value for resistance (a) is taken from $t = 0$ h. (b) Drift in the tunnel barrier width Δx over time. Normalization values for the barrier width are taken from $t \approx 230$ h.



(a)



(b)

Figure 3.9: Drift in time of the (a) bottom AlO_x interface barrier height Φ_{bottom} and (b) top AlO_x interface barrier height Φ_{top} for several oxidation times.

While the confined device consists of an initially 1.1 nm thick Al layer which is oxidized until ideally no metallic Al remains, the unconfined device utilizes a thicker 10 nm Al layer such that the plasma forms a thin oxide skin on top. A cartoon of both junction stacks is shown in Fig. 3.10(a-b). The confined junction material stack and corresponding mask layer is, again, [40 nm Co (mask 1) / 1 nm Co (no mask) / **1.1 nm Al (no mask) + plasma oxidation (7 s, 160 mTorr, 55-60 W)** / 5 nm Co (mask 2) / 40 nm Cu (mask 2) / 5 nm Au (mask 2)]. In comparison, the unconfined junction material stack and corresponding mask layer is [40 nm Co (mask 1) / **10 nm Al (mask 1) + plasma oxidation (7 s, 160 mTorr, 55-60 W)** / 5 nm Co (mask 2) / 40 nm Cu (mask 2) / 5 nm Au (mask 2)]. In the 10 nm Al case, the oxygen plasma forms a thin oxide skin on top of the thicker Al film where the lower AlO_x edge is not confined by Co and most likely not abrupt. Co, Au, and Cu are deposited at a rate of ≈ 0.05 nm/s and Al is deposited at a rate of ≈ 0.02 nm/s. The relatively low deposition rate of Al is intended to promote conformal coating of the underlying Co layer. After removal from vacuum, all samples were stored in a nitrogen dry-box environment when not under measurement.

Several device wafers with crossed-wire tunnel junctions were processed using the confined architecture and all measurable devices (≈ 10) for this study had R·A products in the range of 26-36 k Ω · μm^2 . These wafers were fabricated using the first generation masks prior to the mask alignment corrections discussed in Chapter 2. As such, device yield was dominated by proper *in situ* alignment of subsequent shadow masks. The nominal resistance values are obtained using a four-point measurements with 1 mA current for each measurement (V-/I- on the bottom electrode

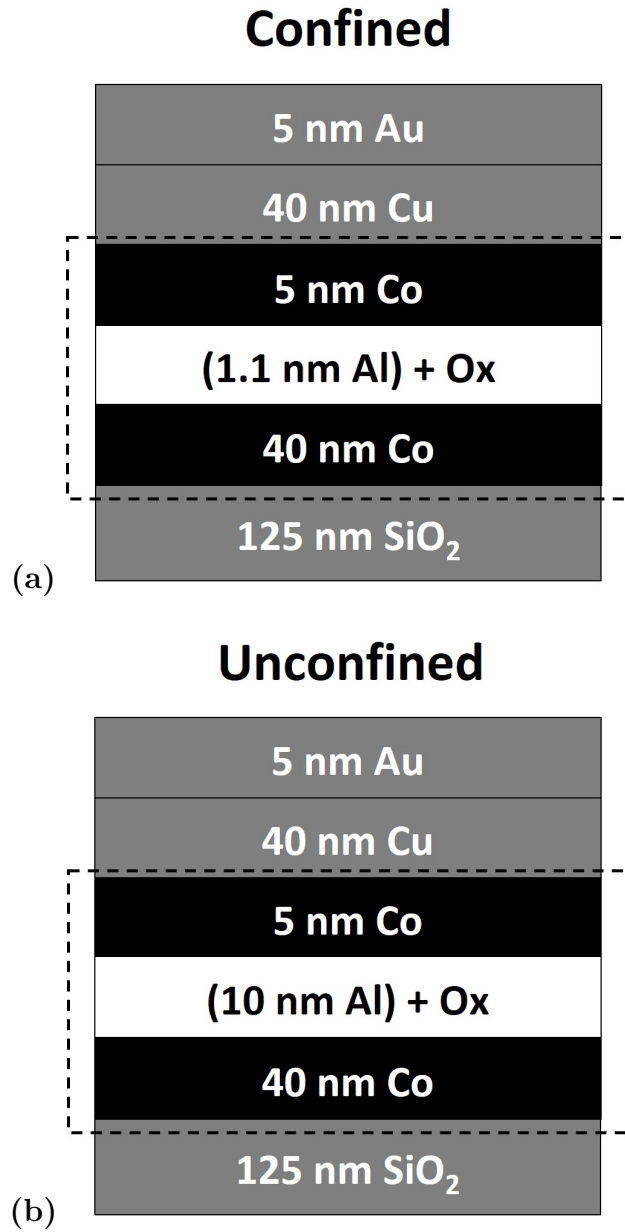
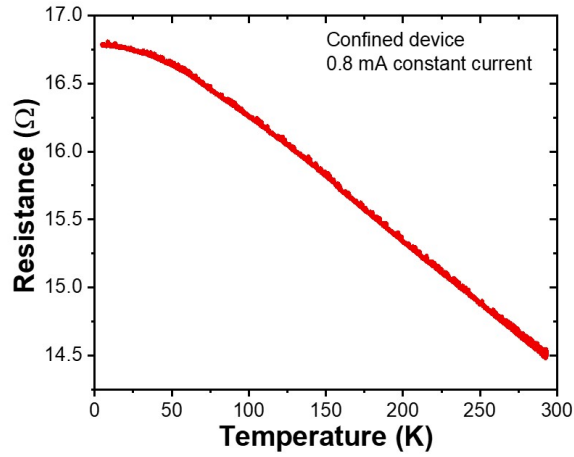


Figure 3.10: Tunnel junction material stacks for the (a) confined and (b) unconfined devices at the crossed wire intersection. While both devices use the same oxidation parameters, the unconfined device has a 10 nm layer of Al and the confined device has a 1.1 nm layer of Al. Reprinted from [70], with the permission of AIP Publishing.

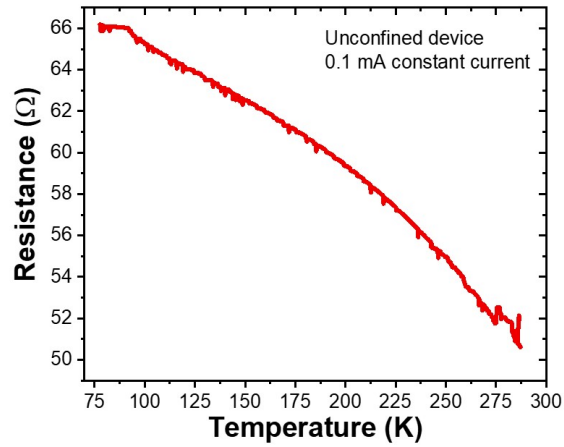
and $V+/I+$ on the top electrode). The resistance between disconnected electrodes, such as between the left and right devices shown in Fig. 3.7(a), is measured on every wafer to ensure that devices are well defined and free of current shunting. Previous transmission electron microscopy (TEM) measurements show continuous and conformal tunnel barrier formation [104]. Tunnel junction resistance as a function of temperature is shown in Fig. 3.11 for representative confined (a) and unconfined (b) devices. As discussed in Chapter 2, the increase in resistance with decreasing temperature fulfills Rowell’s third criteria and is consistent with minimal pinhole conduction [53, 76, 105]. While the measurements in Fig. 3.11 were performed with a constant current as opposed to monitoring $R(0\text{ V})$, the change in resistance as a result of dV/dI curvature away from 0 V is negligible ($< 1\%$) for the sampled bias values compared to the temperature dependent change observed.

3.3.2 Results

The initial $R \cdot A$ products of representative devices at 1 mA current, after negative resistance correction, was $34 \pm 10\text{ k}\Omega \cdot \mu\text{m}^2$ for the confined device and $69 \pm 19\text{ k}\Omega \cdot \mu\text{m}^2$ for the unconfined device. These values differ slightly from the published values in Ref.[70] for several reasons. The confined device discussed in this thesis (150726_13_B1_L) comes from a separate wafer than the confined device discussed in Ref.[70], but processed in a nominally identical fashion. However, monitoring of I-V characteristics began sooner after fabrication (50 h) compared to the confined device discussed in Ref.[70] (150717_17_B1_L, 234 h). In addition, the con-



(a)

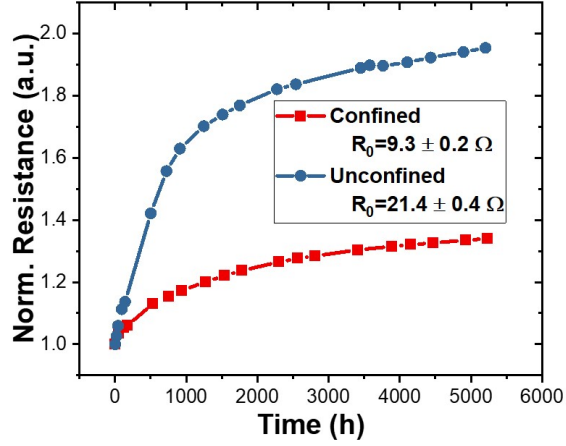


(b)

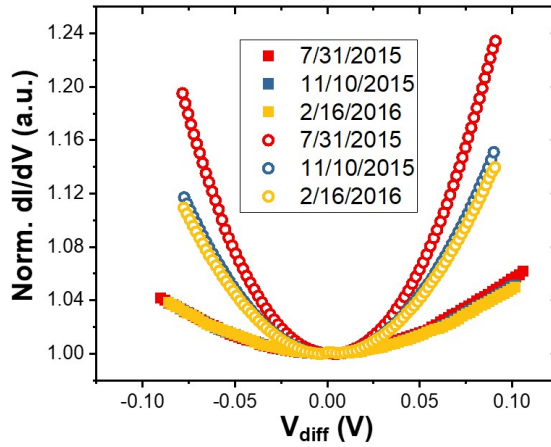
Figure 3.11: Resistance as a function of temperature for a representative (a) confined and (b) unconfined tunnel junction. (a) Measured in a 4 K closed-cycle cryostat, the confined device resistance increases by $\approx 16\%$ from 300 K to 4.4 K. (b) Measured with a liquid nitrogen dipper apparatus, the unconfined device resistance increases by $\approx 31\%$ from 300 K to 78 K.

fined device discussed here (150726_13_B1_L) was fabricated just one day prior to the unconfined device discussed both in this thesis and in Ref.[70] (150727_17_B1_L), as opposed to 10 days prior for the confined device discussed in the Ref.[70]. This proximity helps to ensure a similar deposition chamber environment and e-beam source quality. While the unconfined device is the same between this thesis and Ref.[70], a selection of R_0 closer in time to fabrication and an improved negative resistance correction resulted in slightly different R·A product values and tunnel barrier characteristics (Δx , Φ_{top} , Φ_{bottom}). These changes do not alter the claims of Ref.[70], but are instead intended to strengthen them. Both the confined and unconfined devices came from the same relative wafer position as pictured in Fig. 3.7(a) (B1-L) in order to minimize systematic variations. Device resistances were subsequently measured every 1 to 2 weeks for approximately 8 months. As seen in Fig. 3.12(a), the confined device shows significantly less resistance change (i.e., “aging”) over the first 1500 h, after which the unconfined device ages at a similar rate as the confined device. Over the length of the study, the confined junction resistance increased by $34.0 \pm 5.4 \%$ and the unconfined junction resistance increase by $95.4 \pm 7.8 \%$.

To determine the effective thickness and potential barrier heights of the tunnel barriers, we analyzed $dI/dV(V)$ curves for each device type as shown in Fig. 3.12(b). The $dI/dV(V)$ data are obtained from the numerical derivative of I-V data. The fits of the data using the Chow model, as discussed in Chapter 2, are done within a bias window not exceeding ± 100 mV in order to stay in the low voltage regime [54, 69]. All conductance curves are approximately parabolic, signifying tunneling



(a)



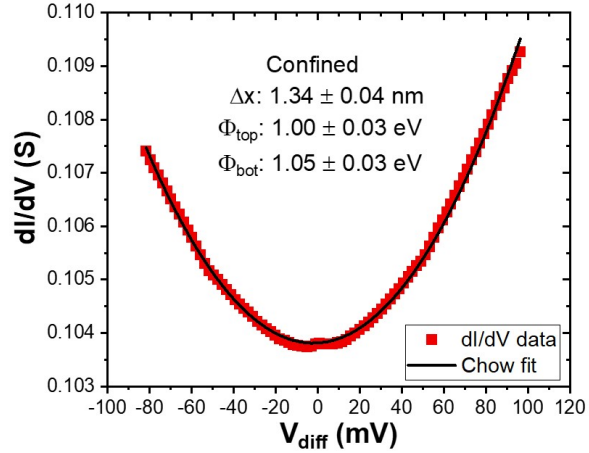
(b)

Figure 3.12: (a) Normalized resistance drift over time for the confined $\text{Co}/\text{AlO}_x/\text{Co}$ (blue circles) and unconfined $\text{Co}/\text{Al}/\text{AlO}_x/\text{Co}$ (red squares) tunnel junctions measured in a four-point geometry. Initial R_0 values are shown in the legend. (b) Normalized differential conductance curves for confined (filled) and unconfined (unfilled) tunnel junctions. Three curves each taken ≈ 100 days apart are displayed to show the relative amount of change seen in the unconfined devices compared to the confined devices, which are relatively indistinguishable as they are all overlapping.

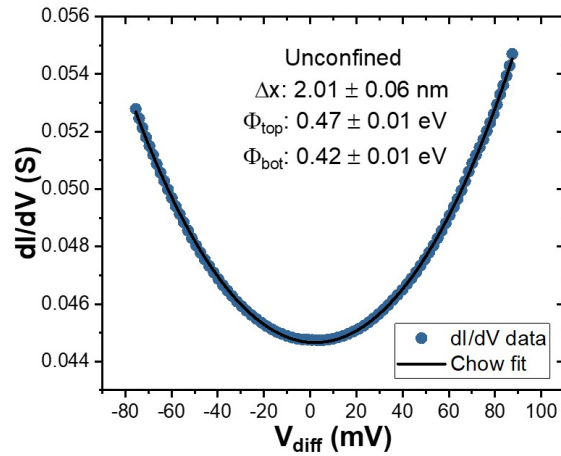
as the dominant transport mechanism. Like the results of the single point resistance measurements, $dI/dV(V)$ data of the confined devices show little change (all overlapping) during the course of the study, while the unconfined devices change significantly over time. While the 1 mA junction resistance was measured starting immediately after fabrication and removal from vacuum, ± 100 mV I-V measurements did not begin until 50 h after fabrication for the confined device and 42 h after fabrication for the unconfined device. These initial $dI/dV(V)$ measurements are seen in Fig. 3.13(a-b) alongside their respective Chow model fits, showing high quality fits for both data sets.

The initial ($t=50$ h) barrier parameters for the confined device are displayed in Fig. 3.13(a). The initial 1.1 nm of elemental Al deposited is expected to expand by ≈ 28 % when oxidized to Al_2O_3 , resulting in a physical barrier width of ≈ 1.4 nm [45]. The difference between 1.4 nm and the extracted fit value of the confined barrier width of 1.34 ± 0.04 nm is within the uncertainty in the initial Al layer thickness, the difference in electrical and physical widths due to effects like the image charge potentials (which tend to electrostatically round off the barrier), and non-uniformities across the device area [67]. The top and bottom barrier heights are almost equivalent within the uncertainties, $\Phi_{\text{top}} = 1.00 \pm 0.03$ eV and $\Phi_{\text{bot}} = 1.05 \pm 0.03$ eV, indicating that the barrier is uniformly oxidized given identical top and bottom Co electrodes. The extracted width and barrier height parameters for the confined device show good agreement with the literature for similar Co/ AlO_x /Co tunnel junctions [96, 100, 106].

In contrast, the initial ($t=42$ h) barrier parameters for the unconfined device,



(a)



(b)

Figure 3.13: (a) Differential conductance data from the confined tunnel junction 50 h after fabrication (filled squares) fitted with the Chow model (unfilled squares). (b) Differential conductance data from the unconfined tunnel junction 42 h after fabrication (filled circles) fitted with the Chow model (unfilled circles). Extracted tunnel junction parameters for each measurement are given with 3 % relative uncertainty.

displayed in Fig. 3.13(b), show a relatively wide and low barrier. Despite the nominally identical oxidation process, the extracted barrier width for the unconfined device is $\Delta x = 2.01 \pm 0.06$ nm. The barrier height fit parameters of the unconfined device are less than half of those for the confined device with $\Phi_{\text{top}} = 0.47 \pm 0.01$ eV and $\Phi_{\text{bot}} = 0.42 \pm 0.01$ eV. This finding suggests that the unconfined tunnel barrier is not as thoroughly oxidized as the confined tunnel barrier, discussed more below. Additionally, the finding of a larger effective thickness in the unconfined device is consistent with the larger initial specific resistance, due to the inverse square dependence of the current density on the barrier thickness in the prefactor of Eq. 2.8.

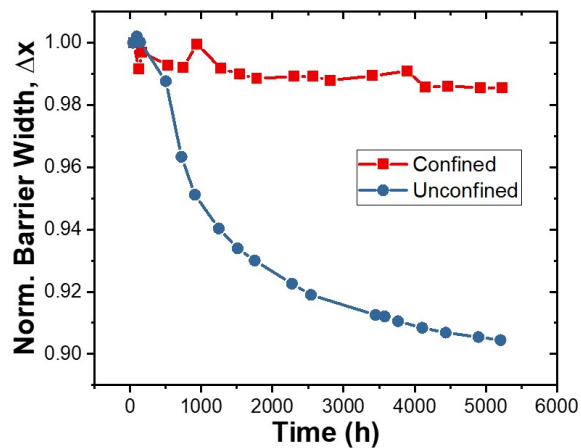
In addition to the resistance, we monitored how the best fits for the barrier parameters changed throughout the study, providing insight into the mechanisms of the resistance drift. Figures 3.14(a-b) show the normalized fit values for barrier width and barrier heights over time. The barrier width of the confined device appears quite stable, decreasing by 1.5 ± 0.5 % over ≈ 5200 h. The barrier heights of the confined device show a small upward drift, as Φ_{top} increased by 11 ± 1 % and Φ_{bot} increased by 4 ± 1 %. The unconfined device shows substantially more drift in all three parameters. Specifically, the effective barrier width Δx decreases by 9.6 ± 0.2 % over ≈ 5200 h while Φ_{top} increased by 34.6 ± 0.5 % and Φ_{bot} increased by 42.8 ± 0.7 %. The change in barrier parameters for the first ≈ 2 days were not captured for either device. While only a few extra data points are included in the raw resistance drift between that ≈ 2 days and the time of fabrication, no qualitative difference in the aging trend for this short period and the sharp aging seen for the

first ≈ 1000 h is seen.

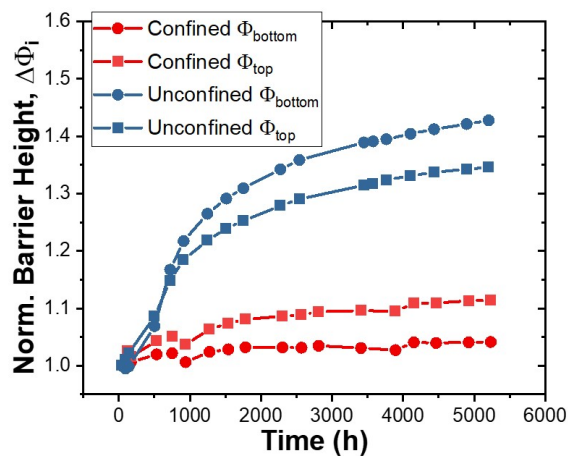
3.3.3 Discussion

For the work reported here, we can reasonably exclude several causes of aging identified in other studies, e.g., (1) aging induced by photoresist residue is not applicable as photolithography was not used here; (2) aging induced by disassociation of hydroxyls in the barrier is unlikely as junctions described here were not exposed to elevated temperatures [85]. Also, diffusion of oxygen and other foreign species from air is not likely to have a significant impact on aging since the tunnel barriers are deeply buried beneath the overgrown electrodes and the tunnel junction areas are large relative to the room temperature diffusion lengths from sidewalls [79, 85]. Furthermore, we do not expect significant out-diffusion of hydrogen from the electrodes to the tunnel barrier given the reported room temperature values for hydrogen diffusivity in Co [107].

Resistance drift of the kind observed in this work is understood to be associated with an evolution of the oxygen concentration profile in the tunnel barrier as a result of an initial nonequilibrium structure and low stoichiometry. Aluminum oxides that have sub-stoichiometric and/or nonuniform oxygen concentration profiles have a large phase space of atomic configurations and undergo a long process of relaxation [43]. As the atomic configurations change, the local electronic states change, resulting in the electrical resistance drift [22]. Typically, during the initial fabrication of AlO_x , the aluminum closest to the surface is oxygen-rich compared



(a)



(b)

Figure 3.14: (a) Normalized effective barrier width parameters over time for the confined (red squares) and unconfined (blue circles) devices. (b) Normalized effective barrier height parameters for the confined (blue symbols) and unconfined (red symbols) over time. The normalization parameters used are the 50 h and 42 h values stated in the text for the confined and unconfined devices, respectively.

to deeper in the aluminum [47, 108]. Once the oxidation is complete, the oxygen concentration profile relaxes with time and temperature from this asymmetric AlO_x towards a more uniform Al_2O_3 -like stoichiometry throughout the barrier [108].

Annealing the barriers accelerates this relaxation process, helping the material to reach a lower energy configuration [44]. Alternatively, improving the oxygen concentration profile created during the initial oxidation can also reduce the resistance drift, since the system is initially closer to a relaxed state [109, 110]. However, annealing typically leads to increases in barrier height and width as trap related conductance pathways are eliminated [44, 111]. For the junction aging seen here, the reduction in barrier width and increase in barrier height with time is consistent with an increase in the density and O/Al ratio. With these changes, the band gap in the oxide is expected to open further alongside the mitigation of trap related conduction paths [22, 112]. It should be noted that the use of plasma oxidation plays a pivotal role in the aging observed, as oxides formed by plasma oxidation opposed to thermal oxidation typically have much higher O/Al ratios which are closer to stoichiometric Al_2O_3 [47].

Similar logic is applied between the confined and unconfined case. During the plasma oxidation, a sub-stoichiometric Al-rich oxidation front moves through the metallic Al, with oxide forming initially at Al grain boundaries. In the confined case, the O/Al ratio does not increase significantly until the oxidation front reaches an underlying layer acting as a oxidation stop, e.g., the Co under layer in our tunnel junctions [47, 109]. At this point, oxygen content builds up towards Al_2O_3 from the top down. Compared to the confined case, the unconfined barrier does not

have an oxidation stop beneath the barrier and the WKB fit parameters confirm a relatively wide barrier with low barrier heights, which contracts with increasing time. Furthermore in the unconfined device, the slightly larger Φ_{top} compared to Φ_{bottom} is consistent with the oxygen content slowly building up from the surface down. In the confined devices, the large difference in ΔG_f between Al oxide and the Co oxides allows nearly all of the metallic Al to be oxidized prior to the oxidation front moving beyond the Al [45, 46, 78, 108]. The aging is then less severe for the confined devices, due to the initial oxygen profile being more uniform and the stoichiometry closer to that of the more stable Al_2O_3 . The higher O/Al ratio and Al-coordination constrains atomic motion, decreasing the density of TLS from configuration changes and the related from TLS relaxation. In addition, there are likely fewer oxygen vacancies acting as charge traps, which are thought to contribute to aging as they are annealed over time [22]. Therefore, incorporating plasma processing and free energy confinement (using compatible materials) could provide an athermal and fast route to mitigate this source of decoherence for solid state quantum information devices.

3.4 Chapter Summary

In this chapter, I discuss the plasma processing of thin Al layers on Co under layers. Oxygen radicals, O^* , supplied by the plasma enhance the field-assisted diffusion of Al ions towards the exposed surface, resulting in an oxide structure with higher O/Al ratios in shorter periods of time when compared to those formed by

standard (i.e., room temperature) thermal oxidation. A plasma oxidation recipe is arrived at by mapping and optimizing a recipe used by prior group members on a separate system. Oxygen pressure and plasma power are tuned to maximize O^* density while maintaining a similar power density to the previously used plasma system. With these set points, oxidation time is determined by minimizing device resistance drift across devices with different oxidation times, while also optimizing extracted tunnel barrier parameters (barrier width, heights) to match literature values of fully oxidized Al layers sandwiched between Co layers.

As an extension of this process, the benefit of plasma processing in conjunction with Co confinement is further highlighted by comparison with devices without such Co confinement. Using an identical plasma oxidation process, devices with AlO_x tunnel barriers confined by Co layers (Co/ AlO_x /Co) display significantly less resistance drift in time when compared to devices without such confinement (Co/Al/ AlO_x /Co). Tunnel barrier parameters extracted within a WKB formalism portray the structure of the confined devices as having an AlO_x tunnel barrier with a relatively sharp oxygen profile and O/Al ratio nearer to that of stoichiometric Al_2O_3 . In contrast, tunnel barriers in the unconfined devices are seen to be relatively wide with low barrier heights indicating a sub-stoichiometric barrier stretching further into the Al. The data supports the conclusion of the confined Al layer acting as an oxygen potential well due to the larger (more negative) ΔG_f of Al oxide compared to Co oxides. This likely reduces the density of electrically active defects, such as TLS from oxygen vacancies or changes to atomic configuration, whose relaxation manifests over time as device aging. In addition to the long time stability improve-

ment, mitigation of such defects is likely to result in a reduction in electrical noise from TLS.

Chapter 4: Photoelectron Spectroscopy for Ultrathin AlO_x Layers

4.1 Context

Most of the discussion in Chapter 3 correlated process parameters (plasma oxidation time, pressure, power) with tunnel barrier properties. However, this process feedback loop would greatly benefit from *in situ* materials characterization. As it is non-destructive and compatible with ultra-high vacuum (UHV), photoelectron spectroscopy (PES) can provide such characterization throughout device fabrication, providing valuable information on the composition of a sample and the chemical state of constituent elements. The focus of this chapter will be the role of photoelectron spectroscopy (PES) in evaluating AlO_x tunnel barrier fabrication in mesoscopic tunnel junctions. X-ray photoelectron spectroscopy (XPS) is used to monitor the oxidation of thin Al films on Co and Nb. I provide an overview of PES, specifically regarding XPS, and the experimental apparatus used for my measurements in sections 4.2 and 4.3, respectively. Section 4.4 describes process development using XPS for tunnel barrier formation. Section 4.5 discusses thin film thickness determination using angle-resolved XPS (ARXPS), including a comparison of AlO_x layer thickness as determined by ARXPS and the WKB method discussed in Chapter 2.

XPS is a non-destructive, surface sensitive technique used for elemental and chemical state identification. When developing fabrication processes for meso- or nanoscale electrical devices, materials characterization is often performed on proxy samples due to the use of destructive analysis techniques or the need to break vacuum for inspection. Extrapolating the characteristics of these proxies to the device of interest introduces uncertainties in interpreting device performance by assuming, for example, an identical fabrication environment and process parameters. By integrating XPS into our fabrication system, we have the opportunity to correlate *in-situ* materials characterization with *ex-situ* transport characteristics of the same device. This allows for expedited process development and provides chemical information that may elucidate interesting device characteristics.

In particular, process development using the Al chemical state and AlO_x thickness is discussed here. Chemical state identification assists with the fabrication of AlO_x tunnel barriers by monitoring for metallic Al and unwanted oxides. For example, the confined Al layers discussed in Chapter 3 are intended to be fully oxidized (no metallic Al remaining) with minimal Co oxidation. Measuring the XPS spectra of Al/Co layers with different oxidation parameters allows us to explicitly evaluate those metrics with regards to our plasma oxidation recipe.

Determining the thickness of ultrathin layers remains a difficult and technologically important task [48, 103]. Popular techniques such as transmission electron microscopy (TEM) are destructive, and achieving the necessary resolution is typically quite arduous. Angle-resolved XPS (ARXPS) uses signal attenuation as a function of escape angle to determine film thickness [113]. Tunnel barrier thickness

is often determined using transport characteristics [69]. However, the transport thickness represents the thickness of the potential barrier and is affected by image charges, defects, barrier asymmetry, etc. ARXPS provides an orthogonal thickness measurement based solely on chemical abundance. A correlation between these fundamental approaches would aid in developing fabrication processes.

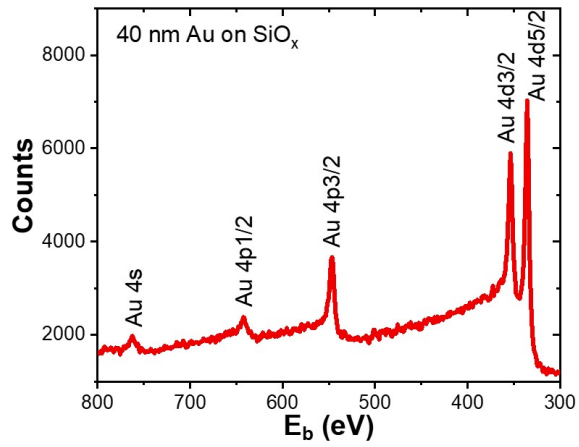
4.2 Background - Photoelectron Spectroscopy

The photoelectron effect is the emission of electrons from a material as a result of absorbing electromagnetic radiation. In order for such a photoelectron to escape a material, the absorbed radiation energy $h\nu$ must exceed the electron binding energy (E_b) and the material work function (Φ_m). Assuming only elastic scattering and that energy is conserved, the kinetic energy (E_k) of the ejected electron is given by

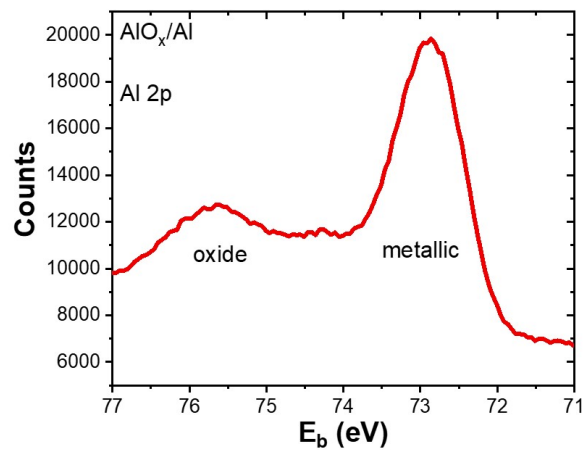
$$E_k = h\nu - E_b - \Phi_m \quad (4.1)$$

Photoelectron spectroscopy (PES) takes advantage of the fact that, by measuring E_k when irradiating a sample with a known $h\nu$, characteristic E_b values can be determined corresponding to atomic orbitals within a specific material. X-ray photoelectron spectroscopy (XPS) uses high energy X-rays, Al $K\alpha$ with an energy of 1486.6 eV in our case, to measure E_b of core electrons. As these energies are unique to each element, the XPS spectrum acts as a chemical fingerprint. For example, the XPS spectrum of a 40 nm Au film is shown in Fig. 4.1(a).

The labels over each peak in Fig. 4.1(a) indicate the atomic orbital from



(a)



(b)

Figure 4.1: (a) XPS spectrum of a sputter cleaned 40 nm Au film on SiO_x. (b) Al 2p peak of AlO_x on Al.

which the corresponding electrons were ejected. XPS peaks are typically labeled in the form nlj , where n is the principle quantum number and l is the angular momentum quantum number. The total angular momentum $j = l \pm s$, where s is the spin angular momentum number of the electron. For any peak corresponding to an orbital with a non-zero angular momentum quantum number (all but s), a peak doublet is measured as a result of parallel or anti-parallel coupling between the s and l .

In addition to elemental identification, XPS can be used to inspect the chemical state of a material. For example, the XPS peaks of a metallic sample will shift in energy when oxidized due to the change in binding energy. The 2p peak of an Al thin film that was briefly exposed to oxygen is shown in Fig. 4.1(b). The oxygen exposure forms a surface layer of AlO_x with mostly Al-O bonding as opposed to Al-Al bonding. The spectrum is then a convolution of the surface Al-oxide layer and the underlying Al film. The Al 2p peaks do not exhibit a doublet structure here, as the splitting between the doublet features is smaller than the measurement resolution.

Although Eq. 4.1 assumes only elastic scattering, inelastic scattering effects feature prominently in XPS spectra. XPS peaks are typically asymmetric, having a tail towards higher binding energy as a result of inelastic scattering. An electron may lose energy through inelastic scattering when leaving the sample and, given the assumptions of Eq. 4.1, would be interpreted as a higher binding energy. The inelastic mean-free path (IMFP) of the photoelectrons is typically only several nanometers. This highlights why XPS is a very surface sensitive technique where

the depth from which information is obtained is $\approx 5\text{-}10$ nm, even though the X-rays penetrate much deeper into the material. This “information depth” is typically estimated to be $3\cdot\lambda$, where λ is the inelastic mean free path [114]. The cumulative signal from inelastically scattered electrons results in a spectrum background. To account for this, peak fitting and analysis of XPS spectra typically use one of several background subtraction methods discussed later in the chapter [115].

4.3 Experimental Apparatus

Alongside the deposition and oxidation chamber, a SPECS photoelectron spectroscopy system is connected to the load lock as seen in Fig. 2.1. The system is also shown and annotated in Fig. 4.2. Central to the XPS system is the analysis chamber which houses the device under measure. The analysis chamber has a base pressure of 2×10^{-10} Torr and is pumped on with a Pfeiffer HiPace 300 turbo pump and an Agilent Starcell ion pump with TSP. A magnetic transfer rod is used to retrieve a wafer cassette from the load lock and move it to the sample manipulator in the center of the analysis chamber. The cassette can be moved laterally and vertically in the chamber, as well as rotated in the polar direction.

The system is equipped with an X-ray light source and a UV light source. Attached to the side of the analysis chamber is a μ Focus (μ F) 350 monochromated small spot X-ray source. The μ F chamber has a base pressure of 3×10^{-9} Torr and is pumped with an Agilent TwisTorr 304 FS turbo pump, in addition to direct connection to the analysis chamber via flex hose. Al $K\alpha$ X-rays are generated and focused

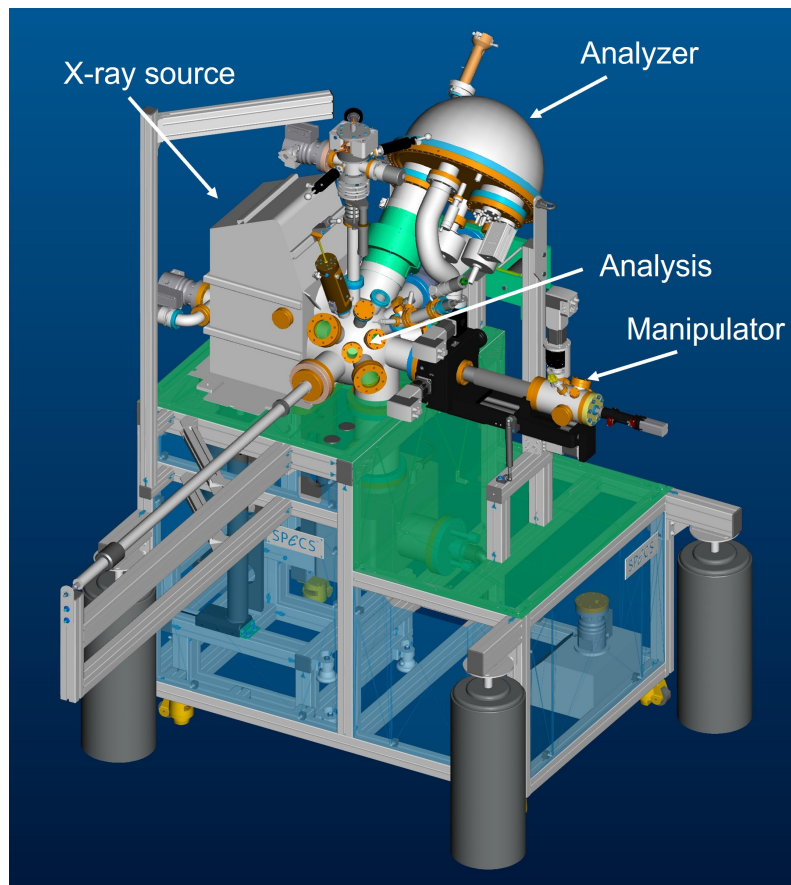


Figure 4.2: CAD rendering of the SPECT's photoelectron spectroscopy system

onto the sample in the analysis chamber. The X-rays are generated by focusing an electron beam onto an Al anode, where the X-ray intensity is parameterized by electrical power deposited on the anode from the electron beam (typically 3-100 W). The minimum X-ray spot diameter is $\approx 35 \mu\text{m}$ and is inversely proportional to the intensity/power. Directly above the analysis chamber sits a SPECS UVS 300 vacuum ultraviolet (VUV) source for ultraviolet photoelectron spectroscopy (UVS). The UVS chamber has a base pressure of 5×10^{-8} Torr and is pumped with a Pfeiffer HiPace 80 turbo pump. Our UVS system utilizes radiation from a He plasma, which is dominated by emission from the He I line at 21.22 eV. A capillary extends from the lamp towards the sample in the analysis chamber and focuses the light onto the sample surface. The lower energy of the UV source makes it suitable for measuring the valence structure and work function of a material. The analysis chamber is also equipped with an additional electron gun for Auger spectroscopy and an Ar sputter gun used for surface cleaning and depth profiling.

A simple measurement diagram is shown in Fig. 4.3. X-rays with $h\nu = 1486.6$ eV are focused onto the sample, which emits photoelectrons with a conical angular distribution. The electrons are collected by a PHOIBOS wide angle lens. The lens is at 49.5° relative to the sample surface normal and accepts electrons between approximately 20° and 80° relative to the surface normal. A lens focuses the electrons into the hemispherical analyzer. A retarding potential in the lens reduces E_k over a particular energy range to match the pass energy, E_{pass} . The electron beam is dispersed according to the spread in E_k as it moves through the analyzer, where only the electrons within a range proportional to E_{pass} can traverse the analyzer.

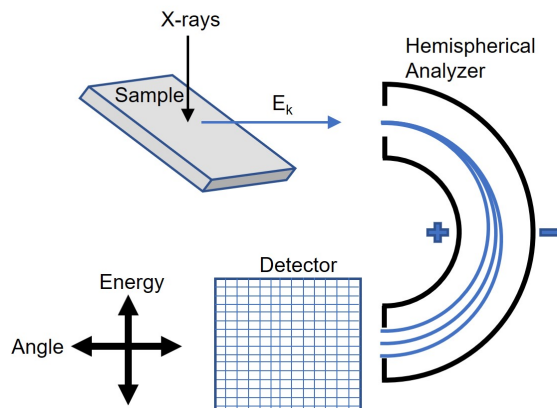


Figure 4.3: Diagram of XPS measurement showing the sample, hemispherical analyzer, and delay-line detector.

The sensitivity (i.e., signal intensity) is proportional to E_{pass} and the energy resolution is inversely proportional to E_{pass} . The retarding potential is swept during a scan to measure the full energy range of electrons emitted from the sample. Once the electrons leave the analyzer, they enter the 2D delay-line detector (DLD). The location of where the electrons enter the detector determines the electrons initial E_k and emission angle.

4.4 Monitoring Oxidation with XPS

In this thesis, AlO_x tunnel barriers are fabricated primarily on top of both Co (Chapter 3) and Nb/Al (Chapter 5) underlying films. In both cases, a 1.1-1.5 nm Al film is e-beam deposited on the underlying film and plasma oxidized. The intent is to oxidize the entire Al film with an Al/O ratio approaching Al_2O_3 , while avoiding oxidation of the metal layer below. XPS can assist with developing the oxidation

process by inspecting the Co/AlO_x or Nb/Al-AlO_x surface [45]. Oxidation of the metal layers results in the metallic peaks, representing metal-metal bonding, shifting to higher binding energy to reflect metal-oxygen bonding. Therefore, the XPS spectrum of the ideally oxidized layer would show an oxidized Al peak with no sign of metallic Al, while showing little to no shift in the underlying Co or Nb metal peak.

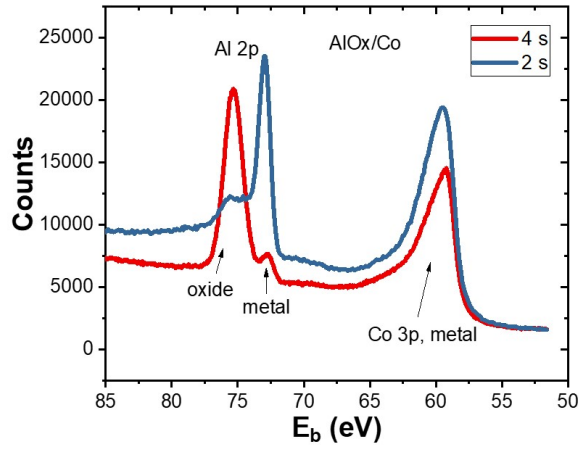
The XPS spectrum of a 1.1 nm Al/40 nm Co film stack is shown in Fig. 4.4(a-b) for several different oxidation times. For 2 s of oxidation shown in Fig. 4.4(a), a relatively small Al-O peak emerges at $E_b \approx 75$ eV. Just as in Chapters 3 and 5, the oxidation power and pressure for all the samples discussed in this chapter are 55-60 W and 160 mTorr, respectively. While Al can have several oxidation states, Al⁺³ is by far the most common resulting in a single primary oxide peak [48]. The metallic Co peak appears as expected, with a tail towards higher E_b due to inelastic losses. At 4 s oxidation, the Al-oxide peak grows and the metallic Al peak diminishes. The relative decrease in amplitude of the Co peak is likely a result of the smaller electron mean free path of the AlO_x layer. The spectrum for a separate device oxidized at 7 s is shown in Fig. 4.4(b). Within the scan resolution, no metallic Al peak is observed. In addition, no satellite Co peak is observed indicating little to no Co oxide has formed. The scan in Fig. 4.4(b) uses a higher E_{pass} and, as a result, has a higher count rate and slightly broader features than those in Fig. 4.4(a). The small overall shift to higher E_b of the features in Fig. 4.4(b) relative to 4.4(a) is within typically observed sample-to-sample variation. The scan in Fig. 4.4(b) indicates that we have met our criteria of a fully oxidized Al film on Co with

a 7 s oxidation time without significantly oxidizing the underlying Co layer.

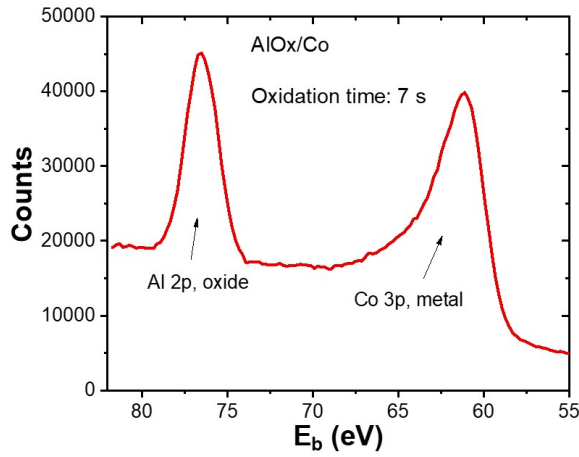
Fig. 4.5 shows the XPS spectrum of two Al/Nb layers plasma oxidized for 7 s. The red trace is from a 1.1 nm Al/40 nm Nb sample and the blue trace is from a 6.1 nm Al/40 nm Nb sample. The 1.1 nm Al sample shows no signs of metallic Al, but Nb oxide peaks are clearly visible. This could be attributed to (1) Nb sapping oxygen from the AlO_x layer and forming NbO_x near the interface or (2) incomplete coverage of the Nb layer by the initial Al layer. With no metallic Al detected to provide a buffer between the AlO_x and Nb, a convolution of both effects is possible. However, small signs of the Nb oxide peaks can still be seen in the 6.1 nm Al sample. Given that the metallic Al peak is still present, it is likely that incomplete coverage of the Nb with thin Al is mostly responsible for the appearance of NbO_x features. This is consistent with transport characteristics of the Nb/Al layers with Al thickness $\lesssim 10$ nm, as discussed in Chapter 5.

4.5 Film Thickness Determination with ARXPS

Thickness estimates of thin surface films with XPS is typically done with the method proposed by Hill *et al* [116, 117]. This “chemical abundance” thickness relies on the exponential attenuation of signal intensity from a substrate as a function of distance traveled through an overlying film. The AlO_x tunnel barrier thicknesses discussed in Chapters 2 and 3 relied on fitting transport data to extract an effective thickness of the potential barrier. Some disagreement between the XPS and transport thickness estimates is expected, as they measure physically distinct char-



(a)



(b)

Figure 4.4: XPS spectrum of 1.1 nm Al/40 nm Co stack for (a) 2 s, (a) 4 s, and (b) 7 s plasma oxidation times. The scans show the Al 2p peak and Co 3p peak. E_{pass} values are (a) 50 eV and (b) 100 eV. The power for both scans is 100 W.

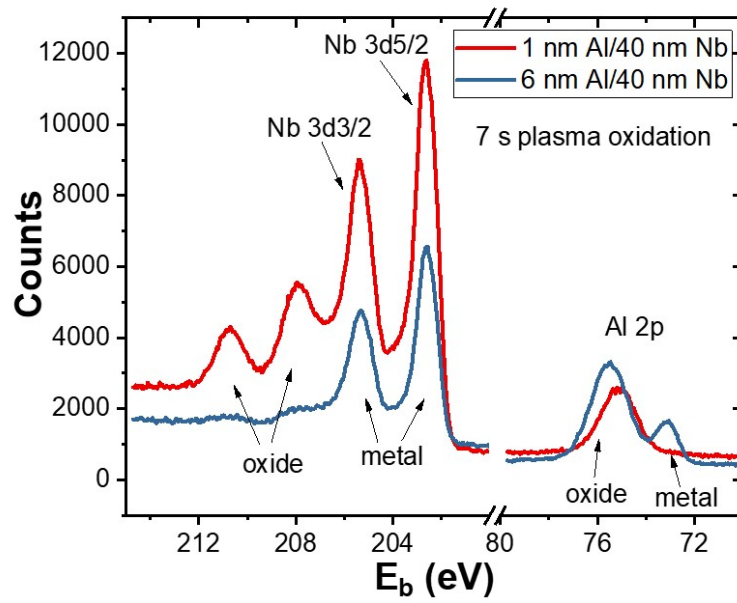


Figure 4.5: XPS spectrum of 1.1 nm Al/40 nm Nb (red line) and 6.1 nm Al/40 nm Nb (blue line) stack for 7 s plasma oxidation time. The scans show the Al 2p peak and Nb 3d peaks. E_{pass} is 50 eV and the power for both scans is 100 W.

acteristics. By relating the chemical structure of the barrier (oxidation state, O/Al ratio) to the resulting potential barrier (height, width), correlation between the methods could prove useful in evaluating process development. Here I will provide several representative examples of determining AlO_x thickness in various film stacks and compare to the transport determined thickness when possible.

As indicated in Fig. 4.6(a), the travel distance of a photoelectron through the overlayer increases as the emission angle relative to the surface normal increases. XPS spectra of an AlO_x/Al stack is shown in Fig. 4.6(b) for several emission angles, with the emission angle relative to surface normal increasing from front to back. By normalizing the scan intensities by the surface AlO_x layer signal, the relative decrease in the underlying Al signal is clearly seen. The Hill equation relates the emission angle (ϕ) with the signal ratio of the underlayer and overlayer films as shown in Eq. 4.2.

$$\ln \left(1 + \frac{R}{R_\infty} \right) = \frac{t_o}{\lambda_o} \frac{1}{\cos(\phi)} \quad (4.2)$$

where t_o is the overlayer thickness, $R_\infty = n_o \lambda_o / n_s \lambda_s$, $\lambda_{o(s)}$ is the electron IMFP in the overlayer (o) or substrate (s), and $n_{o(s)}$ is the atomic density. $R = I_o / I_s$, where $I_{o(s)}$ is the signal intensity from the overlying film or substrate. The intensity is the peak area divided by the relative sensitivity factor, which is specific to the element and atomic orbital of the peak of interest. The relative sensitivity factor is used during quantitative XPS analysis to account for differences in material or measurement characteristics such as photoelectron cross section or energy/intensity transmission function [115]. This form of the Hill equation represents a simplification under the

assumption that $\lambda_s \approx \lambda_o$. This is generally true for electrons emitted from the same element and atomic orbital but different chemical states, such as AlO_x on Al.

Quantitative analysis of XPS spectra requires peak fitting to extract peak intensities. The spectrum background represents the inelastic scattering of electrons as they move through the material. For all spectra shown, I account for the background with the “Shirley” type background function [118]. The Shirley background assumes a constant inelastic scattering probability and determines the background underneath a peak proportional to the integrated peak intensity. It typically resembles a broadened step up from lower to higher E_k similar in shape to a Fermi-Dirac distribution, with the center point coinciding with the peak center. Another background function often seen in the literature is the Tougaard background[115]. However, application of the Tougaard background is complicated as it requires more detailed input on the electronic structure of the measured material. The Shirley background is widely understood to be reasonably accurate and easy to apply repeatedly in most XPS software.

Peaks that appear symmetric, such as the Al 2p oxide peak, are fit with a Voigt function, while asymmetric metallic peaks are fit with a Voigt function having an exponential tail towards higher binding energy. Similar to interpreting the plasma optical spectra in Chapter 2 and 3, Voigt functions are a convolution of Gaussian broadening arising from the measurement process (Doppler effect, detector resolution) and the Lorentzian broadening arising from lifetime effects. Instrumental broadening from the spectrometer resolution is typically the dominant broadening mechanism. Metallic peaks typically appear asymmetric due to the presence of

free electrons in the conductance band. These provide a continuum of states for photoelectrons to scatter into from the peak energy. However for peaks representing materials with a band gap, such as an Al^{+3} peak representing oxidized Al, the emitted photoelectrons are spread to E_k further from the peak and result in a locally symmetric feature. All of the quantitative XPS analysis discussed here is performed with CasaXPS software.

The waterfall plot in Fig. 4.6(b) represents 1 of 3 samples in a set with oxidation times of 5 s, 7 s, and 9 s. The Hill equation plot for each of these samples is shown in Fig 4.7(a), where the left side of Eq. 4.2 is plotted against $1/\cos(\phi)$. The slope multiplied by λ_o provides the ARXPS determined overlayer thickness. The atomic density for Al and AlO_x is taken from Ref.[119] and Ref.[120], respectively. The relative sensitivity factors are taken from the CasaXPS library based on Ref.[121] and IMFP values are taken from the NIST Standard Reference Database [122]. The uncertainty displayed with each thickness value represents one standard deviation in the fit value.

Although the lens of the XPS analyzer captures electrons emitted between 20° and 80° relative to the sample normal, the signal from electrons emitted at high angles (i.e., shallow take-off angle relative to the surface) is typically omitted. An electron emitted from deep in the substrate layer may elastically scatter near the surface and appear as if it was emitted near the surface at a different angle from its original trajectory [117]. This manifests as an artificially higher attenuation length, which affects higher emission angles relative to the surface normal to a much greater degree than smaller angles. In a Hill equation plot, this manifests as a smaller slope

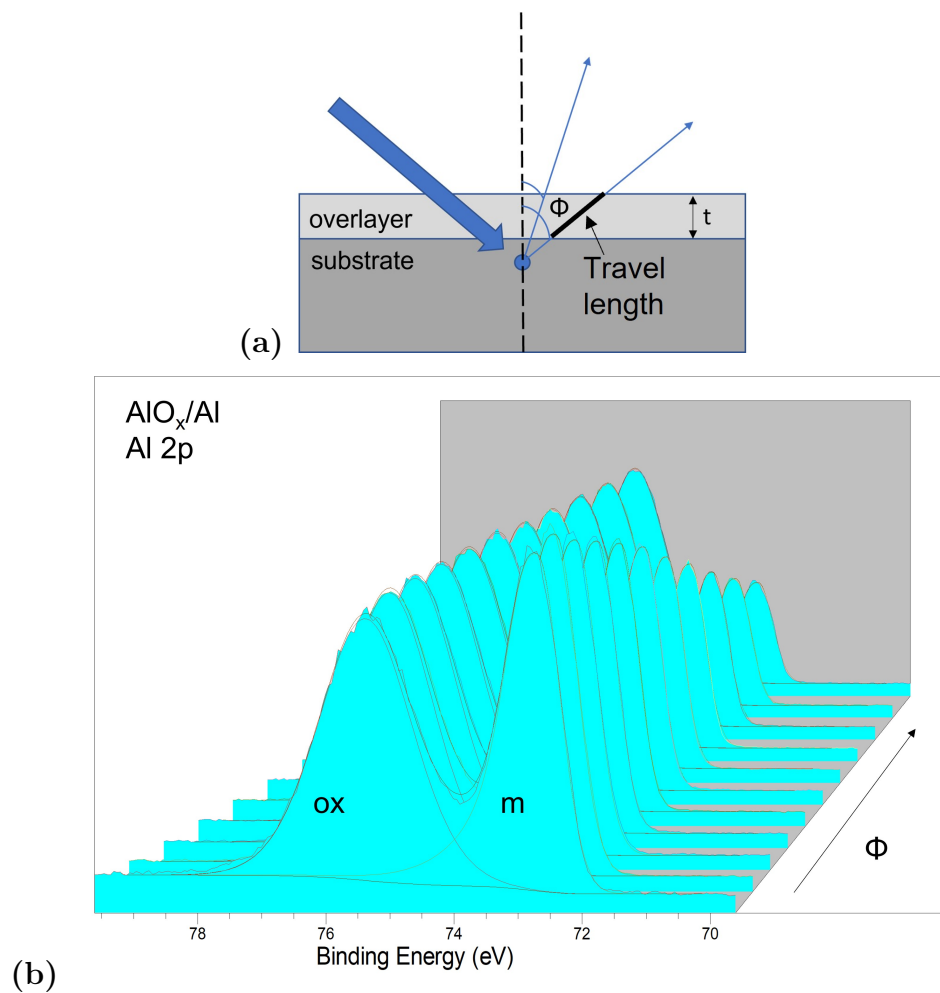
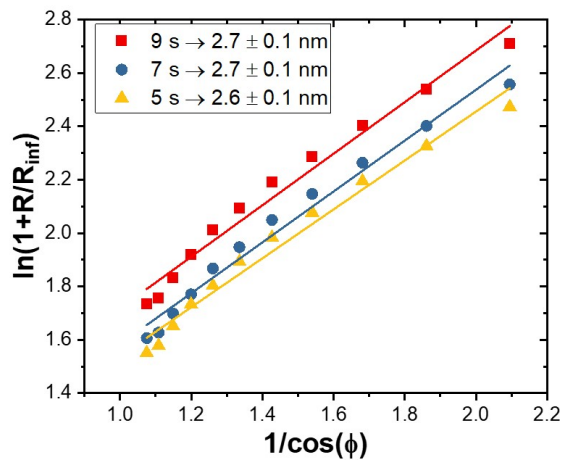
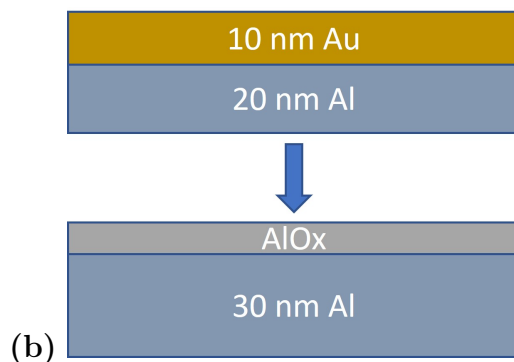


Figure 4.6: (a) The diagram illustrates how the travel distance of photoelectrons through an overlayer increases with increasing emission angle. As a result, the signal intensity decreases and can be used to determine the overlayer thickness. (b) The XPS waterfall plot shows that with increasing emission angle the intensity of the metallic Al 2p peak decreases relative to the oxide Al 2p peak.



(a)



(b)

Figure 4.7: (a) Hill equation plot for an AlO_x/Al layer with several oxidation times. (b) Tunnel junction stack fabricated after XPS measurements.

at higher emission angles (higher $1/\cos(\phi)$) beyond a thickness dependent cutoff angle [116, 117]. For overlayer thicknesses below 5 nm, the cutoff emission angle has been shown to be $\approx 65^\circ$. Therefore, I omit data for emission angles above this value ($1/\cos(\phi) > 2.3$) as is often the procedure seen in the literature [117, 123].

After each sample was measured with XPS, a top layer of Al and Au was deposited to form crossed wire tunnel junctions with the stack illustrated in Fig. 4.7(b): 30 nm Al/ AlO_x /20 nm Al/10 nm Au. Conductance spectra were fit with the WKB-Chow model discussed in Chapters 2 and 3 to extract tunnel barrier characteristics. Fig. 4.8 plots the extracted thicknesses from ARXPS against those from the transport data. The relatively large uncertainty in the ARXPS data makes interpretation difficult, but the thickness does increase with oxidation time as expected. More samples over a larger range of oxidation times would lend greater weight to the correlation between the data sets. It should also be noted that n_o and λ_o values for AlO_x vary in the literature [120, 124]. The values used here, $n_o = 1.77 \times 10^{22}$ atoms/cm³ and $\lambda_o = 2.81$ nm, represent a homogeneous Al_2O_3 film. The effective values may vary between AlO_x films with a different Al/O ratio, where differences in λ_o would significantly change the extracted thickness values.

In addition to the AlO_x/Al on a Si substrate, several samples of AlO_x/Al layers on Nb have also been measured. The waterfall plot in Fig. 4.9(a) corresponds to 10 nm of Al on 40 nm of Nb following 7 s of plasma oxidation. The Hill equation plots for this sample and another with 12 s of plasma oxidation are shown in Fig. 4.9(b). After inspection with XPS, a top layer of 5 nm Au/40 nm Cu/10 nm Au was added to make crossed wire tunnel junctions and transport data was used to

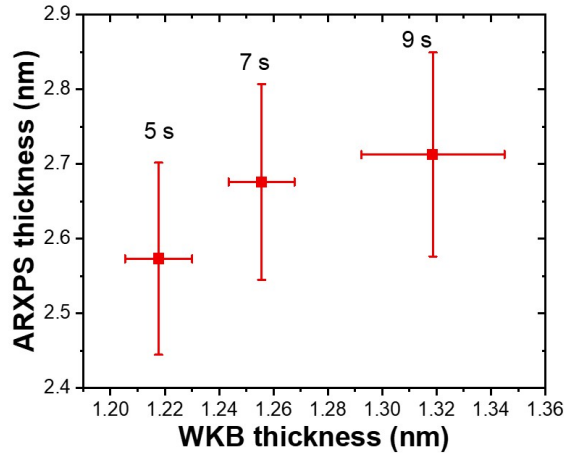


Figure 4.8: Extracted thickness values of an AlO_x layer on Al as determined by ARXPS and WKB modeling.

determine the AlO_x tunnel barrier properties. While both the ARXPS and WKB thicknesses increase with oxidation time, the ARXPS determined thickness is thinner than the WKB determined thickness unlike the data shown in Fig. 4.8. A comparison of the waterfall plots in Fig. 4.6(b) and 4.9(b), both 7 s oxidation of AlO_x/Al layers, shows a slightly different trend in the metallic and oxide Al peaks. In the AlO_x/Al on Si case shown in Fig. 4.6(b), the Al-Al peak is larger than the Al-O peak for the lowest emission angle and becomes smaller than the Al-O peak at higher emission angles. In the AlO_x/Al on Nb case shown in Fig. 4.9(b), the Al-Al peak is always smaller than the Al-O peak. It seems counterintuitive that the sample with the higher Al-O to Al-Al peak intensity has a thinner AlO_x layer, however it is the change in the relative peak intensity that the Hill equation considers. It is currently not clear why these two cases appear qualitatively different. As before, more samples

would help in determining the physical properties responsible, such as a different in Al IMFP or surface roughness.

A waterfall plot and corresponding Hill equation fit for a AlO_x/Co film stack is shown in Fig. 4.10(a-b). The extracted ARXPS thickness of 1.5 ± 0.2 nm is much closer to the WKB determined thickness of 1.22 ± 0.01 nm. However, the Hill equation data appears more nonlinear over the displayed range of emission angles. This suggests a lower cutoff emission angle than the typically used 65° is needed in order to use the linear approximation. Experiments have shown a smaller cutoff angle for thicker films approaching the information depth limit of ~ 10 nm [116, 117], which is certainly not the case here. However, a lower cutoff angle has also been attributed to films with relatively higher surface roughness [125]. If the cutoff angle is decreased, omitting data at $1/\cos(\phi) > 1.4$ in Fig. 4.10(b), the ARXPS estimated thickness is ≈ 2.8 nm. Differences in the relative sensitivity factors and the difference between λ_o and λ_s should be carefully considered moving forward. The difference in IMFP values strains the Hill equation assumption of a constant IMFP, and may warrant a more complex version of the Hill equation or one of the published correction methods [117, 126]. In the AlO_x/Al case, the relative sensitivity factors are equal for the overlayer and underlayer as the photoelectrons in the examined peaks both come from the Al 2p orbital. The CasaXPS library values for the Al (0.537) and Co (1.93) sensitivity factors differ by a factor of ≈ 4 . Similar to IMFP, values for the sensitivity factors vary in the literature depending on the instrumentation or methods used [127].

In order for ARXPS thickness determination to reliably contribute to process

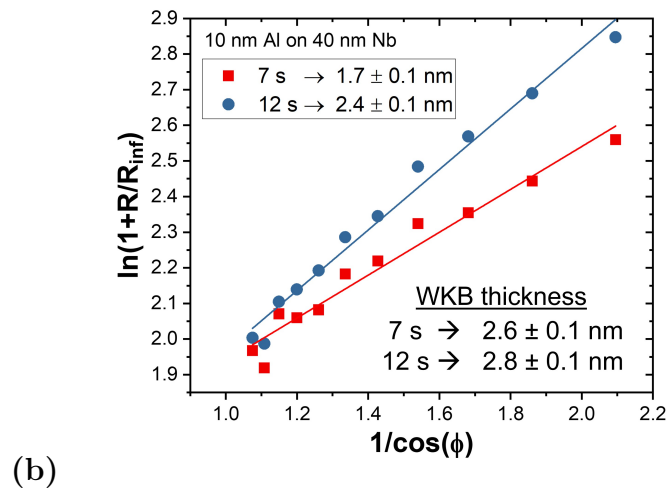
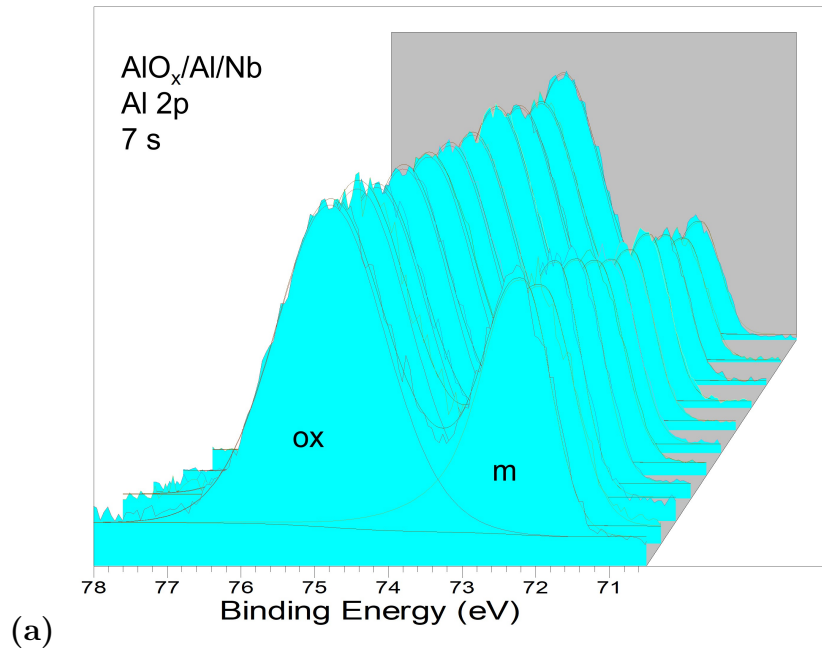


Figure 4.9: (a) Al 2p waterfall plot of an AlO_x/Al/Nb sample with 7 s of plasma oxidation. (b) Hill equation plot for 7 s and 12 s oxidation times. The WKB determined thicknesses are shown in the bottom right. The "ox" and "m" labels refer to the oxide and metallic peaks.

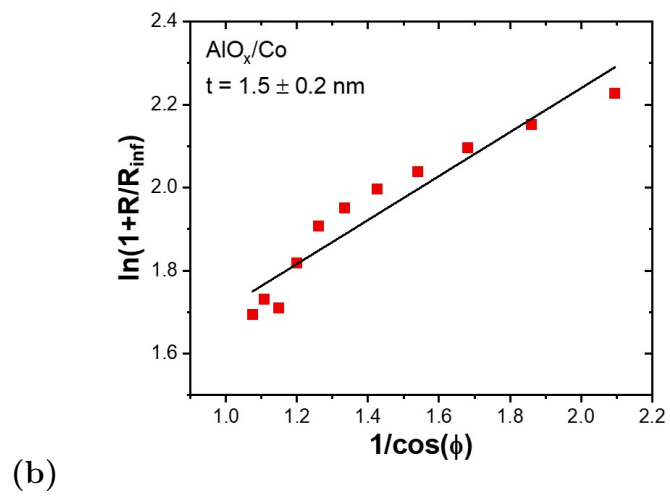
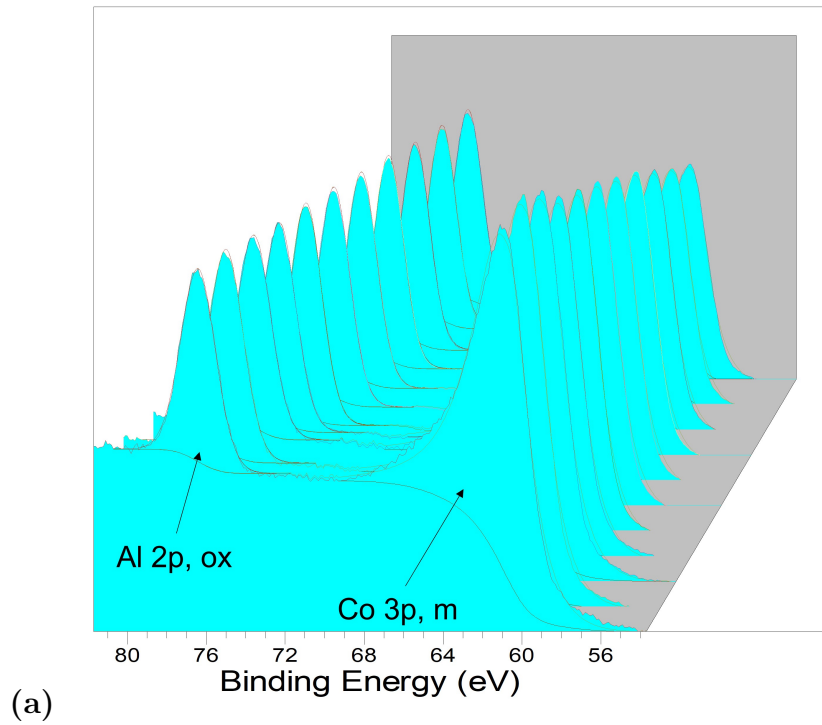


Figure 4.10: (a) Waterfall plot for an AlO_x/Co film stack. (b) Hill equation plot corresponding to the data in (a).

development, input parameters must be calibrated with reference samples or with additional experimental techniques [113]. A series of guides published by Shard describe the most significant sources of error for quantitative XPS [128], several of which I will note here. Relative sensitivity factors depend, in part, on the instrument, so samples with known stoichiometry must be acquired. As shown here, quantifying XPS data for a material (such as AlO_x) can vary significantly depending on the background environment. Therefore, reference samples are needed to accurately subtract the inelastic background from the features of interest. A significant portion (typically $\lesssim 20\%$, sometimes greater than 50%) of the intensity from a given feature may be found in satellite features at lower kinetic energy, thus making it difficult to capture the full intensity without accurately accounting for the background.

4.6 Chapter Summary

In this chapter, I introduced X-ray photoelectron spectroscopy and the instruments used. By effectively measuring the binding energy of emitted photoelectrons, XPS can be used to identify elemental fingerprints. In addition, information on the chemical state of the measured species can be gained due to shifts in the binding energy with bond type (metal-metal, metal-oxide, etc.). Integrating *in situ* XPS with our fabrication system allows for non-destructive material characterization throughout device fabrication and correlation of these measurements with transport data without the need for proxy devices.

The plasma oxidation recipe used for thin Al layers on Co and Nb is evaluated based on chemical state identification. In the case of 1.1 nm Al/40 nm Co, the 7 s plasma oxidation recipe discussed in Chapter 3 results in no metallic Al or oxidized Co peaks within the measurement resolution. While this fulfills the “fully oxidized” criterion, future studies could use the Al and O peak intensities to infer changes in oxide stoichiometry with oxidation time [124]. This would allow for further fine tuning of the oxidation recipe by ensuring the Al/O ratio is close to that of Al₂O₃. For both 1.1 nm Al and 6.1 nm Al on 40 nm Nb, Nb oxide peaks were observed after oxidation. This is likely a result of incomplete Al coverage on Nb. Future efforts to improve the surface coverage of Nb with Al, by changing substrate temperature or Al deposition rate for example, can be tested and iterated *in situ* by using the XPS to look for Nb oxide peaks.

AlO_x tunnel barrier thickness estimates are made using angular-resolved X-ray photoelectron spectroscopy and compared to the WKB estimated thickness using transport data. For the limited sample set available, the correlation and difference in magnitude in AlO_x thicknesses determined for both methods changes depending on the underlying films. This highlights the need for more data from these material systems of interest, both for process development and to study the differences in material properties between the systems.

In the AlO_x/Al on Si cases, the ARXPS determined thicknesses were larger than the WKB determined thicknesses by over a factor of 2. Some difference is expected due to the orthogonal nature of the measurements, with the WKB thickness representing an effective value corresponding to the thinnest parts of the film and

the ARXPS thickness representing the chemical thickness. The correlation between the two methods can be used to infer valuable information on the evolution of the oxide with oxidation time. For example, the significant change in the WKB thickness from 7 s oxidation to 9 s oxidation is accompanied by a nearly constant ARXPS thickness. This could indicate a change in the O/Al ratio of the AlO_x region, where the effective thickness of the potential barrier may change without a significant change in the chemical thickness. Filling out this data set with more oxidation times and high resolution scans of the oxygen peaks, in addition to the Al peaks, could appropriately test the ARXPS-WKB thickness correlation in this way.

Unlike the AlO_x/Al on Si samples, the AlO_x/Al on Nb samples exhibited smaller ARXPS determined AlO_x film thicknesses than their corresponding WKB determined thicknesses. The cause of qualitative differences seen in the waterfall plots is unclear, as the Al oxide and Al metal peaks should have the same sensitivity factors and almost identical IMFP values in both cases. As discussed above, this also presents an opportunity to use additional metrics like the O peak intensities to investigate the differences in film properties between these material stacks.

In the case of AlO_x on Co, the ARXPS determined thickness appears to have a higher emission cutoff angle when performing the Hill equation fit. Using this smaller emission cutoff angle, the ARXPS determined thickness of ≈ 2.8 nm is greater than the WKB thickness by over a factor of 2 as in the AlO_x/Al case. Using one of the published correction methods or a more complicated version of the Hill equation can help account for the difference in inelastic mean free path between Al and Co. By comparing peak intensity when using identical measurement parameters (e.g., pass

energy and power), the relative sensitivity factors can be calibrated by taking high resolution XPS measurements of the peaks of interest (e.g., Al 2p and Co 3p) on bulk samples of each element.

Chapter 5: Tunneling Spectroscopy of Nb-Al Based NIS Junctions

5.1 Context

Often used in conjunction with the AlO_x barriers, Nb and Al are workhorse materials for superconducting quantum information and superconducting electronics. The focus of this chapter is the evolution of the superconducting state in Nb/Al bilayers as a function of Al thickness. Combining Nb/Al with our plasma oxidized AlO_x tunnel barriers enables tunneling spectroscopy of this technologically critical material system and informs future endeavors of device integration within our research group. The spatially dependent quasiparticle density of states (DOS) in the bilayer and the evolution of the DOS with Al thickness is inferred from the conductance spectra of normal metal-insulator-superconductor (NIS) tunnel junctions. The chapter begins with by describing device fabrication, followed by characterization of the tunnel junction and superconducting bilayers. I describe the NIS conductance spectra taken at cryogenic temperatures using characteristic features, including the emergence of a dual-gapped conductance spectra for thick Al. At the end of the chapter, I propose possible mechanisms which could explain the Al thickness dependence of these features.

Nb has the highest elemental superconducting transition temperature ($T_c \approx 9.2$ K)

and superconducting energy gap ($\Delta_0 \approx 1.5$ eV). Therefore, Nb can tolerate relatively high temperatures, regularly utilized at liquid He temperatures, and magnetic fields compared to other popular superconductors like Al, which expands the operating range of superconducting devices [129]. However, Nb is limited by oxides which typically exhibit high leakage currents or dielectric loss [130, 131, 132]. The niobium-oxide phase diagram has a relatively broad variety of stable and meta-stable phases, which likewise vary in electrical character from metallic to insulating. On the other hand, Al is limited by a relatively lower T_c (≈ 1.2 K) and Δ_0 (≈ 0.18 eV), but reliably forms oxides that, when sufficiently oxidized, typically exhibit significantly smaller leakage currents and less dielectric loss [129, 130, 131].

Not surprisingly, combining these material systems to get the best of both worlds has been done for decades, mostly in the form of Nb/Al bilayer devices utilizing a relatively thick ($\gtrsim 100$ nm) Nb layer and thin ($\lesssim 10$ nm) Al layer. This is usually intended to retain the characteristics of the Nb in the superconducting layer, as many properties in the multilayer, such as Δ_0 or coherence length (ξ), are governed by the constituent materials and are partially weighted by film thickness [38]. Gurvitch *et al* used sputter deposition to show that thin (~ 1 nm) Al layers wet a Nb surface well, forming a stable interface and enabling a robust proximity effect [133]. Following their procedure, these Nb/ AlO_x /Nb devices became a launching point for much of the early Josephson junction electronics work.

Nb/Al bilayers in the limit of thin Nb with thick Al are relatively less explored. My interest in Nb/Al bilayers originated in expanding the Al beyond just a perturbation of the Nb superconducting state, specifically with regards to Meservey-Tedrow

spin polarization measurements. In such a measurement, a superconducting electrode is used to analyze the spin polarization of a tunneling current under a parallel magnetic field [51]. Nb/Al bilayers with thick Al were intended to reduce spin-orbit coupling experienced by tunneling electrons, which results in scattering between spin states, but take advantage of the higher T_c of Nb to enable 4 K measurements. This evolved over time to studying the overall evolution in the DOS with Al thickness.

While the Nb/Al bilayer single-particle DOS has been calculated as a function of thickness in the literature, little experimental work has been found which fully captures this evolution in electronic structure. At the limits of bulk-like Nb or bulk-like Al, the DOS is expected to be described by the Bardeen-Cooper-Schrieffer (BCS) theory. As the influence of the Al superconducting state grows beyond a perturbation of the Nb superconducting state, the bilayer DOS is expected to deviate from BCS-like behavior reflecting states from both materials. By observing the DOS as it transitions from primarily Nb-like to primarily Al-like, insight is gained on the interplay of states in both materials.

5.2 Experiment

5.2.1 Fabrication

In order to study the evolution of the Nb/Al bilayer superconducting state as a function of Al thickness, a series of Nb/Al-based normal metal-insulator-superconductor (NIS) tunnel junctions were fabricated with each having a different Al thickness. The layer structure, depicted in Fig. 5.1(a), is as follows: [45 nm Nb

(mask 1) / 5-310 nm Al (mask 1) / 1.3 nm Al (no mask) + plasma oxidation (7 s, 160 mTorr, 55-60 W) / 5 nm Au (mask 2) / 40 nm Cu (mask 2) / 10 nm Au (mask 2)].

As with previous devices discussed, e-beam deposition was used for metals deposition at a deposition rate of ≈ 0.02 nm/s for Al and ≈ 0.05 nm/s for Nb, Cu, and Au. Generation II masks were used in the fabrication of these devices as seen in Fig. 2.7, resulting in junctions with an area of 3500-5000 μm^2 as seen in Fig. 5.1(b). The liquid nitrogen shroud in the deposition chamber was kept at $< 155^\circ$ C in order to reduce chamber pressure during metals deposition. This is especially important during Nb deposition, as Nb is a very reactive getter material and oxygen poisoning can significantly reduce the Nb superconducting critical temperature (T_c) [134]. Nb and Al has several equilibrium alloy phases at room temperature [135]. However, the formation of any significant amount of Nb-Al alloy is not expected. The Nb-Al interface in bilayers has been found to be stable at room temperature, typically requiring annealing treatments in excess of 700° C for alloy formation to occur [133, 136, 137].

Film thicknesses for all devices was determined from quartz crystal microbalance (QCM) readings during fabrication. Cross sectional scanning electron microscopy (SEM) was performed on 4 proxy devices to, in part, provide an additional measurement of film thickness. The Al thickness determined by SEM was found to be lower than the thickness indicated by QCM by a factor of 0.78 ± 0.02 . This value represents the slope of a linear fit when plotting the SEM thickness against the QCM thickness for the 4 devices measured, shown in Fig. B.3. The Al thicknesses described from here out represent the QCM determined thickness (nominally

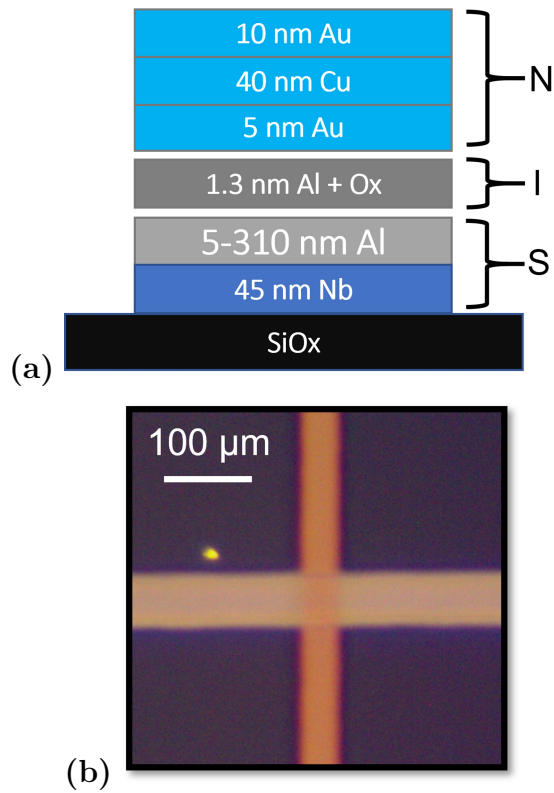


Figure 5.1: (a) Cross section cartoon depicting the NIS tunnel junction layer structure where the wires overlap. The “N” and “S” labels are applicable once the Nb/Al bilayer is cooled below T_c . (b) Optical microscope image of an NIS crossed wire tunnel junction found on an “A” type die. Depending on Al thickness and device location, the junction area is typically $3500\text{-}5000 \mu\text{m}^2$. The vertical wire is Au/Cu/Au and the horizontal wire is Nb/Al/ AlO_x .

5-400 nm Al) multiplied by a factor of 0.78. As seen in Fig. B.1, the Al thickness varies by approximately ± 10 nm over a lateral distance of $\approx 1 \mu\text{m}$. The estimated uncertainty in the Al thickness (± 11 nm), indicated by error bars in Al thickness dependent plots throughout this chapter, is taken as the quadrature sum of this variation (10 nm) and the estimated uncertainty in the thickness measurement from the cross sectional SEM images (≈ 5 nm).

The Nb/Al bilayer conductance per square S_{sq} was tracked, in part, to ensure that the Al thickness and S_{sq} were linearly correlated as seen in Fig. 5.2. As discussed in Chapter 2, S_{sq} (or R_{sq}) is the conductance of the bilayer wire divided by the number of squares (length/width). We observe such linear correlation starting at ≈ 10 -15 nm Al, suggesting partial coverage of the Nb by Al for smaller thicknesses. The uncertainty in the specific conductance is dominated by uncertainty in the wire width, calculated using dual error functions as discussed in Chapter 3. A room temperature Al resistivity of $(5.8 \pm 0.7) \times 10^{-8} \Omega\cdot\text{m}$ is extracted from a linear fit to the data, consistent with thin film Al resistivity values seen in literature [39, 138]. The uncertainty given is dominated by the uncertainty in the wire dimensions followed by the standard error of the fit in Fig. 5.2.

5.2.2 Device Characterization

5.2.2.1 Room Temperature

The room temperature resistance·area (R·A) products of the devices analyzed for this experiment are displayed in Fig. 5.3(a). Starting at $\approx 5 \times 10^5 \Omega\cdot\mu\text{m}^2$ for the

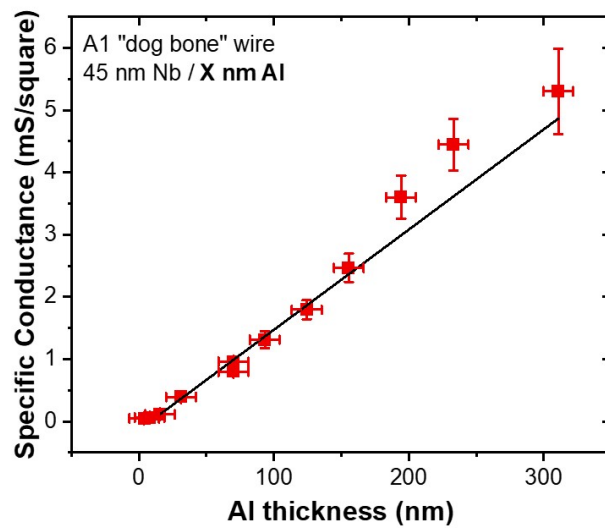
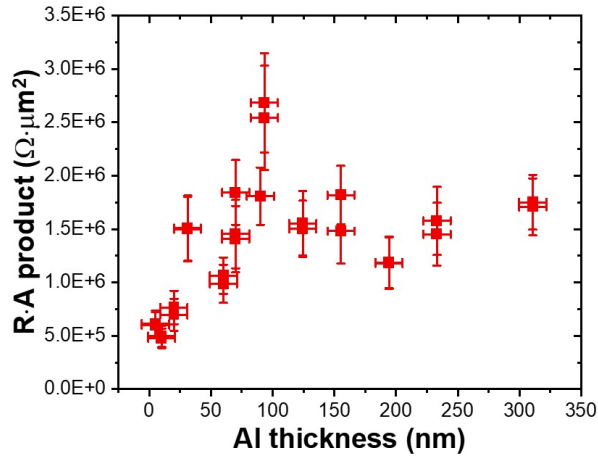


Figure 5.2: Conductance per square of the Nb/Al bilayer as a function of Al thickness. The Nb thickness is ≈ 45 nm for each wire. In order to mitigate systematic variation, the data reflect the conductance per square of the A1 device “dog bone” wire located in the same relative position of each wafer.

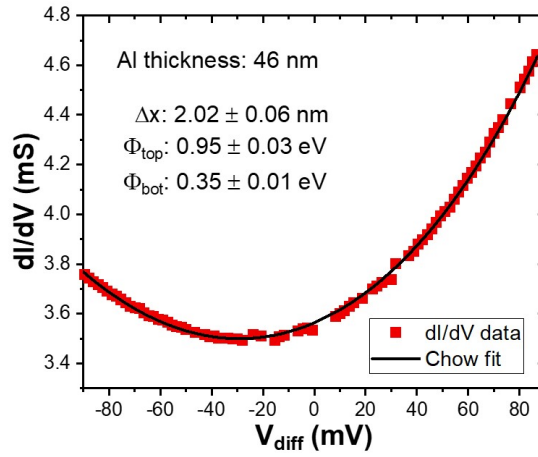
thinnest Al samples, the R·A products are relatively constant around $\approx 1.5 \times 10^6 \Omega \cdot \mu\text{m}^2$ for devices with $\gtrsim 30$ nm Al. As discussed in Chapter 3, the uncertainty in the R·A products is dominated by the uncertainty in the junction areas.

The negative resistance artifact correction is not applied to these samples, as the relatively high $R_{\text{dev}}/R_{\text{sq}}$ ratio (> 15) realized for these devices renders the correction negligible ($\lesssim 1$ % relative error) [64]. Example $dI/dV(V)$ data accompanied by a WKB fit, which is qualitatively representative of each of the devices measured, is shown in Fig. 5.3(b). The 2 nm barrier width is similar to the unconfined devices discussed in Chapter 3, which makes sense given the lack of Co oxidation stop and nominally identical oxidation procedures. However, the extracted barrier height fit values are quite asymmetric as indicated by the horizontal shift in the parabolic $dI/dV(V)$ curve. The disparity in barrier heights is likely a result of both 1) the difference in work function between the bottom Al electrode and top Au electrode, and 2) possible asymmetry in the oxygen profile in the barrier. Reference values of bulk Au and Al work functions are 5.1-5.5 eV and 4.0-4.3 eV, respectively [93]. The tunnel barrier height is, to first order, the difference between the metal electrode work function and the electron affinity of the insulator [69, 139]. Nb/Al/ AlO_x barrier heights are quite varied in literature from 0.17 eV up to > 2 eV [65, 140, 141]. The relatively low ≈ 0.35 eV Nb/Al/ AlO_x barrier height extracted here may suggest under-oxidation (e.g., low O-Al coordination) or defects in the barrier, both of which can manifest as a lower barrier height due to localized states in the barrier or at the Al/ AlO_x interface [142, 143].

The evolution of the WKB fit parameters with Al thickness is shown in Fig.



(a)

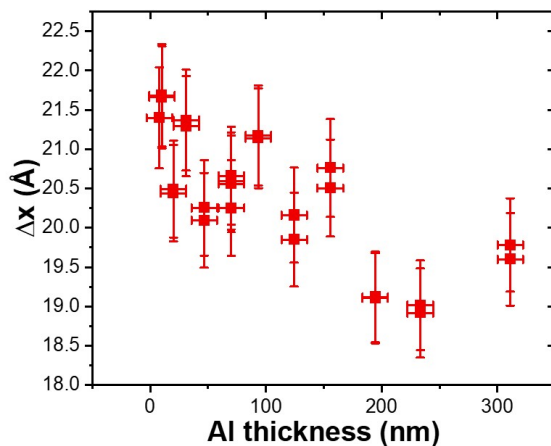


(b)

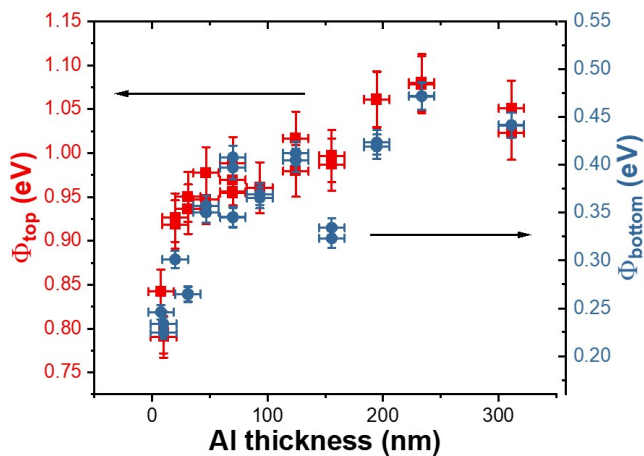
Figure 5.3: (a) Room temperature R·A products of the tunnel junctions for devices analyzed for this experiment are displayed as a function of Al thickness. (b) $dI/dV(V)$ data (filled squares) for the 46 nm Al sample and the corresponding WKB-Chow fit (unfilled squares) show excellent agreement. The horizontal shift in the parabola minimum is reflected in the extracted asymmetric barrier heights.

5.4(a-b). Extracted barrier parameters shown represent two devices of nominally identical Al thickness from the same die, each with $\approx 3\%$ uncertainty as discussed in Chapter 3. The barrier width fit values in Fig. 5.4(a) are almost constant within uncertainties, with a slight downward trend in barrier width with Al thickness. However, the top and bottom barrier heights appear to be asymptotically approaching ≈ 1 eV and ≈ 0.4 eV, respectively. The Al/ AlO_x barrier height of ≈ 0.4 eV is also consistent with the barrier heights of the unconfined devices discussed in Chapter 3.

The trend seen in the barrier heights with Al thickness is similar to the trend seen in the root-mean-square (RMS) surface roughness of the Nb/Al/ AlO_x layer as measured by atomic force microscopy (AFM). AFM measurements were performed by Pradeep Namboodiri at NIST - Gaithersburg. Shown as red squares in Fig. 5.5, the RMS roughness reaches a saturation point of ≈ 4 nm once the Al thickness is above ≈ 10 nm. Each AFM scan was $5 \times 5 \mu\text{m}^2$ and the uncertainty shown represents the standard deviation of roughness values measured in three separate locations. It is unclear why the AFM determined roughness is small compared to the Al thickness variation observed by cross section scanning electron microscopy (≈ 10 - 15 nm), shown in Appendix A. These images shown columnar grain growth that appear slightly rounded at the top. The nearly constant Nb/Al wire conductance per square below ≈ 15 nm suggests incomplete coverage of the Nb with Al. Above ≈ 15 nm of Al, the roughness would then be reflective of the columnar Al film once the Al islands become large enough to form a continuous film and completely cover the Nb. Al thickness near 10 nm is consistent with some literature values of



(a)



(b)

Figure 5.4: Extracted WKB fit parameters for (a) tunnel barrier width, (b) top (AlO_x/Au) and bottom (Al/AlO_x) barrier heights, Φ_{top} and Φ_{bottom} . The top barrier heights are red squares and the bottom barrier heights are blue circles. Fit parameters for two devices at each thickness value are shown with $\approx 3\%$ relative uncertainty.

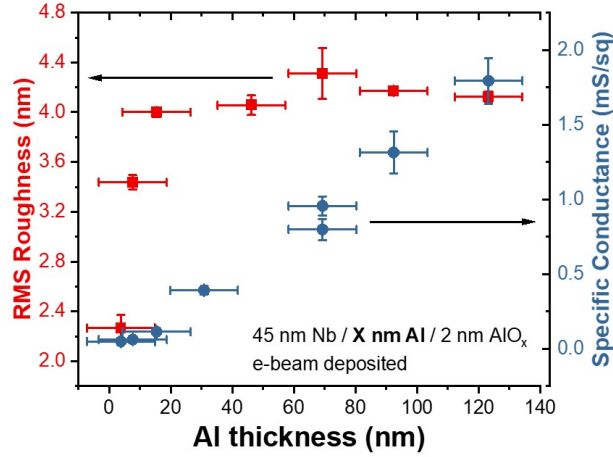


Figure 5.5: Nb/Al/ AlO_x RMS roughness (red squares, left axis) and specific conductance (blue circles, right axis) as a function of Al thickness. The RMS roughness is determined by $5 \times 5 \mu\text{m}^2$ AFM scans. The specific conductance values represent measurements of the Al die “dog bone” wire from each wafer.

Al thickness needed for complete coverage of a Nb film surface [144]. Therefore, the evolution in the barrier heights may be related to patches of Nb/ NbO_x /Au, as NbO_x tunnel barrier potential heights have shown to be lower than AlO_x barriers [145].

5.2.2.2 Cryogenic

As discussed in Chapter 2, the Nb/Al residual resistivity ratio $\rho_{300\text{ K}}/\rho_{10\text{ K}}$ (RRR), shown in Fig. 5.6, can serve as a metric for material quality and character. For example, the nearly constant RRR for Al thickness $\lesssim 15$ nm is consistent with the nearly constant specific conductance in the same thickness range in Fig. 5.5, indicating the conductance is dominated by the Nb in this regime. The ≈ 1.8 RRR

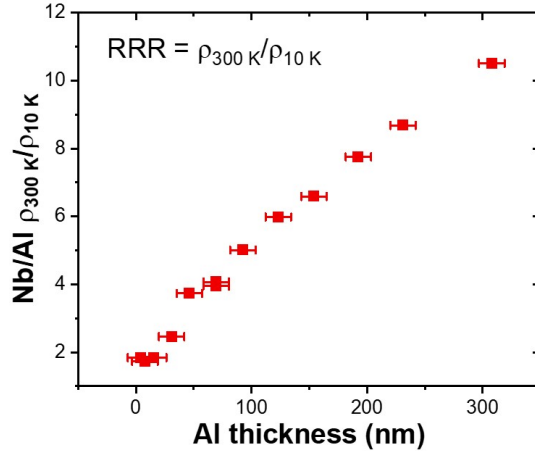


Figure 5.6: Residual resistivity ratio (RRR) as a function of Al thickness in the Nb/Al bilayer.

is typical for polycrystalline Nb with an electron mean free path of ~ 5 nm [39]. The RRR grows with Al thickness above 15 nm, indicating that the electron mean free path of the Al for the thicknesses measured is, in part, limited by size effects such as surface scattering.

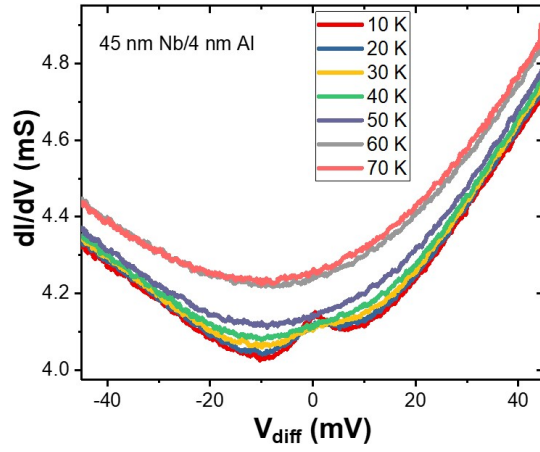
I-V characteristics recorded at several different temperatures during cooldown reveal qualitative changes of the conductance spectra for $T > T_c$. Shown in Fig. 5.7(a), the overall conductance remains roughly parabolic, but a zero-bias conductance peak emerges at $T \approx 30$ K for the 4 nm Al device. This feature is observed for devices with Al thicknesses of 15 nm and below, with the relative amplitude of the peak increasing as Al thickness is decreased. Similar features have been observed in Nb-oxide tunnel junctions and are typically attributed to resonant tunneling mediated by Al impurities in Nb₂O₅ [145, 146]. For devices with thicker Al,

the conductance spectra minimum shifts towards 0 V and becomes cusp-like as seen in Fig. 5.7(b). The overall shape of the conductance spectra changes from roughly parabolic at higher temperatures to roughly linear with bias magnitude at lower temperatures. Both the cusp at 0 V for low temperatures and the approximately linear conductance with bias magnitude have been attributed to inelastic tunneling, mediated by localized states in the barrier. [147, 148].

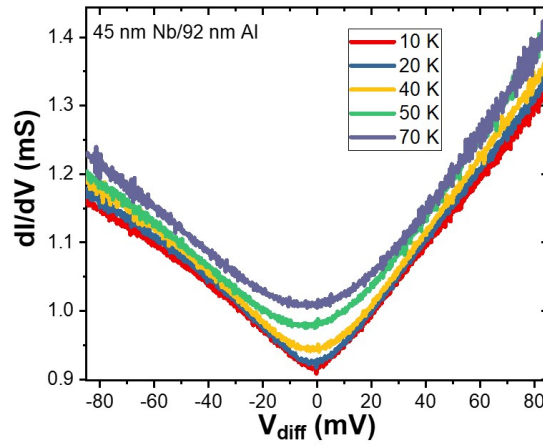
The Nb/Al T_c is determined by measuring the Nb/Al bilayer superconducting critical current (I_c) at subsequent temperature steps until no superconducting current is observed. An example is given in Fig. 5.8(a) for the 45 nm Nb / 31 nm Al bilayer. Each current sweep for $T < 6.8$ K in Fig. 5.8(a) shows a region of increasing current without a corresponding increase in voltage drop across the wire. T_c as a function of Al thickness is shown in Fig. 5.8(b). In general, the T_c decreases with film Al thickness up to 125 nm Al. The uncertainty displayed in Fig. 5.8(a) corresponds to the temperature step size between I_c sweeps and fluctuations seen in the thermometer when set to a constant temperature.

For I_c measurements of thicker Al devices as seen in Fig. 5.9(a), the I_c transitions typically display multiple regions. An initial gradual increase in resistance is followed by a nearly ohmic region (i.e., linear I-V), which then gradually increases in resistance until the wire is completely in the normal state. While most of the thin Al wires have a region of gradual resistance increase prior to fully ohmic behavior, this region dominates the I_c transition in the significantly less resistive thick Al wires.

T_c for several Nb/Al bilayers was determined by measuring the bilayer resistance as a function of temperature in the closed cycle cryo-cooler, as seen in Fig.



(a)

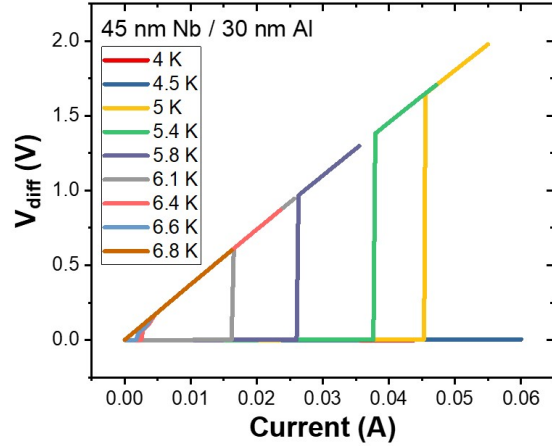


(b)

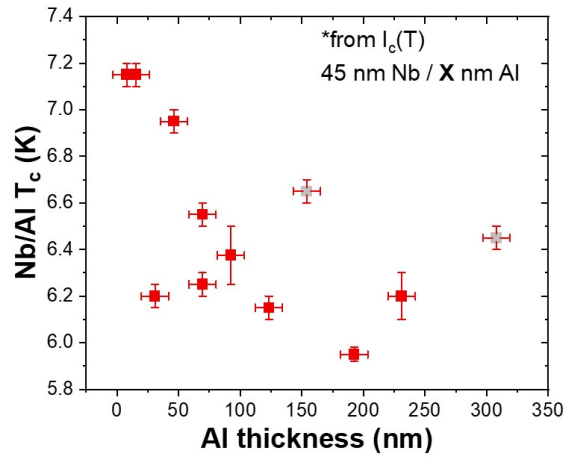
Figure 5.7: Conductance spectra at several different temperatures for (a) a 4 nm Al device and (b) a 92 nm Al device.

5.9(b). The transition in several bilayers exhibits knee features, indicating inhomogeneity in the superconducting state of the bilayer. While this was also indicated by the stretched I_c transitions for thick Al, it is difficult to reconcile the two effects as the knee features in $R(T)$ occur at $\approx 0.6-0.8$ of the full normal state resistance, whereas the difference in resistance between the regions discussed above in the I_c transitions is regularly $< 10\%$. The width of the knee features (temperature) or height (resistance) relative to the full normal state resistance both vary but are not correlated with Al thickness. In order to compare devices, the T_c values extracted from these measurements correspond to the maximum $R(T)$ point of the highest temperature transition. Devices from the same wafer or die may exhibit different knee features, but T_c determined in this way is typically consistent across devices. Most importantly, the conductance spectra for devices on the same die show nearly identical NIS conductance spectra even in the case of qualitatively different knee features, thus indicating the $R(T)$ structure observed may not be relevant to the tunnel junction behavior. For cases in which T_c was determined by both $R(T)$ and $I_c(T)$, which includes Al thickness 4-113 nm, results show nearly identical trends with Al thickness with a 0.3-0.4 K offset.

By extrapolating from the Nb/Al samples with 4 nm and 8 nm Al, I estimate the Nb film T_c to be ≈ 7.2 K. These samples showed a constant T_c so it was assumed that the amount of Al in this thickness range did not significantly alter the Nb T_c . The T_c of 7.2 K is depressed relative to the bulk Nb T_c of 9.3 K. T_c of Nb films have been shown to have a universal scaling with residual resistivity ($\rho_{10\text{ K}}$) [149]. The $\rho_{10\text{ K}}$ of the Nb film $\approx 26\ \mu\Omega\cdot\text{cm}$, using the Nb/Al wire resistance for the 4 nm Al

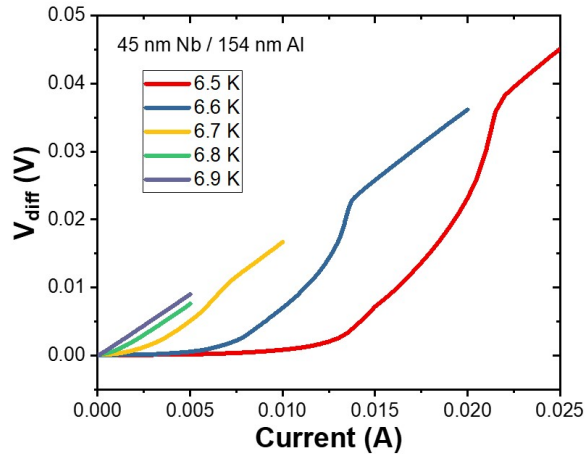


(a)

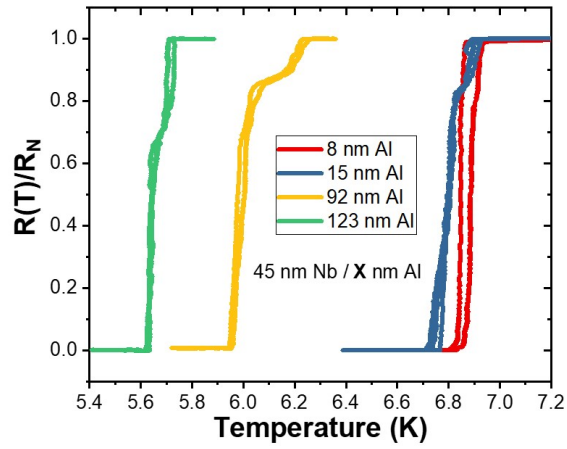


(b)

Figure 5.8: (a) Current bias sweeps starting from 0 A at subsequent temperature steps. Regions of increasing current which show no change in V_{diff} indicate a superconducting current. (b) Superconducting transition temperature (T_c) of the Nb/Al bilayers as a function of Al thickness. Discussing in Appendix A, the 154 nm and 308 nm Al devices (grey) have a relatively high T_c . This is likely a result of thicker Nb.



(a)



(b)

Figure 5.9: (a) Stretched I_c transition of a 154 nm Al sample, which is typical for thicker Al devices. (b) Nb/Al bilayer resistance as a function of temperature for several Al thicknesses. Multiple traces are shown for each device corresponding to subsequent temperature ramps through the transition region.

sample, is consistent with $T_c \approx 7$ K [149, 150]. Several factors have been found to decrease T_c in Nb thin films. For film thickness $\lesssim 50$ nm, the non-superconducting substrate can destroy the superconductivity in a portion of the film through the proximity effect [149]. Nb T_c depression from inclusion of oxygen and hydrogen impurities is well documented, and has been attributed to a decrease in electron-phonon coupling and the electronic density of states at the Fermi energy [134, 150]. I deposited Nb test films which exhibited increasing T_c and RRR as deposition rate was increased. As a faster deposition rate would allow for fewer residual gas impurities to be incorporated in the film, this indicates that the inclusion of such impurities is likely a contributing factor in our T_c depression relative to Nb thin films in the literature [151].

5.2.3 NIS Tunneling

As mentioned previously, the DOS of the superconducting bilayers is inferred from tunnel junction conductance measurements at $T < T_c$. To understand this, we first consider the case of metal 1 biased by V relative to metal 2 in a normal metal-insulator-normal metal tunnel junction. The resulting net current is given by Eq. 5.1,

$$I_{\text{NN}}(V) \propto N_1 N_2 \int_{-\infty}^{\infty} [f(E - eV) - f(E)] dE \quad (5.1)$$

where N_i is the density of states of the electrodes and $f(E)$ is the Fermi-Dirac distribution. This formulation assumes the normal state DOS are constant in energy, as they vary slowly with energy around E_F in the free electron approximation, thus

are outside the integral. However, when one of the electrodes is a superconductor, the BCS quasiparticle density of states N_s must be considered. As a reminder from Chapter 1, the BCS DOS is given below in Eq. 5.2.

$$N_S = N_N \left| \operatorname{Re} \left[\frac{E}{\sqrt{E^2 - \Delta_g^2}} \right] \right| \quad (5.2)$$

N_s is substituted for one of the normal metal density of states terms in Eq. 5.1, but must be moved inside the integral due to the strong energy dependence near E_F . This results in the NIS net tunnel current given by Eq. 5.3.

$$I_{\text{NS}}(V) \propto N_N \int_{-\infty}^{\infty} N_S(E) [f(E - eV) - f(E)] dE \quad (5.3)$$

The interesting experimental implication of this formalism emerges when taking the derivative of Eq. 5.3 with respect to V , as seen in Eq. 5.4,

$$\frac{dI}{dV}(V) \propto N_N \int_{-\infty}^{\infty} N_S(E) k(E - eV) dE \quad (5.4)$$

where $k(E - eV)$ is the derivative of the Fermi function with respect to V . As $T \rightarrow 0$ K, $k(E)$ approaches a Dirac delta function at $E = eV$. Therefore at low temperature, the differential conductance of an NIS tunnel junction represents the BCS density of states.

NIS tunnel junctions often show higher sub-gap conductance or broader features than predicted with the ideal BCS density of states. A multitude of sources have been discussed in literature, such as barrier pinholes and defects, Andreev re-

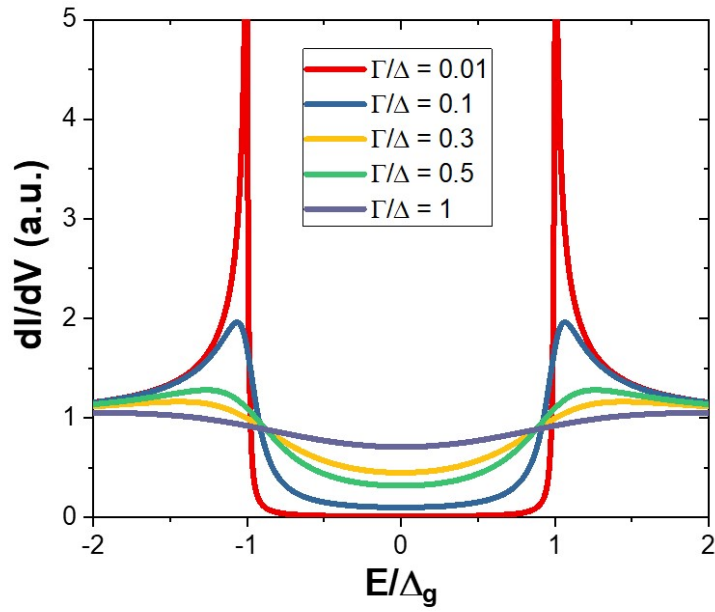
flection, environmentally-assisted tunneling, and quasiparticle lifetime broadening [152, 153, 154, 155, 156]. Several modifications or extensions of the BCS density of states are used to account for such effects. I will describe two formalisms used here and most often in literature: (1) addition of a Dynes broadening parameter (Γ) and (2) Blonder-Tinkham-Klapwijk (BTK) theory.

Broadening by the Dynes parameter is done by inserting an $i\Gamma$ term into the BCS density of states as seen in Eq. 5.5.

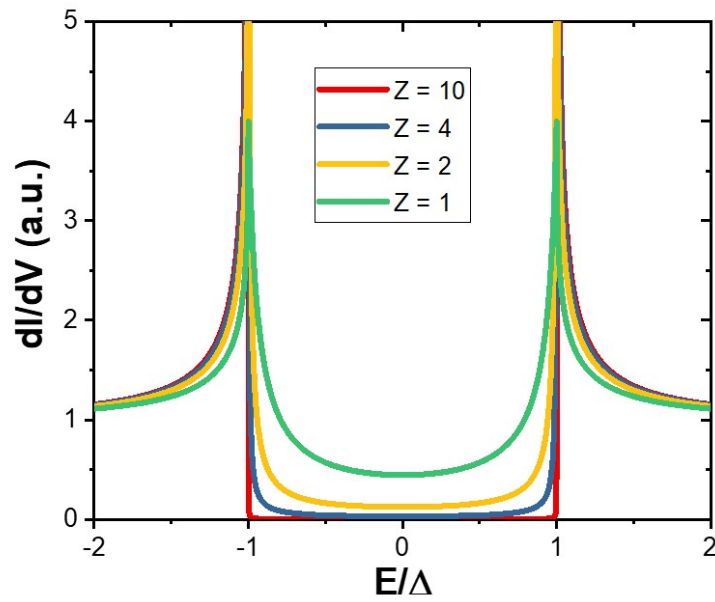
$$\frac{N_S}{N_N} = \left| \operatorname{Re} \left[\frac{E - i\Gamma}{\sqrt{(E - i\Gamma)^2 - \Delta_g^2}} \right] \right| \quad (5.5)$$

While originally formulated to account for the finite lifetime of quasiparticles, Dynes broadening is typically used phenomenologically to account for a range of speculated non-idealities and pair-breaking processes. In this sense, Γ effectively indicates the fraction of quasiparticle density of states in the gap compared to the density in the normal state [157]. Fig. 5.10(a) shows the normalized $dI/dV(V)$ at 0 K for several values of Γ . While the parameter varies throughout the literature, typical values for the Dynes parameter are $\Gamma/\Delta_g \approx 10^{-5}$ - 10^{-4} for Al and $\Gamma/\Delta_g \approx 10^{-2}$ - 10^{-1} for Nb [129, 153, 154, 158].

BTK theory specifically accounts for Andreev reflection between N and S layers [77, 159, 160]. Andreev reflection is a charge transfer process between a superconductor and a normal metal, where an electron incident on an N-S interface results in a retroreflected hole in the N material and a Cooper pair in the S material (i.e., a multiparticle process conserving charge and momentum). When added, the en-



(a)



(b)

Figure 5.10: (a) BCS density of states broadening with the Dynes parameter Γ . (b) BTK density of states for several barrier strength values. High Z values returns the nominal BCS density of states.

ergy of the electron and hole equal the gap energy. While beyond the scope of this overview, the BTK formalism was arrived at by applying the Bogoliubov-de Gennes equations at an N-S interface, which are equations of motion corresponding to the mean-field approximation of BCS theory. In essence, BTK treats the reflection and transmission of carrier wave functions at an N-S interface. The N-S interface is modeled by a repulsive Dirac Delta function potential $V = H\delta(x)$ and parameterized by a “barrier strength” $Z = H/\hbar v_F$. The Z parameter is used to determine the energy dependent transmission coefficient at the interface using the probability of Andreev reflection (A) and the probability of normal reflection (B). Taken from Ref. [77], (A) and (B) are given in Eq. 5.6 and 5.7 as

$$A(E) = \begin{cases} \frac{u_0^2 v_0^2}{\gamma^2} & |E| > \Delta_g \\ \frac{\Delta_g^2}{E^2 + (\Delta_g^2 - E^2)(1 + 2Z^2)^2} & |E| < \Delta_g \end{cases} \quad (5.6)$$

$$B(E) = \begin{cases} \frac{(u_0^2 - v_0^2)^2 Z^2 (1 + Z^2)}{\gamma^2} & |E| > \Delta_g \\ 1 - A & |E| < \Delta_g \end{cases} \quad (5.7)$$

where $u_0^2 = 1 - v_0^2 = \frac{1}{2} \left[1 + \frac{\sqrt{E^2 - \Delta_g^2}}{E} \right]$ and $\gamma = u_0^2 + (u_0^2 - v_0^2)Z^2$. The BCS quasiparticle density of states term in Eq. 5.3 can now be replaced by $[1 + A(E, \Delta_g, Z) - B(E, \Delta_g, Z)]$, resulting in the current equation shown in Eq. 5.8,

$$I_{NS}(V) \propto (1 + Z^2) N_N \int_{-\infty}^{\infty} [1 + A(E) - B(E)] [f(E - eV) - f(E)] dE \quad (5.8)$$

where the normal state transmission is given by $1/(1+Z^2)$. In the limit of high Z , this form returns the standard BCS quasiparticle density of states. In this way, BTK theory can be used to describe conductance through a transparent N-S interface dominated by Andreev reflection ($Z = 0$) up to an opaque NIS junction dominated by single-particle tunneling ($Z \gtrsim 5$). The normalized $dI/dV(V)$ at 0 K is shown in Fig. 5.10(b) for several values of Z .

Fits of the conductance spectra in this chapter utilize BTK theory in addition to Dynes broadening, using the procedure given in Ref.[161]. The adjusted BTK $A(E)$ and $B(E)$ terms are shown in Eq. 5.9 and Eq. 5.10,

$$A(E) = \frac{\sqrt{(\alpha^2 + \eta^2)(\beta^2 + \eta^2)}}{\gamma^2} \quad (5.9)$$

$$B(E) = Z^2 \frac{[(\alpha - \beta)Z - 2\eta]^2 + [2\eta Z + (\alpha - \beta)]^2}{\gamma^2} \quad (5.10)$$

where $u_0^2 = \frac{1}{2} \left[1 + \frac{\sqrt{(E-i\Gamma)^2 - \Delta_g^2}}{E-i\Gamma} \right] = \alpha + i\eta$, $v_0^2 = 1 - \frac{1}{2} \left[1 + \frac{\sqrt{(E-i\Gamma)^2 - \Delta_g^2}}{E-i\Gamma} \right] = \beta - i\eta$, and $\gamma^2 = [\alpha + Z(\alpha - \beta)]^2 + [\eta(2Z^2 + 1)]^2$.

5.2.4 Nb/Al bilayer - quasiparticle density of states

Prior to discussing Nb/Al bilayer conductance data, it is necessary for interpretation to discuss the predicted Nb/Al bilayer density of states. Due to proximity effects discussed in Chapter 1, the electronic structure throughout the bilayer significantly deviates from the uniform BCS case. In the dirty limit, where the mean free path is smaller than the coherence length, superconducting properties of S-S' or S-N

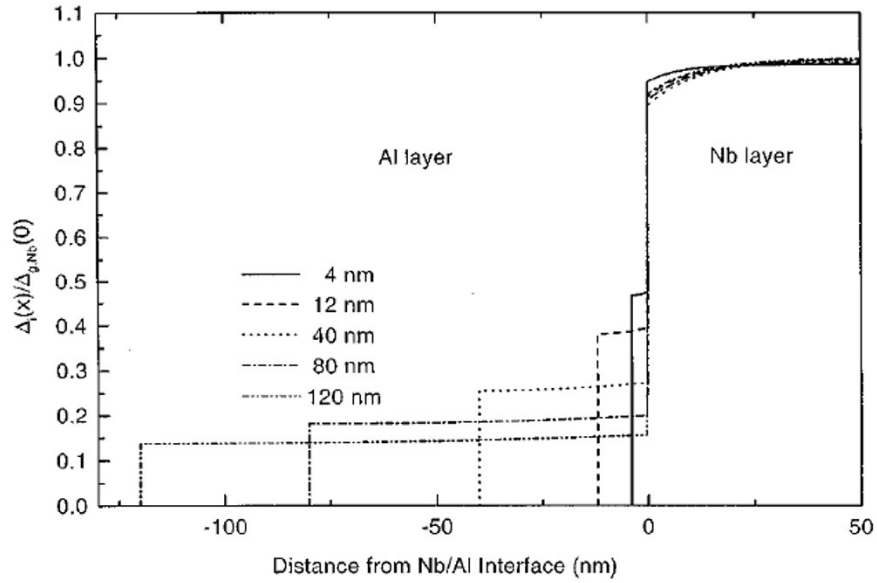
bilayers are typically described using the Usadel equations [38, 39, 162, 163]. These are a set of differential equations that define the spatially dependent quasiparticle density of states (N_s) and order parameter (Δ) throughout a nonuniform superconducting system. In essence, individual film properties (T_c , ξ^*) and the bilayer interface resistance are used to determine boundary conditions for a multilayer, enabling one to quantify the influence exerted on each material via the proximity effect. While the Usadel equations are not used in this thesis, literature examples from bilayer studies can inform expectations concerning the evolution of superconducting properties with thickness.

The calculated thickness dependence of the order parameter and gap of Nb/Al bilayers is shown in Fig.5.11(a-b) [162]. Fig.5.11(a) describes the order parameter of several Nb/Al bilayers at 2.2 K and is taken from Ref.[39]. Given the larger number of carriers and shorter coherence length in the Nb, the order parameter in the Al varies with Al thickness much more than the order parameter in the Nb. The discontinuity in the order parameter from Nb to Al (or any proximitized system) is typically a result of interface resistance, R_b [38, 39]. Interfacial disorder from the lattice mismatch of the body-centered cubic (BCC) Nb and face-centered cubic (FCC) Al (20.4 %) likely contributes to R_b , in addition to any oxide formation at the interface [164]. Fig.5.11(b), recreated from data in Ref.[162], describes the energy gap of several Nb/Al bilayers at 0.3 K. As previously mentioned, the BCS energy gap Δ_g is equivalent to the magnitude of the order parameter Δ in uniform systems. However in nonuniform systems, the energy gap defines the minimum energy for which no quasiparticle excitations are found below, as opposed to the

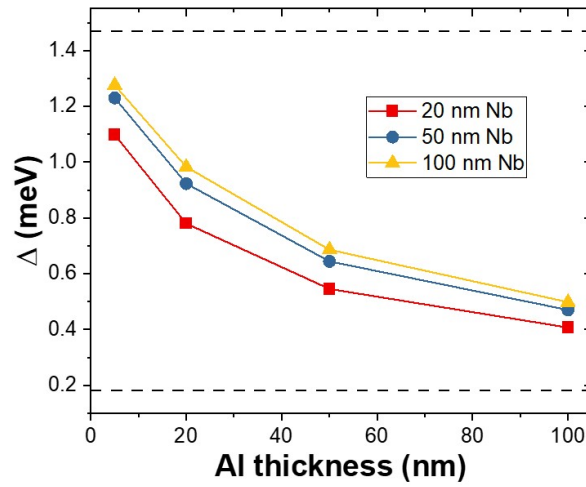
energy of the maximum DOS peaks as in Fig.1.4(a). In thin film bilayers, Δ_g is essentially constant throughout. One can think of the values in Fig.5.11(b) as being proportional to the minimum order parameter values in Fig.5.11(a). In the case of Nb/Al bilayers, this would essentially correspond to the Al order parameter away from the Nb/Al interface. The primary feature to make note of is the decay of the gap towards a bulk-like Al value, which has been shown to change exponentially for thinner Al films (typically less than 100 nm) and changes to a stretched dependence on thickness for thicker Al [39].

The Usadel equations can also be used to calculate the spatially dependent DOS in bilayers. The normalized 0.3 K DOS for a Nb/Al bilayer are calculated in Ref.[162], as shown in Fig.5.12. In the Nb, the energy of the peak in the DOS is proportional to Δ in the Nb, but states are introduced down the Al-like energy gap Δ_g . In simpler terms, the peak DOS in the Nb corresponds to the “Nb-like” gap $\Delta_{g, Nb}$ for a stand-alone Nb film. In the Al, the peak DOS occurs at Δ_g ($\propto \Delta_{Al}$) and has a shoulder feature representing states at the Nb-like gap.

While several studies have investigated the transport characteristics of Nb/Al bilayers, the vast majority are within the context of superconductor-insulator-superconductor (SS'-I-S''S) tunnel junctions, where the transport is complicated by sum-gap and gap-difference features ($\Delta_{g, SS'} \pm \Delta_{g, S''S}$) [39, 162]. In addition, other studies are at temperatures near $T_{c, Al}$, effectively sampling SN layers instead of SS' layers. As I will show later, some conductance spectra features may not be apparent at even at ≈ 1 K. As such, probing the Nb/Al bilayers in an NIS geometry at $T \ll T_{Nb,Al}$ provides valuable perspective to this system.

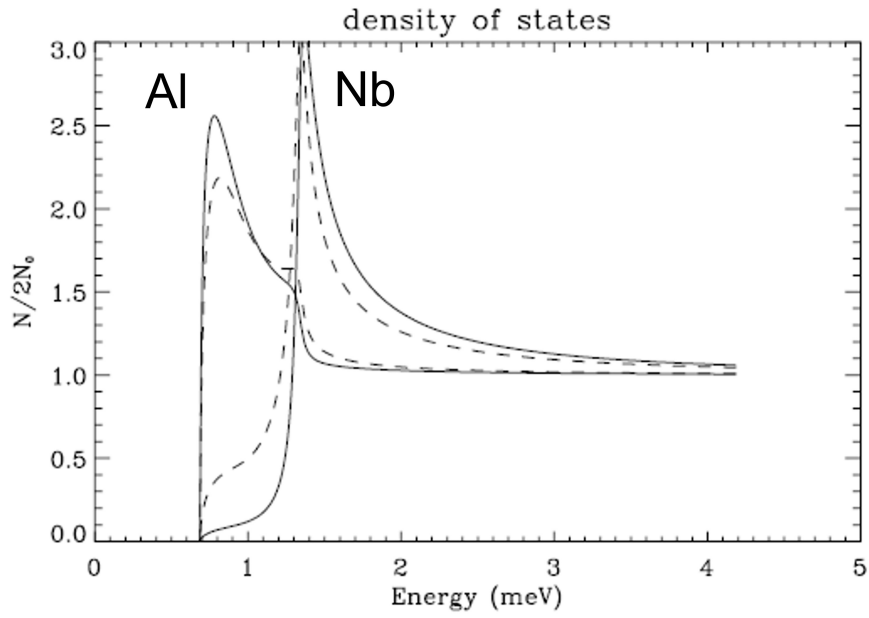


(a)

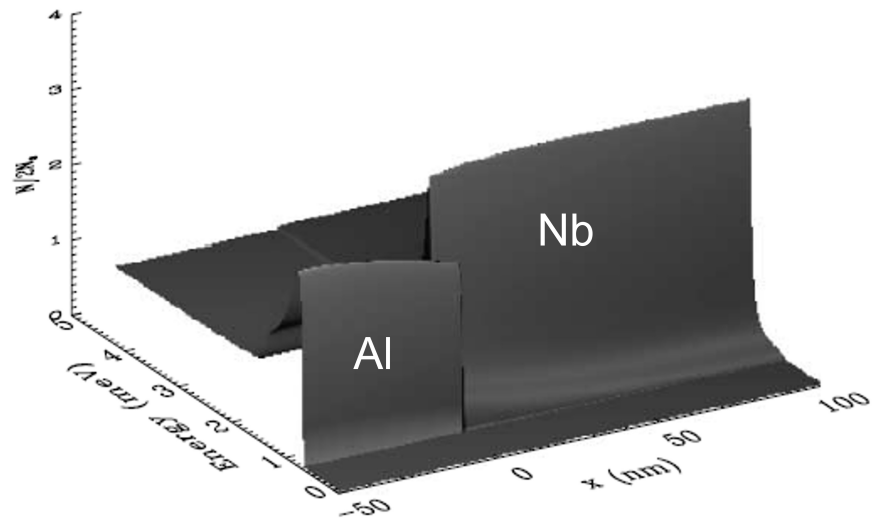


(b)

Figure 5.11: (a) Spatially dependent order parameter calculated for Nb/Al bilayers of several Al thicknesses, reused with permission from Ref.[39] ©(2001) by the American Physical Society. (b) Energy gap as a function of Al thickness calculated for Nb/Al layers of several Nb thicknesses. The gap, defined as the minimum quasi-particle excitation energy in the bilayer, is assumed to be constant throughout the bilayer. The plot in (b) is made from data in Table 2 of Ref. [162] with permission from lead author G. Brammertz.



(a)



(b)

Figure 5.12: Both (a) and (b) show the spatially dependent DOS in a Nb/Al bilayer for 100 nm Nb and 50 nm Al. The solid lines in (a) are line cuts from the free interfaces (-50 nm, 100 nm) in (b) and the dashed lines represent either side of the Nb/Al interface (± 0 nm). Reused from Ref. [162] ©(2001), with permission from Elsevier. The "Al" and "Nb" labels have been added for this thesis.

5.2.5 NIS conductance

5.2.6 Characteristic features

I-V characteristics are measured for each Nb/Al bilayer-based tunnel junction device at the DR base temperature of $T_b \approx 15$ mK and as a function of temperature up to T_c . The NIS conductance spectra, or $dI/dV(V)$, is obtained by taking the numerical derivative of the I-V data. Representative NIS $I(V)$ and corresponding $dI/dV(V)$ data for a 8 nm Al device is shown in Fig. 5.13. The conductance spectrum shown here, as with most displayed for the remainder of the chapter, is normalized by the normal state conductance spectrum measured at $T > T_c$. $dI/dV(V)$ data is collected at $T > T_c$. A background conductance data set is compiled by manually selecting points along the $T > T_c$ conductance spectra and connecting these points with a spline function. This background is then divided out from the lower temperature $dI/dV(V)$ data.

Several characteristic features used in describing the conductance spectra are indicated by the dashed circles in Fig. 5.14(a-b). The arrows surrounding each of the dashed circles indicate the primary “direction” of change in that parameter, discussed further as a function of Al thickness. In the BCS formalism, the symmetric peaks in each conductance spectra correspond to singularities in the superconducting quasiparticle density of states at $\pm\Delta_g$. The peak voltage feature indicated in Fig. 5.14(a) is taken as the Nb-like gap energy, and is expected to be pulled to lower bias with increased Al thickness. The zero-bias conductance (ZBC) is the minimum

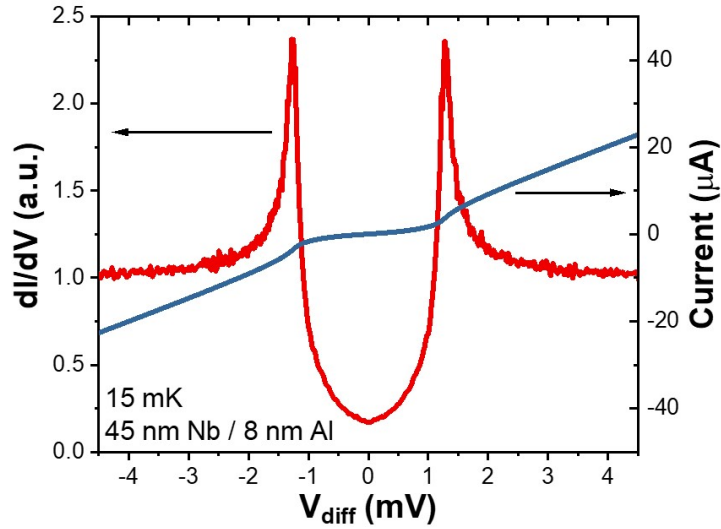
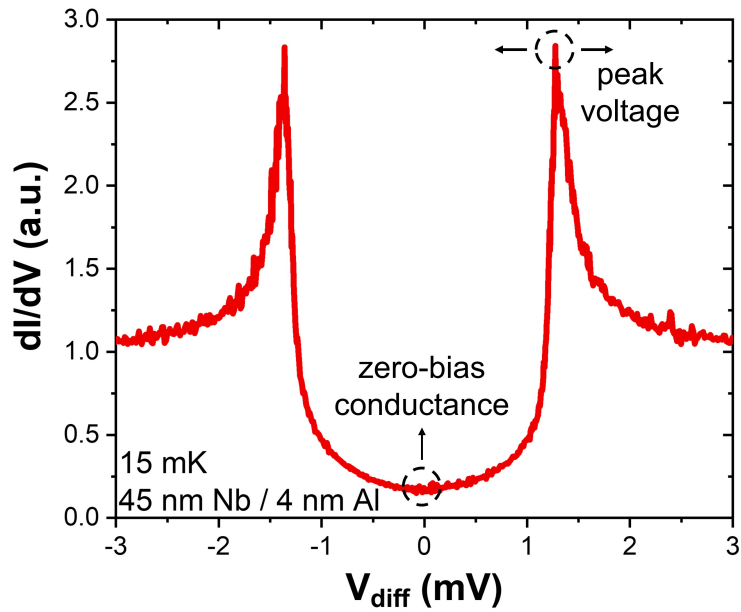


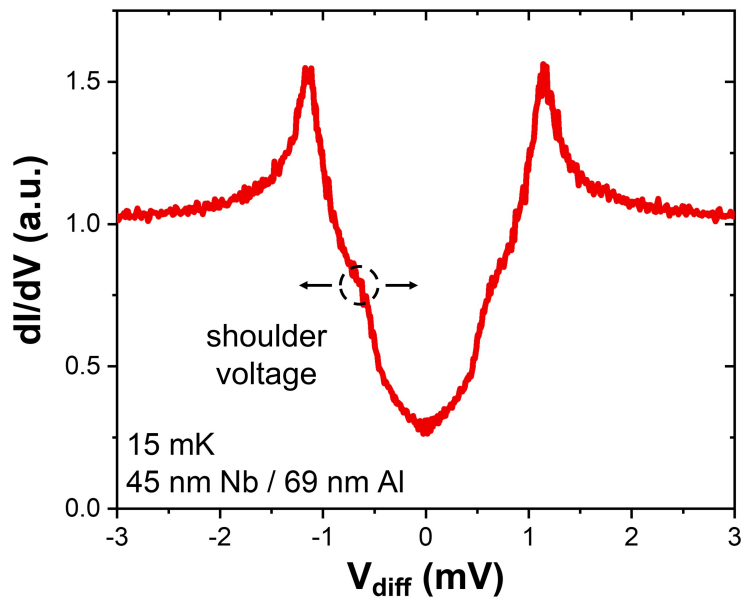
Figure 5.13: Near-gap $I(V)$ (blue line, right axis) and corresponding $dI/dV(V)$ (red line, left axis) of a 8 nm Al device measured at $T_b \approx 15$ mK. The dI/dV data has been normalized by the normal state tunnel junction conductance.

conductance in the gap, where nominally no single-particle states exist. Therefore, the ZBC indicates the contribution from inelastic or higher order processes (i.e., Andreev reflection). As the Al thickness in the Nb/Al bilayer is increased, a sub-gap shoulder feature emerges as a third characteristic feature of interest in the sub-Kelvin conductance spectrum, shown in Fig. 5.14(b). This secondary gap-like feature becomes discernible from the primary DOS peak with increasing Al thickness starting at ≈ 30 nm Al.

Shown in Fig. 5.15(a), the NIS conductance spectra peak heights are extremely sensitive to the effective temperature. The peak heights corresponding to Fig. 5.15(a) are plotted in Fig. 5.15(b) as a function of T_b as measured by a RuOx thermometer in the DR. However, sub-Kelvin electrical measurements of a



(a)



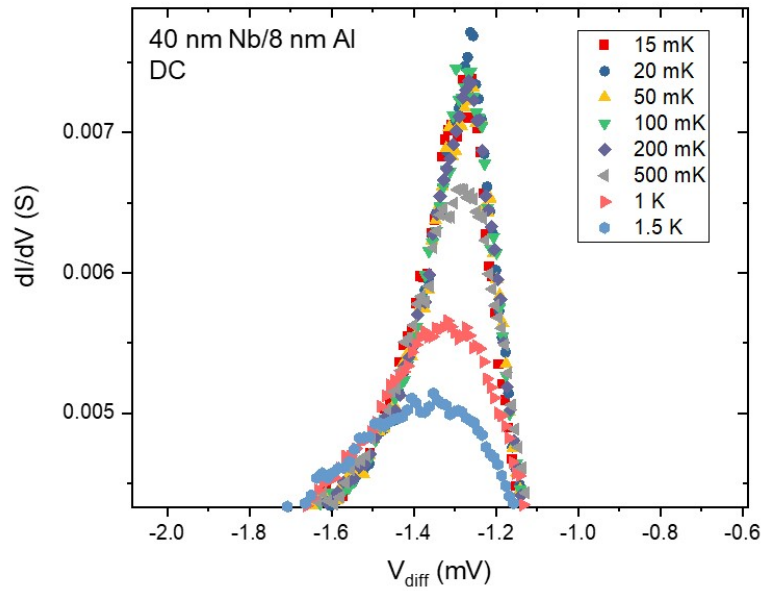
(b)

Figure 5.14: (a) $dI/dV(V)$ of a 4 nm Al sample indicating the peak voltage position and zero-bias conductance features. (b) $dI/dV(V)$ of a 69 nm Al sample indicating the sub-gap shoulder voltage position.

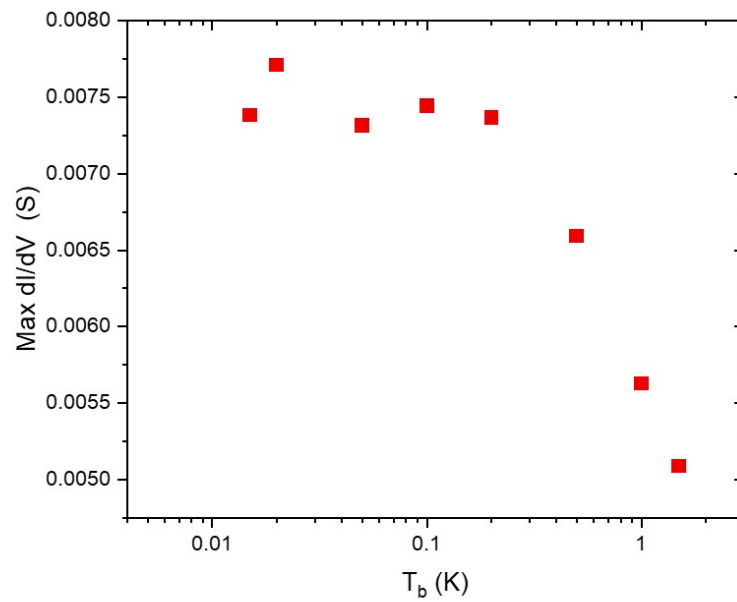
given device are often limited by the effective temperature of the electronic bath, or effective electron temperature (T_e). The lower limits on T_e are typically governed by Johnson-Nyquist noise from higher temperature stages of the cryostat or environmental noise originating from room temperature electronics [165, 166]. Disagreement between T_b and T_e arises at low temperature as the electron-phonon coupling diminishes in the metallic infrastructure of the DR. As T_b is increased from the base value of 15 mK, the knee feature in Fig. 5.15(b) signifies where T_b begins to dominate over the limiting T_e . Therefore, T_e is estimated to be ≈ 200 mK for the base temperature electrical measurements presented here. This estimation is in agreement with previous determinations done for the same system. Concerning the temperature dependence of superconducting properties (Δ , ξ , etc.), this provides reasonable validation to the assumption of $T/T_c \rightarrow 0$ at base temperature $T_b \approx 15$ mK given the maximum T/T_c is $\lesssim 0.05$ [167]. However, an effective temperature of 200 mK is used for the Fermi-Dirac distributions when modeling NIS conductance data.

5.3 Results

The qualitative evolution of the Nb/Al bilayer-based NIS conductance spectra can be seen in Fig. 5.16 for several representative devices. The typical measurement step size in V_{diff} is 20-30 μV . For the thinnest Al device at 45 nm Nb / 4 nm Al, the spectrum displays a single set of symmetric conductance peaks at ± 1.3 mV. As the Al thickness increases, the peak feature decreases in height and bias. In addition,



(a)



(b)

Figure 5.15: (a) NIS conductance peak at the gap edge at multiple temperature steps for a 8 nm Al device. (b) Conductance peak height as a function of bath temperature T_b .

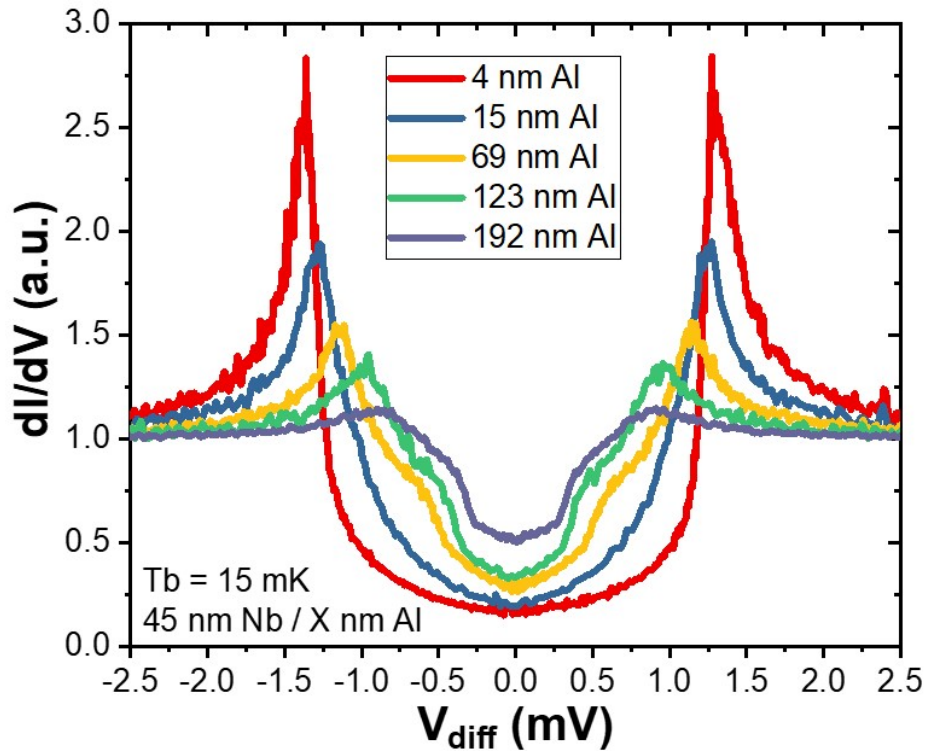


Figure 5.16: Near-gap conductance spectra of Nb/Al bilayer based NIS tunnel junctions for several Al thicknesses. Each spectra is normalized by their respective conductance spectra at $T > T_c$. The measurements were performed at $T_b = 15$ mK.

a sub-gap “shoulder” feature emerges, the position of which also decreases in bias with Al thickness. The characteristic length scales over which these changes occur will provide insight into how this evolution occurs.

5.3.1 Conductance feature trends

The peak feature indicated in Fig. 5.14(a) is taken to reflect $\Delta_{g, \text{Nb}}/e$ of the “Nb-like” superconducting system. The peak voltage position as a function

of Al thickness is shown in Fig. 5.17. The V_{diff} magnitude corresponding to the peak conductance values (ideally symmetric about 0 V) are averaged to negate any measurement offset. The step size in V_{diff} is 20-30 μeV . The uncertainty from the step size is taken as 15 μeV . Variation in the peak positions determined from subsequent measurements is $\approx 15\text{-}30 \mu\text{eV}$. The estimated uncertainty in the peak voltage displayed in Fig. 5.17 is $\pm 25 \mu\text{eV}$ and represents an upper limit on the quadrature sum of these two uncertainties.

As shown in Fig. 5.11(a), the Nb-like order parameter decreases in energy at the Nb/Al interface as a function of Al thickness. The measured peak voltage decreases linearly out to $\approx 235 \text{ nm Al}$. Without an analytical treatment of the system, the expected trend (linear, exponential, etc.) of this feature with Al thickness is unclear. Compared to the trend set by the other devices as a function of Al thickness, the high apparent gap for the 155 nm and 310 nm devices corresponds with relatively high T_c values for those devices. Cross section scanning electron microscopy (SEM) on these samples, discussed in Appendix B, suggest this deviation could be a result of increased Nb thickness.

As the Al thickness is increased to 31 nm Al on 45 nm Nb, the sub-gap shoulder feature is discernible from the primary peak in the conductance spectra. Shown in Fig. 5.18(a), the sub-gap shoulder feature is more easily identified in $d^2I/dV^2(V)$ as indicated by the dashed circle. The voltage position of this feature as a function of Al thickness is shown in Fig. 5.18(b). The uncertainty in the shoulder voltage is the same as the uncertainty in the peak voltage ($\pm 25 \mu\text{eV}$), representing variation in subsequent measurements and measurement step size. The approximately expo-

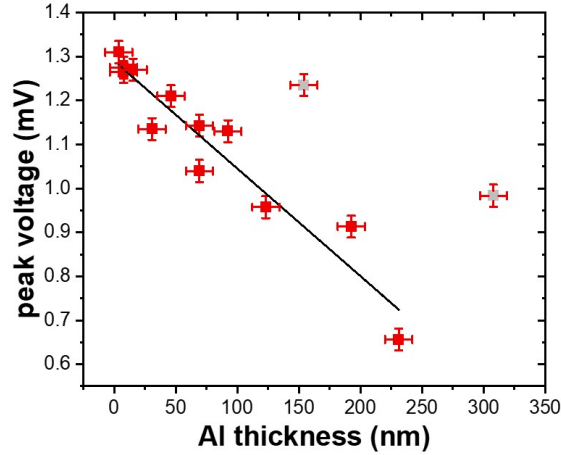


Figure 5.17: The peak voltage as a function of Al thickness at $T_{\text{bath}} = 15$ mK. The linear fit excludes the data points at 154 nm and 308 nm shown in grey, discussed in Appendix.

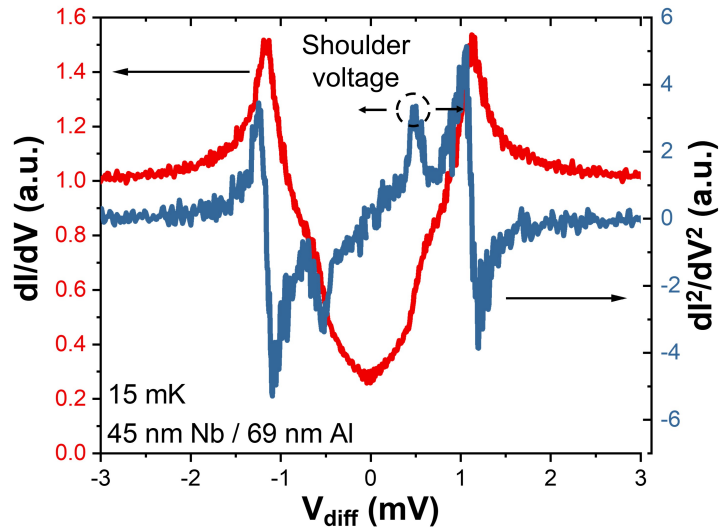
nential dependence of bias position with Al thickness mirrors (both quantitatively and qualitatively) the expected evolution of the bilayer energy gap Δ_g , as shown by the calculated values from Ref. [162] in Fig. 5.11(b).

As a reminder, the bilayer gap energy is proportional to the minimum order parameter throughout the bilayer, which in this case is set by the Al at the Al/ AlO_x interface (i.e., away from the Nb/Al interface). Likewise, Zehnder *et al* study the bilayer energy gap dependence of Nb/Al bilayers as a function of thickness at 2.2 K [39]. Similar to the sub-gap shoulder position seen here, their data show an exponential decay of the energy gap for thinner Al samples, which deviates slightly at thicker Al tending towards the bulk Al energy gap. The similarity to previous experiment and qualitative agreement with literature suggests that the sub-gap shoulder feature represents the Al order parameter, which decreases exponentially with Al

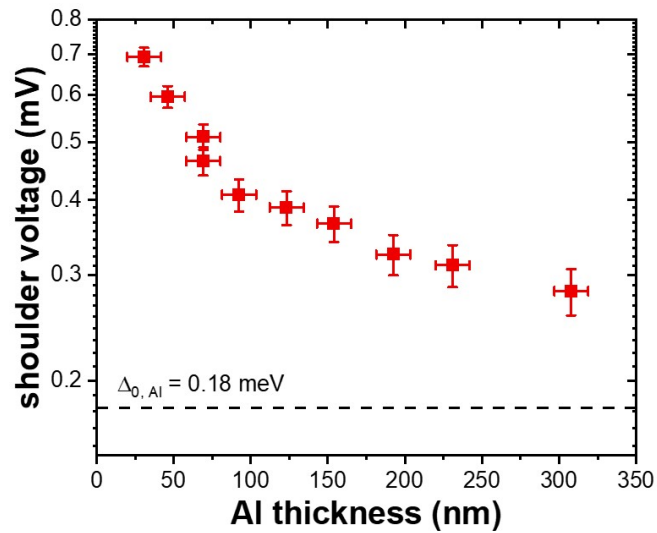
thickness as shown in Fig. 5.11(b). In the case of $T < T_{c, \text{Al}}$, the Al order parameter would eventually decay to the bulk Al order parameter of $\approx 180\text{-}200 \mu\text{eV}$. The 155 nm and 310 nm Al devices, which appear as outliers in the Nb-like peak voltage as a function of Al thickness, do not appear as outliers in the sub-gap shoulder dependence on Al thickness. Assuming the sub-gap shoulder feature corresponds to Δ_g , this is consistent with the relatively weak dependence of Δ_g on the Nb thickness seen in Fig. 5.11(b).

If the sub-gap shoulder represented the proximity enhanced gap in the Al, one may expect the feature size and position to have an effective critical temperature related to that gap energy. Using the BCS relationship $\Delta_0 \approx 1.76k_bT_c$, the observed sub-gap shoulder energies eV_{shoulder} translate to a “ T_c ” ranging from 4.7 K at 31 nm Al to 1.8 K at 308 nm Al. However, the feature corresponding to the sub-gap shoulder in $d^2I/dV^2(V)$ is not resolved above ≈ 1 K regardless of Al thickness, as seen for the 30 nm and 310 nm Al samples shown in Fig. 5.19(a-b). It should be noted that temperature would alter both the native gap of the Al film and the decay length of a proximity enhanced gap away from the Nb/Al interface, thus complicating the temperature dependence [168]. So while this result is not considered to rule out the Al gap as the origin of the sub-gap shoulder, it further demonstrates the departure from a simple BCS-like system.

As both the Nb-like peak voltage and sub-gap shoulder voltage decrease with Al thickness, the zero-bias conductance (ZBC) is observed to generally increase with Al thickness as shown in Fig. 5.20(a). After normalization, the ZBC is taken as the minimum conductance inside the gap. An estimated uncertainty of ± 0.04 in the

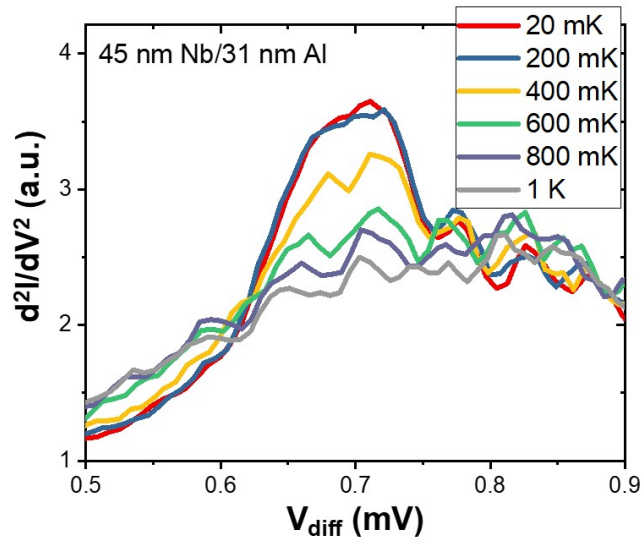


(a)

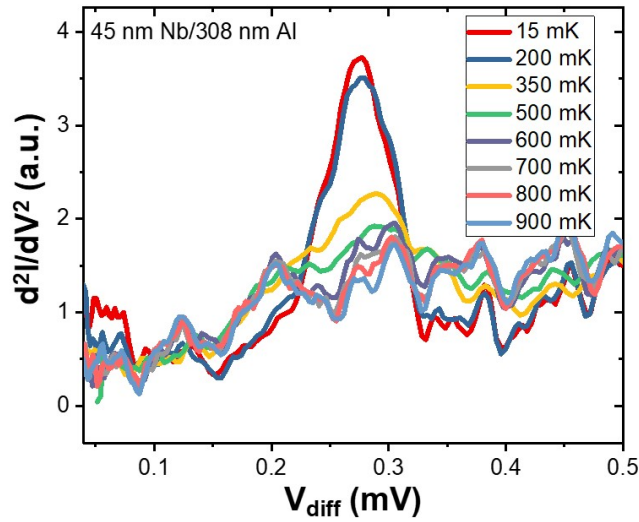


(b)

Figure 5.18: (a) $dI/dV(V)$ and $d^2I/dV^2(V)$ for a 69 nm Al device. The sub-gap shoulder position is indicated by the dashed circle. (b) Sub-gap shoulder voltage as a function of Al thickness.



(a)



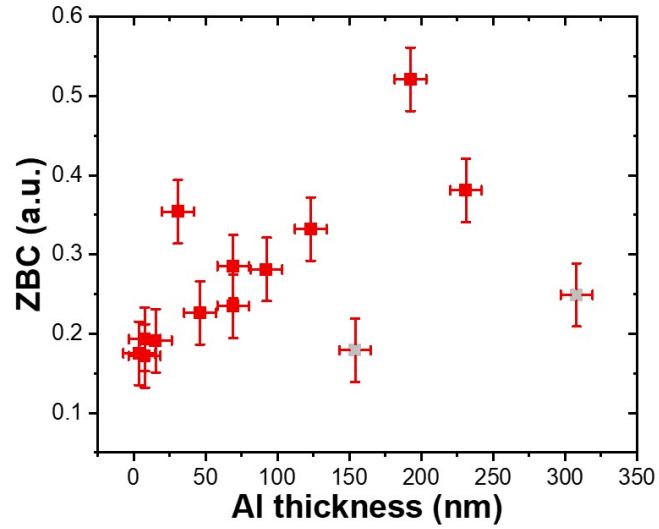
(b)

Figure 5.19: $d^2I/dV^2(V)$ for the (a) 31 nm Al device and (b) 308 nm Al device. Although the Al thickness is significantly different, (i.e., different gap), both features disappear at similar temperatures and do not significantly change their bias position.

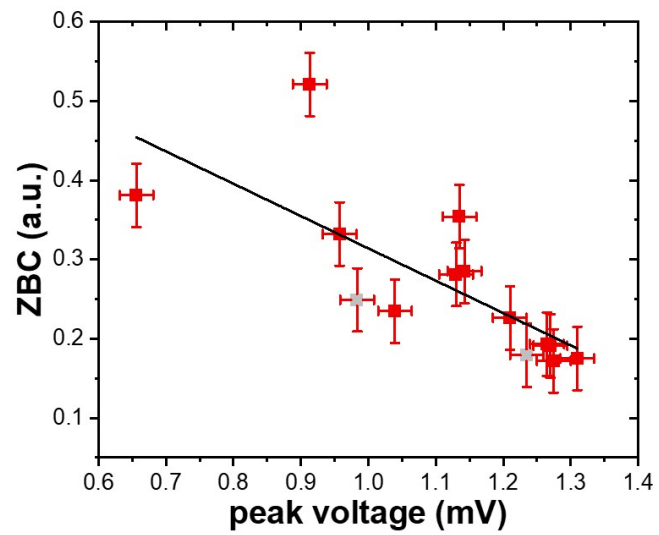
ZBC is shown in the figure. The uncertainty is dominated by variation between subsequent measurements and measurement noise apparent in the conductance trace, taken as the vertical “width” of the $dI/dV(V)$ data well outside the gap in Fig. 5.20(a). Again, the 154 nm and 308 nm devices deviate from this trend and have a relatively low ZBC. With this in mind, the ZBC is plotted against the peak voltage in Fig. 5.20(b) and is found to increase roughly linearly as the peak voltage decreases. This relationship would seem intuitive if Fermi broadening of the density of states was comparable to the effective superconducting gap width, where the 2Δ gap in the conductance spectra is $\approx 0.5\text{-}1.5 \times 10^{-3}$ eV. However as already established, this is not the case with $k_b T_e \approx 1.8 \times 10^{-5}$ eV. Given such negligible thermal smearing, it’s evident that, even in the limit of bulk-like Nb as realized by the thinnest Al device, additional mechanisms (inelastic tunneling, multiparticle processes, etc.) are leading to significant sub-gap conduction.

5.3.2 Temperature dependence

The temperature dependence of the ZBC is shown in Fig. 5.21(a) for several Al thicknesses. The horizontal scale is normalized by T_c as determined by $I_c(T)$. The temperature dependence of the ZBC is consistent with that seen in Ref. [77] with an intermediate barrier strength Z . As temperature and thermal broadening of the density of states decreases, the sub-gap conductance becomes saturated by multiparticle tunneling processes. As the 235 nm Al spectra show in Fig. 5.21(b), the depression in the density of states at 0 V persists above 4 K even for the thickest



(a)



(b)

Figure 5.20: (a) ZBC as a function of Al thickness. (b) ZBC as a function of peak voltage. Both figures correspond to measurements taken at 15 mK.

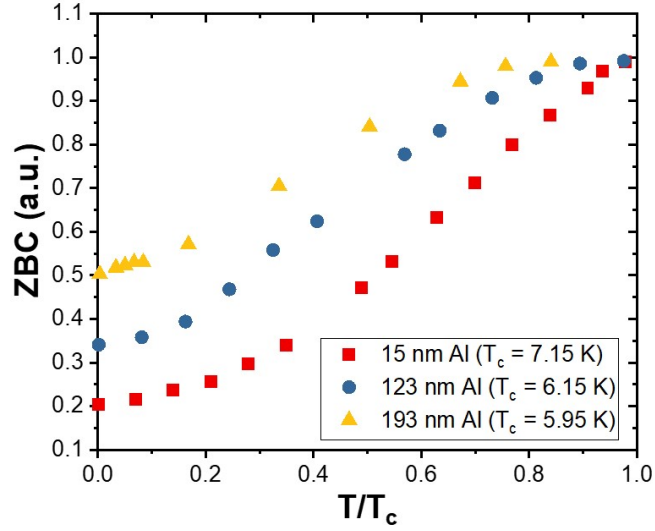
Al films measured. In other words, significant influence of the relatively thin Nb film persists several hundred nm into the Al, where the induced gap does not fully vanish until T is several times that of the bulk Al T_c .

5.4 Discussion

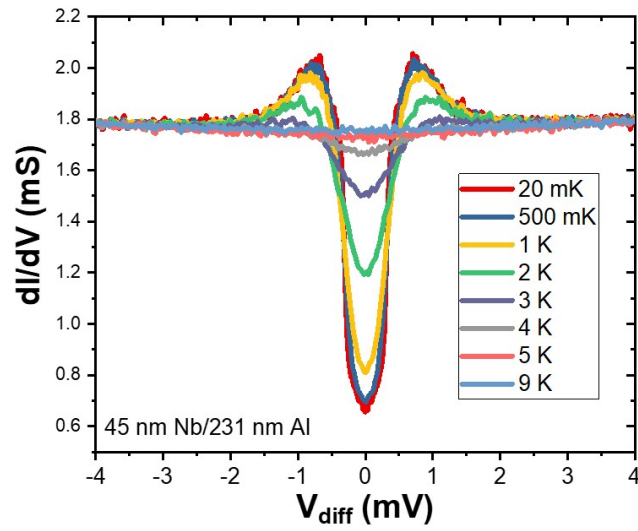
5.4.1 Weighted sum model

In theory, electron tunneling samples the local states in close proximity to the tunnel barrier. Using the calculated Nb/Al density of states in Fig. 5.12, the conductance spectrum for tunneling into the Al side of the bilayer is expected to reflect the modified Al DOS, as seen on the Al line cuts in Fig. 5.12(a). This would be described by conductance (i.e., density of states) maximum at the Al-like gap edge, with a shoulder feature at higher energy corresponding to states at the Nb-like gap edge. However, the opposite is true in the conductance spectra shown here. The sub-gap feature, assumed to represent the quasiparticle states at the Al-like gap, is smaller than the Nb-like peak feature over all thicknesses measured. In other words, a higher density of quasiparticles originating from the Nb-like superconducting system are contributing to tunneling conductance in our devices than those originating from the Al-like state. However, the data clearly shows the contribution of the Al states is increasing with Al thickness.

The cartoon in Fig. 5.22 depicts a scenario which, to first order, could result in the conductance spectra measured here. The right side depicts (coarsely) the spatially varying order parameter of the superconducting Nb/Al bilayer, representing



(a)



(b)

Figure 5.21: (a) ZBC as a function of T/T_c for several Al thicknesses. (b) Temperature dependent NIS spectra of a 235 nm Al device.

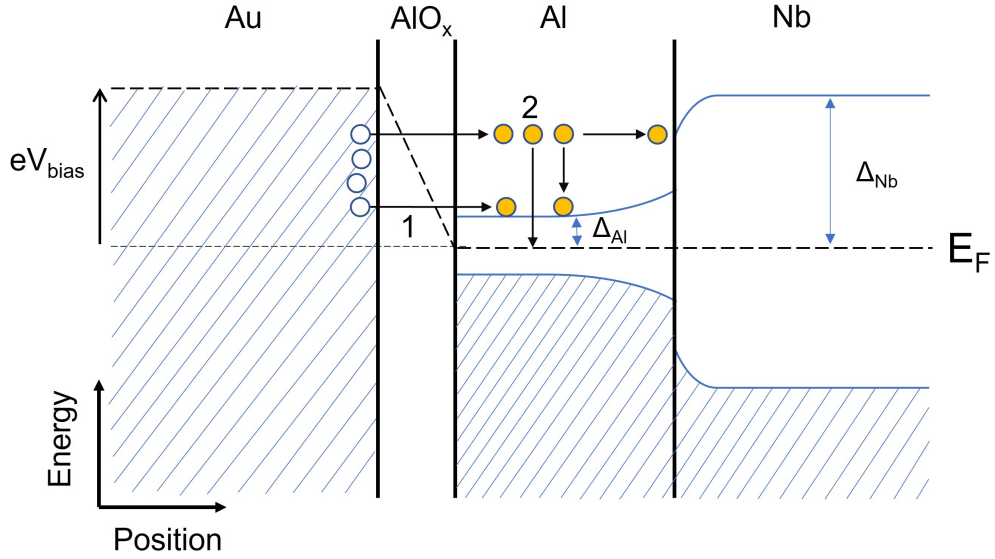


Figure 5.22: Cartoon of the proposed quasiparticle diffusion and tunneling scenario. As depicted, the Au (right side) is positively biased by V relative to the Nb/Al bilayer (left side). The orange circles represent electron-like quasiparticles. $\Delta_{\text{Al}}, \Delta_{\text{Nb}}$ are the spatially varying order parameters in the Al and Nb.

the spatially varying density of states peak energy according to the literature calculations (Fig. 5.12). The left side is the normal metal electrode, negatively biased by V relative to the Nb/Al layer. As $|eV_{\text{bias}}|$ reaches Δ_{Al} , electrons can tunnel from the normal electrode to the quasiparticle states peaked at $\approx \Delta_{\text{Al}}$ (1). Once $|eV_{\text{bias}}|$ reaches Δ_{Nb} , carriers tunnel into the Al and may diffuse to the Nb electrode without scattering, thus sampling the Nb density of states deeper in the superconducting electrode. As these quasiparticles diffuse through the Al, they can recombine with other quasiparticles to form Cooper pairs or thermalize to the Al-like gap edge from scattering over a characteristic length scale. As a result, the height of the peak feature at Δ_{Nb} would decrease as a function of Al thickness.

In essence, the model attempts to explain the conductance spectra observed

here as a convolution of the Al-like DOS near the barrier and the Nb-like DOS deeper into the bilayer. Again, this implies that the decrease in the Nb-like peak voltage with Al thickness corresponds to the change in Δ_{Nb} at the Nb side of the Nb/Al interface. Given the similarity between published experiments and theory, it is difficult to imagine the subgap shoulder as anything other than the spatially dependent gap induced in the Al via the proximity effect. It is currently unclear why this feature appears so broad. While the calculated bilayer DOS from literature exhibit some convolution, the apparent weighting of the Nb-like states is significantly higher in our measurements.

To explore the plausibility of this scenario, I plot conductance spectra corresponding to the devices in Fig. 5.16 with the Dynes broadened BTK formalism. However instead of a single gap parameter (Δ_{g}) and Dynes broadening parameter (Γ), I use a weighted sum of two conductance spectra corresponding to the Nb-like states and the Al-like states. The Nb-like and Al-like contributions to the total conductance are calculated using

$$G_{\text{Nb}} = W(1 + Z^2) \int_{-\infty}^{\infty} [1 + A(\Delta_{\text{Nb}}, \Gamma_{\text{Nb}}, E) - B(\Delta_{\text{Nb}}, \Gamma_{\text{Nb}}, E)] k(E - eV) dE \quad (5.11)$$

$$G_{\text{Al}} = (1 - W)(1 + Z^2) \int_{-\infty}^{\infty} [1 + A(\Delta_{\text{Al}}, \Gamma_{\text{Al}}, E) - B(\Delta_{\text{Al}}, \Gamma_{\text{Al}}, E)] k(E - eV) dE \quad (5.12)$$

where W is the weighting factor and the total conductance is $G_{\text{tot}} = G_{\text{Nb}} + G_{\text{Al}}$. For Δ_{Nb} and Δ_{Al} at a given Al thickness, I use the peak feature energy ($eV_{\text{bias, peak}}$) and

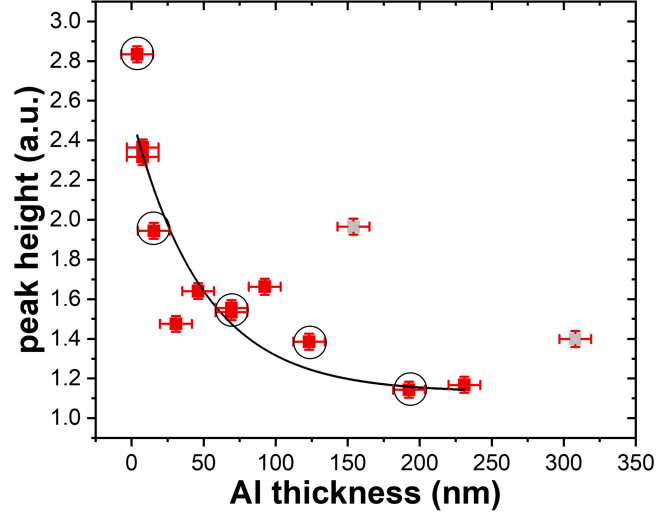


Figure 5.23: The normalized $dI/dV(V)$ peak height of the Nb-like peak feature. The peak height decays exponentially with a characteristic decay length of ≈ 50 nm.

the sub-gap shoulder energy ($eV_{\text{bias, shoulder}}$), respectively. To estimate the thickness dependent weighting factor, I refer to the normalized Nb-like peak feature height, as the height is proportional the number of carriers at the peak energy. The normalized peak height, corresponding to the maximum of the normalized $dI/dV(V)$, is shown as a function of Al thickness in Fig. 5.23. Similar to the ZBC, the estimated uncertainty in the peak height (± 0.05) is dominated by variation between measurements and noise in the conductance trace.

The peak height decays with exponential with a characteristic decay length of ≈ 50 nm. This length is likely related to an inelastic scattering length. However, it's currently unclear how to relate this length to the scattering length of a thick film, given the changing boundary conditions with film thickness (i.e., thickness

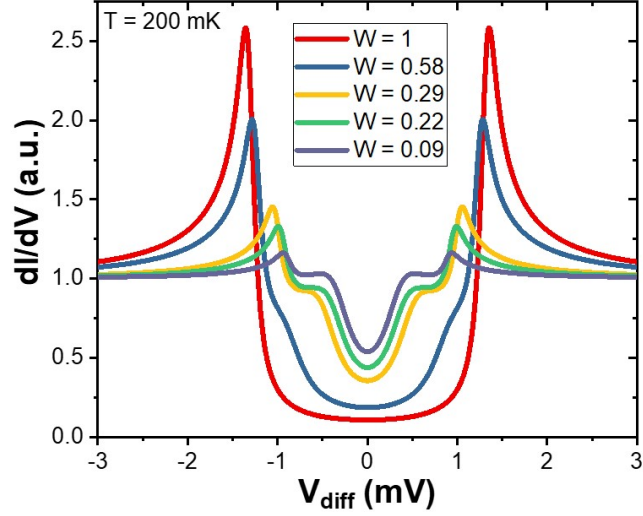


Figure 5.24: Calculated $dI/dV(V)$ spectra using the weighted sum BTK model.

dependence \neq spatial dependence). The five circled data points indicate the five devices highlighted in Fig. 5.16. I take the five circled peak heights values and normalize by the highest value (2.83), corresponding to 4 nm Al. The resulting values are used as the weighting factors for the Nb conductance function. This implicitly assumes that the 5 nm Al conductance spectrum reflects only Nb-like states. As seen in Fig. 5.24, the calculated conductance spectra evolve qualitatively similar to the measured conductance spectra in Fig. 5.16. For simplicity, Γ_{Nb} (0.06 meV), Γ_{Al} (0.2 meV), and Z (2.8) are the same for each conductance spectra. These values were based on preliminary fits to individual spectra. Z depends primarily on the AlO_x tunnel barrier.

In addition to the diffusion-type scenario discussed above, several other mechanisms could possibly result in Nb/Al conductance spectra with sub gap structure.

Direct tunneling into both Nb and Al portions of the bilayer would present as parallel conduction channels, similar to what I observe. Given the exponential decay of tunneling probability with distance, I assume the requirement of direct contact between the Nb and the AlO_x tunnel barrier for direct tunneling into the Nb. For instance, the Nb/Al/ AlO_x /Cu NIS junctions studied by Nevala *et al* exhibit a similar dual-gapped conductance as seen here [129]. Their lateral overspill of the Al deposition on top of the Nb essentially resulted in parallel Nb/Al/ AlO_x /Cu and Al/ AlO_x /Cu junctions, which exhibited a dual gap conductance spectrum. However, I did not discern significant lateral overspill or misalignment between my Nb and Al depositions with optical or scanning electron microscopy. Therefore, I do not find it likely that, for thicknesses above $\approx 10\text{-}15$ nm Al, there is significant direct contact between my Nb layer and AlO_x tunnel barrier. In addition, sub gap structure in tunnel junctions with spatially varying order parameters has been attributed to Andreev bound states [169, 170, 171]. This typically occurs in superconductors separated by weak links (i.e., SNS or SINIS junctions), where quasiparticles from multiple Andreev reflections (MAR) at opposing interfaces of the N material may interfere and form Andreev bound states (ABS). The possible mechanism for forming ABS in the Al layer of my devices is unclear, as the measurements are well below the Al T_c and not bound by separate superconducting layers. In addition, the sub gap structure exhibited by ABS is typically more complex than seen here, displaying multiple sub gap peak features as a result of subsequent Andreev reflection events [169, 170]. However, further work is needed explore this possibility.

5.4.2 BTK fitting of conductance spectra

Fitting of conductance data was initially performed with data measured at ≈ 3.9 K in the cryocooler system. The conductance spectra for several devices are shown in Fig. 5.25. Dynes broadened BTK fits are shown for each data set. Only a single conductance function is used to fit the 3.9 K data (as opposed to the weight sum approach), as $T > T_{c,Al}$ and there is no sub-gap shoulder feature in the data. The fits capture the data well using Δ_g , BTK barrier strength (Z), and Γ as free parameters. The extracted fit parameters are shown in Table 5.1. Δ_g decreases exponentially with Al thickness, which is consistent with the literature for a SN bilayer [168, 172]. While Z varies a bit, it does not seem to be correlated with Al thickness. For a constant number of conduction channels, Z is proportional to the tunneling resistance [77]. Given the relatively constant RA product with Al thickness, shown in Fig. 5.3(a), it would be reasonable to expect a constant Z . However, the degrees of freedom in the model (particularly Z and Γ) are not orthogonal, necessitating further effort to constrain these parameters. The extracted Γ parameters increase with Al thickness and are large compared to those typically seen in the literature for Nb and Al [129, 153, 154]. In addition to Δ_g , Γ is typically seen to be temperature dependent [155, 173]. Z is expected to remain constant in temperature, as no significant change to the tunnel barrier is expected in this temperature range.

Applying the fits to data taken at the DR base temperature effectively removes temperature broadening and helps to fix temperature dependent parameters. As a

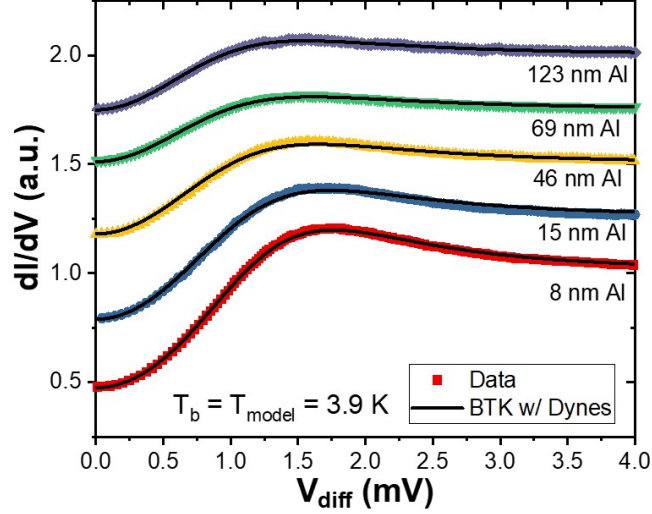


Figure 5.25: Conductance spectra measured at 3.9 K for several NIS devices, with Nb/Al superconducting electrodes. The corresponding fits using the BTK generated conductance with Dynes broadening is represented by the dashed blue lines. Free parameters used in the fits, shown in Table 5.1, are Δ_{model} , Z , and Γ . The spectra are offset by 0.25 for clarity.

Al thickness (nm)	Z	Γ (meV)	Δ_g
8	2.0	0.19	1.15
15	3.4	0.27	0.96
46	2.5	0.31	0.81
69	2.7	0.33	0.8
123	2.8	0.30	0.66

Table 5.1: 3.9 K BTK model fits with Dynes broadening, as seen in Fig. 5.25.

first step, only T is fixed at 200 mK and the other parameters are left free (Z , W , $\Delta_{\text{Nb,Al}}$, $\Gamma_{\text{Nb,Al}}$). Shown in Fig. 5.26(a), the 4 nm Al device is captured well using a single conductance function (i.e., no weighted sum). In other words, the data is described well in the limit of no Al by considering only the Nb-like density of states. As the Al thickness is increased, the spectra exhibit the sub-gap shoulder feature and the fits are done using the weighted sum conductance discussed previously. As shown by the plots in Fig. 5.26(b), the data are well captured when using the weighted sum model. The model parameters used for each spectrum in Fig. 5.26(a-b) are shown in Table 5.2. With temperature broadening significantly diminished compared to the measurements at 4 K, the extracted Z and $\Gamma_{\text{Nb,Al}}$ values do not seem to be correlated with Al thickness. However, the weighting factor for the Nb-like (Al-like) states decreases (increases) with Al thickness. Therefore, the quantitative application of the model shows that the transition from a uniform superconducting electrode (thin Al) to the nonuniform superconducting electrode (thick Al) is described well by convolving the Nb-like and Al-like DOS, with increasing contribution (i.e., weight) from the Al-like states with thickness. The decreasing Nb and Al-like gap values with Al thickness are qualitatively consistent with my expectations in the context of the proximity effect.

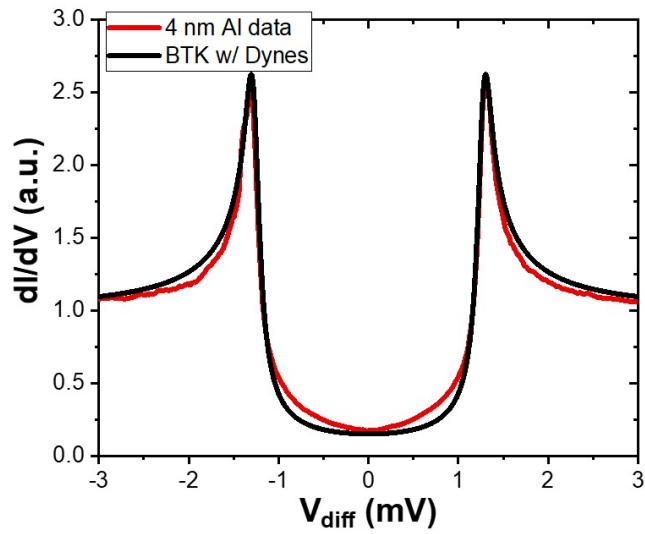
It's difficult to set an expectation for the Al thickness dependence of $\Gamma_{\text{Nb,Al}}$, as broadening captured by this phenomenological parameter has been attributed to a variety of mechanisms. Broadening as a result of pinhole conduction is not likely, given the typical $\approx 55\text{-}60\%$ increase in RA product between 295 K and 10 K for the measured NIS junctions. Discussed in Chapter 2, an insulator-like resistance

t_{Al} (nm)	Z	Γ_{Nb} (meV)	Γ_{Al} (meV)	$\Delta_{\text{g, Nb}}$ (meV)	$\Delta_{\text{g, Al}}$ (meV)	W_{Nb}
4	2.2	0.05	-	1.27	-	-
46	2.3	0.09	0.16	1.17	0.70	0.50
123	2.5	0.09	0.18	0.82	0.47	0.38

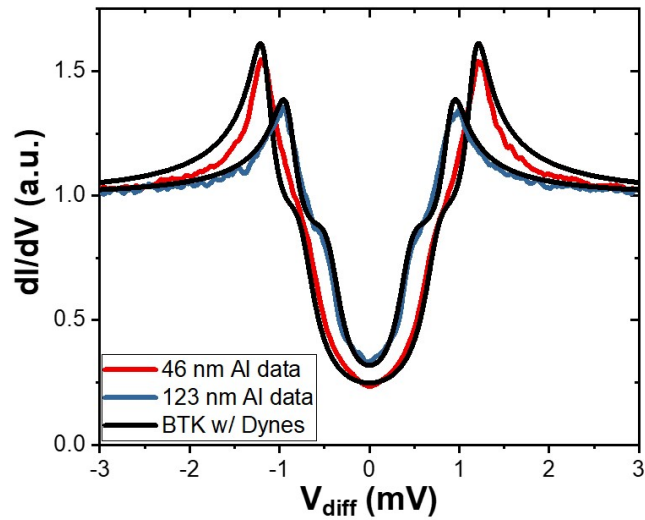
Table 5.2: 15 mK BTK model fits with Dynes broadening, corresponding to the data in Fig. 5.26.

change with temperature (resistance increases as temperature decreases) effectively rules out metallic shorts. As Δ_{g} decreases with increasing Al thickness, Γ may increase with Al thickness from processes such as photon-assisted tunneling. However, Γ attributed to such processes is typically quite small ($\Gamma/\Delta \sim 1/5000$) [154]. In addition, Γ broadening from localized defect states in the barrier or at the insulator interface is not likely thickness dependent, provided the barrier quality does not change appreciably between devices.

As discussed previously concerning Fig. 5.24, the proposed model has succeeded in qualitatively reproducing the NIS conductance spectra evolution with Al thickness. Quantitative application of the model shows that, by increasing the weight of the Al-like states with Al thickness and allowing the gap energies to change in accordance to the proximity effect, our spectra are captured well using a uniform (i.e., single) conductance model in the thin Al limit ($\lesssim 15$ nm) and a nonuniform weighted-sum model in the thick Al limit. Moving forward, detailed interpretation of the data will be given more weight as the degrees of freedom are constrained. Features in the $dI/dV(V)$ data can be used to constrain the fit parameters of individual spectra. As discussed previously, the peak/shoulder voltages can constrain the $\Delta_{\text{Nb,Al}}$ fit parameters and the peak height can constrain the evolution of the weighting factor with Al thickness. In addition, the Z parameter can likely be held



(a)



(b)

Figure 5.26: Conductance spectra measured at 15 mK for a (a) 4 nm Al device, and (b) the 46 nm and 123 nm Al devices. The weighted sum fits, using the Dynes broadened BTK model, are plotted over the data. T is fixed at 200 mK according to Fig. 5.15. The fit parameters are listed in Table 5.2.

constant as a function of thickness.

5.5 Chapter summary

In this chapter, I described the fabrication and characterization of Nb/Al bilayer-based NIS tunnel junctions. The Nb/Al bilayers utilized 45 nm of Nb and 5 nm - 310 nm of Al. The residual resistivity ratio in the Nb/Al wires increased linearly from 1.8 for very thin Al (≤ 10 nm) up to 10.5 at 310 nm Al, indicating the Al residual resistivity is dominated by size effects such as surface scattering over this thickness range. This would translate to a strong Al thickness dependence on relevant superconducting properties such as the mean free path and the Al coherence length. T_c , starting at 7.15 K for 5 nm Al device, decreases with Al thickness as expected within the superconducting proximity effect.

NIS conductance spectra are recorded for each Nb/Al bilayer based tunnel junction. The spectra evolve from exhibiting behavior of a primarily single gapped system to convolution of the Nb and Al-like superconducting states out to 310 nm Al. The conductance peak voltage, attributed to states at the Nb-like gap edge, decreases linearly with Al thickness. As the Al thickness increases beyond 20 nm, a sub-gap shoulder appears in the conductance spectra. The voltage position of this feature decreases exponentially with Al thickness. Qualitative and quantitative agreement with the literature suggests this peak represents Δ_g , proportional to the minimum in the spatially dependent order parameter.

I report on a modified Blonder-Tinkham-Klapwijk (BTK) based model inter-

preting the conductance spectra as a steady-state convolution of the Al-like DOS and the Nb-like DOS in the bilayer. Although literature calculations of Nb/Al bilayers predict some convolution in the density of states, the density of states extracted with transport give considerably more weight to the Nb states deeper in the bilayer. This represents a large athermal ($E \sim 2\Delta_g$) population of quasiparticles in the Al, which may be detrimental to devices such as Josephson junction qubits or NIS thermometers. By using the peak/shoulder feature voltages and the Nb-like peak height to set initial input parameters, the model succeeds in qualitatively capturing the evolution in the measured conductance spectra with Al thickness. I discuss fitting individual conductance spectrum to refine the input parameters and constrain the degrees of freedom in the model. Looking forward, correlating model parameters the weighting factor and Δ can provide insight on quasiparticle generation and diffusion in the system.

Chapter 6: Conclusions and Future Studies

6.1 Conclusions

This thesis describes efforts to improve and provide insight on properties of materials critical for quantum information. By correlating oxidation process parameters with *in situ* materials characterization and *ex situ* transport measurements, the plasma oxidation recipe of ultrathin Al layers on Co was optimized to mitigate device aging, used as a proxy for the density of electrically active defects in AlO_x tunnel barriers. Plasma oxidized AlO_x tunnel barriers were used to inspect the evolution of the Nb/Al bilayer superconducting state in Nb/Al-based normal metal-insulator-superconducting tunnel junctions. Each of these pieces are precursors to hybrid quantum information systems, where Al, AlO_x , and Nb are compatible with both semiconductor and superconductor quantum information platforms.

6.1.1 Plasma Oxidation for AlO_x Tunnel Barriers

Amorphous AlO_x layers, typically formed from the oxidation of an Al base layer, are used ubiquitously as tunnel barriers in quantum device applications, such as Josephson junctions for superconducting quantum information or magnetic tun-

nel junctions for non-volatile memory storage. However, they often suffer from the presence of electrically active defects, which manifest as drifting electrical properties in time (“aging”) [81]. In Chapter 3, tunnel junctions with plasma oxidized AlO_x barriers confined by cobalt layers ($\text{Co}/\text{AlO}_x/\text{Co}$) exhibited significantly less resistance drift (34.0 ± 5.4 % increase over 5230 h) compared to junctions without Co confinement ($\text{Co}/\text{Al}/\text{AlO}_x/\text{Co}$, 95.4 ± 7.8 % increase over 5200 h).

The defects responsible for resistance drift are often attributed to the initial non-equilibrium structure of the amorphous oxide, in addition to oxygen deficiency compared to stoichiometric Al_2O_3 [83, 87, 88]. Both “confined” ($\text{Co}/\text{AlO}_x/\text{Co}$) and “unconfined” ($\text{Co}/\text{Al}/\text{AlO}_x/\text{Co}$) devices utilize plasma oxidation, which produces oxides with relatively high oxygen concentration in significantly shorter fabrication times when compared to thermal oxidation [45, 47]. By confining the AlO_x with top and bottom Co layers, oxygen is confined in the designed tunnel barrier layer. This behavior can be understood as the Al layer between Co electrodes acting as a potential well for oxygen, given the significantly larger (more negative) Gibbs free energy of formation of Al_2O_3 ($\Delta G_f^0 = -1581$ kJ/mol) compared to Co oxides, CoO ($\Delta G_f^0 = -215$ kJ/mol) and Co_3O_4 ($\Delta G_f^0 = -770$ kJ/mol) [78, 96]. The bottom Co layer acts as an oxidation stop, as the less energetically favorable Co oxide formation is typically not observed until nearly all metallic Al is oxidized for thin Al layers on Co [45, 46, 78]. As a result, aging is less severe for confined devices likely due to the initial oxygen profile being more homogeneous with a higher O:Al ratio, indicated by WKB transport fits of confined ($\Delta x = 1.34 \pm 0.04$ nm, $\Phi_{\text{top}} = 1.00 \pm 0.03$ eV, $\Phi_{\text{bot}} = 1.05 \pm 0.03$ eV) and unconfined devices ($\Delta x = 2.01 \pm 0.06$ nm, $\Phi_{\text{top}} =$

0.47 ± 0.01 eV, $\Phi_{\text{bot}} = 0.42 \pm 0.01$ eV).

The improvements to device aging suggest a reduction in electrically active defects, thus mitigating device degradation in applications such tunnel junction-based non-volatile memory or suppressing sources of decoherence hindering quantum information systems. In essence, plasma oxidation and free energy confinement provide a fast (7 s oxidation time) and athermal (room temperature process, no anneal) method for fabricating high quality AlO_x tunnel barriers without additional processing. AlO_x tunnel barriers formed by room temperature thermal oxidation typically take minutes to hours, depending on the oxygen pressure. Similar improvements to uniformity and stoichiometry have been observed in Co confined barriers (Co/ AlO_x /Co compared to Al/ AlO_x /Al) with thermal oxidation, but required a significantly longer and higher temperature oxidation (24 h, 330-470 K) [100]. In addition, time stability has been achieved via high temperature anneals [44]. However, this can result in unpredictably large changes in the tunnel junction resistance and undesired diffusion through the device [43]. The benefits to stoichiometry provided by plasma oxidation and the free energy confinement can be applied to reduce instability, and therefore defect density, in other quantum relevant applications.

Both the plasma oxidation recipe developed here (7 s, 55-60 W constant current, 160 mTorr) and Co confinement have already been applied to AlO_x single electron transistors (SET) [15, 174]. The source-drain current I_s flowing through an SET varies sinusoidally with the gate voltage V_g , where device instability is typically parameterized by drift in the phase of the I_s - V_g behavior called charge offset drift (ΔQ_0). As seen in Fig. 6.1, the charge offset Q_0 for an Al/ AlO_x /Al SET using the

plasma oxidation recipe developed here exhibits much less instability compared to one using thermal oxidation. Co confined, plasma oxidized Co/AlO_x/Co SETs also showed much smaller ΔQ_0 compared to the thermally oxidized Al/AlO_x/Al SET. As evidenced by the above examples, the approach developed here has the potential to be applied to a variety of systems critical to both classical and quantum information systems.

6.1.2 Photoelectron Spectroscopy for Ultrathin AlO_x Layers

As discussed in Chapter 4, *in situ* X-ray photoelectron spectroscopy (XPS) enables nondestructive elemental and chemical state identification on devices without exposure to atmosphere. XPS evaluation of plasma oxidized AlO_x layers on Co found no sign of metallic Al or Co oxide within the measurement resolution, where the XPS detection limit is typically 0.1-1 at.% [175]. To first order, these are the desired conditions to mitigate device aging as a result of underoxidation. Additional efforts to estimate the O:Al ratio of the oxide, discussed in the following section, can potentially refine the oxidation procedures further. Applying the same oxidation process to thin (≈ 1.3 nm) Al layers on Nb revealed the presence on Nb oxides with XPS inspection, which are undesirable given the lossy nature often associated with Nb oxides. The ability to contrast AlO_x formation without exposure to atmosphere in these two material systems (Al on Co and Al on Nb), given nominally identical oxidation procedures and initial Al thickness, demonstrates the utility of *in situ* XPS for process development and provides a launching point for process

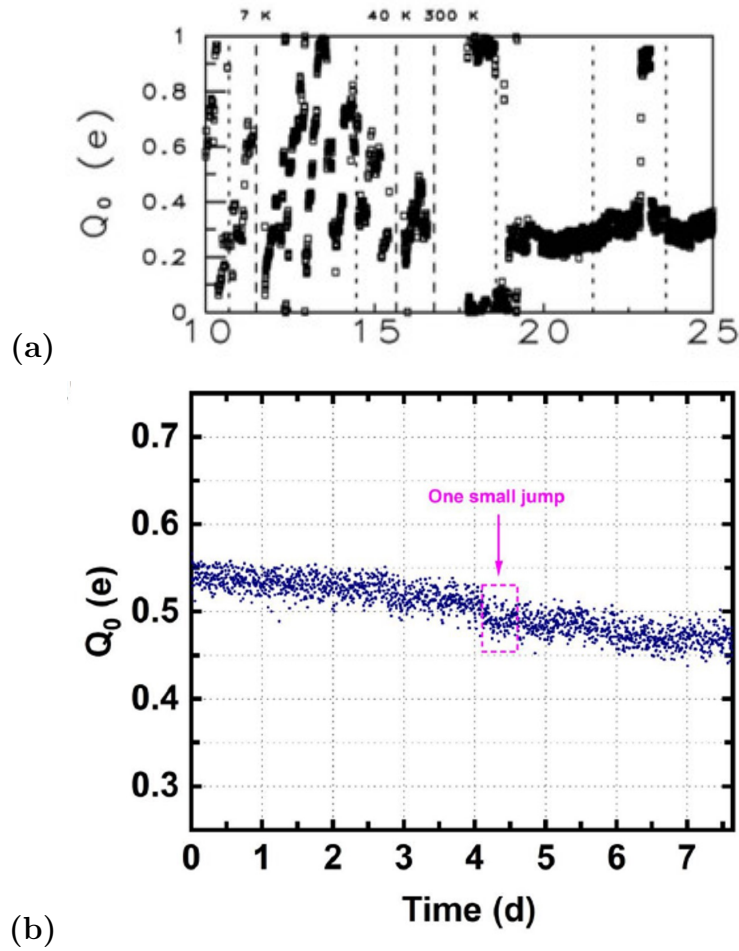


Figure 6.1: The charge offset as a function of time is shown for Al/AlO_x/Al SETs using (a) thermal oxidation and (b) the plasma oxidation recipe developed in this thesis. The horizontal axis in (a) is in days. The plot in (a) is adapted from Ref [110] with permission from AIP publishing. The plot in (b) was adapted from [15], an Open Access article under a Creative Commons Attribution License.

optimization of AlO_x formation on Nb in the system moving forward.

In addition to chemical state identification, AlO_x film thickness is determined with angle-resolved XPS (ARXPS) using the Hill equation approach. Accurate film thickness measurements in the nanometer range remain extremely difficult. Preliminary data show the ARXPS estimated thickness of AlO_x on Al increasing as a function of oxidation time as expected, but the relation between the ARXPS thickness and WKB thickness is different depending on the material system (ARXPS thickness larger than WKB thickness for AlO_x/Al and AlO_x/Co , smaller than WKB thickness for $\text{AlO}_x/\text{Al}/\text{Nb}$). Additional data is needed to provide better statistics, clarify the role of the top layer material in the effective WKB thickness, and calibrate Hill equation input parameters (e.g., system dependent relative sensitivity factors).

6.1.3 Tunneling Spectroscopy of Nb-Al Based NIS Junctions

Nb and Al, in conjunction with ultrathin AlO_x layers such as those discussed above, are critical materials for superconducting electronics and superconducting quantum information. Nb/Al bilayers have typically been used to take advantage of the relatively high T_c of Nb (≈ 9.2 K, bulk) and the relatively uniform oxide formed on Al by room temperature thermal oxidation. In making electrical contact between the materials, the density of states in each material are predicted to be drastically altered by virtue of states in the other. While the spatial and thickness dependent density of states have been predicted in theory, little experimental work has been performed to measure such dependencies. Using the plasma oxidation recipe de-

veloped here, we have studied the evolution of the Nb/Al superconducting density of states as a function of Al thickness in normal metal-insulator-superconducting (NIS) tunnel junctions. The bilayers are comprised of $\approx 45\text{-}50$ nm of Nb and between 5-310 nm of Al. The bilayer T_c , starting at 7.2 K for 5 nm Al, decreases to approximately 6 K for the thickest Al samples. The density of states in the bilayer are extracted from low temperature NIS conductance spectra (electron temperature $T_e \approx 200$ mK). For thin Al ($\lesssim 15$ nm), the spectra exhibit only a single set of coherence peaks, the bias position of which decreases linearly with Al thickness. For thicker Al ($\gtrsim 30$ nm), a sub-gap shoulder feature emerges, the bias position of which decreases exponentially with Al thickness towards the bulk Al gap at ≈ 0.2 mV.

We present a simple model interpreting the conductance spectra as a steady-state convolution of the Al-like DOS near the tunnel barrier and the Nb-like DOS deeper into the superconducting electrode. In contrast to the equilibrium bilayer DOS calculated in the literature with the Usadel equations, which show the density of states maximum in the Al dominated by states at the proximity enhanced Al gap energy (Fig. 5.12), the DOS extracted from tunneling into/out of the Al side of the bilayer are peaked at the Nb-like gap energy for all Al thicknesses measured. This indicates that a significant population of carriers are transiting the Al at the Nb-like gap energy without scattering, thus convolving the Nb-like DOS with the Al-like DOS local to the tunnel barrier. Calculated tunneling conductance spectra, using a Dynes-broadened Blonder-Tinkham-Klapwijk (BTK) theory formalism with weighted contributions from Nb-like states (weight A) and Al-like states (weight $1-A$), lend support to this model. With initial input parameters extracted from feature

bias positions, the calculated spectra evolve in a qualitatively similar manner. In addition, a significant contribution from multiparticle tunneling is apparent given the sub-gap conductance observed in all spectra, parameterized by the BTK barrier strength Z (typically 2-3) and Dynes broadening Γ/Δ (typically $\sim 10^{-1}$).

By observing the persistence of quasiparticles at the Nb-like gap energy in the thick Al, we can provide insight on combining these material systems for device applications. Bilayers with a relatively small amount of Nb (≈ 45 nm compared to > 300 nm Al) maintain a T_c much larger than our thin film Al (~ 6 K compared to 1 K), which may be useful for AlO_x -based devices such as NIS thermometers by extending the operational temperature [176] or Josephson junction qubits by reducing the thermal population of quasiparticles (scales as $e^{-\Delta/kT}$). However, these applications are also sensitive to excess athermal quasiparticles, such as the quasiparticles in the Al at the Nb gap energy seen here, which can cause broadening from pair breaking when these quasiparticles relax or increase error rates in Josephson junction-based qubits by inducing qubit transitions [42]. Therefore, the Nb/Al bilayers with thicker Al, where an Al gap develops separate from the Nb gap, may prove a hindrance to such devices.

6.2 Future Studies

6.2.1 Quantitative XPS Analysis of AlO_x : Correlation with WKB transport modeling

Although the plasma oxidation and free energy confinement improved device aging, there is still much room for further optimization and evaluation. Quantitative XPS analysis can be pursued further to expand our *in situ* characterization capabilities, both to aid in process development and provide valuable connective tissue between material processing and device behavior. One of the factors that was hypothesized in mitigating device aging was an increased O/Al ratio in the confined (Co/ AlO_x /Co) tunnel barriers compared to the unconfined (Co/Al/ AlO_x /Co) tunnel barriers. High resolution XPS scans of the as-fabricated AlO_x layers can be used to provide an estimate of the O/Al ratio [88]. Calibration of the relative sensitivity factors (measurement system dependent, in part) for Al and O would likely be required, which can be performed with a bulk Al_2O_3 sample. This also provides an interesting axis in correlating the *in situ* XPS measurements with *ex situ* transport modeling. Incorporating estimates of the stoichiometry may prove useful in interpreting the difference in ARXPS determined thickness and WKB determined thickness, discussed in Chapter 4. However, it also enables a systematic study to correlate stoichiometry and WKB barrier height. While helpful in process development, this would also connect well to recent computational studies on the evolution of AlO_x tunnel junction behavior with stoichiometry [87, 112]. They find

that, as the O/Al ratio increases past ≈ 1 , the AlO_x band gap opens and grows with O content. By fabricating a series of Co/ AlO_x /Co or Al/ AlO_x /Al tunnel junctions with different initial Al thicknesses and plasma oxidation times, one could attempt to systematically correlate the *in situ* XPS characterization and *ex situ* transport modeling. This could couple with aging or tunneling magnetoresistance measurements to shed more light on the correlation to stoichiometry.

6.2.2 Monolithic Nb/Al-based resonators

As shown in Appendix 6.2.2, I have performed preliminary work towards the goal of integrating monolithic superconducting resonators with quantum dot gates. In essence, gate-based sensing of quantum dot qubits, via a resonator connected to one of the qubit gates, has been identified as a fast, accurate, and scalable readout method. The signal response to state changes in the qubit is proportional to the resonator quality factor, so incorporation of a superconducting resonator ($Q \sim 10^3$ - 10^6) is an attractive option compared to chip mounted resonators ($Q \sim 10^2$). Much work remains to be done in fabricating our resonators with a desired resonance frequency f_0 . Modeling with electromagnetic (EM) analysis software, such as Sonnet or COMSOL, can be used to provide more accurate estimates of f_0 for a given design. Benchmarking our fabrication process using known resonator designs would also be useful in establishing our resonator fabrication process. This can progress in parallel to the integration of monolithic resonators with quantum dot gates, as I have already fabricated Nb resonators with quality factors $Q > 10,000$. This is

significantly larger than the quality factor realized by the often-used chip mounted LC resonators, of order 100.

Utilizing Nb/Al bilayers as superconducting resonators may lead to improved quality factors and reveal interesting physics. Nb resonators typically have lower quality factors (i.e., more loss) compared to Al resonators, attributed in large part to Nb oxides containing a significant population of TLS defects and non-insulating oxide phases [177]. Coverage by an Al layer may improve resonator performance by mitigating Nb oxide formation. In addition, changing the Al thickness on the Nb may result in nonintuitive changes in the resonator kinetic inductance. The kinetic inductance L_K in Nb/Al bilayers has previously been shown to exhibit an atypically strong dependence on temperature and current biasing, attributed to the unique dependence between cooper pair density and these parameters for a system with a spatially varying order parameter [178]. Studying L_K in Nb/Al bilayers as a function of Al thickness, and the temperature/current bias dependencies for each, can provide insight towards their use as tunable elements in microwave circuits. This would call for a series of lumped element Nb/Al resonators connected galvanically to the signal line to allow for current biasing (as opposed to capacitively coupled hanger-style resonators). With these in hand, f_0 can be measured as a function of temperature and current bias, allowing for L_K to be extracted with suitable modeling.

Appendix A: Monolithic Superconducting Resonators For Gate-Based Quantum Dot Readout

Preliminary results are reported on the fabrication and characterization of monolithic superconductor resonators for gate-based readout of metal-oxide-semiconductor (MOS) quantum dot qubits. I fabricated several resonator device wafers in an effort to deterministically realize resonators in agreement with design parameters, specifically in regards to the resonance frequency (f_0). This project was intended to dovetail with the Nb/Al work, where bilayer resonators may exhibit interesting kinetic inductance properties and Al on Nb may improve resonator quality factor compared to Nb resonators [178]. While progress was stalled by COVID-19, I successfully fabricated Nb superconducting resonators with a quality factor $> 10,000$. I will provide a brief introduction on the topic and discuss the progress made.

Large scale quantum computation requires fast and accurate readout of qubit states using scalable hardware. Readout for semiconductor quantum dot spin qubits is often performed using an external charge sensor, such as a single electron transistor [179]. The charge sensor is capacitively coupled to the quantum dot and, via spin-to-charge conversion in the dot, can infer the qubit state from charge displacements (i.e., electron tunneling events). However, the ancillary hardware introduced by an

external charge sensor presents an engineering challenge when scaling up, given the additional gates and leads required in close proximity to the qubits.

Radio frequency (RF) gate-based readout of semiconductor quantum dot spin qubits has been demonstrated as a fast and scalable alternative to traditional charge state detection [180]. In this approach, a resonator is coupled to the qubit via electrical connection to one of the quantum dot gates, applying a small signal to the gate. The qubit state is inferred from the magnitude of the reflected signal. The resonant frequency (f_0) of an L-C resonator circuit is given by

$$f_0 = \frac{1}{2\pi\sqrt{LC}} \quad (\text{A.1})$$

where L is the inductance and C is the capacitance. For typical gate-based sensing schemes, the inductance is comprised of an inductor connected in-line with a quantum dot gate. The capacitance is comprised of the parasitic capacitance to ground C_p of the inductor (including associated leads and wirebonds) and the parametric quantum dot capacitance C_{pm} . In essence, the parametric capacitance refers to a state dependent capacitance of the quantum dot, which changes as a result of charge transitions. State dependent changes in C_{pm} alter f_0 , thus changing the magnitude and phase of the reflected signal (i.e., reflectometry). Scaling up to many devices is made easier by the utilization of existing gates. Monolithic superconducting resonators integrated with the quantum dot gates have the potential to improve measurement response over conventional lumped element, chip-mounted resonators.

The phase response of the reflected signal is given by $\Delta\phi \propto Q \frac{C_{pm}}{C_p}$, where Q

is the quality factor of the resonator. In other words, the signal-to-noise ratio is improved by increasing Q and minimizing C_p . Superconductor resonators provide a higher Q compared to conventional chip mounted resonators as a result of decreased dissipation. Due to a decreased physical footprint and elimination of a number of wirebonds, C_p can be reduced by using a monolithic resonator integrated on chip with the quantum dot. The first step towards this goal is to fabricate resonators in agreement with design parameters.

The superconducting resonators described here are comprised of parallel meander inductors (i.e., superconducting wire) and interdigitated capacitors (IDC). Both geometric inductance (classical inductance) L_G and kinetic inductance L_K contribute to the total conductance. The design drawing of the inductors is used to calculate the geometric inductance with FastHenry electromagnetic (EM) solver software. Kinetic inductance accounts for the inertia of the current carriers. For superconducting meanders, L_K is given by

$$L_K = \left(\frac{l}{w}\right) \frac{R_{sq} h}{2\pi^2 \Delta} \frac{1}{\tanh\left(\frac{\Delta}{2k_B T}\right)} \quad (\text{A.2})$$

where l and w are the wire length and width, R_{sq} is the resistance per square, and Δ is the superconducting gap [181]. The IDC capacitance scales with finger length and the number of fingers, the capacitance of which is estimated using the analytical approach by Beerasha *et al* [182]. The target f_0 was typically 50-150 MHz, depending on the meander and IDC design. Resonator designs, fabrication, and measurement are discussed using the figures below.

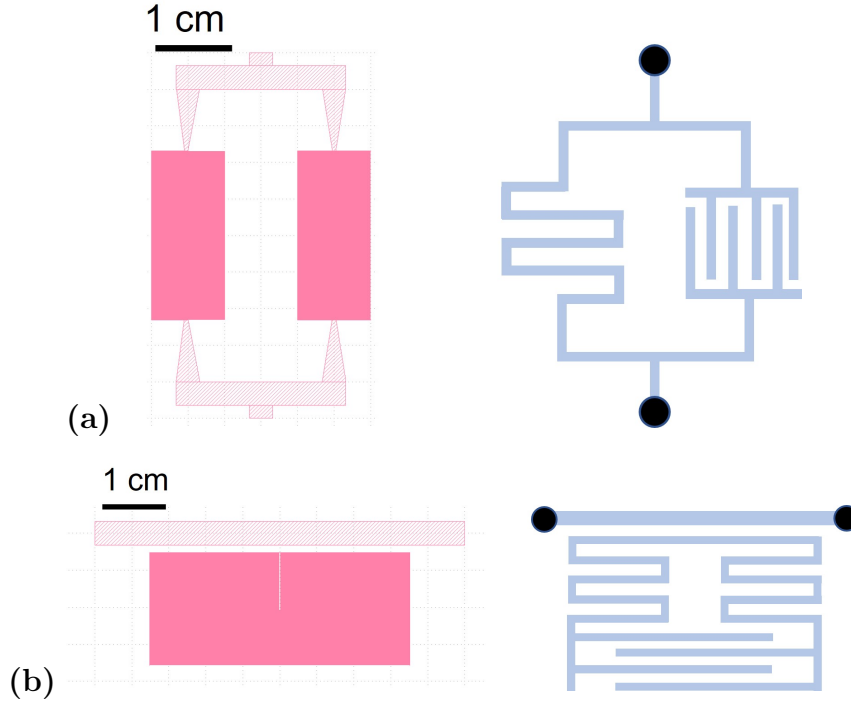


Figure A.1: Design drawing and diagram for two parallel LC resonator implementations. For parallel LC resonators, the circuit impedance is maximized at f_0 . The design in (a) is in line with the signal line, while the design in (b) is capacitively coupled to the signal line. The range of targeted f_0 was 70-150 MHz. The designed wire width and wire spacing were $2 \mu\text{m}$ and $4 \mu\text{m}$, respectively. An R_{sq} of $6 \Omega/\text{sq}$ and Δ of 0.8 meV ($\Delta = 1.76k_{\text{B}}T_c$) were determined from test devices and used to estimate values for L_{K} . The estimated range of IDC capacitance, controlled with the number of IDC fingers, was $0.2\text{-}5 \times 10^{-12} \text{ F}$. The estimated range of L_{K} , controlled with wire length of order $\approx 50 \text{ cm}$, was $4\text{-}7 \times 10^{-7} \text{ H}$. Typical L_{G} values were estimated to be $\approx 1 \times 10^{-7} \text{ H}$ using FastHenry.

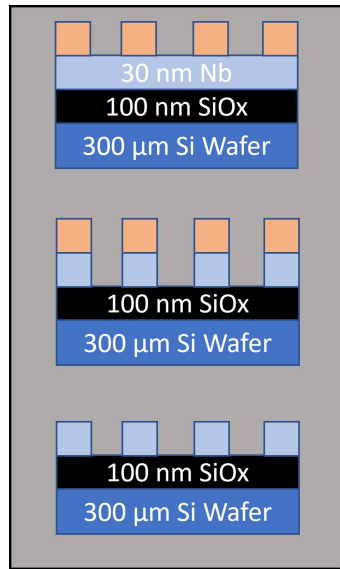


Figure A.2: Fabricating the resonators was done in a cleanroom setting. A 25 nm Nb thin film (light blue) was deposited on a Si wafer with 100 nm of SiO_x. A ma-N 1410 negative tone photoresist mask (orange) is applied to the film. The design drawing is used by an MLA direct writer to expose the mask at $\approx 500 \text{ mJ/cm}^2$. After exposure, the mask is developed using ma-D 533/s developer. Argon ion milling is used to etch the pattern in the Nb film. The remaining mask is removed with a heated IPA bath.

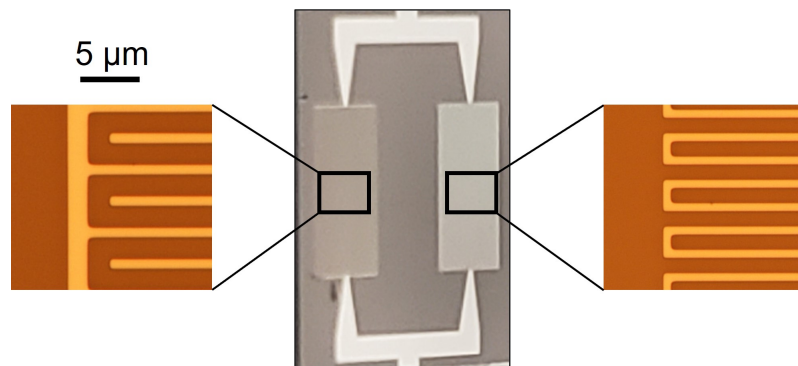


Figure A.3: Microscope images of a representative device are shown. The wire widths and spacing closely align with the design parameters. Several IPA baths were needed to fully remove the remaining resist.

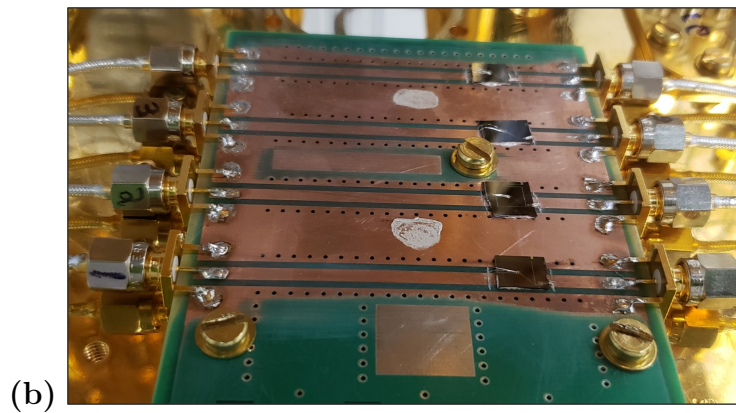
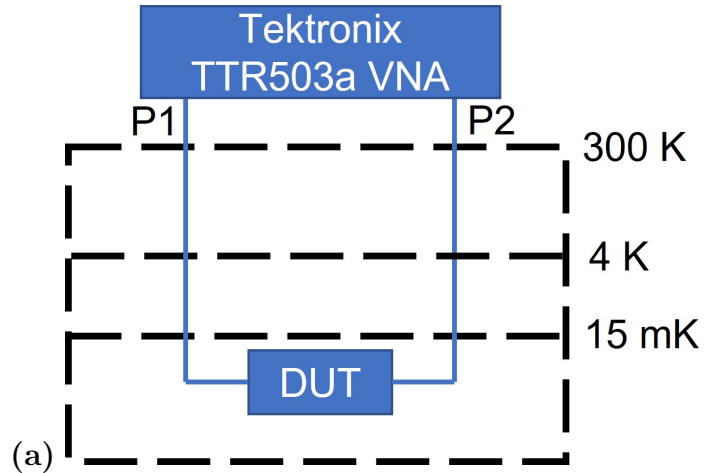
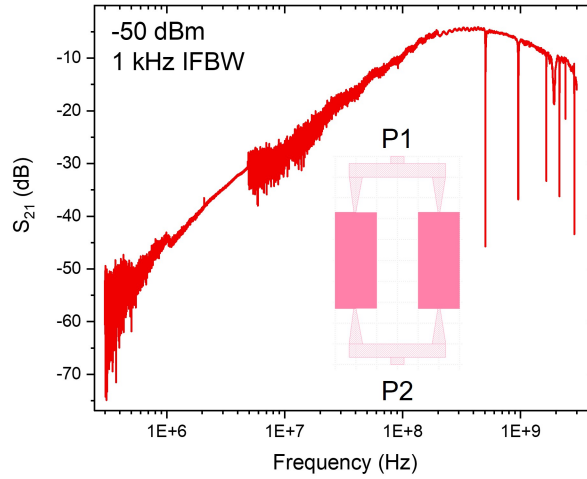
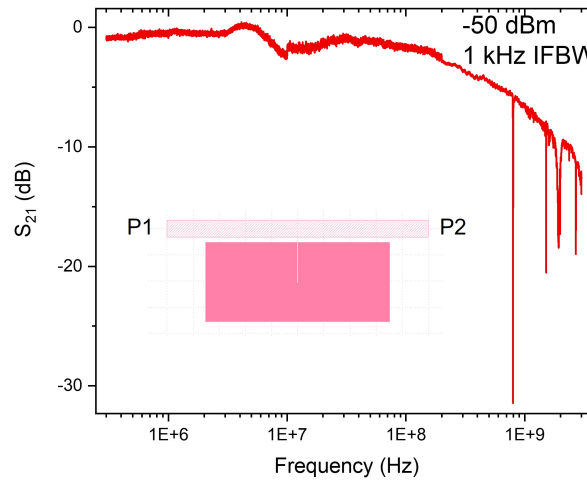


Figure A.4: (a) Diagram of resonator measurements in the dilution refrigerator (DR), where DUT indicates the device under test. High frequency coax signal lines connect the device to ports (P1 and P2) of a Tektronix TTR503a Vector Network Analyzer (VNA). (b) The devices are silver pasted to a custom printed circuit board (PCB). The board consists of several signal lines placed between SMA launches. The resonators are mounted in a trench cut into the signal line. Wire bonds connect the resonator to the signal line on either side of the trench. In this configuration, both transmission ($S_{21,12}$) and reflection ($S_{11,22}$) can be measured.



(a)



(b)

Figure A.5: Representative S_{21} measurements are shown for (a) in line and (b) capacitively coupled resonators. The applied power is -50 dBm. The intermediate frequency bandwidth (IFBW) is 1 kHz. The IFBW essentially sets an aperture time for the measurement. Sharp resonance peaks are observed in each device. However, the resonance peaks are at significantly higher frequencies (≈ 500 -950 MHz) compared to the designed frequencies (70-150 MHz). According to Eq. A.1, this indicates a much smaller L and/or C in our resonant circuit. Moving forward, modelling the RF response of the designed circuit, with EM software such as Sonnet or COMSOL, can more accurately provide estimates of the effective L and C values. In addition, L_K should be the only temperature dependent factor for $T < T_c$. Further analyzing the temperature dependence of f_0 may constrain estimates of L_K .

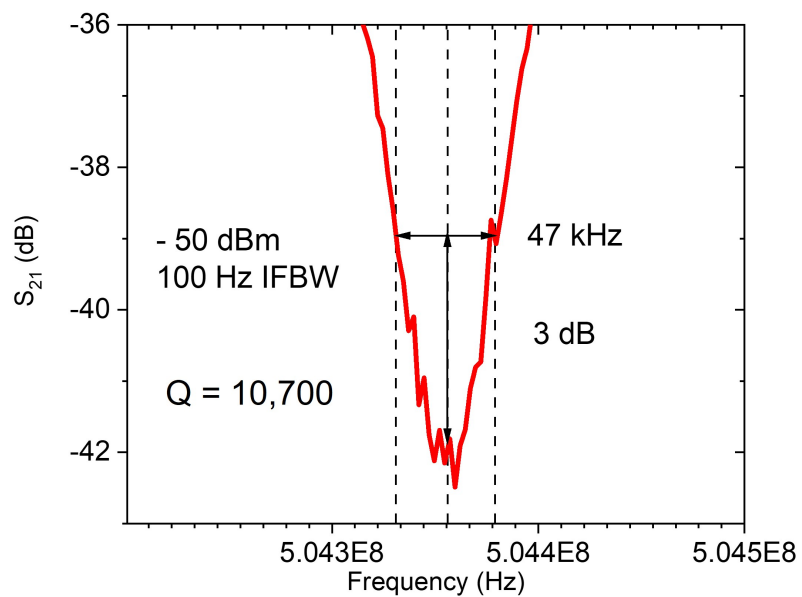
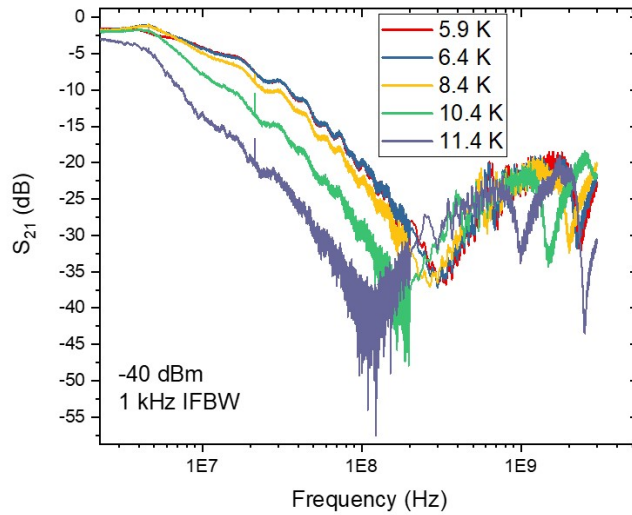
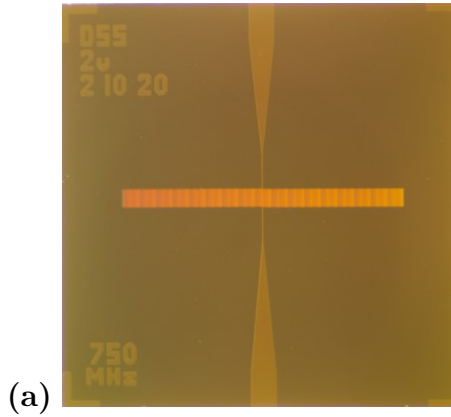


Figure A.6: A high resolution (high data density, low IFBW) S_{21} measurement is taken in the region of f_0 to determine the quality factor Q . The half power point (or 3 dB method) is used to calculate the Q . To determine Q , f_0 is divided by the bandwidth of the peak 3 dB from the peak minimum. With this method, I find quality factors in excess of 10,000.



(b)

Figure A.7: (a) Just prior to COVID-19, I fabricated NbTiN meander inductors without any intentional capacitance, as shown in this microscope image. The ≈ 33 nm NbTiN film was provided by Dr. David Pappas and Dr. Mustafa Bal at NIST - Boulder. With the film in hand, I processed the wafer in the same manner as described above. Due to a relatively high R_{sq} and Δ , NbTiN inductors have high kinetic inductance. Materials with high L_K can be used to reduce the footprint of a resonator, while maintaining the same f_0 compared to a resonator made from a low L_K material. When the film was provided, the expected L_K was estimated to be ≈ 11 pH/Sq at 15 mK. These resonators have not been measured at 15 mK, but measurements in a 4 K closed cycle system show relatively broad resonances.

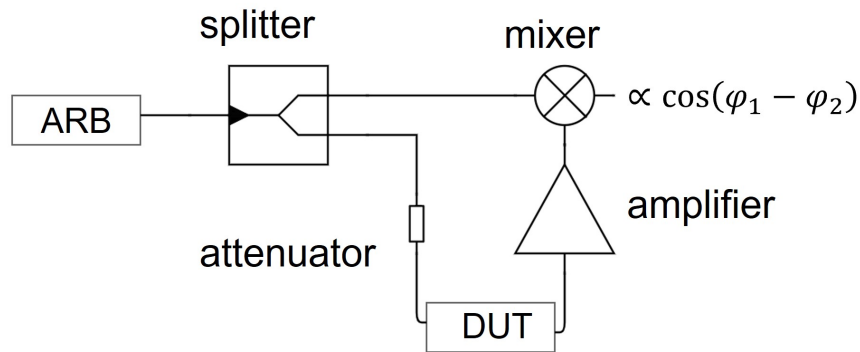


Figure A.8: State dependent readout is typically performed with a homodyne detection circuit. In parallel with device design progress, the high Q Nb resonators that I fabricated can be used to push forward towards the goal of quantum dot integration. The next step would be to demonstrate homodyne detection using the standard circuit shown. An RF signal from an arbitrary waveform generator (ARB) is split, with one component going to a mixer and the other component to the resonator (DUT). At the resonance frequency, the phase for the device signal component is altered by the resonator. The device signal component is amplified and sent to the mixer, which provides a DC output proportional to the phase difference of the input signals. Once this technique is demonstrated, the resonator can be connected to a quantum dot gate to detect tunneling events.

To summarize, I fabricated and characterized monolithic Nb superconducting LC resonators for gate-based readout of quantum dot qubits. The resonators exhibited high quality resonances of $> 10,000$. Disagreement remains between the measured f_0 (≈ 500 - 950 MHz) and the designed f_0 (70 - 150 MHz), indicating the actual LC product is ~ 2 orders of magnitude lower than the realized LC product. This issue can be addressed with more rigorous circuit analysis and fabrication of known resonator designs. Circuit elements were purchased towards implementing homodyne detection, which is an ongoing effort by my advisor Dr. Joshua Pomeroy.

Appendix B: Cross sectional SEM of Nb/Al based NIS junctions

Several devices, specifically the 155 nm and 310 nm Al devices, exhibited relatively high T_c and peak feature voltages ($\propto \Delta_{\text{Nb}}$). This can be seen in Fig. 5.17 and 5.8(b). With a targeted thickness of 40 nm, the Nb films are in a regime where changes in the film thickness has been shown to significantly alter the T_c [151, 183]. Examples in the literature show that, in this film thickness range, a deviation in Nb film thickness of ≈ 10 nm can change T_c by ~ 1 K. The effect is most often attributed to proximity effects with the substrate, where superconducting interactions are depressed in the film near the Nb/substrate interface. Extrapolating from the T_c trend with Al thickness set by the other devices measured here, the T_c for the Nb/Al bilayers in question were ≈ 0.5 K higher than expected.

If the Nb film thickness in the 155 nm and 310 nm Al devices is thicker than the Nb in other devices, the thickness related T_c could provide a plausible explanation for the behavior. Given the low resistivity ρ of Al ($\approx 6 \times 10^{-8} \Omega\cdot\text{m}$) compared to Nb ($\approx 5 \times 10^{-7} \Omega\cdot\text{m}$) in our devices, the Al thickness of these Nb/Al bilayers is high enough that significant changes in the Nb thickness would not significantly change the bilayer R_{sq} . Instead, focused ion beam etching was employed to dig a trench in the bilayer and image the device cross section with scanning electron mi-

croscopy (SEM). Four devices, two nominal devices and the two anomalous devices, were inspected. This work was performed by Dr. Joshua Schumacher at NIST - Gaithersburg.

A cross section SEM image of a nominally behaving device is shown in Fig. B.1. Ignoring a small interface region between Nb and SiO_x, the Nb thickness is ≈ 45 nm and is apparently rather uniform. The Nb/SiO_x interface region may be attributed to NbO_x, which is also detected near the Nb/SiO_x interface in XPS depth profile measurements. In Fig. B.2, cross sectional SEM images for each of the four devices are aligned according to the bright Nb/Al interface. Two nominal devices are on the left and two anomalous devices are on the right. The dashed white line indicates the bottom of the Nb film in the nominal devices. The Nb in the anomalous devices appears ≈ 5 -10 nm thicker compared to the nominal devices. Given the thickness dependence of T_c in this thickness range, this comparison provides a plausible explanation for the relatively high T_c and Δ values observed in the anomalous devices.

The Nb and Al depositions were monitored with separate QCMs. It is not clear what is responsible for the deviation in Nb thicknesses for the outliers discussed here. However, I have not seen any evidence to suggest that the Al thickness (or any other film thicknesses in the devices) deviated in these devices.

The cross sectional SEM also revealed that the apparent Al thickness deviates from the Al thickness expected from QCM monitoring of the deposition. The SEM determined Al thicknesses are plotted against the QCM determined thickness in Fig. B.3. The uncertainty in the SEM thickness is determined by the variation in the

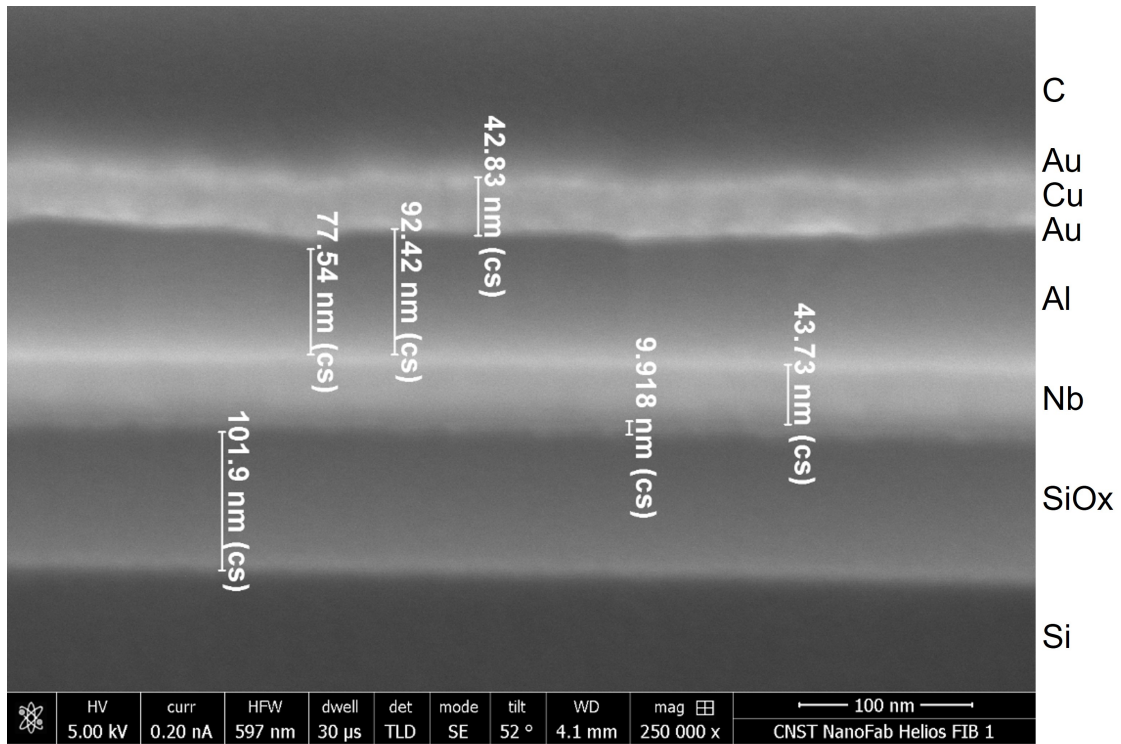


Figure B.1: Cross sectional SEM image of an Nb/Al bilayer based NIS tunnel junction. This device is one of the nominally behaving control devices. A layer of carbon is deposited prior to FIB to protect the surface from damage. The imaging software is used to measure and annotate the layer thicknesses. The elemental labels are inferred from the changes in contrast and the expected film stack.

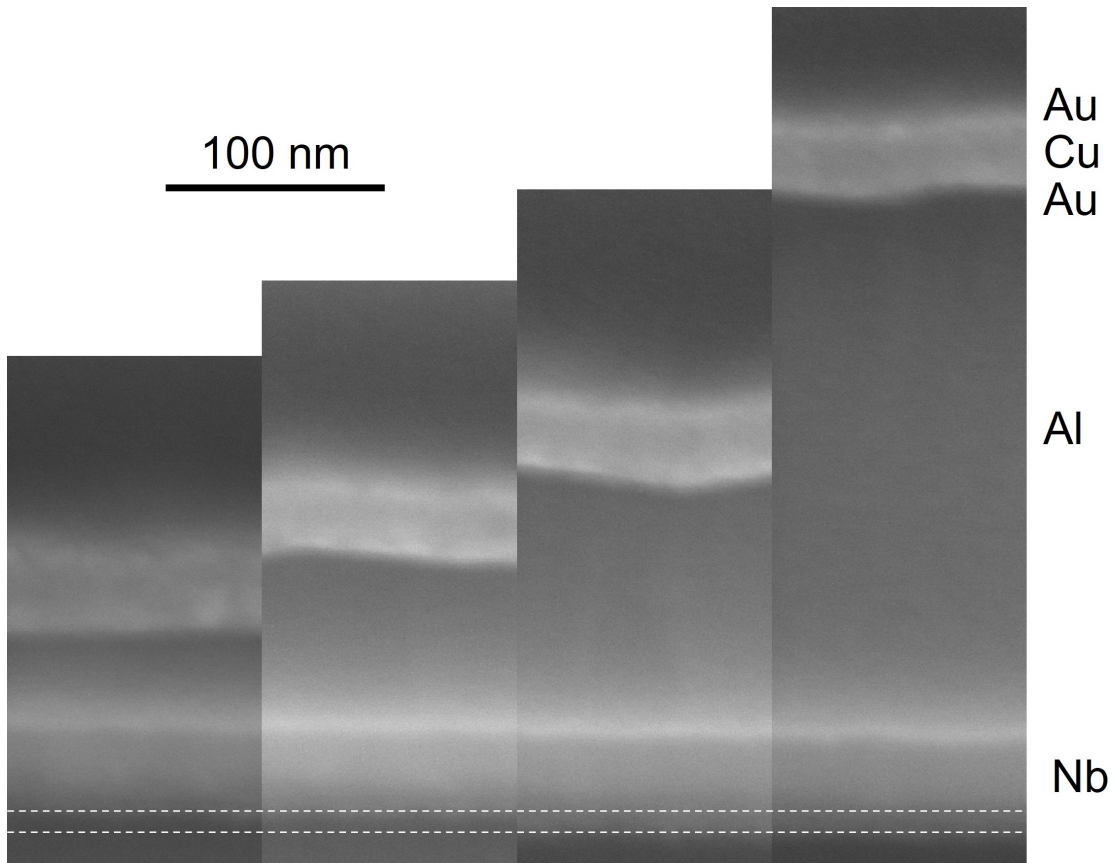


Figure B.2: Cross section SEM images for each film are aligned according to the Nb/Al interface. Each image is taken at 250,000 x magnification. The nominal devices are the two on the left, while the anomalous devices are the two on the right. The white dashed line indicates the bottom of Nb layer for the nominal devices.

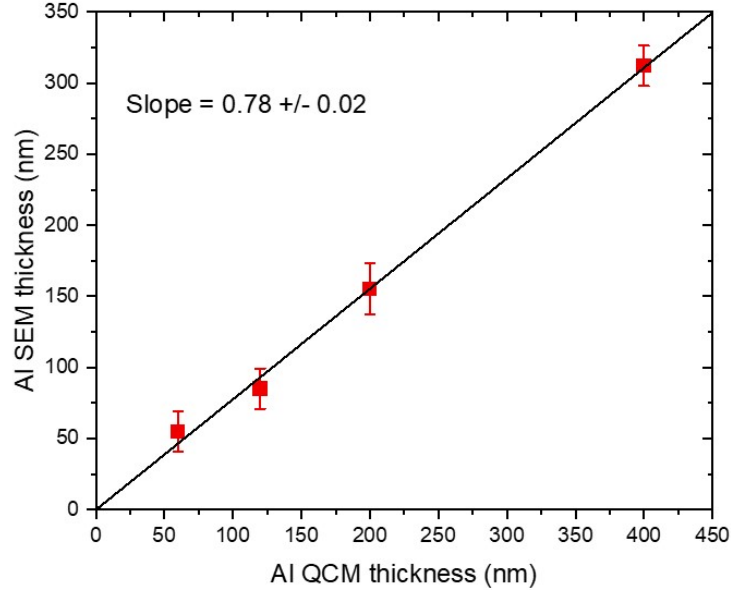


Figure B.3: The Al thickness determined by cross sectional SEM is plotted against the Al thickness expected from quartz crystal microbalance (QCM) monitoring during deposition.

film thickness over a lateral distance of $\approx 1 \mu\text{m}$. A linear fit to the data has a slope of 0.78 ± 0.02 , where the uncertainty is one standard deviation in the fit value. To correct for this deviation, the QCM determined Al film thicknesses for all devices are multiplied by a factor of 0.78. The Al thicknesses used in Chapter 5 are the corrected values.

Bibliography

- [1] Y. Huai. Magnetic tunnel junction having diffusion stop layer, 2009. URL <https://www.google.com/patents/US7576956>.
- [2] N. P. de Leon, K. M. Itoh, D. Kim, K. K. Mehta, T. E. Northup, H. Paik, B. S. Palmer, N. Samarth, S. Sangtawesin, and D. W. Steuerman. Materials challenges and opportunities for quantum computing hardware. *Science*, 372 (6539), 2021. doi: 10.1126/science.abb2823.
- [3] M. Bohr. A 30 year retrospective on dennard’s mosfet scaling paper. *IEEE Solid-State Circuits Society Newsletter*, 12(1), 2014. doi: 10.1109/N-SSC.2007.4785534.
- [4] J. R. Powell. The quantum limit to moore’s law. *Proceedings of the IEEE*, 96 (8), 2008. doi: 10.1109/JPROC.2008.925411.
- [5] T. S. Humble, H. Thapliyal, E. Munoz-Coreas, F. A. Mohiyaddin, and R. S. Bennink. Quantum computing circuits and devices. *IEEE Design and Test*, 36(3), 2019. doi: 10.1109/MDAT.2019.2907130.
- [6] T. Luhmann, R. John, R. Wunderlich, J. Meijer, and S. Pezzagna. Coulomb-driven single defect engineering for scalable qubits and spin sensors in diamond. *Nature Communications*, 10, 2019. doi: 10.1038/s41467-019-12556-0.
- [7] C. Bruzewicz, J. Chiaverini, R. McConnel, and J. M. Sage. Trapped-ion quantum computing: Progress and challenges. *Applied Physics Reviews*, 6 (2), 2019. doi: 10.1063/1.5088164.
- [8] J. Yoneda, W. Huang, M. Feng, C. H. Yang, K. W. Chan, T. Tantt, W. Gilbert, R. C. C. Leon, F. E. Hudson, K. M. Itoh, A. Morello, S. D. Bartlett, A. Laucht, A. Saraiva, and A. S. Dzurak. Coherent spin qubit transport in silicon. *Nature Communications*, 12, 2021. doi: 10.1038/s41467-021-24371-7.
- [9] J. T. Muhonen, J. P. Dehollain, A. Laucht, F. E. Hudson, R. Kalra, T. Sekiguchi, K. M. Itoh, D. N. Jamieson, J. C. McCallum, A. S. Dzurak,

- and A. Morello. Storing quantum information for 30 seconds in a nanoelectronic device. *Nature Nanotechnology*, 9, 2014. doi: 10.1038/nnano.2014.211.
- [10] H. Paik, D. I. Schuster, L. S. Bishop, G. Kirchmair, G. Catelani, A. P. Sears, B. R. Johnson, M. J. Reagor, L. Frunzio, L. I. Glazman, S. M. Girvin, M. H. Devoret, and R. J. Schoelkopf. Observation of high coherence in josephson junction qubits measured in a three-dimensional circuit qed architecture. *Phys. Rev. Lett.*, 107(24), 2011. doi: 10.1103/PhysRevLett.107.240501.
- [11] K. Saeedi, S. Simmons, J. Z. Salvail, P. Dluhy, H. Riemann, N. V. Abrosimov, P. Becker, H. J. Pohl, J. J. L. Morton, and M. L. W. Thewalt. Room-temperature quantum bit storage exceeding 39 minutes using ionized donors in silicon-28. 342(6160), 2013. doi: 10.1126/science.1239584.
- [12] M. Steger, K. Saeedi, M. L. W. Thewalt, J. J. L. Morton, H. Riemann, N. V. Abrosimov, P. Becker, and H. J. Pohl. Quantum information storage for over 180 s using donor spins in a 28si “semiconductor vacuum”. *Science*, 336(6086), 2012. doi: 10.1126/science.1217635.
- [13] P. Scarlino, D. J. van Woerkom, U. C. Mendes, J. V. Koski, A. J. Landig, C. K. Andersen, S. Gasparinetti, C. Reichl, W. Wegscheider, K. Ensslin, T. Ihn, A. Blais, and A. Wallraff. Coherent microwave-photon-mediated coupling between a semiconductor and a superconducting qubit. *Nature Communications*, 10, 2019. doi: 10.1038/s41467-019-10798-6.
- [14] M. Benito and B. Guido. Hybrid superconductor-semiconductor systems for quantum technology. *Applied Physics Letters*, 116, 2020. doi: 10.1063/5.0004777.
- [15] Y. Hong, R. Stein, M. D. Stewart Jr., N. M. Zimmerman, and J. M. Pomeroy. Reduction of charge offset drift using plasma oxidized aluminum in sets. *Scientific Reports*, 10, 2020. doi: 10.1038/s41598-020-75282-4.
- [16] W. D. Oliver and P. B. Welander. Materials in superconducting quantum bits. *MRS Bulletin*, 38(10: Materials issues for quantum computation), 2013. doi: 10.1557/mrs.2013.229.
- [17] D. Vion, A. Aassime, A. Cottet, P. Joyez, H. Pothier, C. Urbina, D. Esteve, and M. H. Devoret. Manipulating the quantum state of an electrical circuit. *Science*, 296(5569), 2002. doi: 10.1126/science.1069372.
- [18] J. Koch, T. M. Yu, J. Gambetta, A. A. Houck, D. I. Schuster, J. Majer, A. Blais, M. H. Devoret, S. M. Girvin, and R. J. Schoelkopf. Charge-insensitive qubit design derived from the cooper pair box. *Phys. Rev. A*, 76(4), 2007. doi: 10.1103/PhysRevA.76.042319.
- [19] A. A. Houck, J. Koch, M. H. Devoret, S. M. Girvin, and R. J. Schoelkopf. Life after charge noise: recent results with transmon qubits. *Quantum Information Processing*, 8, 2009. doi: 10.1007/s11128-009-0100-6.

- [20] A. Bilmes, S. Volosheniuk, A. V. Ustinov, and J. Lisenfeld. Probing defect densities at the edges and inside josephson junctions of superconducting qubits. *npj Quantum Information*, 8(24), 2022. doi: 10.1038/s41534-022-00532-4.
- [21] J. Lisenfeld, A. Bilmes, S. Matityahu, S. Zanker, M. Marthaler, M. Schecter, Gerd Schon, A. Shnirman, G. Weiss, and A. V. Ustinov. Decoherence spectroscopy with individual two-level tunneling defects. *Scientific Reports*, 6, 2016. doi: 10.1038/srep23786.
- [22] J. R. Nesbitt and A. F. Hebard. Time-dependent glassy behavior of interface states in al-al_x-al tunnel junctions. *Phys. Rev. B*, 75, 2007. doi: 10.1103/PhysRevB.75.195441.
- [23] J. M. Martinis, K. B. Cooper, R. McDermott, M. Steffen, M. Ansmann, K. D. Osborn, K. Cicak, S. Oh, D. P. Pappas, R. W. Simmonds, and C. C. Yu. Decoherence in josephson qubits from dielectric loss. *Phys. Rev. Lett.*, 95(21), 2005. doi: 10.1103/PhysRevLett.95.210503.
- [24] M. Steffen, M. Ansmann, R. McDermott, N. Katz, R. C. Bialczak, E. Lucero, M. Neeley, E. M. Weig, A. N. Cleland, and J. M. Martinis. State tomography of capacitively shunted phase qubits with high fidelity. *Physical Review Letters*, 97(5), 2006. doi: 10.1103/PhysRevLett.97.050502.
- [25] S. Nakano, S. Taguchi, Y. Kamakura, and K. Taniguchi. Time evolution of resistance drift of magnetic tunnel junctions with ultrathin alox films. *ECS Transactions*, 19(2), 2009. doi: 10.1149/1.3122126.
- [26] S. Fritz, A. Seiler, L. Radtke, R. Schneider, M. Weides, G. Weiss, and D. Gerthsen. Correlating the nanostructure of al-oxide with deposition conditions and dielectric contributions of two-level systems in perspective of superconducting quantum circuits. *Scientific Reports*, 8, 2018. doi: 10.1038/s41598-018-26066-4.
- [27] E. Schiliro, P. Fiorenza, C. Bongiorno, C. Spinella, S. Di Franco, G. Greco, R. Lo Nigro, and F. Roccaforte. Correlating electron trapping and structural defects in al₂o₃ thin films deposited by plasma enhanced atomic layer deposition. *AIP Advances*, 10(12), 2020. doi: 10.1063/5.0023735.
- [28] T. C. DuBois, M. C. Per, S. P. Russo, and J. H. Cole. Delocalized oxygen as the origin of two-level defects in josephson junctions. *Physical Review Letters*, 110(7), 2013. doi: 10.1103/PhysRevLett.110.077002.
- [29] L. J. Zeng, D. T. Tran, C. W. Tai, G. Svensson, and E. Olsson. Atomic structure and oxygen deficiency of the ultrathin aluminium oxide barrier in al/alox/al josephson junctions. *Scientific Reports*, 6, 2016. doi: 10.1038/srep29679.

- [30] S. Oh, K. Cicak, R. McDermott, K. B. Cooper, K. D. Osborn, R. W. Simmonds, M. Steffen, J. M. Martinis, and D. P. Pappas. Low-leakage superconducting tunnel junctions with a single-crystal Al_2O_3 barrier. *Superconductor Science and Technology*, 18(10):1396–1399, 2005. ISSN 0953-2048 1361-6668. doi: 10.1088/0953-2048/18/10/026.
- [31] F. Arute, K. Arya, R. Babbush, D. Bacon, J. C. Bardin, R. Barends, and R. Biswas. Quantum supremacy using a programmable superconducting processor. *Nature*, 574, 2019. doi: 10.1038/s41586-019-1666-5.
- [32] O. Dial. Eagle’s quantum performance progress, 2022. URL <https://research.ibm.com/blog/eagle-quantum-processor-performance>.
- [33] N. Yoshikawa. Superconducting digital electronics for controlling quantum computing systems. *IEICE Trans. Electron.*, 102(3), 2019. doi: 10.1587/transele.2018SDI0003.
- [34] L. Howe, M. Castellanos-Beltran, A. J. Sirois, D. Olaya, J. Biesecker, P. D. Dresselhaus, S. P. Benz, and P. F. Hopkins. Digital control of a superconducting qubit using a Josephson pulse generator at 3 k. *PRX Quantum*, 3(1), 2022. doi: 10.1103/PRXQuantum.3.010350.
- [35] D. Bach, H. Stormer, R. Schneider, D. Gerthsen, and J. Verbeeck. EELS investigations of different niobium oxide phases. *Microscopy and Microanalysis*, 12(5), 2006. doi: 10.1017/S1431927606060521.
- [36] C. E. Murray. Material matters in superconducting qubits. *Materials Science and Engineering R*, 146, 2021. doi: 10.1016/j.mser.2021.100646.
- [37] J. Bardeen, L. N. Cooper, and J. R. Schrieffer. Theory of superconductivity. *Phys. Rev.*, 108(5), 1957. doi: 10.1103/PhysRev.108.1175.
- [38] S. Zhao, D. J. Goldie, C. N. Thomas, and S. Withington. Calculation and measurement of critical temperature in thin superconducting multilayers. *Superconductor Science and Technology*, 31(10), 2018. doi: 10.1088/1361-6668/aad788.
- [39] A. Zehnder, Ph. Lerch, S. P. Zhao, Th. Nussbaumer, E. C. Kirk, and H. R. Ott. Proximity effects in Nb-Al-AlOx-Al-Nb superconducting tunneling junctions. *Physical Review B*, 59(13), 1999. doi: 10.1103/PhysRevB.59.8875.
- [40] M. Tinkham. *Introduction to Superconductivity*. Dover Publications, 2004. ISBN 0486435032.
- [41] J. Clark. The proximity effect between superconducting and normal thin films in zero field. *Journal de Physique Colloques*, 29, 1968. doi: 10.1051/jphyscol:1968201.

- [42] K. Serniak, M. Hays, G. de Lange, S. Diamond, S. Shankar, L. D. Burkhardt, L. Frunzio, M. Houzet, and M. H. Devoret. Hot nonequilibrium quasiparticles in transmon qubits. *Physical Review Letters*, 121(15), 2018. doi: 10.1103/PhysRevLett.121.157701.
- [43] A. B. Pavolotsky, D. Dochev, and V. Belitsky. Aging- and annealing-induced variations in nb/al-al_x/nb tunnel junction properties. *J. Appl. Phys.*, 109, 2011. doi: 10.1063/1.3532040.
- [44] P. J. Koppinen, L. M. Vaisto, and I. J. Maasilta. Complete stabilization and improvement of the characteristics of tunnel junctions by thermal annealing. *Applied Physics Letters*, 90(5):053503, 2007. ISSN 00036951. doi: 10.1063/1.2437662.
- [45] A. E. T. Kuiper, M. F. Gillies, V. Kottler, G. W. 't Hooft, J. G. M. van Berkum, C. van der Marel, Y. Tamminga, and J. H. M. Snijders. Plasma oxidation of thin aluminum layers for magnetic spin-tunnel junctions. *J. Appl. Phys.*, 89(3), 2001. doi: 10.1063/1.1334644.
- [46] M. F. Gillies, A. E. T. Kuiper, R. Coehoorn, and J. J. T. M. Donkers. Compositional, structural, and electric characterization of plasma oxidized thin aluminum layers for spin tunnel junctions. *Journal of Applied Physics*, 88(1): 429–434, 2000. doi: 10.1063/1.373677.
- [47] C.A.M. Knechten. *Plasma oxidation for magnetic tunnel junctions*. Thesis, 2005.
- [48] M. R. Alexander, G. E. Thompson, X. Zhou, G. Beamson, and N. Fairley. Quantification of oxide film thickness at the surface of aluminium using xps. *Surf. Interface. Anal.*, 34, 2002. doi: 10.1002/sia.1344.
- [49] Yuriy Makhlin, Gerd Schön, and Alexander Shnirman. Quantum-state engineering with josephson-junction devices. *Reviews of Modern Physics*, 73(2): 357–400, 2001. doi: 10.1103/RevModPhys.73.357.
- [50] Jukka P. Pekola, Olli-Pentti Saira, Ville F. Maisi, Antti Kemppinen, Mikko Möttönen, Yuri A. Pashkin, and Dmitri V. Averin. Single-electron current sources: Toward a refined definition of the ampere. *Reviews of Modern Physics*, 85(4):1421–1472, 2013. ISSN 0034-6861 1539-0756. doi: 10.1103/RevModPhys.85.1421.
- [51] R. Meservey and P.M. Tedrow. Spin-polarized electron tunneling. *Physics Reports*, 238(4):173–243, 1994. doi: 10.1016/0370-1573(94)90105-8.
- [52] E. L. Wolf. *Principles of electron tunneling spectroscopy*. Oxford University Press, 2nd edition edition, 2012. ISBN 9780199589494.
- [53] *Tunneling Phenomena in Solids*. 1 edition, 1969. ISBN 978-0-306-30362-3. doi: 10.1007/978-1-4684-1752-4.

- [54] Russell E. Lake. *Interaction of Highly Charged Ions with Ultrathin Dielectric Films*. Thesis, 2012.
- [55] J. H. Moore, C. C. Davis, and M. A. Coplan. *Building scientific apparatus: a practical guide to design and construction*. 1983.
- [56] L. Wang, Y. Zhong, J. Li, W. Cao, Q. Zhong, X. Wang, and X. Li. Effect of residual gas on structural, electrical and mechanical properties of niobium films deposited by magnetron sputtering deposition. *Materials Research Express*, 5(4), 2018. doi: 10.1088/2053-1591/aab8c1.
- [57] Inc. Thermionics Laboratory. *DSC Digital Sweep Controller Instruction Manual*. Hayward, CA, 2020.
- [58] INFICON Inc. *SQC-310TM thin Film Deposition Controller Operating Manual*. East Syracuse, NY, 2011.
- [59] Galit Levitin, Christopher Timmons, and Dennis W. Hess. Photoresist and etch residue removal. *Journal of The Electrochemical Society*, 153(7):G712, 2006. ISSN 00134651. doi: 10.1149/1.2203096.
- [60] M. Johnson and R. H. Silsbee. Spin-injection experiment. *Phys Rev B Condens Matter*, 37(10):5326–5335, 1988. ISSN 0163-1829 (Print) 0163-1829 (Linking). doi: 10.1103/physrevb.37.5326.
- [61] Amorn Thedsakhulwong and Warawoot Thowladda. Removal of carbon contamination on silicon wafer surfaces by microwave oxygen plasma. *Journal of Metals, Materials, and Minerals*, 18(2):137–141, 2008.
- [62] Fumitoshi Sugimoto and Sigeru Okamura. Adsorption behavior of organic contaminants on a silicon wafer surface. *Journal of The Electrochemical Society*, 146(7):2725–2729, 1999.
- [63] KEPCO Inc. *DC power supply BHK-MG full rack series operator’s manual*. Flushing, NY, 2019. URL www.kepcopower.com.
- [64] J. M. Pomeroy and H. Grube. “negative resistance” errors in four-point measurements of tunnel junctions and other crossed-wire devices. *Journal of Applied Physics*, 105(9):094503, 2009. ISSN 00218979. doi: 10.1063/1.3122503.
- [65] B. J. Jónsson-Åkerman, A. H. Romero, R. Escudero, C. Leighton, S. Kim, I. K. Schuller, and D. A. Rabson. Reliability of normal-state current-voltage characteristics as an indicator of tunnel-junction barrier quality. *Applied Physics Letters*, 77(12), 2000. doi: 10.1063/1.1310633.
- [66] D. A. Rabson, B. J. Jónsson-Åkerman, A. H. Romero, R. Escudero, C. Leighton, S. Kim, and I. K. Schuller. Pinholes may mimic tunneling. *Journal of Applied Physics*, 89(5), 2001. doi: 10.1063/1.1344220.

- [67] J. G. Simmons. Generalized formula for the electric tunnel effect between similar electrodes separated by a thin insulating film. *Journal of Applied Physics*, 34(6), 1963. doi: 10.1063/1.1702682.
- [68] W. F. Brinkman, R. C. Dynes, and J. M. Rowell. Tunneling conductance of asymmetrical barriers. *Journal of Applied Physics*, 41(5), 1970. doi: 10.1063/1.1659141.
- [69] C. K. Chow. Square-mean-root approximation for evaluating asymmetric tunneling characteristics. *Journal of Applied Physics*, 36(2):559–564, 1965. doi: 10.1063/1.1714030.
- [70] Z. S. Barcikowski and J. M. Pomeroy. Reduced resistance drift in tunnel junctions using confined tunnel barriers. *Journal of Applied Physics*, 122(18):185107, 2017. doi: 10.1063/1.4996497. URL <https://aip.scitation.org/doi/abs/10.1063/1.4996497>.
- [71] H. Ibach and H. Lüth. *Solid-State Physics: An Introduction to Principles of Materials Science*. 4 edition, 2009. ISBN 978-3-540-93803-3. doi: 10.1007/978-3-540-93804-0.
- [72] A. Andreone, A. Cassinese, M. Iavarone, R. Vaglio, II Kulik, I. I., and V. V. Palmieri. Relation between normal-state and superconductive properties of niobium sputtered films. *Phys Rev B Condens Matter*, 52(6):4473–4476, 1995. ISSN 0163-1829 (Print) 0163-1829 (Linking). doi: 10.1103/physrevb.52.4473.
- [73] R. Stratton. Volt-current characteristics for tunneling through insulating films. *J. Phys. Chem. Solids*, 23:1177–1190, 1962. doi: 10.1016/0022-3697(62)90165-8.
- [74] John G. Simmons. Generalized thermal j-v characteristic for the electric tunnel effect. *Journal of Applied Physics*, 35(9):2655–2658, 1964. ISSN 0021-8979 1089-7550. doi: 10.1063/1.1713820.
- [75] Y. Xu, D. Ephron, and M. R. Beasley. Directed inelastic hopping of electrons through metal-insulator-metal tunnel junctions. *Physical Review B*, 52(4), 1995. doi: 10.1103/PhysRevB.52.2843.
- [76] U. Rüdiger, R. Calarco, U. May, K. Samm, J. Hauch, H. Kittur, M. Sperlich, and G. Güntherodt. Temperature dependent resistance of magnetic tunnel junctions as a quality proof of the barrier. *Journal of Applied Physics*, 89(11):7573–7575, 2001. ISSN 0021-8979 1089-7550. doi: 10.1063/1.1361055.
- [77] G. E. Blonder, M. Tinkham, and T. M. Klapwijk. Transition from metallic to tunneling regimes in superconducting microconstrictions: Excess current, charge imbalance, and supercurrent conversion. *Physical Review B*, 25(7):4515–4532, 1982. ISSN 0163-1829. doi: 10.1103/PhysRevB.25.4515.

- [78] P. LeClair, J. T. Kohlhepp, A. A. Smits, H. J. M. Swagten, B. Koopmans, and W. J. M. De Jonge. Optical and in situ characterization of plasma oxidized al for magnetic tunnel junctions. *Journal of Applied Physics*, 87(9):6070–6072, 2000.
- [79] T. Shiota, T. Imamura, and S. Hasuo. Fabrication of high quality nb/al_x-al/nb josephson junctions - iii: Annealing stability of al_x tunneling barriers. *IEEE Transactions of Applied Superconductivity*, 2(4), 1992. doi: 10.1109/77.182734.
- [80] Guo-Xing Miao, Krishna B. Chetry, Arunava Gupta, William H. Butler, Koji Tsunekawa, David Djayaprawira, and Gang Xiao. Inelastic tunneling spectroscopy of magnetic tunnel junctions based on cofeb/mgo/cofeb with mg insertion layer. *Journal of Applied Physics*, 99(8):08T305, 2006. ISSN 0021-8979 1089-7550. doi: 10.1063/1.2162047.
- [81] D. Dochev, A. Pavolotsky, Z. Lai, and V. Belitsky. The influence of aging and annealing on the properties of nb/al-al_x/nb tunnel junctions. *J. Phys.: Conf. Ser.*, 234, 2010. doi: 10.1088/1742-6596/234/4/042006.
- [82] R. C. Sousa, J. J. Sun, V. Soares, and P. P. Freitas. Large tunneling magnetoresistance enhancement by thermal anneal. *Appl. Phys. Lett.*, 73, 1998. doi: 10.1063/1.122747.
- [83] W. A. Phillips. Tunneling states in amorphous solids. *Journal of Low Temperature Physics*, 7, 1971. doi: 10.1007/BF00660072.
- [84] I. M. Pop, T. Fournier, T. Crozes, F. Lecocq, I. Matei, B. Pannetier, O. Buisson, and W. Guichard. Fabrication of stable and reproducible submicron tunnel junctions. *Journal of Vacuum Science and Technology B*, 30, 2012. doi: 10.1116/1.3673790.
- [85] J. V. Gates, M. A. Washington, and M. Gurvitch. Critical current uniformity and stability of nb/al-oxide-nb josephson junctions. *J. Appl. Phys.*, 55, 1984. doi: 10.1063/1.333235.
- [86] Aaron D. O’Connell, M. Ansmann, R. C. Bialczak, M. Hofheinz, N. Katz, Erik Lucero, C. McKenney, M. Neeley, H. Wang, E. M. Weig, A. N. Cleland, and J. M. Martinis. Microwave dielectric loss at single photon energies and millikelvin temperatures. *Applied Physics Letters*, 92(11):112903, 2008. ISSN 0003-6951 1077-3118. doi: 10.1063/1.2898887.
- [87] M. J. Cyster, J. S. Smith, J. A. Vaitkus, N. Vogt, S. P. Russo, and J. H. Cole. Effect of atomic structure on the electrical response of aluminum oxide tunnel junctions. *Physical Review Research*, 2(1), 2020. ISSN 2643-1564. doi: 10.1103/PhysRevResearch.2.013110.

- [88] E. Tan, P. G. Mather, A. C. Perrella, J. C. Read, and R. A. Buhrman. Oxygen stoichiometry and instability in aluminum oxide tunnel barrier layers. *Physical Review B*, 71(16), 2005. ISSN 1098-0121 1550-235X. doi: 10.1103/PhysRevB.71.161401.
- [89] L. P. H. Jeurgens, W. G. Sloof, F. D. Tichelaar, and E. J. Mittemeijer. Growth kinetics and mechanisms of aluminum-oxide films formed by thermal oxidation of aluminum. *J. Appl. Phys.*, 92(3), 2002. doi: 10.1063/1.1491591.
- [90] N. F. Mott. The theory of the formation of protective oxide films on metals iii. *J. Faraday Soc.*, 43, 1947.
- [91] N. Cabrera and N. F. Mott. Theory of the oxidation of metals. *Rep. Prog. Phys.*, 12, 1949.
- [92] A. T. A. Wee, S. X. Wang, and K. Sin. In-situ characterization of oxide growth for fabricating spin dependent tunnel junctions. *IEEE Transactions on Magnetism*, 35(5), 1999. doi: 10.1109/20.801043.
- [93] J. R. Rumble. *CRC Handbook of Chemistry and Physics - Internet Version 2021*. 102 edition, 2021.
- [94] J. S. Moodera, L. R. Kinder, T. M. Wong, and R. Meservey. Large magnetoresistance at room temperature in ferromagnetic thin film tunnel junctions. *Phys Rev Lett*, 74(16):3273–3276, 1995. ISSN 1079-7114 (Electronic) 0031-9007 (Linking). doi: 10.1103/PhysRevLett.74.3273.
- [95] J. S. Moodera and G. Mathon. Spin polarized tunneling in ferromagnetic junctions. *Journal of Magnetism and Magnetic Materials*, 200(1-3), 1999. doi: 10.1016/S0304-8853(99)00515-6.
- [96] Donkoun Lee and Jongill Hong. The redistribution of oxygen at alox/cofe interface of magnetic tunnel junctions through thermal treatment. *Journal of Applied Physics*, 97(9):093905, 2005. ISSN 00218979. doi: 10.1063/1.1885185.
- [97] W. C. Martin and W. L. Wiese. Atomic spectroscopy - a compendium of basic ideas, notation, data, and formulas, 2019. URL <https://www.nist.gov/pml/atomic-spectroscopy-compendium-basic-ideas-notation-data-and-formulas>.
- [98] P. K. Chu, S. Qin, C. Chan, N. W. Cheung, and P. K. Ko. Instrumental and process considerations for the fabrication of silicon-on-insulators (soi) structures by plasma immersion ion implantation. *IEEE Transactions on Plasma Science*, 26(1):79–84, 1998. doi: 10.1109/27.659535.
- [99] J. Bohdanský, J. Roth, and H. L. Bay. An analytical formula and important parameters for low-energy ion sputtering. *Journal of Applied Physics*, 51(5), 1980. doi: 10.1063/1.327954.

- [100] N. Arakawa, Y. Otaka, and K. Shiiki. Evaluation of barrier height and thickness in tunneling junctions by numerical calculation on tunnel probability. *Thin Solid Films*, 505(1-2):67–70, 2006. ISSN 00406090. doi: 10.1016/j.tsf.2005.10.043.
- [101] P. R. Aghdam, H. M. Rashid, A. Pavolotsky, V. Desmaris, and V. Belitsky. Dependence of the scatter of the electrical properties on local non-uniformities of the tunnel barrier in nb alox nb junctions. *Journal of Applied Physics*, 119:054502, 2016. doi: 10.1063/1.4941346].
- [102] L. J. Zeng, S. Nik, T. Greibe, P. Krantz, C. M. Wilson, P. Delsing, and E. Olsson. Direct observation of the thickness distribution of ultra thin aloxbarriers in al/alox/al josephson junctions. *Journal of Physics D: Applied Physics*, 48(39):395308, 2015. ISSN 0022-3727 1361-6463. doi: 10.1088/0022-3727/48/39/395308.
- [103] T. Aref, A. Averin, S. van Dijken, A. Ferring, M. Koberidze, V. F. Maisi, H. Q. Nguyend, R. M. Nieminen, J. P. Pekola, and L. D. Yao. Characterization of aluminum oxide tunnel barriers by combining transport measurements and transmission electron microscopy imaging. *Journal of Applied Physics*, 116(7):073702, 2014. ISSN 0021-8979 1089-7550. doi: 10.1063/1.4893473.
- [104] J. M. Pomeroy, H. Grube, P. L. Sun, and R. E. Lake. Magnetic tunnel junctions fabricated using ion neutralization energy as a tool. *AIP Conference Proceedings*, 13:111–114, 2010.
- [105] Yu-Ren Lai, Kai-Fu Yu, Yong-Han Lin, Jong-Ching Wu, and Juhn-Jong Lin. Observation of fluctuation-induced tunneling conduction in micrometer-sized tunnel junctions. *AIP Advances*, 2(3):032155, 2012. ISSN 2158-3226. doi: 10.1063/1.4749251.
- [106] O. Kurnosikov, F. C. de Nooij, P. LeClair, J. T. Kohlhepp, B. Koopmans, H. J. M. Swagten, and W. J. M. de Jonge. Stm-induced reversible switching of local conductivity in thinal2o3films. *Physical Review B*, 64(15), 2001. ISSN 0163-1829 1095-3795. doi: 10.1103/PhysRevB.64.153407.
- [107] G. R. Caskey Jr., R. G. Derrick, and M. R. Louthan Jr. Hydrogen diffusion in cobalt. *Scripta Metallurgica*, 8:481–486, 1974.
- [108] T. Holmqvist, M. Meschke, and J. P. Pekola. Double oxidation scheme for tunnel junction fabrication. *Journal of Vacuum Science and Technology B: Microelectronics and Nanometer Structures*, 26(1):28, 2008. ISSN 10711023. doi: 10.1116/1.2817629.
- [109] K. S. Yoon, J. H. Park, J. H. Choi, J. Y. Yang, C. H. Lee, C. O. Kim, J. P. Hong, and T. W. Kang. Performance of co/al2o3/nife magnetic tunnel junctions prepared by a two-step rf plasma oxidation method. *Applied Physics Letters*, 79(8):1160, 2001. ISSN 00036951. doi: 10.1063/1.1391407.

- [110] Neil M. Zimmerman, William H. Huber, Brian Simonds, Emmanouel Hourdakis, Akira Fujiwara, Yukinori Ono, Yasuo Takahashi, Hiroshi Inokawa, Miha Furlan, and Mark W. Keller. Why the long-term charge offset drift in si single-electron tunneling transistors is much smaller (better) than in metal-based ones: Two-level fluctuator stability. *Journal of Applied Physics*, 104(3): 033710, 2008. ISSN 0021-8979 1089-7550. doi: 10.1063/1.2949700.
- [111] J. K. Julin, P. J. Koppinen, and I. J. Maasilta. Reduction of low-frequency 1/f noise in al-al₂O₃-al tunnel junctions by thermal annealing. *Appl. Phys. Lett.*, 97(15), 2010. doi: 10.1063/1.3500823.
- [112] P. Lapham and V. P. Georgiev. Computation study of oxide stoichiometry and variability in the al/alox/al tunnel junction. *Nanotechnology*, 33(26), 2022. doi: 10.1088/1361-6528/ac5f2e.
- [113] H. Iwai, J. S. Hammond, and S. Tanuma. Recent status of thin analyses by xps. *Journal of Surface Analysis*, 15(3), 2009. doi: 10.1384/jsa.15.264.
- [114] G. Greczynski and L. Hultman. X-ray photoelectron spectroscopy: Towards reliable binding energy referencing. *Progress in Materials Science*, 2020. doi: 10.1016/j.pmatsci.2019.100591.
- [115] M. P. Seah, I. S. Gilmore, and S. J. Spencer. Quantitative xps i. analysis of x-ray photoelectron intensities from elemental data in a digital photoelectron database. *Journal of Electron Spectroscopy and Related Phenomena*, 120, 2001. doi: 10.1016/S0368-2048(01)00311-5.
- [116] J. M. Hill, D. G. Royce, C. S. Fadley, L. F. Wagner, and F. J. Grunthaner. Properties of oxidized silicon as determined by angular-dependent x-ray photoelectron spectroscopy. *Chemical Physics Letters*, 44(2), 1976. doi: 10.1016/0009-2614(76)80496-4.
- [117] Thermo Fisher Scientific. Angle resolved xps - application note 31014. Report, 2008.
- [118] M. H. Engelhard, D. R. Baer, A. Herrera-Gomez, and P. M. A. Sherwood. Introductory guide to backgrounds in xps spectra and their impact on determining peak intensities. *J. Vac. Sci. Technol. A*, 38, 2020. doi: 10.1116/6.0000359.
- [119] D. R. Lide. *CRC handbook of chemistry and physics: a ready-reference book of chemical and physical data*. CRC Press, 85 edition, 2004. ISBN 978-0-8493-0566-5.
- [120] V. Cimalla, M. Baeumler, L. Kirste, M. Prescher, B. Christian, T. Passow, F. Benkhelifa, F. Bernhardt, G. Eichapfel, M. Himmerlich, S. Krischok, and J. Pezoldt. Densification of thin aluminum oxide films by thermal treatments. *Materials Sciences and Applications*, 5, 2014. doi: 10.4236/msa.2014.58065.

- [121] J. H. Scofield. Hartree-slater subshell photoionization cross sections at 1254 and 1487 ev. *Journal of Electron Spectroscopy and Related Phenomena*, 8(2), 1976. doi: 10.1016/0368-2048(76)80015-1.
- [122] C. J. Powell and A. Jablonski. *NIST Electron Inelastic-Mean-Free-Path Database Version 1.2 SRD 71*. National Institute of Standards and Technology, Gaithersburg, MD, 2010.
- [123] M.P. Seah, S.J. Spencer, F. Bensebaa, I. Vickridge, H. Danzebrink, M. Krumrey, T. Gross, W. Oesterle, E. Wendler, and B. Rheinländer. Critical review of the current status of thickness measurements for ultrathin sio₂ on si part v: Results of a ccqm pilot study. *Surf. Interface. Anal.*, 36:1269–1303, 2004. doi: 10.1002/sia.1909.
- [124] X. Batlle, B. J. Hattink, and A. Labarta. Quantitative x-ray photoelectron spectroscopy study of al/alox bilayers. *Journal of Applied Physics*, 91(12), 2002. doi: 10.1063/1.1478791.
- [125] Y. L. Yan, M. A. Helfand, and C. R. Clayton. Evaluation of the effect of surface roughness on thin film thickness measurements using variable angle xps. *Applied Surface Sicens*, 37, 1989. doi: 10.1016/0169-4332(89)90500-X.
- [126] P. J. Cumpson. The thickogram: a method for easy film thickness measurement in xps. *Surf. Interface. Anal.*, 29(6), 2000.
- [127] C. D. Wagner, L. E. Davis, M. V. Zeller, J. A. Taylor, R. H. Raymond, and L. H. Gale. Empirical atomic sensitivity factors for quantitative analysis by electron spectroscopy for chemical analysis. *Surf. Interface. Anal.*, 3(5), 1981. doi: 10.1002/sia.740030506.
- [128] A. G. Shard. Practical guides for x-ray photoelectron spectroscopy: Quantitative xps. *J. Vac. Sci. Technol. A*, 38(4), 2020. doi: 10.1116/1.5141395.
- [129] M. R. Nevala, S. Chaudhuri, J. Halkosaari, J. T. Karvonen, and I. J. Maasilta. Sub-micron normal-metal/insulator/superconductor tunnel junction thermometer and cooler using nb. *Applied Physics Letters*, 101(11), 2012. doi: 10.1063/1.4751355.
- [130] K. Kukli, M. Ritala, and M. Leskela. Development of dielectric properties of niobium oxide, tantalum oxide, and aluminum oxide based nanolayered materials. *Journal of The Electrochemical Society*, 148(2), 2001. doi: 10.1149/1.1343106.
- [131] J Geerk, M. Gurvitch, D. B. McWhan, and J. M. Rowell. Electron tunneling into nb/al multilayers and into nb with al overlays. *Physica 109 and 110B*, 1982. doi: 10.1016/0378-4363(82)90200-5.

- [132] S. Morohashi, F. Shinoki, A. Shoji, A. Masahiro, and H. Hayakawa. High quality nb/al-alox/nb josephson junction. *Applied Physics Letters*, 46, 1985. doi: 10.1063/1.95696.
- [133] M. Gurvitch, M. A. Washington, and H. A. Huggins. High quality refractory josephson tunnel junctions utilizing thin aluminum layers. *Appl. Phys. Lett.*, 42(5), 1982. doi: 10.1063/1.93974.
- [134] C. C. Koch, J. O. Scarbrough, and D. M. Kroeger. Effects of interstitial oxygen on the superconductivity of niobium. *Phys Rev B Condens Matter*, 9(3), 1974. doi: 10.1103/PhysRevB.9.888.
- [135] N. Koutná, P. Erdely, S. Zöhrer, R. Franz, and Y. Du. Experimental chemistry and structural stability of alnb₃ enabled by antisite defects formation. *Materials*, 12, 2019. doi: 10.3390/mal2071104.
- [136] K. Barmak, K. R. Coffey, D. A. Rudman, and S. Foner. Phase formation sequence for the reaction of multilayer thin films of nb/al. *J. Appl. Phys.*, 67(12), 1990. doi: 10.1063/1.344517.
- [137] J. M. Vandenberg, M. Hong, R. A. Hamm, and M. Gurvitch. Reactive diffusion and superconductivity of nb₃al multilayer films. *J. Appl. Phys.*, 58(1), 1985. doi: 10.1063/1.335623.
- [138] Abdennaceur Karoui. Aluminum ultra-thin films grown by physical vapor deposition for solar cell electric nanocontacts. *ECS Transactions*, 41(4), 2011. doi: 10.1149/1.3628605.
- [139] K. Mistry, M. Yavuz, and K. P. Musselman. Simulated electron affinity tuning in metal-insulator-metal (mim) diodes. *Journal of Applied Physics*, 121(18), 2017. doi: 10.1063/1.4983256.
- [140] X. Kang, L. Ying, H. Wang, G. Zhang, W. Peng, X. Kong, X. Xie, and Z. Wang. Measurements of tunneling barrier thicknesses for nb/al-alox/nb tunnel junctions. *Physica C: Superconductivity*, 2014. doi: <http://dx.doi.org/10.1016/j.physc.2014.05.006>.
- [141] S. K. Tolpygo, E. Cimpoiasu, X. Liu, N. Simonian, Y. A. Polyakov, J. E. Lukens, and K. K. Likharev. Tunneling properties of barriers in nb/al/alox/nb junctions. *IEEE Trans Appl Supercond*, 13(2), 2003. doi: 10.1109/TASC.2003.813655.
- [142] R. Ferreira, P. P. Freitas, M. Mackenzie, and J. N. Chapman. Low-resistance magnetic tunnel junctions prepared by partial remote plasma oxidation of 0.9 nm al barriers. *Applied Physics Letters*, 86(19), 2005. doi: 10.1063/1.1925318.
- [143] K. Gloos, P. J. Koppinen, and J. P. Pekola. Properties of native ultrathin aluminum oxide tunnel barriers. *Journal of Physics: Condensed Matter*, 15(10), 2003. doi: 10.1088/0953-8984/15/10/320.

- [144] J. Du, A. D. M. Charles, K. D. Petersson, and E. W. Preston. Influence of nb film surface morphology on the sub-gap leakage characteristics of nb/alox-al/nb josephson junctions. *Superconductor Science and Technology*, 20:S350–S355, 2007. doi: 10.1088/0953-2048/20/11/S10.
- [145] J. M. Rowell, M. Gurvitch, and J Geerk. Modification of tunneling barriers on nb by a few monolayers of al. *Physical Review B*, 24(4), 1981. doi: 10.1103/PhysRevB.24.2278.
- [146] J. Halbritter. On tunneling through inhomogeneous potential barriers showing resonances exemplified for nb₂o₅ barriers. *Surface Science*, 159(2-3), 1985. doi: 10.1016/0039-6028(85)90444-3.
- [147] J. R. Kirtley and D. J. Scalapino. Inelastic-tunneling model for the linear conductance background in the high-*t_c* superconductors. *Physical Review Letters*, 65(6), 1990. doi: 10.1103/PhysRevLett.65.798.
- [148] J. R. Kirtley, S. Washburn, and D. J. Scalapino. Origin of the linear tunneling conductance background. *Physical Review B*, 45(1), 1992. doi: 10.1103/PhysRevB.45.336.
- [149] S. I. Park and T. H. Geballe. *T_c* depression in thin nb films. *Physica B and C*, 135(1-3), 1985. doi: 10.1016/0378-4363(85)90447-4.
- [150] S. Morohashi, N. Takeda, S. Tsujimura, M. Kawanishi, K. Harada, S. Maekawa, N. Nakayama, and T. Noguchi. Characteristics of superconducting nb layer fabricated using high-vacuum electron beam evaporation. *Jpn. J. Appl. Phys.*, 40, 2001. doi: 10.1143/JJAP.40.576.
- [151] A. I. Gubin, K. S. Il'in, S. A. Vitusevich, M. Siegel, and N. Klein. Dependence of magnetic penetration depth on the thickness of superconducting nb thin films. *Phys. Rev. B.*, 72(6), 2005. doi: 10.1103/PhysRevB.72.064503.
- [152] T. Greibe, M. P. V. Stenberg, C. M. Wilson, T. Bauch, V. S. Shumeiko, and P. Delsing. Are “pinholes” the cause of excess current in superconducting tunnel junctions? a study of andreev current in highly resistive junctions. *Physical Review Letters*, 106(9), 2011. doi: 10.1103/PhysRevLett.106.097001.
- [153] P. J. Koppinen, T. Kuhn, and I. J. Maasilta. Effects of charging energy on sinis tunnel junction thermometry. *J. Low Temp Phys*, 154, 2009. doi: 10.1007/s10909-009-9861-7.
- [154] J. P. Pekola, V. F. Maisi, S. Kafanov, N. Chekurov, A. Kemppinen, Y. A. Pashkin, O. P. Saira, M. Mottonen, and J. S. Tsai. Environment-assisted tunneling as an origin of the dynes density of states. *Physica Review Letters*, 105(2), 2010. doi: 10.1103/PhysRevLett.105.026803.

- [155] H. Zhao, O. Mehio, W. K. Park, and L. H. Greene. Ultra-thin planar tunnel junctions grown on nb thin films by atomic layer deposition. *Thin Solid Films*, 612, 2016. doi: <http://dx.doi.org/10.1016/j.tsf.2016.06.015>.
- [156] R. C. Dynes, J. P. Garno, G. B. Hertel, and T. P. Orlando. Tunneling study of superconductivity near the metal-insulator transition. *Physica Review Letters*, 53(25), 1984. doi: 10.1103/PhysRevLett.53.2437.
- [157] O. P. Saira, A. Kemppinen, V. F. Maisi, and J. P. Pekola. Vanishing quasi-particle density in a hybrid al/cu/al single-electron transistor. *Phys. Rev. B.*, 85(1), 2012. doi: 10.1103/PhysRevB.85.012504.
- [158] T. Proslie, J. F. Zasadzinski, L. Cooley, C. Antoine, J. Moore, J. Norem, M. Pellin, and K. E. Gray. Tunneling study of cavity grade nb: Possible magnetic scattering at the surface. *Applied Physics Letters*, 92(21), 2008. doi: 10.1063/1.2913764.
- [159] J. Gifford. *Andreev Reflection Spectroscopy: Theory and Experiment*. Thesis, 2015.
- [160] V. Lukic. *Conductance of Superconductor-Normal metal Contact Junction Beyond Quasiclassical Approximation*. Thesis, 2005.
- [161] A. Plecenik, M. Grajcar, and S. Benacka. Finite-quasiparticle-lifetime effects in the differential conductance of $\text{bi}_2\text{sr}_2\text{cacu}_2\text{o}_y/\text{au}$ junctions. *Physical Review B*, 49(14), 1994. doi: 10.1103/PhysRevB.49.10016.
- [162] G. Brammertz, A. A. Golubov, A. Peacock, P. Verhoeve, E. B. Golden, and R. Venn. Modelling the energy gap in transition metal/aluminum bilayers. *Physica C: Superconductivity*, 350(3-4), 2001. doi: 10.1016/S0921-4534(00)01607-5.
- [163] J. M. Martinis, G. C. Hilton, K. D. Irwin, and D. A. Wollman. Calculation of t_c in a normal-superconductor bilayer using the microscopic-based usadel theory. *Nuclear Instruments and Methods in Physics Research Section A: Accelerators, Spectrometers, Detectors and Associated Equipment*, 444(1-2), 2000. doi: 10.1016/S0168-9002(99)01320-0.
- [164] K. Kang, J. Wang, and I. J. Beyerlein. Atomic structure variations of mechanically stable fcc-bcc interfaces. *J. Appl. Phys.*, 111(5), 2012. doi: 10.1063/1.3693015.
- [165] A. Di Marco, V. F. Maisi, F. W. J. Hekking, and J. P. Pekola. Effect of photon-assisted andreev reflection in the accuracy of a sinis turnstile. *Phys Rev B Condens Matter*, 92(9), 2015. doi: 10.1103/PhysRevB.92.094514.
- [166] M. Houzet, K. Serniak, G. Catelani, M. H. Devoret, and L. I. Glazman. Photon-assisted charge-parity jumps in a superconducting qubit. *Physical Review Letters*, 123(10), 2019. doi: 10.1103/PhysRevLett.123.107704.

- [167] Y. Hong, A. N. Ramanayaka, R. Stein, M. D. Stewart, and J. M. Pomeroy. Developing single-layer metal-oxide-semiconductor quantum dots for diagnostic qubits. *J. Vac. Sci. Technol. B*, 39(1), 2021. doi: 10.1116/6.0000549.
- [168] V. Cherkez, J. C. Cuevas, C. Brun, T. Cren, G. Menard, F. Debontridder, V. S. Stolyarov, and D. Roditchev. Proximity effect between two superconductors spatially resolved by scanning tunneling spectroscopy. *Physical Review X*, 4, 2014. doi: 10.1103/PhysRevX.4.011033.
- [169] I. P. Nevirkovets, J. B. Ketterson, S. E. Shafranjuk, and S. Lomatch. Possible manifestation of andreev bound states in double-barrier nb/al/alox/al/alox/nb tunnel junctions. *Physics Letters A*, 269(4), 2000. doi: 10.1016/S0375-9601(00)00263-2.
- [170] E. Zhitlukhina, I. Devyatov, O. Egorov, M. Belogolovskii, and P. Seidel. Anomalous inner-gap structure in transport characteristics of superconducting junctions with degraded interfaces. *Nanoscale Res. Lett.*, 11(58), 2016. doi: 10.1186/s11671-016-1285-0.
- [171] M. Hatano, T. Nishino, H. Hasegawa, F. Murai, T. Kure, and H. Nakane. Study of superconducting proximity effect by measuring interference effect of andreev-reflected quasiparticles. *J. Appl. Phys.*, 69(11), 1991. doi: 10.1063/1.347546.
- [172] W. Belzig, C. Bruder, and Gerd Schon. Local density of states in a dirty normal metal connected to a superconductor. *Phys. Rev. B.*, 54(13), 1996. doi: 10.1103/PhysRevB.54.9443.
- [173] F. Herman and R. Hlubina. Microscopic interpretation of the dynes formula for the tunneling density of states. *Phys. Rev. B.*, 94(14), 2016. doi: 10.1103/PhysRevB.94.144508.
- [174] Y. Hong. *Device Development and Characterization for Solid-State Quantum Computation*. Thesis, 2021.
- [175] A. G. Shard. Detection limits in xps for more than 6000 binary systems using al and mg $k\alpha$ x-rays. *Surf. Interface. Anal.*, 46(3), 2014. doi: 10.1002/sia.5406.
- [176] J. K. Julin and I. J. Maasilta. Applications and non-idealities of submicron al-alox-nb tunnel junctions. *Superconductor Science and Technology*, 29(10), 2016. doi: 10.1088/0953-2048/29/10/105003.
- [177] A. P. M. Place, L. V. H. Rodgers, P. Mundada, B. M. Smitham, M. Fitzpatrick, and Z. Leng. New material platform for superconducting transmon qubits with coherence times exceeding 0.3 milliseconds. *Nature Communications*, 12, 2021. doi: 10.1038/s41467-021-22030-5.

- [178] J. H. Claasen, S. Adrian, and R. J. Soulen. Large non-linear kinetic inductance in superconductor / normal metal bilayer films. *IEEE Trans Appl Supercond*, 9(2), 1999. doi: 10.1109/77.783948.
- [179] R. J. Schoelkopf, P. Wahlgren, A. A. Kozhevnikov, P. Delsing, and D. E. Prober. The radio-frequency single-electron transistor (rf-set): A fast and ultrasensitive electrometer. *Science*, 280(5367), 1998. doi: 10.1126/science.280.5367.1238.
- [180] J. I. Colles, A. C. Mahoney, J. M. Hornibrook, A. C. Doherty, H. Lu, A. C. Gossard, and D. J. Reilly. Dispersive readout of a few-electron double quantum dot with fast rf gate sensors. *Phys. Rev. Lett.*, 110(4), 2013. doi: 10.1103/PhysRevLett.110.046805.
- [181] A. J. Annunziata, D. F. Santavicca, L. Frunzio, G. Catelani, M. Rooks, A. Frydman, and D. E. Prober. Tunable superconducting nanoinductors. *Nanotechnology*, 21(44), 2010. doi: 10.1088/0957-4484/21/44/445202.
- [182] R. S. Beeresha, A. M. Khan, and H. V. Manjunath Reddy. Design and optimization of interdigital capacitor. *International Journal of Research in Engineering and Technology*, 5(21), 2016. ISSN 2319-1163.
- [183] K. S. Ilin, S. A. Vitusevich, B. B. Jin, A. I. Gubin, N. Klein, and M. Siegel. Peculiarities of the thickness dependence of the superconducting properties of thin nb films. *Physica C: Superconductivity*, 408-410, 2004. doi: 10.1016/j.physc.2004.03.118.